

**INVESTIGATION OF GLYCOLIPIDS SELF-ASSEMBLIES
USING FLUORESCENCE SPECTROSCOPY AND
SMALL-ANGLE X-RAY SCATTERING**

NOOR IDAYU BINTI MAT ZAHID

**THESIS SUBMITTED IN FULFILMENT OF
THE REQUIREMENTS FOR THE DEGREE OF
DOCTOR OF PHILOSOPHY**

**DEPARTMENT OF CHEMISTRY
FACULTY OF SCIENCE
UNIVERSITY OF MALAYA
KUALA LUMPUR**

2013

UNIVERSITI MALAYA

ORIGINAL LITERARY WORK DECLARATION

Name of Candidate: **NOOR IDAYU BINTI MAT ZAHID** (I.C /Passport No: **860518-14-5096**)

Registration/Matric No: **SHC090056**

Name of Degree: **DOCTOR OF PHILOSOPHY**

Title of Project Paper/Research Report/Dissertation/Thesis ("this Work"):

**INVESTIGATION OF GLYCOLIPIDS SELF-ASSEMBLIES USING FLUORESCENCE
SPECTROSCOPY AND SMALL-ANGLE X-RAY SCATTERING**

Field of Study: **PHYSICAL CHEMISTRY**

I do solemnly and sincerely declare that:

- (1) I am the sole author/writer of this Work;
- (2) This Work is original;
- (3) Any use of any work in which copyright exists was done by way of fair dealing and for permitted purposes and any excerpt or extract from, or reference to or reproduction of any copyright work has been disclosed expressly and sufficiently and the title of the Work and its authorship have been acknowledged in this Work;
- (4) I do not have any actual knowledge nor do I ought reasonably to know that the making of this work constitutes an infringement of any copyright work;
- (5) I hereby assign all and every rights in the copyright to this Work to the University of Malaya ("UM"), who henceforth shall be owner of the copyright in this Work and that any reproduction or use in any form or by any means whatsoever is prohibited without the written consent of UM having been first had and obtained;
- (6) I am fully aware that if in the course of making this Work I have infringed any copyright whether intentionally or otherwise, I may be subject to legal action or any other action as may be determined by UM.

Candidate's Signature

Date: **25/07/2013**

Subscribed and solemnly declared before,

Witness's Signature

Date: **25/07/2013**

Name: **RAUZAH HASHIM**
Designation: **PROFESSOR**

ABSTRACT

Glycolipids are one of the essential components of the cell membranes to carry out selected biological functions. Even though the study to resolve the ambiguity of biological membrane processes is continuously pursued, it is now generally recognized that the lipids form lyotropic mesophases in the membranes. These phases are important biologically and technologically, thus our interest to characterize them. Herein, we investigate the microenvironment of various lipidic phases formed by mono- and dialkylated synthetic glycolipids using fluorescence technique. Both single and branched-chain synthetic glycolipids were observed to exhibit normal and inverse mesophases respectively. The polarity of different regions of the hydrophilic head group was estimated on the basis of a parallel study in different solvents using small fluorescent probes namely tryptophan (Trp) and two of its ester derivatives (Trp-C₄ and Trp-C₈). In contrast, the hydrophobic nature of pyrene is expected to favour the tail region of the self-assembly. The ratio of the two peak intensities (I_1/I_3) in the pyrene fluorescence spectra was used to elucidate the local environment of pyrene since it is environmentally sensitive. In addition, the lifetimes of all fluorescent probes in buffer and lipid were measured. We have also performed thermotropic and lyotropic investigations on four anomeric-epimeric related branched-chain glycolipids derived from Guerbet alcohols using small-angle X-ray scattering to obtain their detailed structural information as well as their partial binary phase diagram. Similar fluorescence study was carried out for one of these branched-chain glycolipids, which gave extensive inverse bicontinuous cubic phase. The results presented here are believed to be important for a better understanding of the glycolipids fundamental properties which may help uncover some biological mysteries.

ABSTRAK

Glikolipid merupakan salah satu komponen utama membran sel untuk menjalankan fungsi biologikal tertentu. Walaupun kajian bagi merungkai kesamaran dalam proses membran biologi masih lagi berterusan, kini, umum telah mengiktiraf bahawa lipid membentuk mesofasa-mesofasa liotropik di dalam membran. Fasa-fasa ini penting secara biologi dan teknologi, oleh yang demikian, adalah perlu untuk mencirikannya dalam tesis ini. Kami menyiasat persekitaran mikro pelbagai fasa lipid yang dibentuk oleh glikolipid sintetik mono- dan dialkil menggunakan teknik pendafluor. Kedua-dua rantaian tunggal dan bercabang glikolipid sintetik masing-masing dilihat mempamer mesofasa normal dan songsang. Kekutuban bahagian berbeza pada kumpulan kepala berkutub telah dianggar berasaskan kajian selari di dalam larutan yang berlainan dengan menggunakan prob pendafluor kecil iaitu tryptophan (Trp) dan dua terbitan esternya (Trp-C₄ dan Trp-C₈). Sebaliknya, sifat hidrofobik pyrene dijangka cenderung kepada bahagian ekor suar penyusunan. Nisbah keamatan dua puncak (I_1/I_3) pada spektra pendafluor pyrene yang sensitif terhadap persekitaran telah digunakan untuk menjelaskan persekitaran setempat pyrene. Selain itu, masa hayat semua prob pendafluor di dalam bufer dan lipid telah diukur. Siasatan termotropik dan liotropik juga telah dijalankan bagi empat glikolipid bercabang terbitan alkohol Guerbet yang berkait secara anomerik dan epimerik menggunakan penyerakan sinar-X bersudut kecil untuk mendapatkan maklumat struktur dan gambarajah fasa separa binari sebatian tersebut. Kajian pendafluor seperti di atas telah dilakukan terhadap salah satu glikolipid rantaian bercabang yang memberi fasa kubik dwisambungan songsang. Hasil kajian ini penting untuk pemahaman yang lebih mendalam tentang sifat asas glikolipid yang mampu membantu mendedahkan beberapa misteri biologikal.

ACKNOWLEDGMENTS

First of all, I would like to express my utmost gratitude to my supervisor, Professor Dr. Rauzah Hashim for her guidance, patience and encouragement throughout my studies and research. Thank you for your motivation and enthusiasm for science to follow in the coming days of my research career.

Acknowledgements are also extended to Associate Professor Dr. Osama K. Abou-Zied from Sultan Qaboos University for his support and continuous discussions during his supervision on the fluorescence work. I would like to extend my thanks to Professor Dr. John M. Seddon, Dr. Charlotte E. Conn and Dr. Nicholas J. Brooks for giving me the opportunities to come and spend time in their labs.

I also would like to thank University Malaya, Sultan Qaboos University, and CSIRO Manufacturing, Materials & Minerals for providing equipments and facilities for the research. Not to forget, a special thanks to Dr. Nigel Kirby, Dr. Stephen Mudie and Dr. Adrian Hawley at the Australian Synchrotron for their assistance.

In addition, I would like to express a big thank you to my colleagues Dr. Karem Sabah, Associate Professor Dr. Thorsten Heidelberg, Dr. Rusnah Syahila, Dr. Noraini Ahmad, Seyed Mirzadeh Hosseini, Faramarz Aliasghari Sani, Vijayan Manickam Achari, Nguan Hock Seng, Sara Ahmadi, Zahrabatoul Mosapour and Hairul Amani for their help in the equipments and techniques as well as for the useful discussions.

I am also deeply grateful to my beloved family and friends whose love and guidance are with me in whatever I pursue. They are the strongest supporters.

I extend my thanks to Skim Latihan Akademik Bumiputera Fellowship, Postgraduate Research Grant, Student Exchange Program Grant, OCAR Grant and High Impact Research Grants (Chancellery and Faculty) for the financial supports.

TABLE OF CONTENTS

ABSTRACT	iii
ABSTRAK	iv
ACKNOWLEDGEMENTS	v
TABLE OF CONTENTS	vi
LIST OF FIGURES	x
LIST OF TABLES	xvi
LIST OF SYMBOLS AND ABBREVIATIONS	xviii
LIST OF APPENDICES	xxi
 CHAPTER 1: INTRODUCTION AND LITERATURE REVIEW	 1
1.1 Natural Glycolipids	2
1.2 Synthetic Glycolipids	6
1.3 Glycolipids as Liquid Crystal	9
1.4 General Descriptions of Liquid Crystals	10
1.5 Thermotropic Liquid Crystals	14
1.5.1 Monophilic Liquid Crystals	14
1.5.2 Amphiphilic Liquid Crystals	21
1.6 Lyotropic Liquid Crystals	22
1.6.1 Hypothetical Binary Phase Diagram	28
1.6.2 Molecular Packing Parameter	32
1.6.3 Interfacial Curvature	33
1.7 Theory of Liquid Crystals	36
1.8 Structure-Property Relationship	38
1.8.1 Head Group	38

1.8.2	Linkage	42
1.8.3	Hydrocarbon Chain	43
1.9	Objectives and Overview of Thesis	44
CHAPTER 2: TECHNIQUES AND METHODS		47
2.1	Optical Polarizing Microscopy (OPM)	49
2.1.1	Defect and Texture of Mesophases	52
2.1.2	Thermotropic Phase Behaviour	59
2.1.3	Lyotropic Phase Behaviour	59
2.2	Differential Scanning Calorimetry (DSC)	60
2.3	Small-Angle X-ray Scattering (SAXS)	62
2.4	Fluorescence	66
2.4.1	Steady-State Fluorescence Spectroscopy	70
2.4.2	Time-Resolved Fluorescence Spectroscopy	71
CHAPTER 3: CHARACTERIZATION OF THE HEAD GROUP AND THE HYDROPHOBIC REGIONS OF A GLYCOLIPID LYOTROPIC HEXAGONAL PHASE USING FLUORESCENT PROBES		74
3.1	Introduction	75
3.2	Research Methodology	78
3.2.1	Materials	78
3.2.2	Sample Preparation	79
3.2.3	Instrumentation	80
3.3	Results and Discussion	80
3.3.1	Probing the Polar Region of the Lipid	80
3.3.2	Probing the Hydrophobic Region of the Lipid	86
3.4	Conclusions	91

CHAPTER 4: FLUORESCENCE PROBING OF THE TEMPERATURE-INDUCED PHASE TRANSITION IN A GLYCOLIPID SELF-ASSEMBLY: HEXAGONAL MICELLAR AND CUBIC LAMELLAR	93
4.1 Introduction	94
4.2 Research Methodology	96
4.2.1 Materials	96
4.2.2 Sample Preparation	96
4.2.3 Instrumentation	97
4.3 Results and Discussion	98
4.3.1 Probing the Polar Region of the Lipid	98
4.3.2 Probing the Hydrophobic Region of the Lipid	103
4.4 Conclusions	109
 CHAPTER 5: INVESTIGATION ON THE EFFECT OF SUGAR STEREOCHEMISTRY ON BRANCHED-CHAIN GLYCOLIPIDS SELF-ASSEMBLY BY SMALL- ANGLE X-RAY SCATTERING	 111
5.1 Introduction	112
5.2 Research Methodology	116
5.2.1 Preparation of Compounds	116
5.2.2 Optical Polarizing Microscopy (OPM)	117
5.2.3 Differential Scanning Calorimetry (DSC)	117
5.2.4 Binary Phase Behaviour	118
5.2.5 Small-Angle X-ray Scattering (SAXS)	118
5.2.6 Calculation of Structural Parameters	119
5.3 Results and Discussion	121
5.3.1 Thermotropic Phase Behaviour	121
5.3.2 Lyotropic Phase Behaviour	127

5.3.3	Anomeric-Epimeric Relationships	145
5.4	Conclusions	147
CHAPTER 6: CHARACTERIZATION OF THE INVERSE PHASE OF A BRANCHED-CHAIN GLYCOLIPID SELF- ASSEMBLY USING FLUORESCENT PROBES		149
6.1	Introduction	150
6.2	Research Methodology	152
6.2.1	Materials	152
6.2.2	Sample Preparation	152
6.2.3	Instrumentation	153
6.3	Results and Discussion	153
6.3.1	Probing the Polar Region of the Lipid	153
6.3.2	Probing the Hydrophobic Region of the Lipid	158
6.4	Conclusions	162
CHAPTER 7: CONCLUSIONS		164
APPENDIX A: DIFFERENTIAL SCANNING CALORIMETRY SPECTRA		169
APPENDIX B: SMALL-ANGLE X-RAY SCATTERING DATA		173
REFERENCES		185
LIST OF SCIENTIFIC CONTRIBUTIONS		196

LIST OF FIGURES

Figure 1.1 : The cell membrane and its components. Adopted from [11].	3
Figure 1.2 : A few examples of natural GLs. (a) and (b) are glycosphingolipids, (c) and (d) are glycoglycerolipids and (e) is a glycosyl phosphopolyrenol. Red box: sphingoid base. Blue box: glycerol backbone.	4
Figure 1.3 : A few examples of synthetic GLs.	9
Figure 1.4 : Geometry used for defining the order parameter. Redrawn from [56].	12
Figure 1.5 : Preferred molecule orientation, \hat{n} within a domain (represented by a loosely-defined boundary).	12
Figure 1.6 : Molecular structure of a rod-like liquid crystal. Redrawn from [57].	13
Figure 1.7 : Molecular shapes of monophilic liquid crystals. Redrawn from [60].	14
Figure 1.8 : The molecular organization of calamatic liquid crystals. The vector, \hat{n} represents the director and k is the layer normal. Redrawn from [60].	15
Figure 1.9 : Some examples of compounds that exhibit nematic phase together with their liquid crystals phase behaviours (Cr means crystal, I stands for isotropic and N denotes nematic phase) [63].	16
Figure 1.10: Cholesteryl benzoate that exhibits cholesteric phase together with its liquid crystals phase behaviours. (Cr means crystal, I stands for isotropic and N* denotes chiral nematic phase) [66].	17
Figure 1.11: Some examples of compounds that exhibit smectic phase together with their liquid crystal phase behaviours (Cr means crystal, I stands for isotropic, N refers to nematic, SmA denotes smectic A and SmC implies smectic C phase) [53].	18
Figure 1.12: A typical chemical structure of discotic mesogens: (a) hexa-n-alkanoates of triphenylene and hexa-n-alkoxytriphenylene (b) hexakis ((4-octylphenyl)ethynyl) benzene [53].	19
Figure 1.13: Schematic illustration of discotic liquid crystals. Redrawn from [57].	20
Figure 1.14: Rod-like polymeric liquid crystal. Redrawn from [53].	21
Figure 1.15: Structural models of GLs. Redrawn from [19].	22

Figure 1.16: Schematic structures of lamellar phases. Redrawn from [48].	24
Figure 1.17: The bicontinuous cubic phase of an amphiphilic molecule. Redrawn from [84].	25
Figure 1.18: Structures of inverse bicontinuous cubic phases. Adopted from [81].	26
Figure 1.19: Polyhedral micellar arrangement of discontinuous cubic phase. Adopted from [79].	27
Figure 1.20: Schematic structures of hexagonal phases. Redrawn from [79].	28
Figure 1.21: Hypothetical lipid/water binary phase diagram. Redrawn from [95].	30
Figure 1.22: An example of binary phase diagram of <i>n</i> -octyl- β -D-glucoside in water by (a) small angle X-ray scattering [96] (b) fluorescence spectroscopy [97].	30
Figure 1.23: Sign convention adopted for mean curvature, H of a lipid monolayer. Redrawn from [103].	35
Figure 1.24: Saddle surface of negative Gaussian curvature, K . Redrawn from [103].	36
Figure 1.25: The chemical structures of the 1,3-di- <i>O</i> -dodecyl-2- <i>O</i> -(β -glycosyl) glycerols bearing a series of (a) maltose and (b) cellobiose oligosaccharides as the head group [109].	39
Figure 1.26: The chemical structures of macrocyclic ethers on lauryl glucoside at positions (a) O-2 and O-3 and (b) O-4 and O-6 [110].	40
Figure 1.27: The chemical structures of methyl-6- <i>O</i> -dodecanoyl- α -D-glucoside [111].	41
Figure 1.28: Examples of compounds with (a) sulphur linkage [112] and (b) amide linkage [113].	42
Figure 1.29: The general chain length dependency of homologous series. Redrawn from [19].	43
Figure 2.1 : Schematic setup of an optical polarizing microscope. Redrawn from [60].	50
Figure 2.2 : Basic principle of an optical polarizing microscope. Adopted from [122].	51
Figure 2.3 : Alignment of liquid crystals in nematic phase. Redrawn from [56].	52
Figure 2.4 : Director configurations due to defect lines in nematic Schlieren	53

textures. Adopted from [60].

Figure 2.5 : Textures of nematic phases. Adopted from [60].	54
Figure 2.6 : Three types of disclinations in cholesteric phase. Adopted from [57].	54
Figure 2.7 : Textures of cholesteric phases. Adopted from [60].	55
Figure 2.8 : The general case when the smectic layers form Dupin cyclides. Adopted from [53].	56
Figure 2.9 : Textures of smectic phases. Adopted from [60].	57
Figure 2.10: Interference colour chart or Michel-Lévy chart. Adopted from [124].	58
Figure 2.11: The water penetration techniques. Redrawn from [6].	60
Figure 2.12: Schematic diagram of a (a) differential scanning calorimeter and (b) typical DSC curve. Redrawn from [128].	61
Figure 2.13: Bragg's Law. Redrawn from [134].	63
Figure 2.14: The form factor, $P(q)$ of a particle is an interference pattern. $ \vec{E}_s(q) ^2$ is the squared amplitude of the wave as a function of q . Redrawn from [131].	64
Figure 2.15: The components of an SAXS instrument. Redrawn from [131].	66
Figure 2.16: A typical Jablonski diagram. Redrawn from [137].	67
Figure 2.17: Possible electronic states (1L_a and 1L_b) of the indole system of tryptophan [152].	69
Figure 2.18: Schematic diagram of steady-state fluorescence spectrometer. Redrawn from [137].	71
Figure 2.19: Schematic diagram of the time-resolved fluorescence spectrometer (stroboscopic technique). Redrawn from [136].	72
Figure 3.1 : The chemical structure of n-dodecyl β -D-maltoside (β -Mal-OC ₁₂).	76
Figure 3.2 : The chemical structures of the fluorescent probes.	77
Figure 3.3 : A schematic diagram showing one layer of the lipid self-assembly with the expected locations of the probes. Pink: tryptophan (Trp). Red: Trp-C ₈ . Green: pyrene.	78
Figure 3.4 : Fluorescence spectra of tryptophan in different solvents. $\lambda_{ex} = 280$ nm.	81
Figure 3.5 : Fluorescence spectra of tryptophan and its derivatives in buffer of pH 7.2. $\lambda_{ex} = 280$ nm.	82

Figure 3.6 : Fluorescence spectra of tryptophan and its derivatives in lipid. The spectrum of tryptophan in buffer is included for comparison. The spectra are normalized for easy comparison. $\lambda_{\text{ex}} = 280$ nm.	83
Figure 3.7 : Fluorescence spectra of pyrene dissolved in buffer and cyclohexane. $\lambda_{\text{ex}} = 340$ nm.	87
Figure 3.8 : Fluorescence spectra of lipid containing pyrene (Py) and Py + Trp-C ₈ . $\lambda_{\text{ex}} = 340$ nm.	88
Figure 3.9 : Fluorescence decay transients of pyrene probed using Schott WG- 380 filter. Black: pyrene in buffer. Blue: pyrene in buffer containing Trp-C ₈ . Green: pyrene in lipid. Red: pyrene in lipid containing Trp-C ₈ . Pink: pyrene in buffer probed using Schott WG-455 filter. $\lambda_{\text{ex}} = 340$ nm. IRF is shown by a dashed line.	90
Figure 4.1 : The chemical structure of n-octyl β -D-glucoside (β -Glc-OC ₈).	95
Figure 4.2 : Fluorescence spectra of tryptophan and its derivatives in different solvents and in the hexagonal phase of the β -Glc-OC ₈ lipid. $\lambda_{\text{ex}} = 280$ nm.	98
Figure 4.3 : Fluorescence spectra of Trp-C ₈ embedded in the hexagonal phase of the maltoside lipid (β -Mal-OC ₁₂) and the glucoside lipid (β -Glc-OC ₈). $\lambda_{\text{ex}} = 280$ nm.	100
Figure 4.4 : Fluorescence spectra of Trp-C ₈ embedded in the cubic phase and lamellar phase of the β -Glc-OC ₈ . $\lambda_{\text{ex}} = 280$ nm.	101
Figure 4.5 : Fluorescence decay transients of Trp-C ₈ in buffer alone and in buffer containing the hexagonal phase of the β -Glc-OC ₈ lipid. $\lambda_{\text{ex}} = 280$ nm. IRF is shown by a dashed line.	102
Figure 4.6 : Fluorescence spectra of pyrene dissolved in cyclohexane, and in buffer alone, and buffer containing the cubic phase of the β -Glc-OC ₈ . $\lambda_{\text{ex}} = 340$ nm.	104
Figure 4.7 : A schematic diagram showing the effect of the different geometries of the cubic phase (left) and the lamellar phase (right) on the exposure of pyrene to water. Water direction is represented by arrows.	106
Figure 5.1 : The chemical structures of the four branched-chain C ₁₆ glycopyranosides.	116
Figure 5.2 : The liquid crystalline texture at 30 °C upon cooling for the four compounds at magnification factor of 20.	122
Figure 5.3 : The solid crystalline texture of β -Gal-OC ₁₀ C ₆ at magnification factor of 10: (a) at room temperature (b) the same position at 42 °C.	123

Figure 5.4 :	DSC scans for the four compounds at heating rate of 5 °C/min.	125
Figure 5.5 :	Water penetration scans for the four compounds at magnification factor of 20. We label the unidentified cubic phases as, Q_{II} , Q_{II}^1 , and Q_{II}^2 .	128
Figure 5.6 :	Partial binary phase diagrams of the four compounds in the heating direction. SAXS results are represented as L_2 (●); L_α (●); Q_{II}^G (×); Q_{II}^D (◇); H_{II} (▲). Polarizing microscopy results are shown as shaded areas. The phases observed include an anisotropic phase, a viscous isotropic phase and a co-existence of both anisotropic and viscous isotropic phases. The excess water points are represented by bold dashed lines.	130
Figure 5.7 :	Representative small-angle X-ray scattering (SAXS) patterns for (a) dry α -Glc-OC ₁₀ C ₆ at 30°C. The first order reflection of an L_α phase is seen. (b) dry β -Gal-OC ₁₀ C ₆ at 44°C. The $\sqrt{1}$, $\sqrt{3}$, $\sqrt{4}$, $\sqrt{7}$ and $\sqrt{9}$ reflections of a H_{II} are observed. (c) β -Glc-OC ₁₀ C ₆ with 10% (w/w) at 10°C. The $\sqrt{6}$, $\sqrt{8}$, $\sqrt{14}$, $\sqrt{16}$, $\sqrt{20}$, $\sqrt{22}$ and $\sqrt{24}$ reflections of a Q_{II}^G phase are seen. (d) α -Gal-OC ₁₀ C ₆ with 60% (w/w) at 10°C. The $\sqrt{2}$, $\sqrt{3}$, $\sqrt{4}$, $\sqrt{6}$, $\sqrt{8}$, $\sqrt{9}$ and $\sqrt{10}$ reflections of a Q_{II}^D phase are seen. (e) Co-existing L_α and Q_{II}^G phases of α -Glc-OC ₁₀ C ₆ with 20% (w/w) at 12°C. The first order reflection of an L_α phase is seen. (f) Co-existing Q_{II}^G and Q_{II}^D phases of β -Glc-OC ₁₀ C ₆ with 60% (w/w) at 30°C. The $\sqrt{2}$, $\sqrt{3}$, $\sqrt{4}$ and $\sqrt{6}$ reflections of a Q_{II}^D phase are seen, together with the Q_{II}^G peaks.	134
Figure 5.8 :	SAXS patterns under dry and wet conditions: (a) L_α at 44 °C, (b) Q_{II}^D at 30 °C with 80% (w/w), (c) H_{II} at 44 °C, (d) Q_{II}^G at 30 °C with 80% (w/w), (e) Q_{II}^G at 44 °C, (f) Q_{II}^D at 24 °C with 80% (w/w), (g) H_{II} at 44 °C, (h) H_{II} at 30 °C with 80% (w/w).	138
Figure 5.9 :	Temperature dependence of the lattice parameter of the mesophases for α -Glc-OC ₁₀ C ₆ /water. Symbols: L_α (●); Q_{II}^G (×); Q_{II}^D (◇).	141
Figure 5.10:	Temperature dependence of the lattice parameter of the mesophases for β -Glc-OC ₁₀ C ₆ /water. Symbols: Q_{II}^G (×); Q_{II}^D (◇).	141
Figure 5.11:	Temperature dependence of the lattice parameter of the mesophases for α -Gal-OC ₁₀ C ₆ /water. Symbols: H_{II} (▲); Q_{II}^G (×); Q_{II}^D (◇).	142
Figure 5.12:	Temperature dependence of the lattice parameter of the mesophases for β -Gal-OC ₁₀ C ₆ /water. Symbols: H_{II} (▲); Q_{II}^G (×); Q_{II}^D (◇).	142
Figure 5.13:	Composition dependence of the lattice parameter of the mesophases at 24 °C. Symbols: L_α (●); Q_{II}^G (×); Q_{II}^D (◇); H_{II} (▲).	143
Figure 5.14:	Shape factor, γ values for cubic phases and their (a) water content and (b) temperature dependence for α -Gal-OC ₁₀ C ₆ /	144

water. Symbols: $Q_{II}^G (\times)$; $Q_{II}^D (\diamond)$.

Figure 5.15: $\langle H_{hc} \rangle$ values for cubic phases and their (a) water content and (b) temperature dependence for α -Gal-OC ₁₀ C ₆ /water. Symbols: $Q_{II}^G (\times)$; $Q_{II}^D (\diamond)$.	145
Figure 6.1 : The chemical structure of 2-hexyl-decyl- β -D-glucopyranoside (β -Glc-OC ₁₀ C ₆).	151
Figure 6.2 : Fluorescence spectra of tryptophan and its derivatives in different solvents and in the inverse cubic phase of the β -Glc-OC ₁₀ C ₆ lipid. $\lambda_{ex} = 280$ nm.	153
Figure 6.3 : Fluorescence spectra of Trp embedded in the normal cubic phase of β -Glc-OC ₈ and the inverse cubic phase of β -Glc-OC ₁₀ C ₆ . $\lambda_{ex} = 280$ nm.	154
Figure 6.4 : Fluorescence decay transients of Trp-C ₈ in buffer alone and in buffer containing the inverse cubic phase of β -Glc-OC ₁₀ C ₆ . $\lambda_{ex} = 280$ nm. IRF is shown by a dashed line.	158
Figure 6.5 : Fluorescence spectra of pyrene dissolved in cyclohexane, in buffer alone and buffer containing the inverse cubic phase of the β -Glc-OC ₁₀ C ₆ lipid. $\lambda_{ex} = 340$ nm.	159
Figure 6.6 : A schematic diagram showing the pyrene molecule in the hydrophobic region of the cubic <i>Ia3d</i> phase. The continuous blue area is the aqueous channel of size 23 Å.	160

LIST OF TABLES

Table 1.1 :	Water channel network of inverse bicontinuous cubic phase.	26
Table 1.2 :	Preferred geometries for different values of critical packing parameter. Redrawn from [101].	33
Table 1.3 :	Mean and Gaussian curvature of interfaces of different types of aggregate [80, 103].	34
Table 3.1 :	Fluorescence spectral peak maxima of tryptophan and its derivatives in different solvents and lipid.	81
Table 3.2 :	Fluorescence lifetime (ns) measurements of tryptophan and its derivatives in buffer and lipid.	86
Table 3.3 :	Fluorescence intensity ratio of the vibronic peaks of pyrene (I_1/I_3) in the hexagonal phase of the β -Mal-OC ₁₂ lipid. $\lambda_{ex} = 340$ nm.	89
Table 3.4 :	Fluorescence lifetime (ns) measurements of pyrene and pyrene with Trp-C ₈ in buffer and lipid.	90
Table 4.1 :	Fluorescence spectral peak maxima of tryptophan and its derivatives in hexagonal phase of different lipid. $\lambda_{ex} = 280$ nm.	100
Table 4.2 :	Fluorescence intensity ratio of the vibronic peaks of pyrene (I_1/I_3) in different phases of the β -Glc-OC ₈ lipid: hexagonal (H_1); micellar (I_1); cubic (Q_1); and lamellar (L_α). $\lambda_{ex} = 340$ nm.	105
Table 4.3 :	Fluorescence lifetime (ns) measurements of pyrene, pyrene + Trp, and pyrene + Trp-C ₈ in 65% (w/w) aqueous formulation of lipid.	108
Table 4.4 :	Fluorescence lifetime (ns) measurements of pyrene, pyrene + Trp, and pyrene + Trp-C ₈ in 80% (w/w) aqueous formulation of lipid.	108
Table 5.1 :	Thermotropic phase transition temperatures measured above 23 °C by OPM.	124
Table 5.2 :	Thermotropic phase transition temperatures and [enthalpies] at heating rate of 5 °C/min.	126
Table 5.3 :	Phase assignments and lattice parameters for α -Glc-OC ₁₀ C ₆ as a function of water content and temperature. Error in lattice parameter measurements is < 0.1 Å.	131
Table 5.4 :	Phase assignments and lattice parameters for β -Glc-OC ₁₀ C ₆ as a function of water content and temperature. Error in lattice parameter measurements is < 0.1 Å.	132

Table 5.5 :	Phase assignments and lattice parameters for α -Gal-OC ₁₀ C ₆ as a function of water content and temperature. Error in lattice parameter measurements is $< 0.1 \text{ \AA}$.	132
Table 5.6 :	Phase assignments and lattice parameters for β -Gal-OC ₁₀ C ₆ as a function of water content and temperature. Error in lattice parameter measurements is $< 0.1 \text{ \AA}$.	132
Table 5.7 :	Characteristics spacing ratios of phases obtained.	137
Table 5.8 :	Anomeric-Epimeric relationship of thermotropic liquid crystalline phases determined by OPM (above 23°C).	146
Table 6.1 :	Fluorescence spectral peak maxima of tryptophan and its derivatives in the normal cubic phase of β -Glc-OC ₈ and the inverse cubic phase of β -Glc-OC ₁₀ C ₆ . $\lambda_{\text{ex}} = 280 \text{ nm}$.	155
Table 6.2 :	Fluorescence intensity ratio of the vibronic peaks of pyrene (I_1/I_3) in the normal cubic phase of the β -Glc-OC ₈ lipid and the inverse cubic phase of the β -Glc-OC ₁₀ C ₆ lipid. $\lambda_{\text{ex}} = 340 \text{ nm}$.	161
Table 6.3 :	Fluorescence lifetime (ns) data of pyrene, pyrene + Trp, and pyrene + Trp-C ₈ in the inverse cubic phase of the β -Glc-OC ₁₀ C ₆ lipid.	162

LIST OF SYMBOLS AND ABBREVIATIONS

% (w/w)	Mass fraction
γ	Shape factor
τ	Lifetime
1-D	One-dimensional
2-D	Two-dimensional
3-D	Three-dimensional
α	Alpha
AG	Alkyl glycoside
APG	Alkyl polyglycoside
β	Beta
Col	Columnar
Cr	Crystalline
DGDG	Digalactosyl diacylglycerol
DPD	Dissipative Particle Dynamics
DSC	Differential Scanning Calorimetry
e.g.	exempli gratia; for example
et al.	et alii; and others
etc.	et cetera; and the others
FWHM	Full Width at Half Maximum
Gal	Galactose
GL	Glycolipid
Glc	Glucose
ΔH	Enthalpy
H	Mean curvature
H_I	Normal hexagonal phase
H_{II}	Inverse hexagonal phase
I	Isotropic phase
I_I	Normal discontinuous cubic phase
I_I/I_3	Vibronic peaks intensity ratio
I_{II}	Inverse discontinuous cubic phase
i.e.	id est; that is
IRF	Instrument Response Function

k	Layer normal
K	Gaussian curvature
λ	Wavelength
λ_{ex}	Excitation wavelength
λ_{max}	Wavelength at maximum peak
L_1	Normal micellar solution
L_2	Inverse micellar solution
L_α	Lamellar liquid crystal phase
L_β	Gel phase
$L_{\beta'}$	Tilted gel phase
L_c	Lamellar crystal
LED	Light Emitting Diode
MBBA	4-methoxybenzylidene-4'- <i>n</i> -butylaniline
MGDG	Monogalactosyl diacylglycerol
\hat{n}	Director axis
N	Nematic phase
N*	Cholesteric phase
N _D	Nematic phase for of disc-like molecules
NMR	Nuclear Magnetic Resonance
OH	Hydroxyl group
OPM	Optical Polarizing Microscopy
P	Pitch
$P_{\beta'}$	Rippled phase
PC	Phosphatidylcholine
Py	Pyrene
Q _I	Normal bicontinuous cubic phase
Q _{II}	Inverse bicontinuous cubic phase
Q _{II} ^D	Schwarz diamond inverse bicontinuous cubic phase
Q _{II} ^G	Schoen gyroid inverse bicontinuous cubic phase
Q _{II} ^P	Primitive inverse bicontinuous cubic phase
S	Order parameter
SmA	Smectic A phase
SmC	Smectic C phase
SANS	Small-Angle Neutron Scattering
SAXS	Small-Angle X-ray Scattering

SQDG	Sulphoquinovosyl diacylglycerol
T _c	Clearing temperature
TLC	Thin Layer Chromatography
T _m	Melting temperature
TPMS	Triply Periodic Minimal Surface
Trp	Tryptophan
Trp-C ₄	Tryptophan butyl ester
Trp-C ₈	Tryptophan octyl ester
vs.	Versus
WAXS	Wide-Angle X-ray Scattering
χ^2	Reduced chi-squared
XRD	X-Ray Diffraction

LIST OF APPENDICES

Figure A1 : DSC scans for α -Glc-OC ₁₀ C ₆ at heating and cooling rates of 5 °C/min.	169
Figure A2 : DSC scans for β -Glc-OC ₁₀ C ₆ at heating and cooling rates of 5 °C/min.	170
Figure A3 : DSC scans for α -Gal-OC ₁₀ C ₆ at heating and cooling rates of 5 °C/min.	171
Figure A4 : DSC scans for β -Gal-OC ₁₀ C ₆ at heating and cooling rates of 5 °C/min.	172
Table B1 : Lattice parameter of α -Glc-OC ₁₀ C ₆ as a function of water content and temperature.	173
Table B2 : Lattice parameter of β -Glc-OC ₁₀ C ₆ as a function of water content and temperature.	176
Table B3 : Lattice parameter of α -Gal-OC ₁₀ C ₆ as a function of water content and temperature.	179
Table B4 : Lattice parameter of β -Gal-OC ₁₀ C ₆ as a function of water content and temperature.	182

CHAPTER 1

INTRODUCTION AND LITERATURE REVIEW

INTRODUCTION AND LITERATURE REVIEW

Cells are the building block of life. All living things are made up of one or more cells with specific parts performing specific functions. Inside a cell, there are thousands of organelles which perform a variety of specialized jobs. Each cell has a membrane that acts as the main barrier to the aqueous surrounding [1-4]. Glycolipids or GLs (this term will be used throughout the thesis for simplicity) are one of the essential cell membrane components which carry out some of these functions. These membrane constituents are also related to various diseases. For instance, the deposition of GLs called glucosyl ceramide (glucocerebroside) in the spleen and kidneys can lead to Gaucher's disease which is the most common inherited lysosomal storage disease caused by a deficiency in glucocerebrosidase enzyme [5, 6]. Given this knowledge, we are keen to more intensively study these GL molecules in particular, to understand their fundamental properties which may help uncover some biological mysteries.

This introductory chapter gives a brief review of both natural and synthetic GLs. Since these molecules give rise to liquid crystal phases, we also review the physics and chemistry of these materials, including their liquid crystal classification and structure-property relationship.

1.1 Natural Glycolipids

GLs are one of the components present in biological membranes, apart from phospholipids, proteins, carbohydrates and cholesterol. They are normally found on the exterior of cell surface membranes (see Figure 1.1) and have special physicochemical properties. For example, due to their location, GLs are excellent biomarkers for the isolation of various subsets of cells from the central nervous

system [7]. GLs are carbohydrate-attached lipids. The hydrophilic part comprises the sugar head group while the aliphatic hydrocarbon chain builds up the hydrophobic part of the molecule [8]. Therefore they are amphiphilic molecules which act as a mediator between the hydrophilic and lipophilic environments due to their unique chemical structure. Most GLs in biomembranes are double-chained (saturated and/or unsaturated) with 16 to 18 carbons per chain, thus allowing the formation of typically wedge-like molecular structures (similar to those of phospholipids) which are also ubiquitous in cell membranes [9, 10].

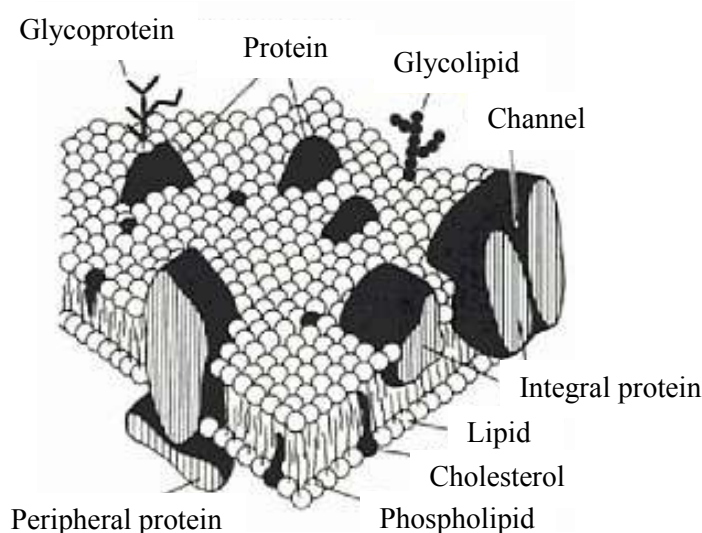
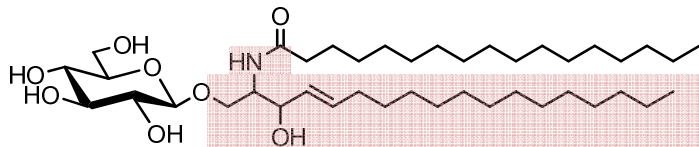


Figure 1.1: The cell membrane and its components. Adopted from [11].

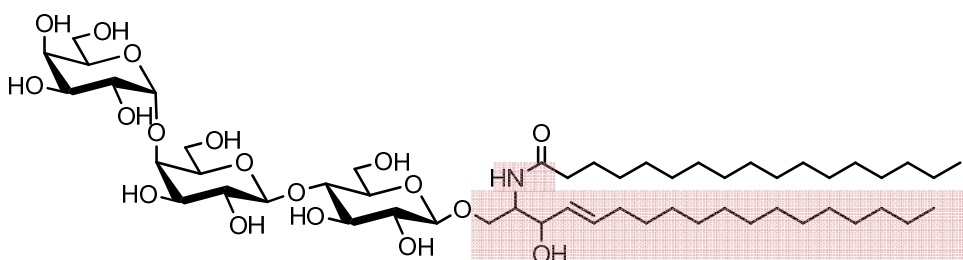
GLs are mainly found in tissues of plants, animals and microorganisms [12]. Even though not as abundant as other constituents of biomembranes, GLs play an important role in many cell processes [13] such as endo- and exocytosis, apoptosis, molecular recognition at the cell surface specific to the cell type [14], and stabilization of the membrane structures, for example, archaebacteria that grow under extreme environmental conditions [15]. GLs can be divided into three main

groups: *glycosphingolipids*, *glycoglycerolipids*, and *glycosyl phosphopolyprenols*.

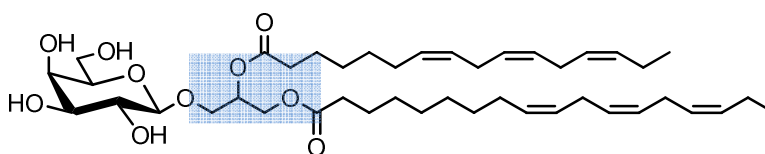
Some examples are shown in Figure 1.2.



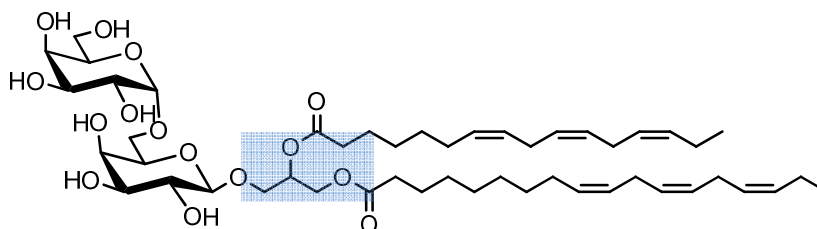
(a) Glucosyl ceramide (cerebroside). A component of nervous tissue [10].



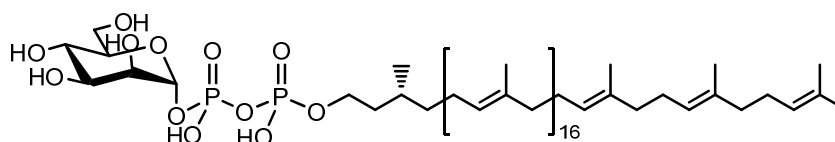
(b) Globotriaosyl ceramide (globoside-3). Minor component of tissue [10].



(c) Monogalactosyl diacylglycerol (MGDG). Found in chloroplasts [16].



(d) Digalactosyl diacylglycerol (DGDG). Found in chloroplasts [16].



(e) Mannosyl diphospho eicosaprenol. Found in bacterial system [17].

Figure 1.2: A few examples of natural GLs. (a) and (b) are glycosphingolipids, (c) and (d) are glycoglycerolipids and (e) is a glycosyl phosphopolyprenol. Red box: sphingoid base. Blue box: glycerol backbone.

Glycosphingolipids are formed when a carbohydrate moiety (hydrophilic part) is linked to the primary hydroxyl group of the sphingoid base (hydrophobic part) and they are subclassified into cerebrosides, globosides and gangliosides. The structure of glycosphingolipids is such that the carbohydrate is attached to C1 of sphingosine via the hydroxyl group and a fatty acid substituent on the amino group at C2. Glycosphingolipids are widely found in mammalian tissues and cells, although some may also be found in invertebrates, plants and microorganisms [18].

The second group of natural GLs is glycoglycerolipid which consists of 1,2-di-*O*-acyl-*sn*-glycerol joined by a glycosidic linkage at a position *sn*-3 to a carbohydrate moiety [19]. Glycoglycerolipids have been identified as significant GLs in bacteria, blue-green algae and plants, especially in chloroplast membranes. There are three glycoglycerolipids that are found in photosynthetic membrane [20, 21]. The two neutral galactolipids are monogalactosyl diacylglycerol (MGDG) and digalactosyl diacylglycerol (DGDG). Both account for about 80% of the lipid composition of thylakoid membrane (lipids make up about 50% of the thylakoid mass). The third class glycoglycerolipid, which is an anionic sulfolipid called sulphoquinovosyl diacylglycerol (SQDG) makes up about 10% of the thylakoid membrane [21].

Glycosyl phosphopolyprenols are biochemically different from other GLs. The linkage between sugar and lipid by a phosphate bridge is distinctive in GLs. Since this involves a sugar-1-phosphate bond, the transfer potential is similar to that of nucleotide diphosphate sugars, which leads to a difference in their respective function. Other GLs are seen primarily as end products of metabolism, or as intermediates solely as acceptors of further sugar residues. Glycosyl phosphopolyprenols for instance readily donate their glycosyl residues to some appropriate acceptor and are thus termed lipid-linked intermediates. The coenzymic

role of phosphopolyprenols differs in different types of organisms. For example, in bacteria, phosphopolyprenols are involved in the formation of the complex polysaccharides of the cell wall while in green plants, they are accountable for the production of glucans [22].

1.2 Synthetic Glycolipids

Recently, GLs have been recognized as a new class of amphiphilic surfactant in the field of colloid and interface science. They have attracted great interest in fundamental studies [15, 23, 24] and shown to have many possible applications [25-27]. However, natural GLs, for example, the MGDG and DGDG from photosynthetic thylakoid membrane of plants and algae are difficult to extract and purify in large quantities. Because of their growing potential in industrial applications, coupled with the difficulty of getting pure natural lipids with high yield, the demand for synthetic GLs is increasing. At the same time, it is a challenging task analyzing the mesogenic properties of well-defined compounds and how they relate to membrane properties [28]. Compared to other common generic surfactants, these synthetic GLs can be prepared chemically or enzymatically from renewable resources like oligosaccharides and fatty alcohols that are biodegradable, non-ionic and environmentally-friendly materials [15, 19].

Synthetic GLs may be grouped into those containing only a single chain and those containing branched chains. Single alkyl chain GLs are also known commonly as *sugar-based surfactants* [29]. Some examples of this group are sorbitan esters, sucrose esters, methyl glucoside esters, alkyl polyglycosides, and methyl glucamides. Among these, the most common is alkyl polyglycosides (APGs). Because of their favourable environmental character, these sugar surfactants have been widely used in the formulation of utility day-care products (e.g. washing,

dishwashing, and cleaning liquids). They also have wide application in the cosmetics industry since they exhibit good dermatological compatibility and biodegradability [30].

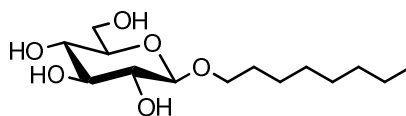
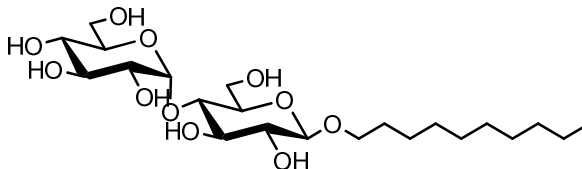
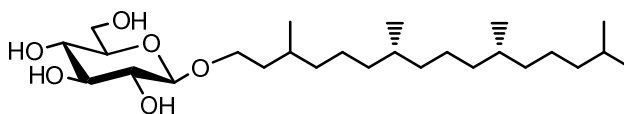
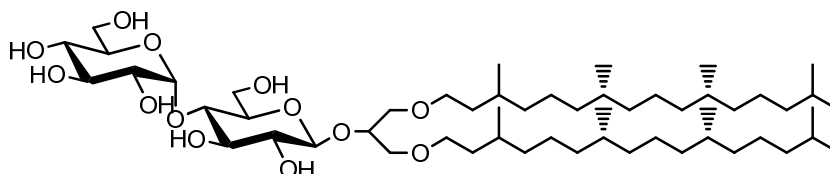
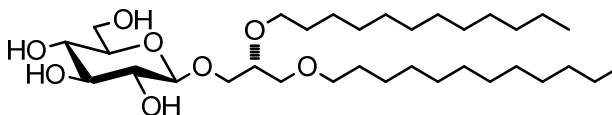
In 1893, the first alkyl glycosides (AGs) were synthesized and identified by Emil Fischer where he reacted glucose and alcohol in the presence of an acidic catalyst [31]. Fischer noticed that AGs have high stability towards oxidation and hydrolysis, especially in a very alkaline media essential for surfactant applications [32]. The nonionic AGs/APGs differ from fatty-alcohol ethoxylates by their characteristic structures which considerably affect the association of molecules in solution, phase behaviour, and interfacial activity. The hydrophilic head of the sugar in AGs/APGs form hydrogen bonds with the surrounding water molecules. However, the hydration is low compared to that in fatty alcohol ethoxylates. Therefore basic phenomena like cloud point, thermal phase inversion, or gel formation in medium concentrations of pure solutions cannot be observed in the case of AGs/APGs. This is due to the contribution of stronger intralayer hydrogen bonding between the sugar head groups in the molecules and weaker interlayer hydrogen bonding between the carbohydrate moiety and water molecules [33, 34]. The behaviour of AGs/APGs in aqueous solution gives important indications for the handling and formulation of a product with regard viscosity, flow behaviour, and phase stability [32].

A number of researchers have performed comprehensive investigations on AG/water systems by various techniques and methods [35-37]. Sakya et al. studied the phase behaviour of monoalkyl glycosides using optical polarizing microscopy (OPM), differential scanning calorimetry (DSC) and X-ray diffraction (XRD) [35]. They showed that a slight change (i.e. chain length, anomeric effects, and type of sugar) in chemical structure can lead to large changes in the phase behaviour (i.e.

melting point, clearing point and solubility). A study of α - and β -alkyl glucosides at air-water interface has revealed that the anomeric configuration has small influence on interfacial adsorption properties [36]. The formation of non-spherical micellar of *n*-octyl- β -D-glucoside (shown in Figure 1.3(a)) was observed using the nuclear magnetic resonance (NMR) self-diffusion experiment [37]. Detailed discussion of phase will be explained in a later section.

The second group of synthetic GLs constitutes analogues of *naturally mimicking membrane lipids*. Some examples are diacyl glycolipids and dialkyl glycolipids [38-41]. Milkereit et al. have described their work on this type of synthetic GLs in a two-part report [40, 41]. In these works, several dialkyl- and diacyl glycolipids with disaccharide (maltose and melibiose) and trisaccharide (maltotriose) head groups bearing saturated, unsaturated and methyl branched-chains were synthesized. They managed to synthesize these GLs in short-synthetic steps and obtained good yields (43–98%) compared to the synthesis of a single diacyl-glycerol with unsaturated fatty acid chains prepared by von Minden et al. The latter involved at least nine synthetic steps, and an overall yield in the range of 3–26% [28].

Another class of synthetic GLs is a 1,3-di-*O*-phytanyl-2-*O*-(glycosyl)glycerols (see Figure 1.3(d)) possessing maltooligosaccharide head groups. These methyl-branched phytanyl-chained lipids have been used as model archaeobacterial GLs [42]. Previously, this group had successfully synthesized GLs, mainly 1,3-dialkyl-glycolipids with *n*-dodecyl and *n*-tetradecyl alkyl chains and oligomaltose and cellobiose head groups in good yields and in a relatively short-synthetic sequence [43]. A few examples of synthetic GLs are shown in Figure 1.3.

(a) *n*-octyl- β -D-glucoside [35].(b) *n*-decyl- β -D-maltoside [36].(c) 1-*O*-phytanyl- β -D-glucoside [39].(d) 1,3-di-*O*-phytanyl-2-*O*-(β -D-maltosyl)glycerol [42].(e) Di-dodecyl- β -D-glucosyl glycerol [38].**Figure 1.3:** A few examples of synthetic GLs.

1.3 Glycolipids as Liquid Crystal

Emil Fischer and Burckhardt Helferich had observed a "double melting" phenomenon in one of the long-chain alkyl glucopyranoside, i.e. hexadecyl β -D-glucopyranoside [44]. This finding was the first reported observation of thermotropic liquid crystalline properties from this amphiphilic carbohydrate. As for lyotropic behaviour, Robert Koch made the first observation in alkylated sugar where he observed an unusual optical texture of aqueous dispersions while analysing the extracts from tuberculosis bacteria [45]. Both thermotropic and

lyotropic terms will be further discussed in Sections 1.5 and 1.6 respectively. The driving force for the mesophase formation of these amphiphilic molecules is the microphase separation of the hydrophilic and hydrophobic groups leading to a structural aggregation of oppositely-behaved moieties. The self-assembly structure is maintained by both the hydrophobic force (short-range repulsion) dominant within the alkyl chain region and the hydrogen bonding network in the hydrophilic region, each stabilising the formed mesophase [46, 47].

However, the fundamental difference between GLs and other amphiphiles resides in the complexity of interactions among hydroxyl groups within the sugar moieties. This adds a greater intricacy to the usual hydrophilic–hydrophobic balance governing the self-assembly, where the head group plays the attractive role and chain group the repulsive one. Unlike biological amphiphiles aggregating in lamellar-type assemblies (i.e. phospholipids) whose structural arrangement is controlled by the hydrophobic tails [48], studies on GLs showed that "small" differences in the sugar head group, like those between glucose, galactose and mannose, can give rise to new features in the liquid crystalline behaviour [12, 49].

1.4 General Descriptions of Liquid Crystals

The official discovery date of liquid crystal is in 1888, when Austrian botanist Friedrich Reinitzer observed the "double melting" phenomenon of cholesteryl benzoate and cholesteryl acetate. However, he did not call it liquid crystal nor recognize it as such. Later he consulted a German physicist Otto Lehman who characterized the phase under a polarizing microscope in 1889 [50]. Therefore both Reinitzer and Lehman have been credited for this discovery, although it was Lehman who suggested the name "*flüssige krystalle*" (liquid crystal) or "*fließende*

krystalle" (flowing crystal), and proposed some physical explanation of the nature of these phase transitions and related optical properties [51].

The term "liquid crystal" refers to a phase considered as an intermediate state of matter between liquids and solids (having some of the ordering properties of a solid, but flowing like a liquid). In a perfect crystalline state, the motions of molecules are limited to only the zero-point vibrations (the normal modes), whereas in the liquid state the molecules have access to other forms of motion including rotation and translation [52, 53]. The liquid state may be achieved by increasing the temperature, where the molecules fully gain 6 degrees of freedom from the translational and rotational motions. In liquid crystal phase, only some of these degrees of freedom are gained by the system. For example, in the simplest case, a nematic liquid crystal gains 3 translational degrees of freedom, but rotationally, only some degrees of freedom is attained, maintaining one degree of orientational ordering. This results in a time-averaged structure, where molecules are aligned within a limited range called a domain, in a parallel or near-parallel arrangement [54] described by a simple order parameter, S [52, 53, 55]. The order parameter can be defined as the average of the second Legendre polynomial:

$$S = \overline{P_2(\cos \theta)} = \frac{3}{2} \langle \cos^2 \theta \rangle - \frac{1}{2}, \quad (\text{Equation 1.1})$$

where θ is the angle, the long molecular axis makes with the director axis, \hat{n} (see Figure 1.4) and the angular brackets denote a statistical average of $\cos^2 \theta$. A director is a vector to represent the direction of preferred molecule orientation within a domain (see Figure 1.5). For instance, when $\theta = 0$ and 180° (parallel alignment), $S = 1$. If $\theta = 90^\circ$ (perpendicular alignment), $S = -\frac{1}{2}$. Finally, if the

molecular orientations are random i.e. θ takes all values, $\langle \cos^2 \theta \rangle = \frac{1}{3}$ and $S = 0$ [52]. The order parameter can be measured experimentally by several types of experiment, such as diamagnetic susceptibilities, NMR or XRD [55].

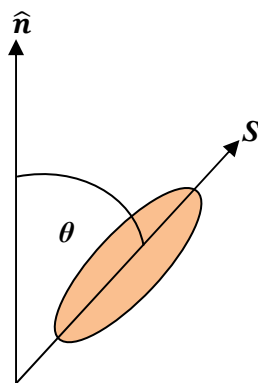


Figure 1.4: Geometry used for defining the order parameter. Redrawn from [56].

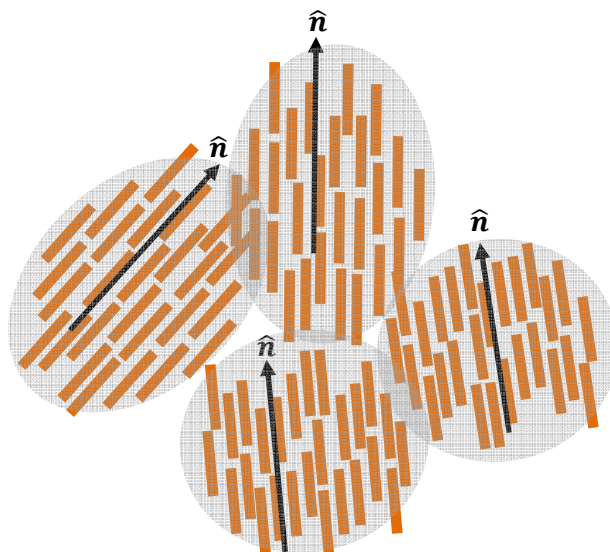


Figure 1.5: Preferred molecule orientation, \hat{n} within a domain (represented by a loosely-defined boundary).

A general molecular structure of a typical liquid crystal molecule is depicted in Figure 1.6. There are two core groups (C_1 and C_2), a bridging group (B), two terminal units (R_1 and R_2), two groups linking the terminal units to the cores (L_1 and L_2), and two lateral substituents on the cores (X_1 and X_2). The units and their

combinations are the key factor for the type of liquid crystal and physical properties exhibited by a compound [56]. The core units (C_1 and C_2) are usually linearly-linked aromatic systems (e.g. 1,4-phenyl, 2,5-pyrimidinyl) or alicyclic (e.g. *trans*-1,4-cyclohexyl). These units contribute rigidity which is required to provide the anisotropic molecular structure. They are joined by a bridging group (B) which maintains the linearity of the core (e.g. $-\text{CO}_2$, $-\text{CH}_2\text{CH}_2-$). The flexibility which is needed to obtain low melting points and molecular alignment stabilization within the mesophase structure is provided by the terminal substituents (R_1 and R_2). They are normally straight alkyl or alkoxy chains with one terminal unit, often a small polar substituent (e.g. CN, F, NO_2). Chiral molecules can be obtained when the terminal chains are branched, and the branching unit can be non-polar (e.g. CH_3) or polar (e.g. CN, F). As for the lateral substituents (X_1 and X_2), F is the most useful due to its small size and high electronegativity apart from Cl, CN and CH_3 [56].

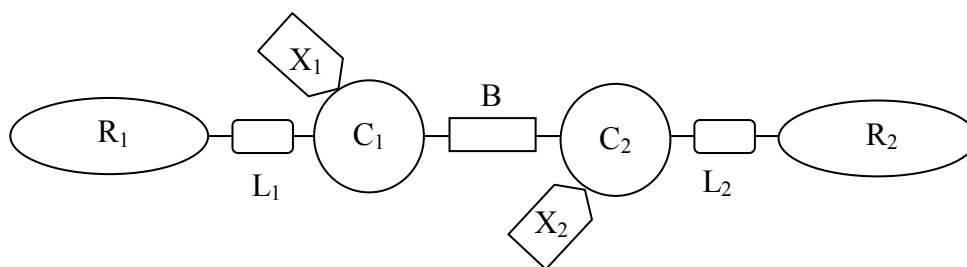


Figure 1.6: Molecular structure of a rod-like liquid crystal. Redrawn from [57].

In general, liquid crystals can be divided into two categories, the *thermotropic* and the *lyotropic* mesophases. The Greek word "mesophase" means "in between" (i.e. the solid crystal and liquid phases). Certain mesogens (compounds forming mesophase) may exhibit both thermotropic and lyotropic phases and they are also called *amphitropic* [58, 59]. GLs used in the present thesis are classified as

amphitropic liquid crystals since they can form both lyotropic liquid crystals in solvent and a thermotropic liquid crystal phase in dry form.

1.5 Thermotropic Liquid Crystals

When a liquid crystal phase appears upon heating or cooling (i.e. by the temperature variation), this phase is classified as thermotropic [58]. Thermotropic liquid crystal forms from crystalline solid to liquid crystal when the temperature is raised above the melting point (T_m). When the temperature is further increased, the phase of the substance changes from liquid crystalline phase to isotropic liquid phase. This temperature is called the clearing point (T_c). The molecular organization of thermotropic liquid crystal is influenced strongly by its chemical architecture and will be described in the next section.

1.5.1 Monophilic Liquid Crystals

Monophilic liquid crystals can be derived from a simple geometrical form of the molecule. This material is further distinguished according to its basic molecular shape such as *calamitic* (rod-like), *discotic* (disk-like) [53, 56, 57] and the recently-described *sanidic* (lath-like) liquid crystal [60] (see Figure 1.7).

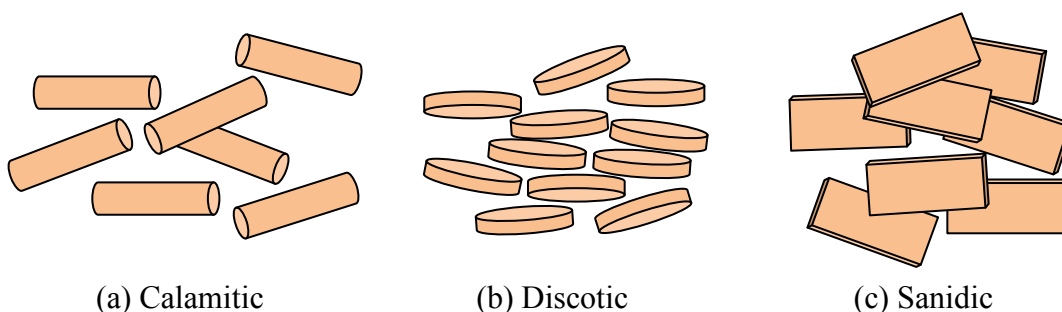


Figure 1.7: Molecular shapes of monophilic liquid crystals. Redrawn from [60].

Calamatic materials usually consist of rod-shaped molecules in which one molecular axis is much longer than the other two axes that are assumed to be equivalent [56]. A common characteristic of calamitic mesogens is a relatively rigid core as found in phenyl and biphenyl groups, and with two flexible endgroups (either alkyl or alkoxy chains) [60]. As proposed by Georges Friedel [51], there are three basic types of liquid crystals namely, *nematic*, *cholesteric* (*chiral nematic*) and *smectic*. These phases are depicted in Figure 1.8.

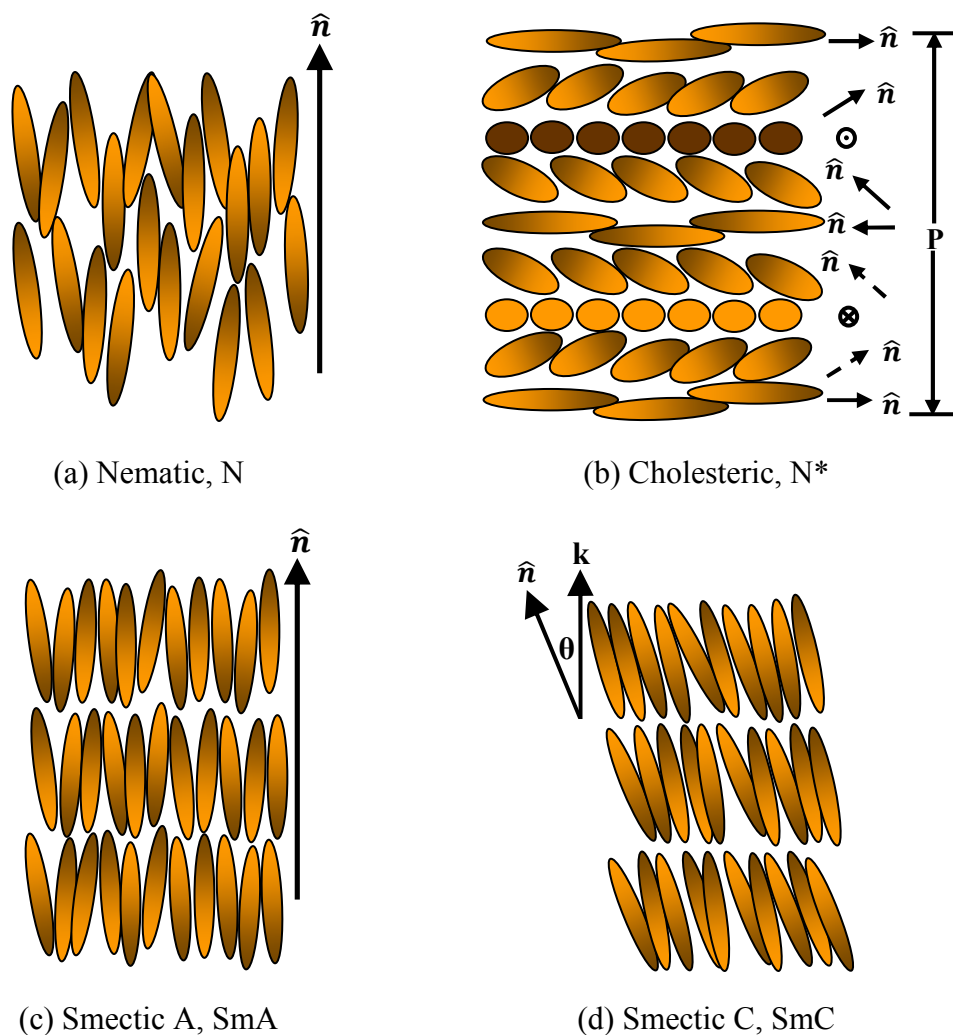
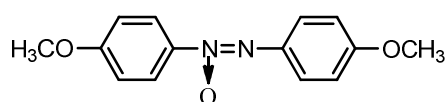
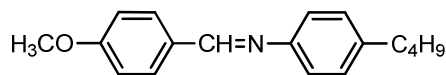


Figure 1.8: The molecular organization of calamatic liquid crystals. The vector, \hat{n} represents the director and k is the layer normal. Redrawn from [60].

The word "nematic" in liquid crystal comes from $\nu\eta\mu\alpha$ (nema), the Greek word "nematos" which means "thread" [57, 60]. The nematic phase is the most liquid-like structure (low viscosity) similar to isotropic liquid. However, it exhibits anisotropy characteristic due to the molecular long axes arranging themselves almost parallel to the director, \hat{n} [53, 60]. The nematic state possesses long-range orientational order and short-range positional order. The molecules are mobile in three directions because there is no periodic arrangement and they can rotate freely about one axis. Under a polarizing microscope, they display mainly thread-like disclination line textures which are related to structural discontinuities in the material [54]. Common examples are 4,4'-dimethoxyazoxy benzene (p-azoxyanisole), and the first moderately stable room temperature liquid crystal, 4-methoxybenzylidene-4'-*n*-butylaniline (MBBA). Their chemical structures are shown in Figure 1.9. This liquid crystal that exhibits nematic phase at room temperature with a weakly aligned director which can be manipulated easily enabling the development of liquid crystal display [61, 62].



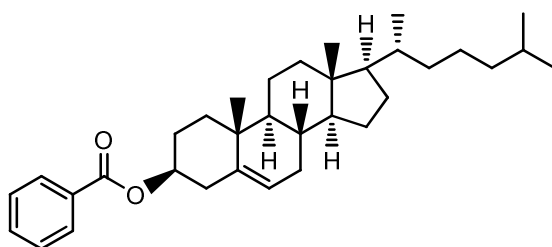
p-azoxyanisole
Cr 117 N 137 I



MBBA
Cr 21 N 45 I

Figure 1.9: Some examples of compounds that exhibit nematic phase together with their liquid crystals phase behaviours (Cr means crystal, I stands for isotropic and N denotes nematic phase) [63].

Cholesteric liquid crystal, also known as a chiral nematic, is produced when the director in a nematic mesophase has a helical superstructure with a twist axis perpendicular to the local director, \hat{n} . The nematic and cholesteric structures are similar, except on a large scale when the cholesteric director follows a helical form [54, 55]. The pitch, P of the structure refers to the distance needed to rotate the director by 2π along the helix axis. P usually ranges between 2000 Å and macroscopic values, and an infinite P corresponds to the normal nematic [55]. Cholesterics of low P (below 5000 Å), exhibit what are known as *blue* phases which exist over a small temperature range (~ 1 °C) between the cholesteric liquid crystal phase and the isotropic liquid. Cholesteryl benzoate shows a cholesteric liquid crystal phase, and the first observation of a blue phase was recognized by Friedrich Reinitzer in 1888 [53]. Figure 1.10 shows the chemical structure of cholesteryl benzoate. Cholesteric liquid crystal materials have the ability to change colour (due to the high sensitivity of the pitch) as a function of temperature, mechanical stress, electric fields or non-chiral solute molecules [55]. These characteristics make these materials useful as a thermal sensor in thermometers and other thermometry technical applications [64, 65].



Cholesteryl benzoate

Cr 145 N* 178 I

Figure 1.10: Cholesteryl benzoate that exhibits cholesteric phase together with its liquid crystals phase behaviours. (Cr means crystal, I stands for isotropic and N* denotes chiral nematic phase) [66].

The third category of liquid crystal phase is the "smectic" phase, from the Greek word for "soap" [57]. The molecules in this phase are parallel to one another and are arranged in layers with the mean direction of the long axes of the molecules normal to the layers. Smectic liquid crystals are fluid but are far more viscous than nematic liquid crystals. Their fluidity is due to the flexibility of the layers and weak interlayer attractions compared to that of lateral intermolecular forces, which enable the layers to slide over one another easily while still remaining essentially parallel. Thus when observed under a polarizing microscope, they exhibit different characteristic textures such as homeotropic, focal conic, batonnets, and fan-like textures [54]. There are many different types of smectic phases (A, B, C, F, I...). The two most common are smectic A (SmA) and smectic C (SmC). The molecules in SmA are on average normal to the layers, while the molecules in SmC phase are on average tilted with respect to the layer normal (see Figure 1.8) [56].

Certain compounds possess more than one mesophase (polymorphism). For instance, 4'-n-octyl-4-cyanobiphenyl has two liquid crystal phases whereas 4-n-pentylbenzenethio-4'-n decyloxybenzoate shows three liquid crystal phases. Their molecular structures are depicted in Figure 1.11.

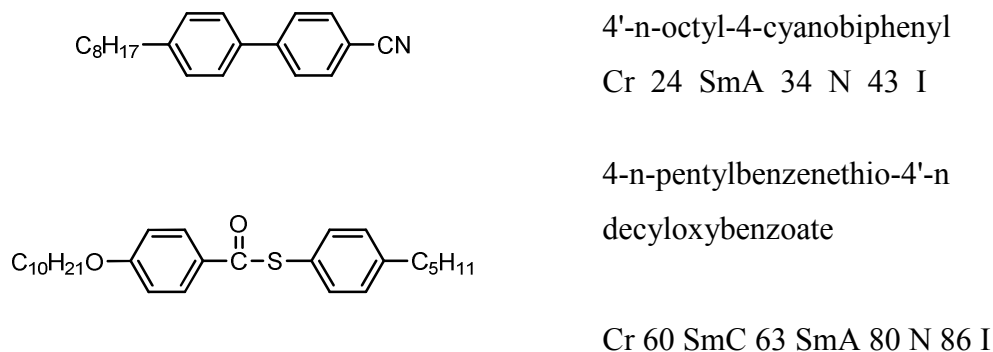


Figure 1.11: Some examples of compounds that exhibit smectic phase together with their liquid crystal phase behaviours (Cr means crystal, I stands for isotropic, N refers to nematic, SmA denotes smectic A and SmC implies smectic C phase) [53].

Disc-like molecules which normally form discotic liquid crystals are molecules with one molecular axis shorter than the other two. The core of discotic liquid crystals is usually based on benzene, triphenylene, or truxene with six or eight flexible side chains [56] (see Figure 1.12). Due to their unique structural and electronic properties, they show potential for application in fields such as charge transport [67], molecular electronics [68] and high-efficiency organic photovoltaics [69]. Generally, they can be categorized into two distinct phases: *nematic* and *columnar* [53].

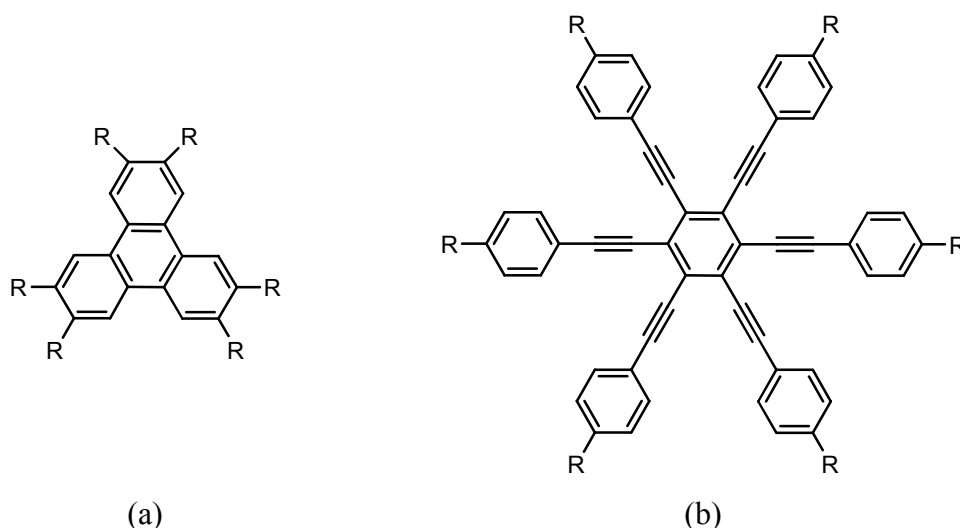


Figure 1.12: A typical chemical structure of discotic mesogens: (a) hexa-n-alkanoates of triphenylene and hexa-n-alkoxytriphenylene (b) hexakis ((4-octylphenyl)ethynyl) benzene [53].

As shown in Figure 1.13(a), the most simple discotic phase is the nematic phase. It possesses orientational order but no positional order. Unlike the typical nematic of rod-like molecules, this phase is optically negative [53]. The nematic phase of discotic mesogens is usually found in shorter chain compounds. Therefore, increasing the chain length in a homologous series of disc-like molecules will result in the disappearance of the nematic phase [70].

The positional order of discotic liquid crystals causes a tendency for the molecules to arrange themselves in columns. Hence, in the plane perpendicular to the columns, the disc-like molecules tend to align in a two-dimensional lattice, either rectangular or hexagonal, as they diffuse throughout the sample. This is also known as the columnar phase (see Figure 1.13(b)).

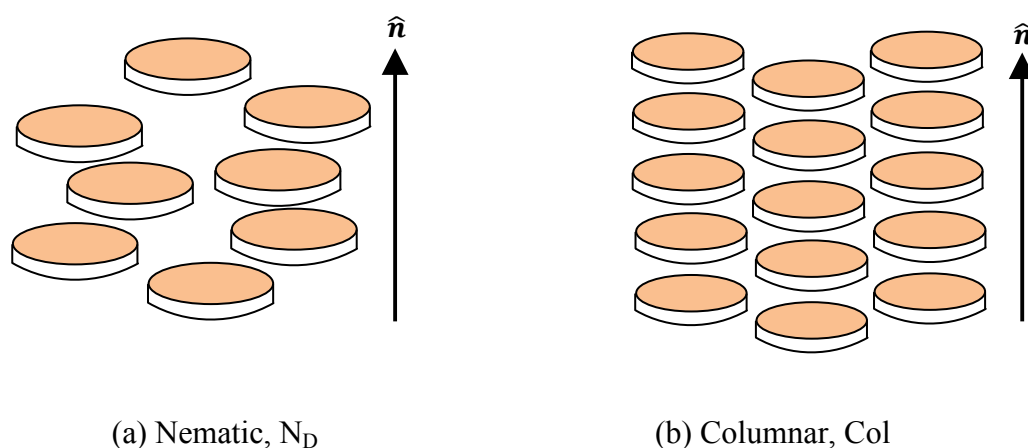


Figure 1.13: Schematic illustration of discotic liquid crystals. Redrawn from [57].

Chiral nematic discotic liquid crystals are also found. In this phase, the director rotates in a helix fashion throughout the sample similar to the rotation of the chiral nematic calamitic liquid crystal [57, 60].

Sanidic-like liquid crystal is the phase when board-shape molecules assemble in stacks packed parallel to one another on a one- or two-dimensional lattice. Rotation of the molecules around their long axes is considerably hindered and they are expected to form the biaxial nematic mesophase [58].

Another type of liquid crystals is polymer liquid crystals. The basic monomer units are low mass mesogens, rod-like or disc-like, and are attached to the polymer backbone in the main chain or as side groups (see Figure 1.14). As for the former, the rigid structural units are separated by flexible hydrocarbon chains

whereas in the latter, the rigid parts are attached to a long flexible polymer chain by short flexible hydrocarbon chains [53, 56]. Nematic, cholesteric and smectic phases have been found in polymers.

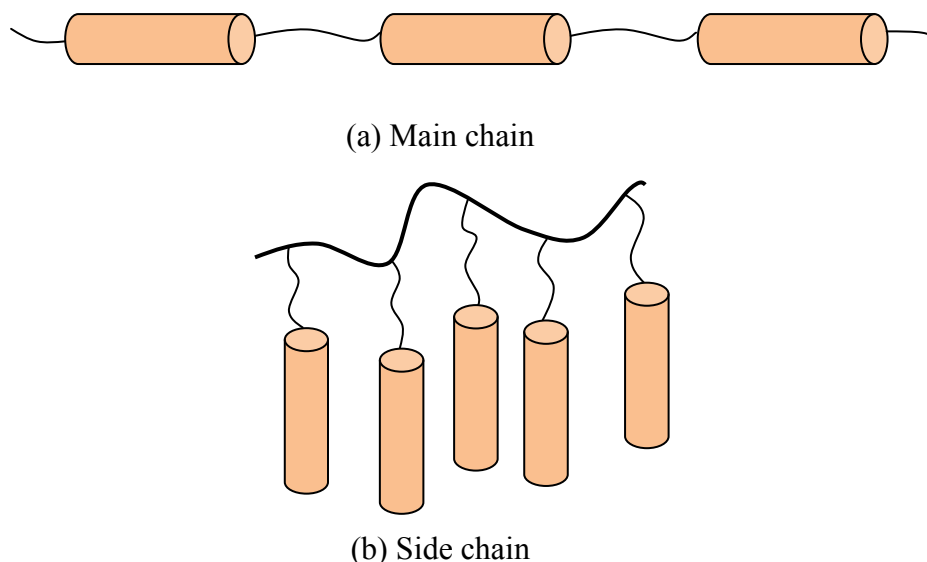


Figure 1.14: Rod-like polymeric liquid crystal. Redrawn from [53].

1.5.2 Amphiphilic Liquid Crystals

Possible molecular shapes of GLs are given in Figure 1.15. The dual-character of this amphiphilic molecule results in microseparation that gives rise to mesomorphic properties. The relationship of these molecular shapes to the thermotropic phase behaviour can be summarized as follows [19]. Elongated amphiphiles in the case of A, B and C will exhibit smectic phase. Forked or pie-shaped mesogens (D and E) usually prefer columnar phase. The non-linear dialkylated sugars like F will also give columnar phase. Banana-shaped amphiphiles (G) and elongated forks (H) are between smectic and columnar phases, or may even form bicontinuous cubic phase. The cone-shaped molecule, J can give discontinuous cubic phase. Lastly, star-like substituted molecules will prefer columnar phase. If

this star is asymmetric like K, then rectangular and tetragonal columnar phases are possible to be formed. In this work, the structural models of the monosaccharide-branched compounds that we have prepared are represented by molecular shape D. Hence, they are predicted to give non-lamellar or curved mesophases like columnar and bicontinuous cubic phases.

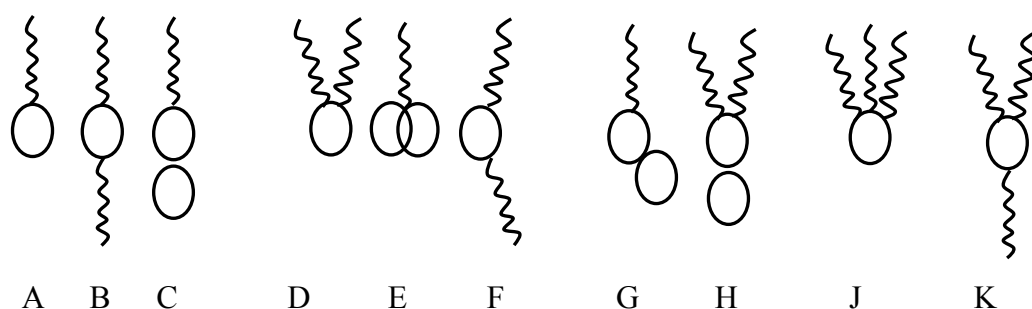


Figure 1.15: Structural models of GLs. Redrawn from [19].

1.6 Lyotropic Liquid Crystals

When amphiphilic materials such as ethylene oxide are mixed with suitable solvents, the mixtures can display different liquid crystal phases under appropriate conditions of concentration, temperature and pressure. This class of liquid crystals is termed lyotropic [58]. The word "lyo"- refers to the concentration of the solvent [71]. It may form a variety of structures above some critical concentration and temperature, governed by the geometrical constraint of the molecule and the interfacial curvature which in turn, is determined by intra-micellar forces occurring in different planes. As the composition increases, inter-micellar forces become more important and may cause either a change in the critical packing parameter (see Section 1.6.2) leading to a further shape transition, or disorder/order transition to the liquid crystalline state [54].

The lyotropic phases have a broad and wide range of applications in different fields such as the cosmetics industry [72], in pharmacy as drug-delivery systems [25, 26, 73-75], in the food industry [76], in situ templating [77] and in membrane protein crystallization [78]. A typical example of lyotropic liquid crystals is mixtures of alkali *n*-alkoates (soaps) and water. The lyotropic mesophases are namely *lamellar*, *cubic* and *hexagonal* phases.

One-dimensional translational order lyotropic phases are called lamellar phases (L_a). The structural unit of lamellar phase is simple, consisting of repetitive bilayers separated by solvent. The bilayers pack parallel to one another and are separated from one another by a water layer, as shown in Figure 1.16(a). The hydrophilic head group of the molecules is in contact with the aqueous solvent, whereas the lipophilic hydrocarbon chains are either interdigitated, tilted or fluid disorder, to avoid water. The double layer is usually smaller than twice the amphiphilic molecule length. Both bilayer and water layer thickness values are very much dependent on temperature and concentration of the lamellar phase. The bilayer forms the main matrix of the biological membranes containing phospholipids as lyotropic compounds.

There are a variety of conformations of the lamellar phase which are β (parallel) and β' (tilted) as shown in Figure 1.16(b)–(d). The lamellar in β' is all distorted due to the distortion propagating from layer to layer. An optical characteristic of this phase is its birefringent texture since the bilayer ordering is not affected by gravitational effect and can slip easily one upon the other [79].

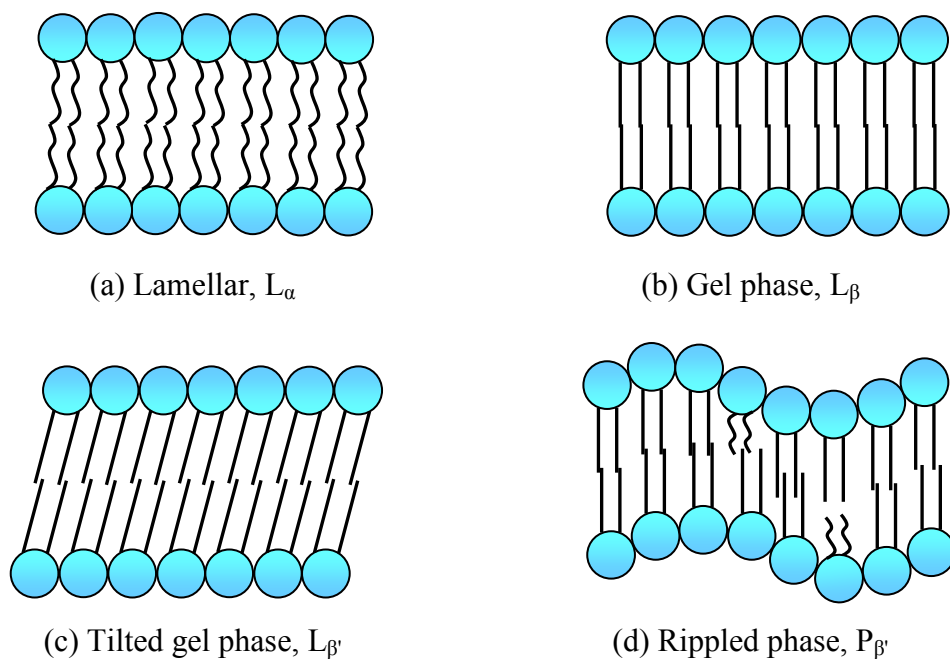


Figure 1.16: Schematic structures of lamellar phases. Redrawn from [48].

In general, the highly-ordered cubic phases are more viscous than those of isotropic micellar solutions and even the hexagonal phase. The high viscosity is due to the lack of shear planes within the structure that would allow a sliding movement. Therefore, under an optical polarizing microscope, the cubic phases exhibit no texture because they are optically isotropic, and yet cubic phases can be distinguished from the isotropic micellar solutions by their viscosity. The isotropic nature of the cubic phase often makes it difficult to observe them under the optical polarizing microscope and so they are sometimes undetected [56]. However, the structural information of the cubic phases can be obtained through X-ray techniques. The cubic phase can be categorized into two groups which are bicontinuous based on the triply periodic minimal surfaces (TPMS), and the other type is micellar or discontinuous cubic phase based on the complex packing of discrete micellar aggregates [79-81].

The bicontinuous cubic phase of an amphiphilic molecule can be divided into the normal (direct) and inverse (reverse) phases [82, 83]. Figure 1.17(a) shows the normal phase (denoted as Q_I in this thesis [82]) in which water film is centred on the TPMS while the surfactant molecules are filling the two disjoint subspaces. The second group is an inverse phase (denoted as Q_{II} [82]) where the TPMS is occupied by a surfactant bilayer and the two channels are filled with water (see Figure 1.17(b)) [83, 84]. The TPMS can be further categorized into three structures: Schwarz diamond (D), primitive (P) and Schoen gyroid (G) minimal surfaces, with crystallographic space groups of $Pn3m$ (224), $Im3m$ (229) and $Ia3d$ (230) respectively [81-85].

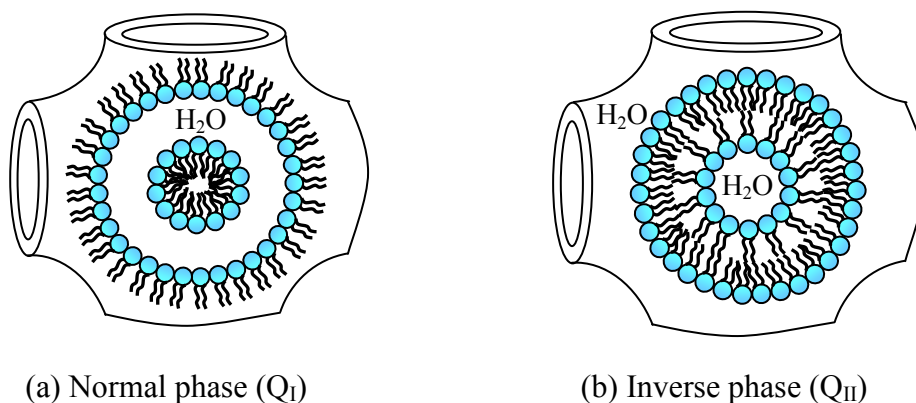


Figure 1.17: The bicontinuous cubic phase of an amphiphilic molecule. Redrawn from [84].

Among the bicontinuous phases, $Pn3m$ and $Im3m$ are usually inverse. On the other hand, $Ia3d$ is commonly observed either as a normal or an inverse cubic phase. The inverse $Ia3d$ is formed by a limited number of known lipid systems whereas the normal type is rather common in surfactant systems [82]. The inverse bicontinuous cubic phase (Q_{II}) forms at relatively low curvatures. They consist of a single, continuous bilayer draped over the TPMS and subdividing space into two

interpenetrating, but not connected, water channel networks. The structures of inverse bicontinuous cubic phase are shown in Figure 1.18.

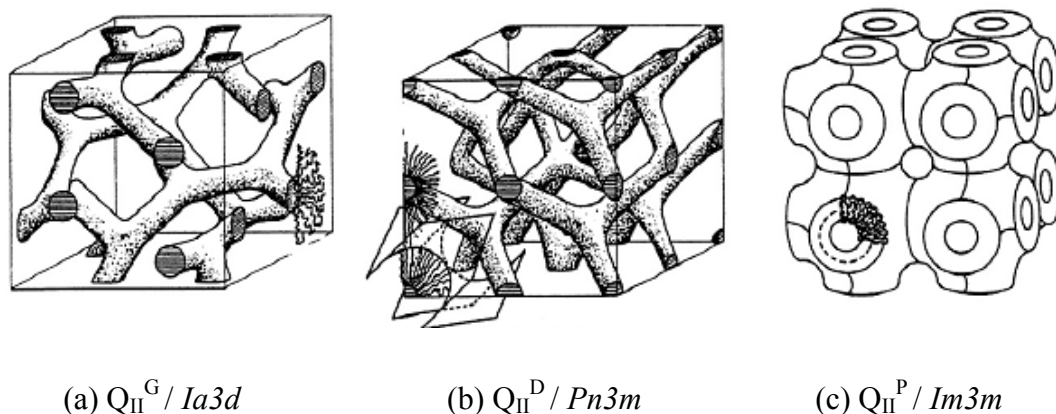


Figure 1.18: Structures of inverse bicontinuous cubic phases. Adopted from [81].

These inverse bicontinuous cubic phases have two identical networks of water channel. Unlike the Q_{II}^P and Q_{II}^D mesophases, the two water regions in the Q_{II}^G phase are no longer identical. Each has a chirality associated with it, and the two regions are enantiomeric [85]. Table 1.1 shows details of the water channel networks in each inverse bicontinuous cubic phase.

Table 1.1: Water channel network of inverse bicontinuous cubic phase.

Phase	Number of water channel junctions	Angle of water channel meet
Q_{II}^P	6	90°
Q_{II}^D	4	109°
Q_{II}^G	3	120°

Of particular interest is the inverse bicontinuous cubic phase which has very specific and controllable water channel sizes and a large membrane area [86]. These features can be exploited for drug delivery systems which involve incorporation and

controlled release of drugs of varying size, polarity and biodegradability [25, 26, 75], as well as *in meso* crystallization of membrane proteins [78, 87].

Meanwhile, the discontinuous cubic phase has a simpler structure which based upon discontinuous packing of micelles. There are three different normal micellar cubic phases, of space group $Pm3n$ (223), $Fm3m$ (225) and $Im3m$ (229) which have been identified [88, 89] (see Figure 1.19(a)–(c)). The polyhedral volume of $Pm3n$ consists of spherical micelles located at the centre of the two dodecahedra and disc-like micelles at the centre of the six tetradecahedra [90].

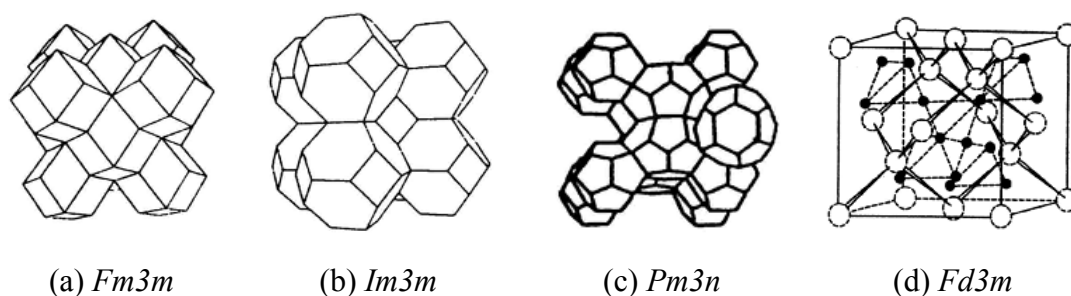


Figure 1.19: Polyhedral micellar arrangement of discontinuous cubic phase. Adopted from [79].

Seddon et al. [91] reported an inverse micellar cubic phase of space group $Fd3m$ observed for the first time in a fully hydrated synthetic 1,2-di-*O*-alkyl-3-*O*-(α - or β -D-xylopyranosyl)-*sn*-glycerols/water system. Figure 1.19(d) shows the $Fd3m$ unit cell which contains 24 quasi-spherical inverse micelles of eight larger ones (polar cores shaded light) and 16 smaller ones (polar cores shaded dark). The remaining volume is filled with the fluid hydrocarbon chains of the lipid.

Cubic mesophases are not only widely found in lyotropic system but also in thermotropic conditions as shown by rod-like, polycatenar, polyhydroxy and dendritic molecules [92].

When solvent concentration is increased further in the cubic phase, a two-dimensional hexagonal phase occurs and forms a normal hexagonal phase, H_I or inverse hexagonal, H_{II} , depending on the solvent polarity. The hexagonal phase consists of micellar cylinders of indefinite length packed in a hexagonal arrangement (Figure 1.20). The diameter of the micellar cylinders is usually 10–30% shorter than twice the length of an "all-trans" non-polar chain. The spacing between each cylinder varies between 10 and 50 Å depending on the relative amounts of water and surfactant. This phase exhibits a birefringent texture when examined under an optical polarizing microscope [56].

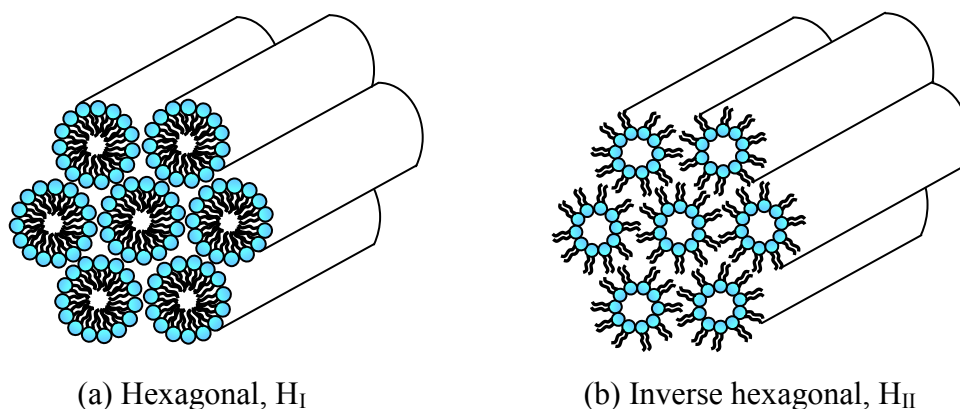


Figure 1.20: Schematic structures of hexagonal phases. Redrawn from [79].

1.6.1 Hypothetical Binary Phase Diagram

The thermodynamic properties of amphiphiles in solution are controlled by the tendency for the hydrophobic region to avoid water. This tendency is called the hydrophobic effect [93]. When an amphiphilic material is mixed with water, the amphiphiles begin to arrange themselves into spheres with the polar head groups on the outside and the hydrocarbon tails toward the centre. This structure is called a micelle (L_1) and is stable as long as the amount of amphiphilic material is above its

critical micelle concentration [57]. An intermediate phase between micellar and hexagonal phases is often a discontinuous cubic phase (I_1). At higher concentrations of amphiphilic material, the micelles combine to form larger structures called hexagonal phase (H_1) in which long cylindrical rods of amphiphilic molecules arrange the long axes of the rods in a hexagonal array. As we increase the concentration of the material, the lamellar phase (L_a) is formed whereby the amphiphilic molecules form flat normal bilayers and are separated by water. Sometimes, the discontinuous cubic phase (Q_1) is formed at concentrations between the hexagonal and lamellar phases. This viscous isotropic phase is made up of spheres of amphiphilic molecules that arrange themselves into two networks of continuous cubic lattices called bicontinuous cubic or mesh structure [93].

When the water becomes the minority phase, inverse structures are favourable i.e. inverse micellar liquid phase (L_2), inverse micellar cubic phase (I_{II}), inverse hexagonal (H_{II}), which is a rod-like water channel in an amphiphile matrix, and inverse bicontinuous cubic phase (Q_{II}). The inverse bicontinuous cubic phases (Q_{II}) form at relatively low curvatures. An increased tendency for curvature is associated with a more wedge-shape structure of the molecule which results in the formation of an inverse hexagonal phase (H_{II}). At an extremely high curvature, the inverse micelle phase (L_2) may be formed where hydrophilic head groups are arranged towards water cores while hydrophobic chains point outwards [94].

The hypothetical sequence of phases formed by varying the concentration and temperature is illustrated in Figure 1.21. In reality, not all amphiphilic surfactants have the same phase sequences as presented here, but the hydration process always ends in the isotropic liquid state for all of them [79]. For instance, binary phase diagram of *n*-octyl- β -D-glucoside/water system measured by two different methods, namely small-angle X-ray scattering (Figure 1.22(a)) and

fluorescence spectroscopy (Figure 1.22(b)), form normal liquid crystalline mesophases of L_α , Q_I and H_I as predicted by the hypothetical binary phase diagram. The exception is the I_I phase.

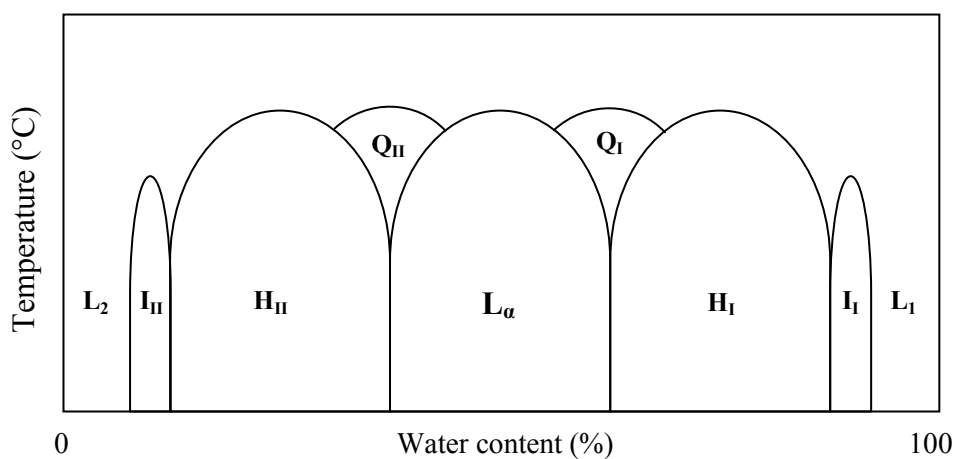
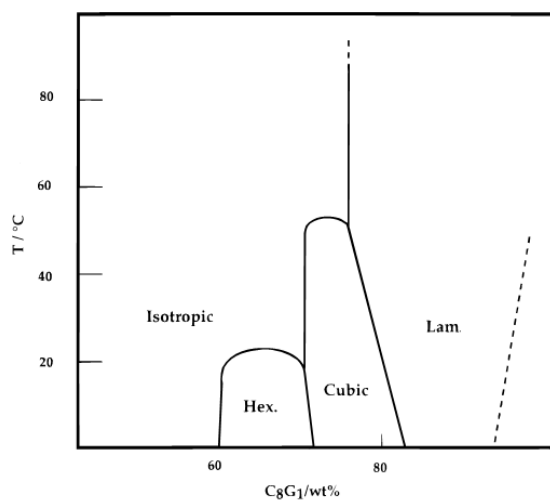
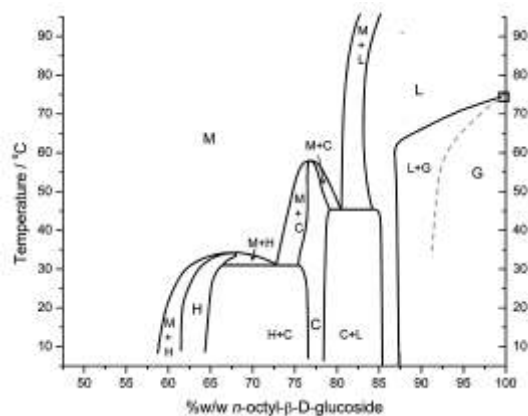


Figure 1.21: Hypothetical lipid/water binary phase diagram. Redrawn from [95].



(a)



(b)

Figure 1.22: An example of binary phase diagram of *n*-octyl- β -D-glucoside in water by (a) small angle X-ray scattering [96] (b) fluorescence spectroscopy [97].

A phase diagram is governed by the *Gibbs phase rule* and *lever rule* [98].

The Gibbs phase rule is given in the following equation:

$$C - P + 2 = F, \quad (\text{Equation 1.2})$$

where C = number of components in the system, P = number of phases coexisting under a particular set of conditions and F = number of degrees of freedom. The variables refer to pressure, temperature and phase composition. In a lipid/water binary phase diagram for example, there is constant pressure. Thus, the phase rule for this system is reduced to:

$$C - P + 1 = F. \quad (\text{Equation 1.3})$$

If the system is a two-component system (i.e. $C = 2$), F includes only temperature and phase composition. The maximum number of phases, P that can exist in equilibrium with one another is determined by setting $F = 0$ in Equation 1.3. So, as many as three phases can coexist in the lipid/water system. When $F = 0$, neither the temperature nor the composition of the three coexisting phases is independently variable. The phase diagram of monomyristolein/water and monopentadecenoin/water systems exhibits such behaviour [99, 100].

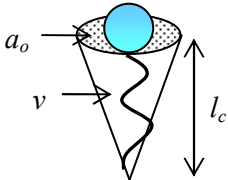
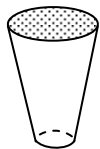

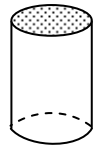
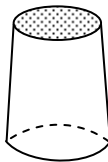
The lever rule is another equilibrium test for phase coexistence. The rule states that the relative amounts of two coexisting phases is equal to the relative lengths of the horizontal tie-lines that intersect the boundaries of the coexistence region in the phase diagram. In addition, the composition of the coexisting phases is constant along a single isotherm and is equal to the composition corresponding to the points where the tie-lines intersect these boundaries [99].

1.6.2 Molecular Packing Parameter

The relationship of molecular structure to phase geometry is important for the design strategy of new materials. Jacob Israelachvili proposed a simple packing theory which can predict the phase behaviour from the knowledge of packing geometry parameter [101]. The packing geometry of a molecule depends on its equilibrium area per molecule at the aggregate interface, a_o , the hydrocarbon chain volume, v and the critical hydrocarbon chain length, l_c . The value of the dimensionless packing parameter, also known as shape factor, $v/a_o l_c$ determines whether they form spherical micelles, non-spherical or cylinder micelles, vesicles or bilayers, or inverted structures. The preferred phase formed corresponds to the minimum-sized aggregate in minimum free energy. In general, the molecular packing parameter concept emphasizes the importance of the surfactant head group in predicting the shape and size of equilibrium aggregates. However, one should not forget that the surfactant tail also has a controlling role in some cases [102].

Apart from that, there are a few factors affecting changes from one structure to another such as head group size, ionic strength, chain saturation, temperature, and lipid mixtures. In nature, the two most common GLs namely DGDG and MGDG are packed as a truncated cone ($v/a_o l_c < 1$) and wedge ($v/a_o l_c > 1$) respectively [101]. Table 1.2 illustrates the possible structures formed by lipids with different critical packing shapes.

Table 1.2: Preferred geometries for different values of critical packing parameter. Redrawn from [101].

Lipid	Critical Packing Parameter ($v/a_o l_c$)	Critical Packing Shape	Preferred Phase Geometry
Single-chained lipids with large head group areas	$< 1/3$	 Cone	Spheres
Single-chained lipids with small head group areas	$1/3-1/2$	 Truncated cone	Cylinders
Double-chained lipids with large head group areas, fluid chains	$1/2-1$	 Truncated cone	Flexible bilayers
Double-chained lipids with small head group areas, anionic lipids in high salt	~ 1	 Cylinder	Planar bilayers
Double-chained lipids with small head group areas, non-ionic lipids, poly (<i>cis</i>) unsaturated chains, high temperature	> 1	 Inverted truncated cone / wedge	Inverse structures

1.6.3 Interfacial Curvature

In addition to the structural parameters such as the interfacial area per molecule, the curvature of the interface is also important. There are two fundamental types of curvature which characterize each point on the surface, namely the *mean curvature*, H and the *Gaussian curvature*, K . They are related to the principal

curvatures c_1 and c_2 at a point P on the surface by the following equation, respectively:

$$H = \frac{1}{2}(c_1 + c_2), \quad (\text{Equation 1.4})$$

$$K = c_1 c_2, \quad (\text{Equation 1.5})$$

where $c_1 = 1 / r_1$ and $c_2 = 1 / r_2$. Both r_1 and r_2 are principal radii of a curvature [80, 103]. H and K may or may not be uniform along the interface, and may be positive, zero or negative (see Table 1.3).

Table 1.3: Mean and Gaussian curvature of interfaces of different types of aggregate [80, 103].

Sign of K	Sign of H	Form of Interface	Aggregate Shape	Aggregate Type
Positive	Positive or negative	Elliptic	Sphere / Ellipsoid	Ellipsoidal micelles
Zero	Positive or negative	Parabolic	Cylinder	Cylindrical micelles
Zero	Zero	Parabolic	Plane	Bilayers
Negative	Positive or negative or zero	Hyperbolic	Saddle surface	Bicontinuous phases

A positive value of H denotes the interface curves towards the hydrophobic chain region (type I) since r_1 and r_2 are positive (the surface curves upwards around P). A negative value of H denotes a curvature towards the polar aqueous region (inverse, type II). In this case, both r_1 and r_2 are negative (the surface curves downwards). The mean curvature orientation is depicted in Figure 1.23.

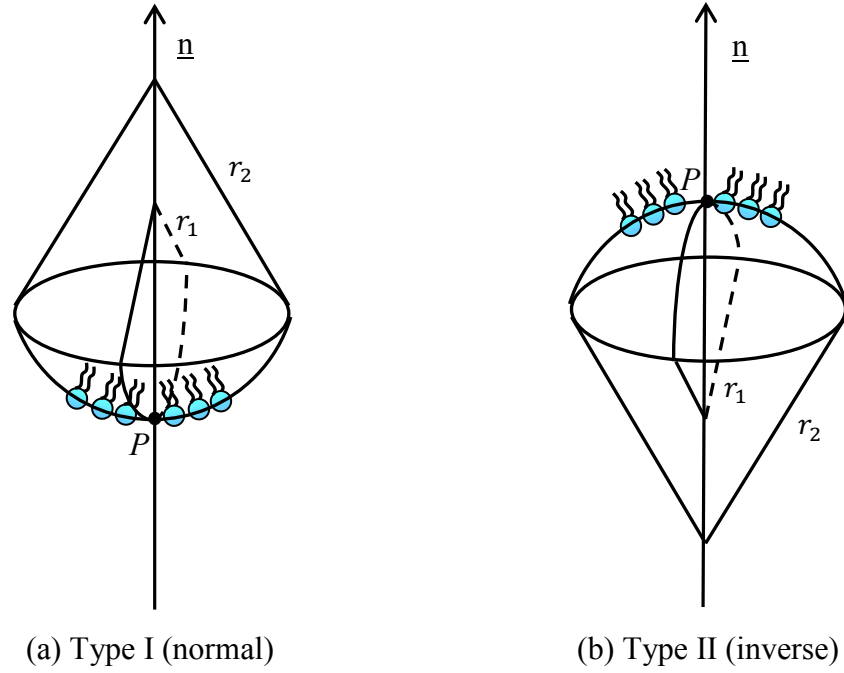


Figure 1.23: Sign convention adopted for mean curvature, H of a lipid monolayer. Redrawn from [103].

The sign of K determines the form of the interface. The simplest example for positive value of K is a sphere whereas the surface of the cylinder or plane has zero Gaussian curvature. The surface of negative K has two principal curvatures, c_1 and c_2 of opposite signs. An example is the saddle surface, formed when a thin fluid film is draped onto a tetrahedral wire frame as shown in Figure 1.24. The Gaussian curvature is most negative at the saddle point and the K value approaches zero when moving along the surface towards the apex point. The saddle surface is also known as the minimal surface since it has zero H value at all points and they appear to form the basis of a bicontinuous cubic phase [103].

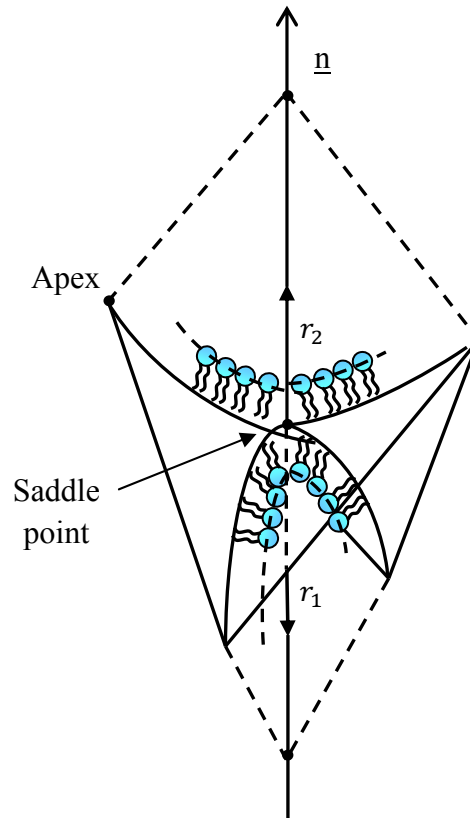


Figure 1.24: Saddle surface of negative Gaussian curvature, K . Redrawn from [103].

1.7 Theory of Liquid Crystals

Liquid crystals are now classified under the newly defined field of soft material which encompasses colloids, surfactants and polymers, and can be induced to flow under certain conditions. This new field is at the interface between chemistry, physics and biology. Unlike a well-ordered crystalline solid, the weak ordering within the liquid crystal phase is due to the lack of long-range positional order, leading to its softness. The main intermolecular forces responsible for the formation of soft materials includes the long-range electrostatic dispersion, and short-range repulsion [93]. The phenomenological theory that best describes the nature of phase transition in liquid crystals is based on the Landau-de Gennes theory. It describes the overall consistency of the microscopic characteristics of the transitions and the results of the measurement of various macroscopic quantities

such as thermal and optical properties [104]. It is the characteristic of liquid crystals specifically and soft materials in general that phase transitions are often weak. This implies that the Landau-de Gennes theory is applicable to a system with continuous phase transitions or to weak first-order transitions, where the enthalpy and entropy change is small [105].

The two classes of liquid crystals (thermotropic and lyotropic) may form a few types of specific phase structures which depend on molecular orderings within these phases. This implies that the transition from solid to liquid state is not a single one, but a succession of transitions passing through several thermodynamically stable phases. These different liquid crystalline phases can be investigated for example via microscopic measurement (texture observation) and differential scanning calorimetry (DSC) [79].

In contrast to the phenomenological theory by de Gennes, a simple microscopic theory that describes the liquid crystal phase was formulated by German physicist Alfred Saupe, in his 1958 thesis under the supervision of Wilhelm Maier [106, 107]. The theory became known as the Maier-Saupe theory. It begins with the assumption that the most important force between liquid crystal molecules is the dispersion force [57, 63]. Accordingly, it is assumed that the interaction between permanent electrical dipole moments, as intermolecular interactions, are important, not for the orientational order, but only for the arrangements of the centres of gravity of the molecules and for the energy content of the isotropic distribution along the axes [63]. The dominant force for the orientational order between molecules is an interaction between induced dipoles. A momentary dipole moment of one molecule induces a momentary moment on the neighbouring molecule, resulting in an attractive dispersion force keeping the two molecules aligned [57, 63]. Besides that, it is assumed that the molecules are cylindrically

symmetric in their long axes. As a result, the potential energy between two molecules can depend only on the angle between their long axes, with an angular dependence proportional to the second Legendre polynomial of this angle [63]. Finally, it is assumed that the degree of orientational order of the molecules enters into the mean-field potential in a linear fashion, i.e. the larger the orientational order, the larger the effective potential [63].

1.8 Structure-Property Relationship

In this section, we briefly but systematically describe the effect of modification on the molecular structure of synthetic GLs on their liquid crystalline properties. The carbohydrate head groups allow opportunity to study the effect of varying the chemical constitution or configuration of one part of the amphiphile while retaining the other part intact. Many authors have written complete and informative reviews on carbohydrate-based liquid crystals [6, 8, 13, 19, 48, 108]. In addition, the infinite diversity of the chemical structures of GLs has opened a wide area of possible research on liquid crystal phase behaviours which very much depend on the type and number of sugar units in the head groups, type of linkages and variety of hydrocarbon tails.

1.8.1 Head Group

Most of the studies on the phase behaviour of GLs have been done on monosaccharide compounds. For example, Sakya et al. [35] investigated the thermotropic and lyotropic phase behaviour of different head groups of monoalkyl glycosides (i.e. glucose, galactose and mannose) which implies that small modifications in chemical structure can lead to large changes in the phase behaviour. This finding is consistent with the behaviour of dialkyl GLs [14], where

it was found that both glucose and galactose head group adopt the L_α phase upon cooling from the H_{II} phase. However, below the chain-melting transition, the glucoside forms a metastable L_β gel phase whereas the galactoside forms only a crystalline lamellar phase (L_c).

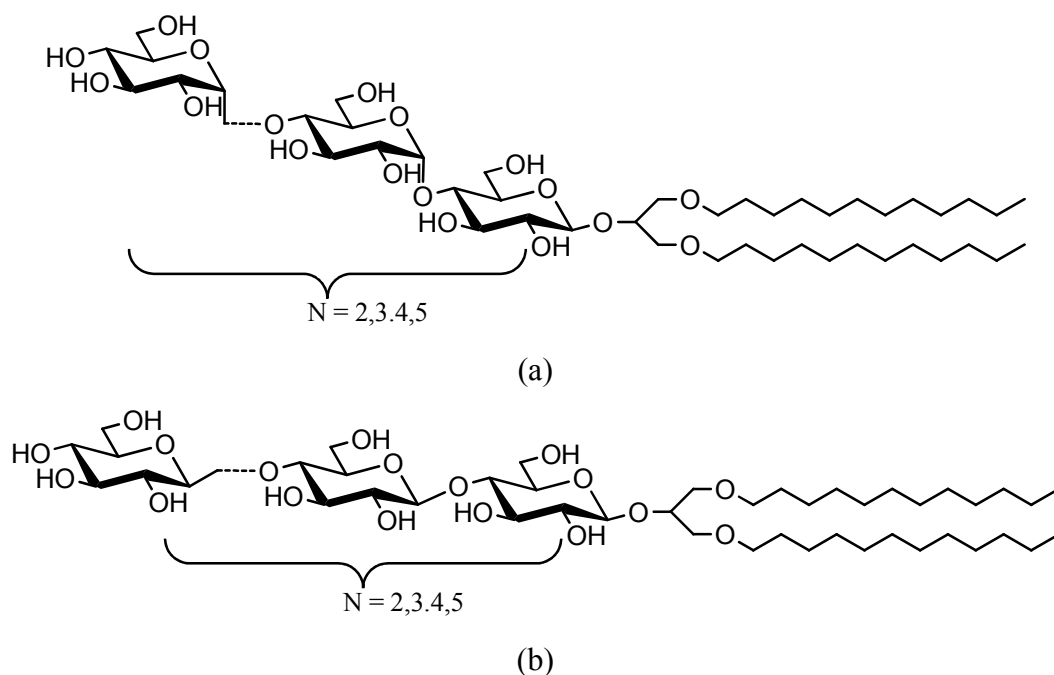


Figure 1.25: The chemical structures of the 1,3-di-*O*-dodecyl-2-*O*-(β -glycosyl) glycerols bearing a series of (a) maltose and (b) cellobiose oligosaccharides as the head group [109].

At the same time, the effect of increasing the degree of head group polymerization has also been studied. For example, maltooligosaccharides greatly increase the solubility of the surfactant in water when the number of glucose units, N is increased [24, 36], and it also improves the stability of the thermotropic liquid crystalline state [36]. Nevertheless, the stereochemistry of oligosaccharide head groups has a strong effect on the physical properties of aqueous synthetic GLs [109]. It has been found that an increase in N of the maltooligosaccharide containing lipids decreases the melting point, (T_m) of hydrated solid/liquid crystalline phase, thus

increasing the “hydrophilicity” of the lipid. Meanwhile the T_m of cellooligosaccharide containing lipids increases with increasing N. The opposite results can be explained by the different conformations of the head groups, that is, a “helical” conformation of the maltooligosaccharides and an “extended” conformation of the cellooligosaccharides (see Figure 1.25).

Recently, a series of crown ethers involving lauryl glucoside were synthesized and their self-assembly in water was studied by Sabah et al. [110]. These compounds contain macrocycles group of variable sizes, ranging from 15-crown-5 to 21-crown-7, attached at different positions on the sugar head group. Figure 1.26 shows some examples of crown ether attached GLs. The crown ethers enhance the solubility of the surfactants in water slightly, thus increasing the critical micellar concentration. Due to their affinity for cation complexation, crown ether attached GLs exhibit higher solubility in the presence of suitable sized cations.

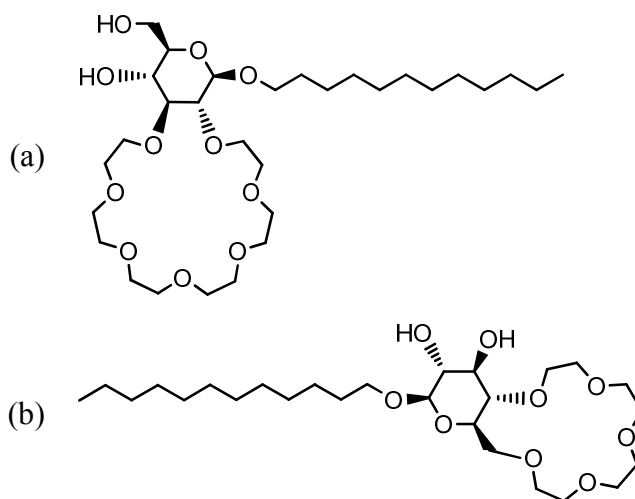


Figure 1.26: The chemical structures of macrocyclic ethers on lauryl glucoside at positions (a) O-2 and O-3 and (b) O-4 and O-6 [110].

So far, the discussion has focused on the linkage between the sugar and lipid parts occurring at C1 (the anomeric carbon). In a few cases, the C6 position may also be involved, as reported by Cook et al. [111]. The methyl-6-*O*-(*n*-acyl)- α -D-glucopyranosides with hydrocarbon chain lengths between 12 and 16 exhibit a monotropic SmA phases (see Figure 1.27 for example). Their T_m initially increases on increasing chain lengths but subsequently decreases on further increase in chain length. This is attributed to the disruption of molecules packing due to back folding of the alkyl chain.

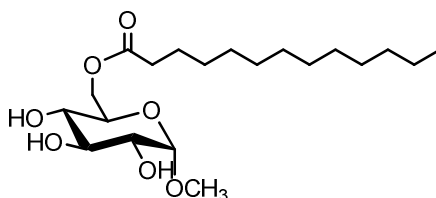


Figure 1.27: The chemical structures of methyl-6-*O*-dodecanoyl- α -D-glucoside [111].

The effect of anomeric configuration has also been investigated [36, 37, 89]. The results found by Boyd et al. [36] show that the phase transition temperatures are influenced significantly by the anomeric configuration in the shorter octyl derivatives, but less pronounced in the longer alkyl chain derivatives. In shorter octyl chain GLs, the α -anomers have a higher clearing point (T_c) than the β -anomers. This is due to α -anomers having greater space for the chain groups to vibrate, therefore making the liquid crystalline phases more stable at higher temperatures.

1.8.2 Linkage

Apart from oxygen linkage, a sulphur link may also be involved in linking the carbohydrate and hydrocarbon chain such as in n-octyl-1-*S*- β -D-glucopyranoside [112] (see Figure 1.28). In this work, the presence of the sulphur linkage suppresses the formation of the hexagonal phase and stabilizes the cubic phase, which is in contradiction to what has been observed in the case of n-octyl-1-*O*- β -D-glucopyranoside. The thio linkage differs from the oxygen linkage in three ways. First, the bond angle in oxygen linkage is higher (113°) compared to that of thio linkage (96°) and this affects the angle of the sugar head group to the hydrocarbon chain. Second, the sulphur has a greater steric bulk than the oxygen, and the third reason is the sulphur has weaker hydrogen bond bonding capability because it is less ionic in character than the oxygen [112].

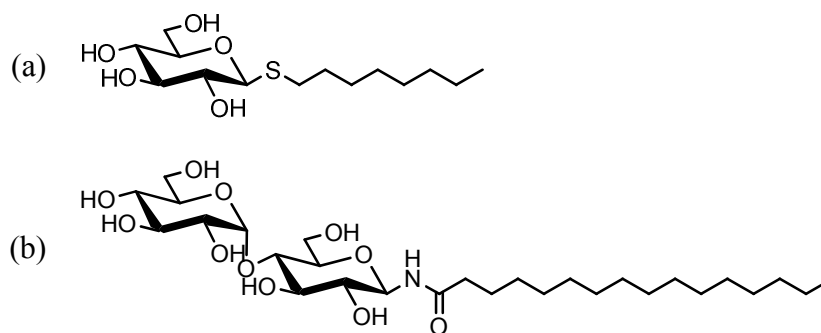


Figure 1.28: Examples of compounds with (a) sulphur linkage [112] and (b) amide linkage [113].

When a series of amide-linkage disaccharide GLs (see Figure 1.28) were investigated, [113] the results show the existence of uni- and multilamellar structures which seem to be correlated with the intrinsic high conformational order of the amide linkage of these compounds which inhibit the formation of non-lamellar phases.

1.8.3 Hydrocarbon Chain

The modification in hydrocarbon tail also plays an important role in determining liquid crystalline phase behaviour. Increasing the straight alkyl chain length results in higher thermal stability in both thermotropic and lyotropic phases [35, 36]. This is because the longer the chain, the stronger the van der Waals interactions between them, and thus the greater the energy required to melt them.

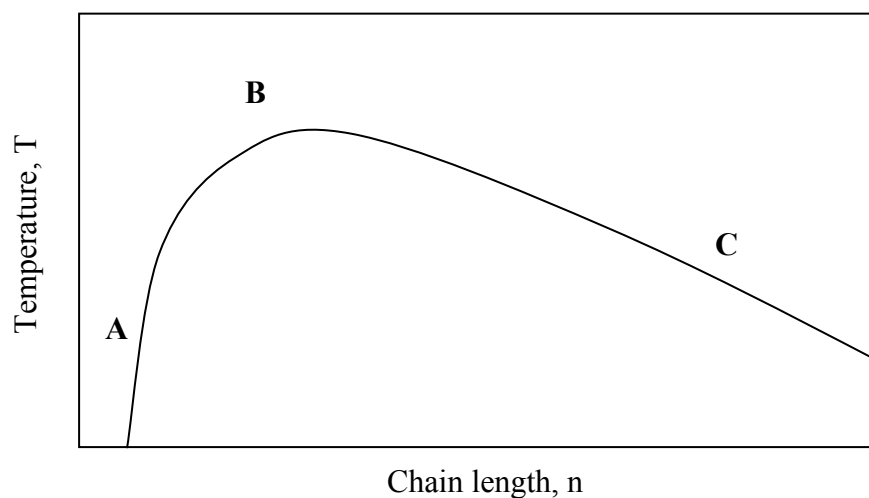


Figure 1.29: The general chain length dependency of homologous series. Redrawn from [19].

In general, a homologous series has a dependency of the transition temperatures on the chain length as shown in Figure 1.29. The mesophase behaviour starts with minimal chain lengths of 6, 7 or 8 (A). An elongation of the paraffin chain will give a big increase of the clearing temperature. The plateau B is characterized by an optimal relationship between polar and non-polar molecular parts. Thus, higher numbers of OH groups would require higher numbers of CH₂ groups. After the plateau, a change of the chain length has only a small effect on the mesophase behaviour. Region C is characterized by a dominating paraffin chain. The clearing temperature decreases gradually with the chain length [19].

Hashim et al. [114] found a trend when they increased the chain length of branched GLs. The shorter chains seem to favour smectic phases while longer chains prefer a columnar arrangement, due to the significantly increased bulkiness of the alkyl chain. This behaviour is not found for straight chains, because they do not show an equivalent increase in bulkiness on increasing the chain length.

The introduction of a double bond into the aliphatic chain has led to the formation of highly curved lyotropic phases [38, 115-117]. This is due to the molecules having a wedge shape structure since the hydrophilic head group is small compared to the volume occupied by the hydrophobic chain (see Figure 1.3(c)-(d) for example). Besides, in a thermotropic study, the branching effect leads to a decrease in the T_m of the GLs and the mesophase can be obtained at ambient temperature [118].

1.9 Objectives and Overview of Thesis

This thesis consists of four projects involving synthetic GLs (i.e. single and branched alkyl chains). Our first objective is to characterize the hexagonal phase of commercially available single alkyl chain GLs namely *n*-dodecyl- β -D-maltoside (β -Mal-OC₁₂) by fluorescence spectroscopy, in the presence of small molecular probes. Secondly, we investigate the temperature-induced phase transition in hexagonal, H_I \leftrightarrow micellar, I_I and normal bicontinuous cubic, Q_I \leftrightarrow lamellar, L _{α} of *n*-octyl- β -D-glucoside (β -Glc-OC₈) using the same fluorescent probes and techniques. Both single-tailed GLs only exhibit normal mesophases. Our third objective is to understand the phase behaviour of four branched-chain alkylglycosides derived from the Guerbet alcohols with 16 total carbon atoms which are predicted to give inverse structures when dispersed in water according to the literatures [114, 119]. They are 2-hexyl-decyl- α -D-glucopyranoside (α -Glc-OC₁₀C₆), 2-hexyl-decyl- β -D-

glucopyranoside (β -Glc-OC₁₀C₆), 2-hexyl-decyl- α -D-galactopyranoside (α -Gal-OC₁₀C₆) and 2-hexyl-decyl- β -D-galactopyranoside (β -Gal-OC₁₀C₆). Then we construct their partial binary phase diagram extensively by small-angle X-ray scattering (SAXS). Finally, our fourth aim is to study the fluorescence properties of the inverse cubic phase formed by branched-chain GLs namely β -Glc-OC₁₀C₆, in the presence of fluorescent probes.

Chapter 1 is an introduction to the GLs and their function in biological membranes, and the relevance of synthetic GLs. This chapter introduces the liquid crystal properties of synthetic GLs, covering history, fundamentals and theories related to liquid crystals in general, and both thermotropic and lyotropic systems in particular. The findings of structure-property relationship studies on GLs are described and rationalized in Section 1.8, while the objectives and overview of the thesis complete this chapter.

Chapter 2 is devoted to the techniques employed, including methods and operating principles of the instruments used in this work, starting from optical polarizing microscopy (OPM), through differential scanning calorimetry (DSC), followed by small-angle X-ray scattering (SAXS). Finally, the common principle of the fluorescence spectroscopy (both steady-state and time-resolved) is described.

The characterization of the head group and hydrophobic regions in hexagonal phase (H_I) of β -Mal-OC₁₂/water system by fluorescence spectroscopy is discussed in Chapter 3. Two types of fluorescent probes are used, namely tryptophan (and its ester derivatives, spanning the level of probing) and pyrene. The former molecule is used to probe the polar head group region and the latter to probe the hydrophobic region of the lipid. The outcomes are discussed in terms of fluorescence emission spectra, lifetime and polarity of the microenvironment.

Chapter 4 extends the idea from the previous chapter where we exploit the fluorescence properties of the tryptophan, its ester derivatives and pyrene to investigate the temperature-induced phase transitions (hexagonal, $H_I \leftrightarrow$ micellar, I_I and normal bicontinuous cubic, $Q_I \leftrightarrow$ lamellar, L_α). In this work, we choose β -Glc-OC₈/water system since it is able to form different lyotropic phases.

Chapter 5 focuses on the thermotropic and lyotropic phase behaviour studies of four nature-like double-chain GLs with glucose and galactose head group linked at α - and β -position of same branched-chain length (α -Glc-OC₁₀C₆, β -Glc-OC₁₀C₆, α -Gal-OC₁₀C₆ and β -Gal-OC₁₀C₆). The mesophase textures and transition temperatures are obtained from OPM whereas the DSC gives the enthalpy change of transition and transition temperature. We confirm the liquid crystal phases observed by OPM and obtain the structural parameters and crystallographic space group of cubic phase from the SAXS. From these results, we are able to construct the partial binary phase diagram for each of the prepared compounds. Most of the mesophases are found to give inverse structures like inverse hexagonal, H_{II} and bicontinuous cubic phase, Q_{II} . The anomeric-epimeric relationship of these four branched-chain GLs are also discussed in this chapter.

In Chapter 6, we continue to characterize the inverse bicontinuous cubic phase, Q_{II}^G (with space group $Ia3d$) formed by β -Glc-OC₁₀C₆/water system using the same probes and techniques to complete the fluorescence investigation on lyotropic liquid crystalline phases using branched-chain glycoside.

Finally, Chapter 7 presents our conclusions and suggestions for future works.

CHAPTER 2

TECHNIQUES AND METHODS

TECHNIQUES AND METHODS

Liquid crystal materials exhibit such a complex phase behaviour that it took nearly 30 years of research from the time when these materials were first discovered, to establish the phase true identity and the driving forces [66]. Therefore, a combination of different techniques is required to identify and determine a liquid crystal phase. Amongst the most common ones are differential scanning calorimetry (DSC) to determine phase transition properties and optical polarizing microscopy (OPM) in which melting behaviour is examined and "fingerprint" mesophase textures are observed, photographed and compared with textures of known phases [60]. In addition, small-angle X-ray scattering (SAXS), small-angle neutron scattering (SANS), and nuclear magnetic resonance (NMR) techniques can give data about structural information of these phases [56]. Finally, miscibility investigation is also useful, in which, when a known liquid crystalline phase is miscible with an unknown phase, the two phases are identical [120].

In the present work, three methods are used to characterize the mesophase, namely OPM, DSC and SAXS. In addition, we have used steady-state and lifetime fluorescence spectroscopy techniques to obtain information on the dynamics of the mesophase using fluorescent probes. The basic principles of these techniques along with some detailed measurements and procedures related to our work is described in the following sections.

2.1 Optical Polarizing Microscopy (OPM)

OPM is a convenient technique for observing textures to differentiate phases. In many cases, the difference between the various liquid crystals is small. Therefore, the measurement and interpretation of OPM textures require a lot of experience [56], and any ambiguities should be resolved by applying another technique for confirmation. The function of an optical polarizing microscope is to differentiate between isotropic and anisotropic media. An optical polarizing microscope allows the determination of both phase transition temperatures and phase type. The nature of phase is characterized by a particular observed texture generated due to the presence of defects within the phase [56, 60].

Figure 2.1 illustrates a typical setup of an optical polarizing microscope. It consists of a white light source which is reflected upwards by a mirror. The light passes through a lens and a sheet of polarizer which can be rotated 360°. The condensor collects the light and in order to ensure uniform illumination of the sample, the aperture iris must be adjusted. Opening it too wide or too small will result in a blurred image (reduction of reduced contrast) or a dark image respectively. After passing through the mounted sample on the rotatable heating stage, it goes into the objective of either x5, x10, x20 or x40 magnification. A removable analyzer (a second polarizer) which is usually at a right angle to the polarizer will receive the light. The eyepiece serves to magnify the image further. Alternatively, the image is observed using a camera which is mounted on the microscope. A hot stage is mostly used to increase the temperature of the material studied [60].

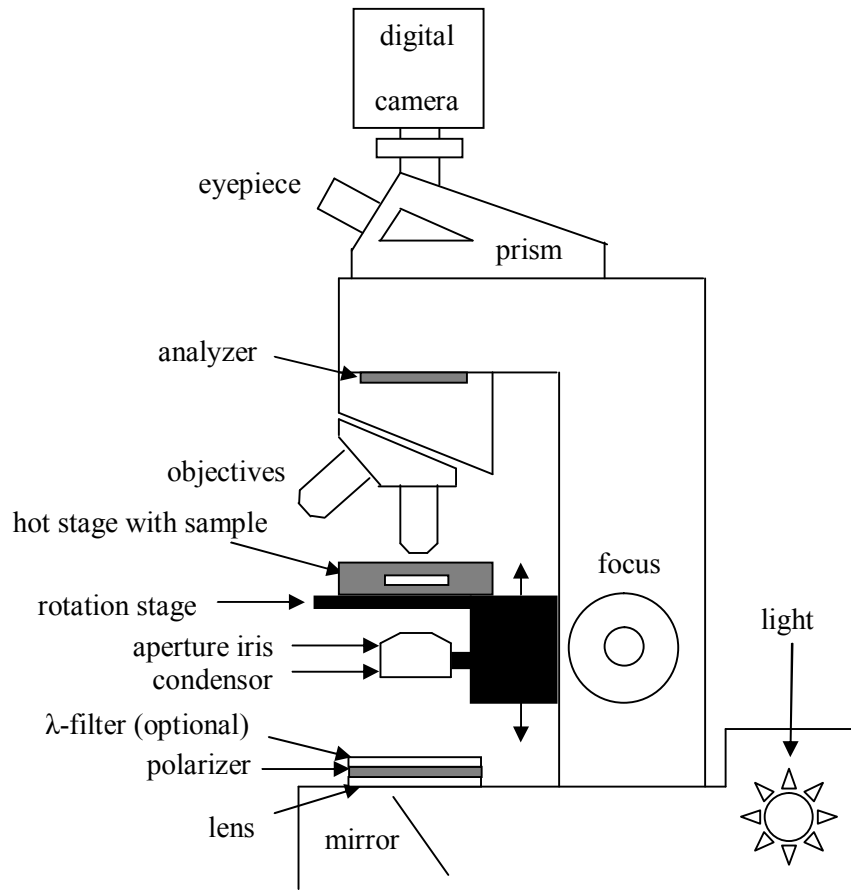


Figure 2.1: Schematic setup of an optical polarizing microscope. Redrawn from [60].

In practice, the liquid crystalline phases identified by an optical polarizing microscope involves magnified viewing of a thin and uniform mesogenic sample sandwiched between a glass slide and a glass cover slip [56, 121]. The glass slide containing the material under study is placed on a temperature-controlled stage, between two polarizers which are crossed at 90° to each other. For an isotropic sample, the wavelength of the polarized light remains unaffected by the sample and is extinct when passing through the analyzer. Thus, no texture is observed and the sample image appears black. On the contrary, in the case of an anisotropic sample, the wavelength of the polarized light is modified, leading to a phase difference upon recombination when passing through the analyzer. As a result, an optical texture can

be seen since not all light vectors are extinct. Figure 2.2 illustrates the basic principle of an optical polarizing microscope passing through an anisotropic sample.

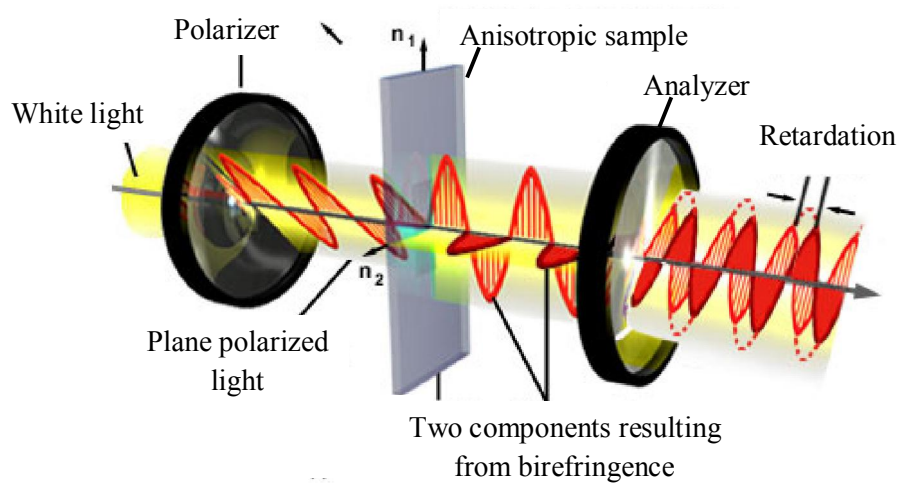


Figure 2.2: Basic principle of an optical polarizing microscope. Adopted from [122].

The texture observed under an optical polarizing microscope may also depend on the alignment due to surface modification. The basic forms of alignment are homeotropic and homogeneous (planar) [56] (see Figure 2.3 for example). In homeotropic alignment, the directors of the bulk phase are oriented normal to the supporting substrate. Accordingly the polarized light is unaffected by the sample and it cannot pass through the analyzer, resulting in a dark image. In homogeneous alignment, the directors of the liquid crystal phase are oriented parallel to the supporting substrate and that is usually made possible by treating the surface substrate [123]. A thin sample tends to generate a homeotropic alignment whereas a thicker or bulky sample tends to give a combination of homeotropic and homogenous alignment.

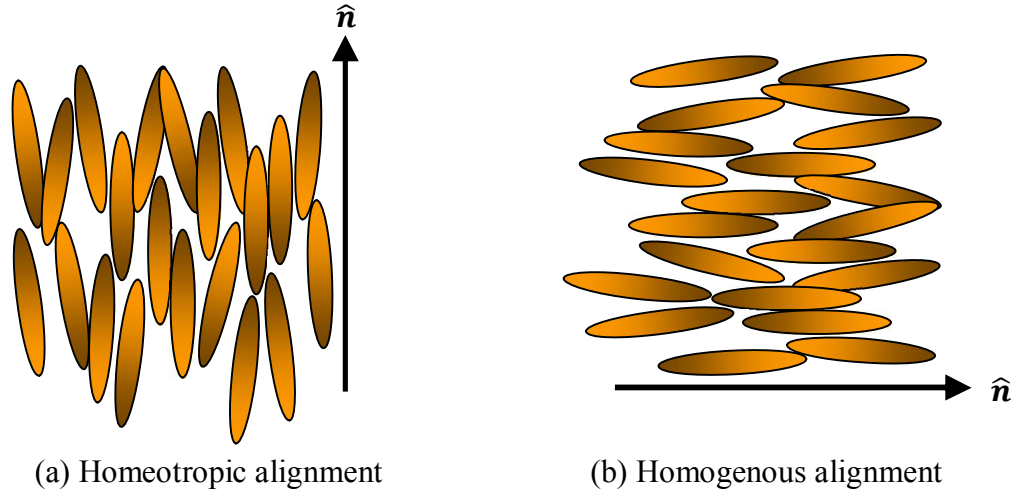


Figure 2.3: Alignment of liquid crystals in nematic phase. Redrawn from [56].

2.1.1 Defect and Texture of Mesophases

The characteristics of several monophilic thermotropic liquid crystal phases are described in Section 1.5.1 (Chapter 1). In this section, we discuss their textures and defects. The appearance of textures when a liquid crystal sample is observed under an optical polarizing microscope is due to the presence of defects within the sample [57].

In a nematic liquid crystal, a *Schlieren* texture is observed between crossed polarizers when the molecular orientations are not homogenous but vary slowly in the plane of the substrate [60]. Schlieren textures often exhibit a characteristic set of two-fold or four-fold curved dark brushes corresponding to the extinction position of the nematic director field. Accordingly, the director, \hat{n} lies either parallel or perpendicular to the polarizer or analyzer axes. The points where two or four brushes meet correspond to the director singularities and are called disclination points. The singularities are topological defects which have a certain strength, s . In an experiment, $s = \pm 1/2$ (two brushes) and $s = \pm 1$ (four brushes) defects are observed for nematic liquid crystals (see Figure 2.4). The positive sign indicates the

dark brushes rotate in the same direction of the polarizers, while the negative sign indicates they rotate in the opposite direction [60]. The Schlieren textures are shown in Figure 2.5(a).

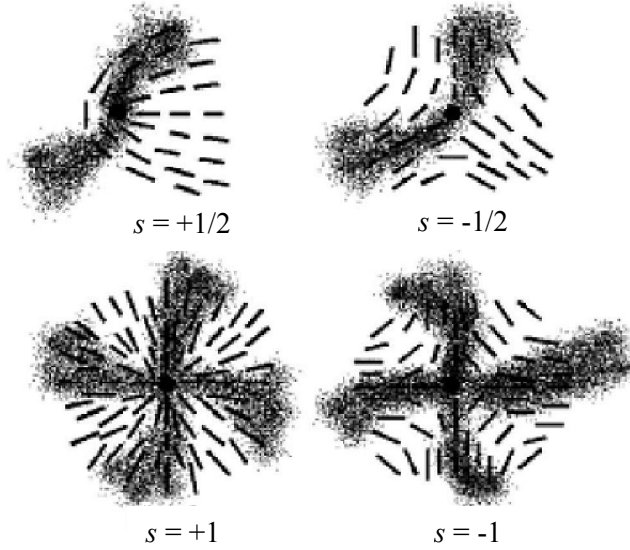
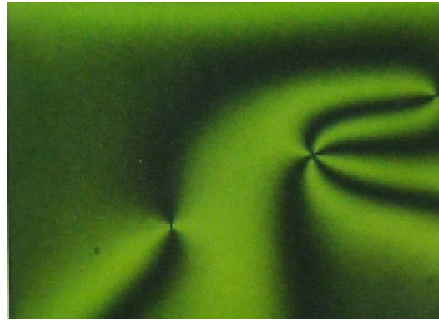
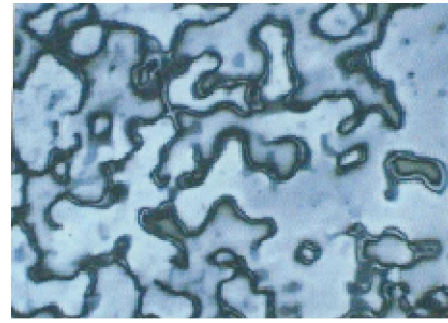


Figure 2.4: Director configurations due to defect lines in nematic Schlieren textures. Adopted from [60].

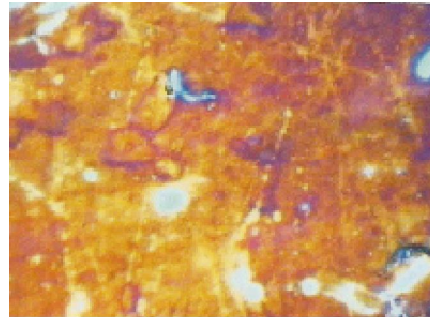
Another common texture for the nematic phase is the *thread-like* texture, which is the one that gives the nematic phase (Figure 2.5(b)) its name ("nematos"). The dark lines (i.e. threads) are line singularities, which either connect two $s = \pm 1/2$ point defects or form closed loops. However, the most frequently observed nematic texture is the *marble* texture, which is usually seen in a thin sample preparation. An example of marble texture is in Figure 2.5(c) [60].



(a) Schlieren



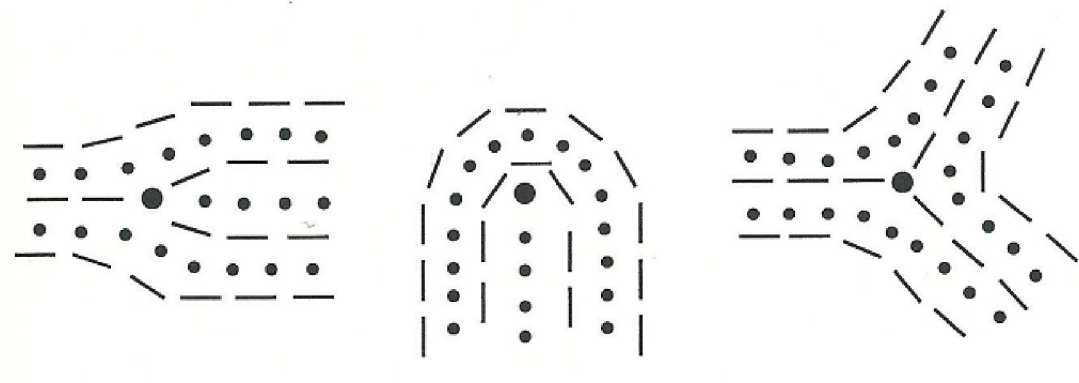
(b) Thread-like



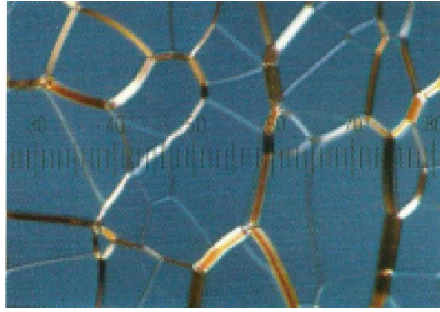
(c) Marble

Figure 2.5: Textures of nematic phases. Adopted from [60].

The cholesteric phase is the chiral version of the nematic phase. Defects in the cholesteric differ from the nematic due to the presence of the twisted director distribution. The cholesteric can be deformed in many ways but changing the pitch of a cholesteric director is the most difficult deformation [57]. Figure 2.6 shows some of the types of disclinations that may be found in cholesteric liquid crystals.

**Figure 2.6:** Three types of disclinations in cholesteric phase. Adopted from [57].

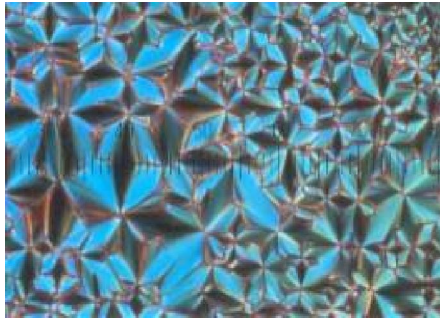
The three most commonly observed textures of the cholesteric phase are *oily-streaks*, *fan-shaped* or *fan-like*, and *polygonal* textures [66]. The director in the cholesteric phase that gives oily-streak texture is basically anchored under planar conditions at the substrate. A fan-like texture is exhibited by strongly twisted cholesteric materials, while a fan-shaped texture that displays a focal conic texture is found in materials with a slightly smaller twist. The latter texture is similar to that of a smectic A (SmA) phase but with a smoother appearance of the fan. The cholesteric polygonal texture is observed for samples with higher pitch value such as in the helical superstructure. Typical textures of cholesteric phase are shown in Figure 2.7.



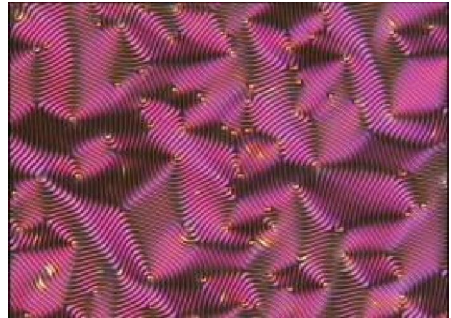
(a) Oily-streaks



(b) Fan-like



(c) Fan-shaped



(d) Polygonal

Figure 2.7: Textures of cholesteric phases. Adopted from [60].

As mentioned before, there is a variety of smectic liquid crystals (A, B, C, F, I...). In this section, we have chosen SmA as an example to describe defect and texture presence in a smectic phase. The smectic layers are basically perpendicular

to the substrate plane and arranged in Dupin cyclides where the circle becomes an ellipse and the straight line a hyperbola [53, 60]. The presence of these conic sections (plane slices through a cone) is the reason this texture is called the focal conic texture [57]. The corresponding smectic layer and director configuration are depicted in Figure 2.8.

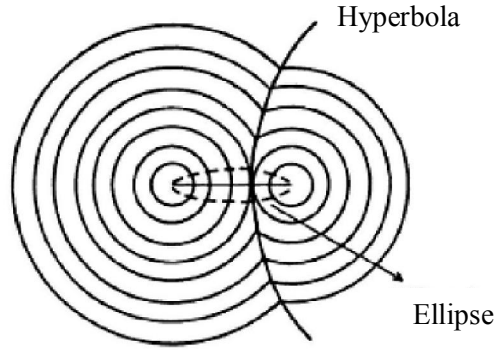
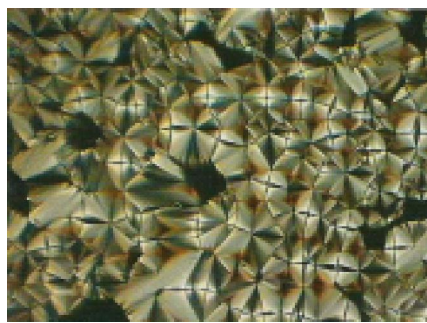


Figure 2.8: The general case when the smectic layers form Dupin cyclides. Adopted from [53].

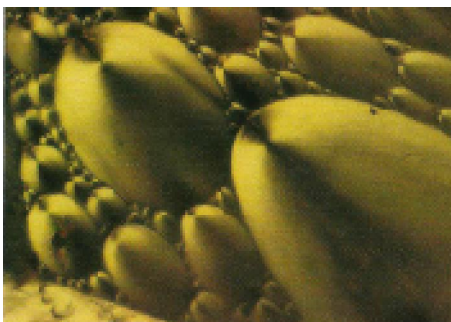
The most commonly observed texture for a SmA phase is the *fan-shaped* texture. The fan-shaped or focal conic textures are perpendicular to the substrate plane and ellipse. These textures are observed in thin samples as shown in Figure 2.9(a) and (b). On the other hand the *polygonal* texture is preferably observed in thick sample preparations (see Figure 2.9(c)). In smectic C (SmC), the *broken fan-shaped* texture is usually found when the SmA fan-shaped texture undergoes cooling into the SmC (see Figure 2.9(d)). The *Schlieren* texture of SmC is very similar to that of the nematic phase, except that in SmC, the Schlieren texture only exhibits four-fold brushes. This is depicted in Figure 2.9(e).



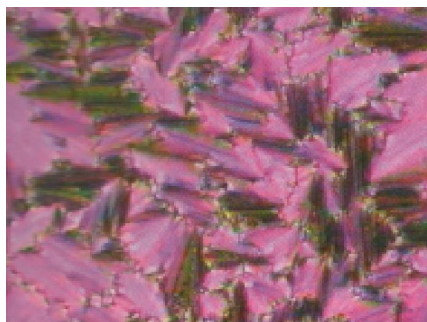
(a) Fan-shaped



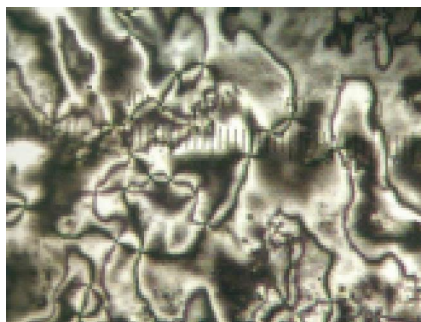
(b) Focal conic



(c) Polygonal



(d) Broken fan-shaped



(e) Schlieren

Figure 2.9: Textures of smectic phases. Adopted from [60].

Figure 2.10 shows Michel-Lévy's birefringence chart which is commonly used to correlate the phase difference between ordinary and extraordinary rays, thickness and birefringence of the sample examined under an optical polarizing microscope [124, 125]. From the OPM textures given above, the conventional liquid crystal compounds exhibit colourful liquid crystalline textures. However, in GL compounds, dull grey textures (see later in Chapter 5) are commonly observed due to their low birefringence. From Figure 2.10, we deduce that the GLs have

birefringence smaller than 0.005, which is several times smaller than is usual for typical liquid crystal materials. Unlike commonly-used liquid crystals especially those containing conjugated systems such as benzene ring, the absence of electron delocalization in these amphiphilic carbohydrate liquid crystals makes the value of the birefringence small. Hence the textures of these samples appear uncolourful.

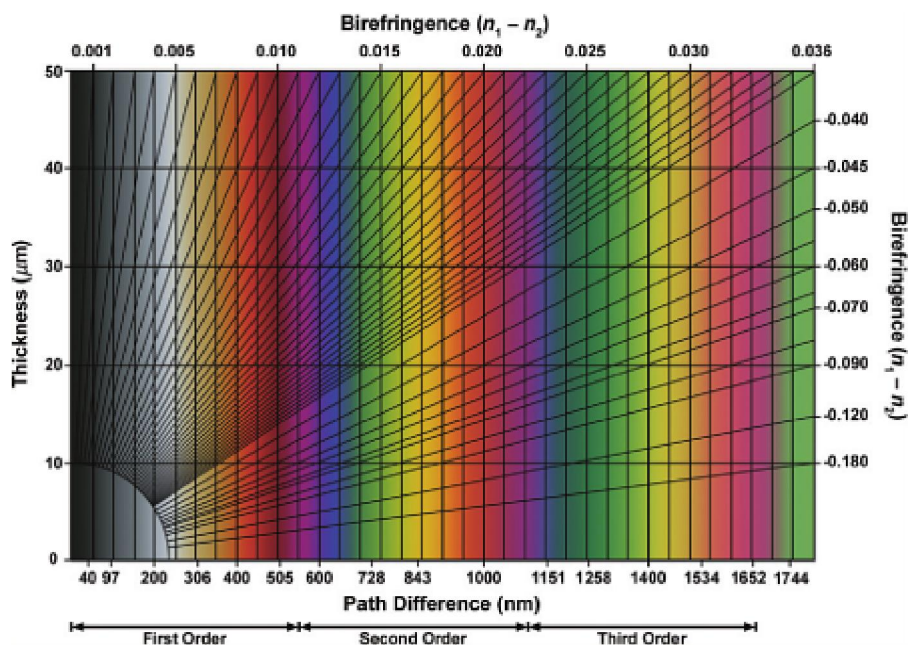


Figure 2.10: Interference colour chart or Michel-Lévy chart. Adopted from [124].

We have used an optical polarizing microscope extensively to investigate the thermotropic and lyotropic phase behaviours of the Guerbet branched-chain GLs in Chapter 5. A general discussion on how the thermotropic and lyotropic studies are conducted is separately described in the following section.

2.1.2 Thermotropic Phase Behaviour

Different thermotropic liquid crystal textures may be obtained by controlling the temperature. In the measurement, the sample is put on a slide without the cover slip, and heated on a temperature-controlled hot stage in order to remove any moisture trapped within the sample, since GLs are a hygroscopic material (easily absorbing moisture/water). When it reaches the isotropic phase, the sample is covered with a cover slip and gently pressed to make a uniform sample thickness before being cooled back to room temperature. A second heating is applied to determine the transition temperature. Once the isotropic temperature is achieved, the sample is cooled at a slower rate until it reaches room temperature. This gives better observation of the texture of the liquid crystals since the texture is clearer upon cooling [123]. Different phases are identified by their characteristic textures.

2.1.3 Lyotropic Phase Behaviour

Water penetration scan technique has been used to establish the lyotropic phase diagram qualitatively [126, 127]. The sample is prepared using the same method as for thermotropic measurement. However, when it is cooled to room temperature for the second time and a clear texture image emerges, a drop of distilled water is placed at the edge of cover slip. In the present study, water is used as a solvent since it is a common polar solvent and is important to many biological systems. The water drop is slowly brought into closer contact with the sample and the formation of various liquid crystal phase textures can be seen along the concentration gradient. Figure 2.11 shows the schematic representation of the water penetration technique. The exact concentration of the sample is unknown. However, we can assume that the most diluted area is located on the outside of the material

and it gets more concentrated towards the centre of the sample. The mesophase textures formed are recorded at variable temperatures, typically at 30, 40, 50, 60, 70 and 80°C.

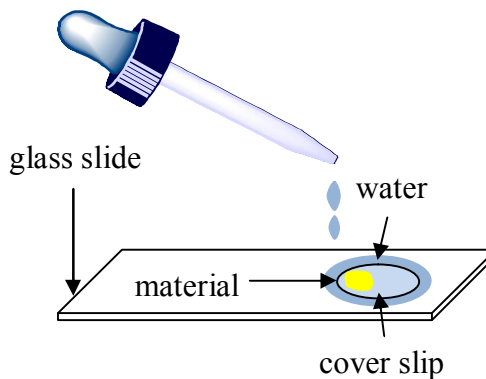


Figure 2.11: The water penetration techniques. Redrawn from [6].

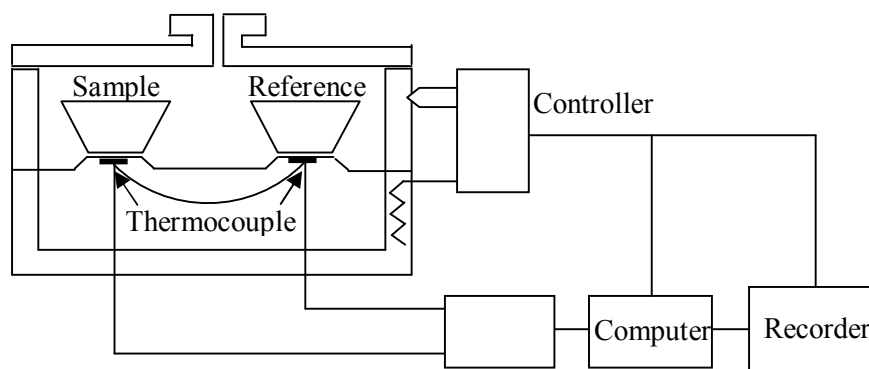
2.2 Differential Scanning Calorimetry (DSC)

DSC is usually employed as a complementary tool to OPM. DSC reveals the presence of liquid crystal phases by detecting the enthalpy change of a phase transition and the transition temperature. However, this technique cannot identify the type of phase but the magnitude of enthalpy (hence entropy) change gives some information on the degree of molecular ordering within a mesophase [56].

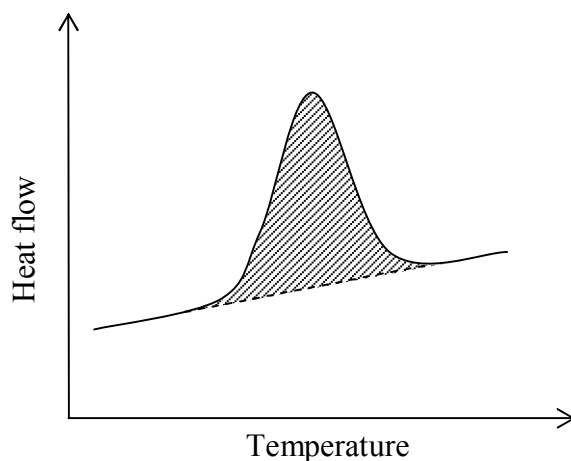
In general, DSC measures the difference in the heat flow rate between the sample and a reference sample while it is being subjected to a controlled temperature program [128, 129]. The two furnaces are separately heated but connected by two control loops to ensure that the temperature and rate of both remain the same during the heating and cooling cycles. A differential signal is generated which is proportional to the difference between the heat flow rates to the sample and the reference denotes by $(dH/dT)_S$ and $(dH/dT)_R$ respectively:

$$\Delta \frac{dH}{dT} = \left(\frac{dH}{dT} \right)_S - \left(\frac{dH}{dT} \right)_R. \quad (\text{Equation 2.1})$$

The energy required to maintain identical temperatures is measured and recorded by DSC as a peak. In this work, calibration of the DSC instrument is performed with indium for temperature and enthalpy accuracies. Figure 2.12 illustrates the schematic diagram of a differential scanning calorimeter and a typical DSC curve.



(a)



(b)

Figure 2.12: Schematic diagram of a (a) differential scanning calorimeter and (b) typical DSC curve. Redrawn from [128].

Based on the DSC measurements described in Chapter 5, the sample is weighed in an aluminium pan and dried over phosphorus pentoxide placed in a vacuum at 50 °C for 48 hours to remove any moisture. The sample is then immediately reweighed before being crimp-sealed with an aluminium top prior to

the measurement. The experiment is done for both heating and cooling cycles with variations of temperature, with ranges depending on the existence of liquid crystal phases previously identified by OPM.

2.3 Small-Angle X-ray Scattering (SAXS)

In 1898, X-ray was discovered by Wilhelm Roentgen [130, 131]. It is an electromagnetic wave similar to the visible light but with a shorter wavelength (<0.3 nm) than the latter (~ 500 nm). Today X-ray scattering has become an important tool for atomic structure studies and has evolved from a simple analytical method to a "category" of techniques [130]. Since SAXS responds to changes in electron density, it is reliable for structural analysis of various non-crystalline samples, macromolecular systems and heterogeneous solutions. SAXS is a non-destructive method which makes it particularly useful for biological systems [130, 131]. Apart from SAXS, nuclear magnetic resonance (NMR) is also a common method for obtaining high-resolution structural information. However, it is often complex and difficult to interpret without further supporting information [132]. In liquid crystal phase identification, the results from SAXS usually complement those from OPM.

SAXS measures the scattering intensity of a molecule as a function of the scattering angle, with a resolution ranging typically from 10 to 1000 Å (i.e. with scattering angles $< 5^\circ$). The resulting scattering patterns are characteristic of particle size, shape and internal structure [131, 133]. The basic principle of SAXS involves an elastic collision between an incoming wave and a particle, causing the reflected wave to scatter in all directions. The formation of scattering peaks is due to the constructive interference of reflected waves with one another along certain angles [130]. In 1913, William Lawrence Bragg and William Henry Bragg introduced a simple relationship between the wavelengths of X-ray to the spacing of atomic

planes. Parallel planes of atoms reflect the incident beam of X-ray as shown in Figure 2.13 [134, 135]. Using geometry and the Pythagorean theorem, Bragg's Law for a simple scattering is derived, as in the equation:

$$n\lambda = 2d \sin\theta, \quad (\text{Equation 2.2})$$

where n is an integer representing the order of the diffraction peak ($n = 1, 2, 3, \dots$), λ is the wavelength of the X-ray, d is the inter-plane distance (d-spacing) and θ is the angle between the reflected ray and the plane formed by the sample surface [17, 22].

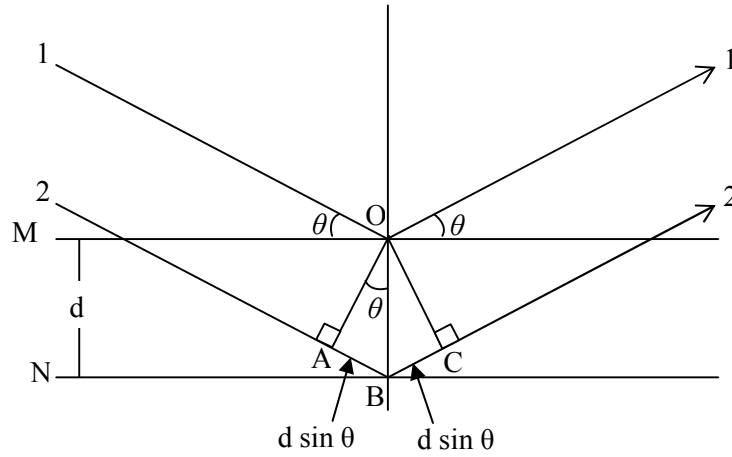


Figure 2.13: Bragg's Law. Redrawn from [134].

Scattering patterns are usually presented as a function of q , which is the length of the scattering vector and is given in Equation 2.3:

$$q = \frac{4\pi}{\lambda} \sin\theta. \quad (\text{Equation 2.3})$$

The scattering pattern is normally known as the structure in reciprocal space (with unit of \AA^{-1}), whereas the particle is referred to as the structure in real space (with unit of \AA) [131]. The equation of scattering function is expressed in terms of the reciprocal spacing, s as given in the following equation:

$$s = \frac{2}{\lambda} \sin \theta. \quad (\text{Equation 2.4})$$

The scattering of one particle consisting of many atoms results from the detected interference pattern produced by all the waves from every atom inside the particle. A summation of all the wave amplitudes at the detector position and the square of this sum results in an interference scattering pattern (see Figure 2.14). This oscillating pattern is a characteristic for the shape or form of the particle. Therefore it is called 'the form factor', $P(q)$ and must be scaled with a constant in order to match the experimental intensity. However, for structure determination, the scaling factor is not crucial [131].

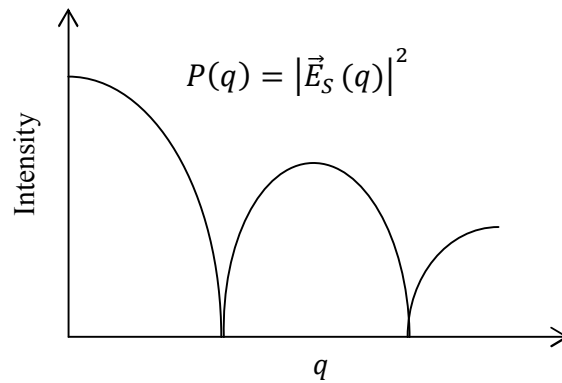


Figure 2.14: The form factor, $P(q)$ of a particle is an interference pattern. $|\vec{E}_S(q)|^2$ is the squared amplitude of the wave as a function of q . Redrawn from [131].

In a concentrated sample, the molecular distances relative to one another are in the same order of magnitude as the atomic distances within the particles. Hence, the interference pattern will contain contributions from neighbouring particles as well. The extra interference pattern multiplied with the form factor of the single particle is termed 'the structure factor', $S(q)$. Eventually, this wave can develop into a pronounced peak when the particles align themselves into a highly ordered and periodic arrangement (i.e. crystalline). This is called the Bragg peak [131].

The peaks in the structure factor become more pronounced when the particle positions become increasingly ordered. When the domain size of ordered particles increases, the system is said to be crystallized. The structure factor of a crystalline substance is normally called the lattice factor. It is a set of narrow and intensive peaks at well-defined angles. The ratios of the peak positions on the q -scale have typical values, for example,

Lamellar:	1, 2, 3, 4, 5, ...
Cubic ($Pn3m$):	$\sqrt{2}$, $\sqrt{3}$, $\sqrt{4}$, $\sqrt{6}$, ...
Cubic ($Im3m$):	$\sqrt{2}$, $\sqrt{4}$, $\sqrt{6}$, $\sqrt{8}$, ...
Cubic ($Ia3d$):	$\sqrt{6}$, $\sqrt{8}$, $\sqrt{14}$, $\sqrt{20}$, ...
Hexagonal:	1, $\sqrt{3}$, $\sqrt{4}$, $\sqrt{7}$, $\sqrt{9}$, ...

The basic components of an SAXS instrument are an X-ray source, a collimation system, a sample holder, a beam stop and a detection system, as illustrated in Figure 2.15. The source such as an X-ray tube, synchrotron or rotating anode irradiates the sample and the detector measures the out-coming radiation from the sample at a certain range of angles. The collimation system makes the beam narrow and defines the zero-angle position. The beam stop prevents the intense

incident beam hitting the detector which would overshadow the relatively weak scattering of the sample and would even destroy some of the detectors [131].

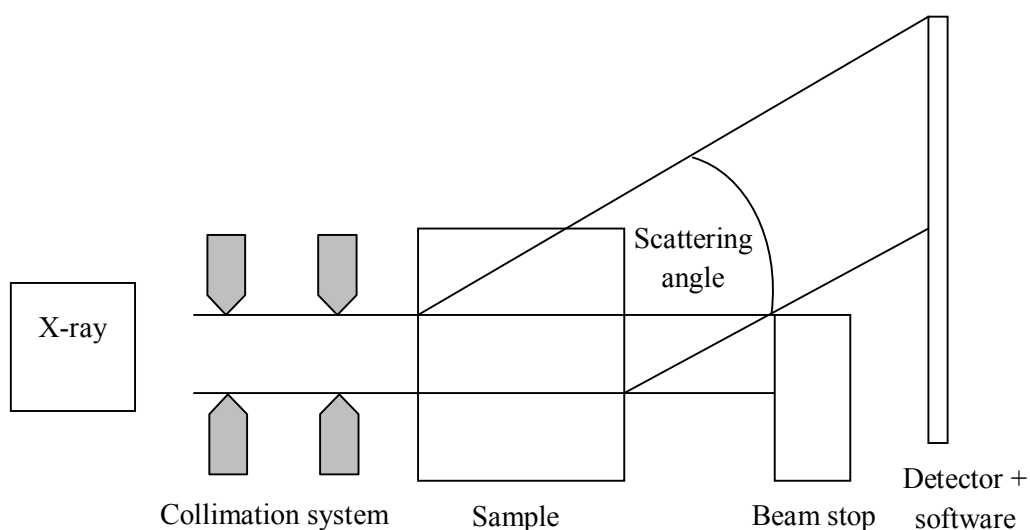


Figure 2.15: The components of an SAXS instrument. Redrawn from [131].

2.4 Fluorescence

The emission of light from electronically excited states of any material is called luminescence, and can be divided further into fluorescence and phosphorescence. The first type of luminescence which is fluorescence, was introduced by a physicist and mathematics professor, Sir George Gabriel Stokes, in the middle of the 19th century. However, the first reported observation of fluorescence had been made by Nicolas Monardes in 1565 on the peculiar blue colour of an infusion of a wood called *Lignum Nephriticum* [136].

When light of an appropriate wavelength is absorbed by a molecule, the molecular electronic state transforms from the ground state to the excited electronic state, which is usually the first excited singlet state, S_1 . The molecule in this excited state may undergo several relaxation processes to its ground state. Fluorescence is one of the processes and results in the emission of light. The lifetime of fluorescence

is short (approximately 10^{-8} s) so that in many molecules it can compete favourably with other relaxation processes, including phosphorescence.

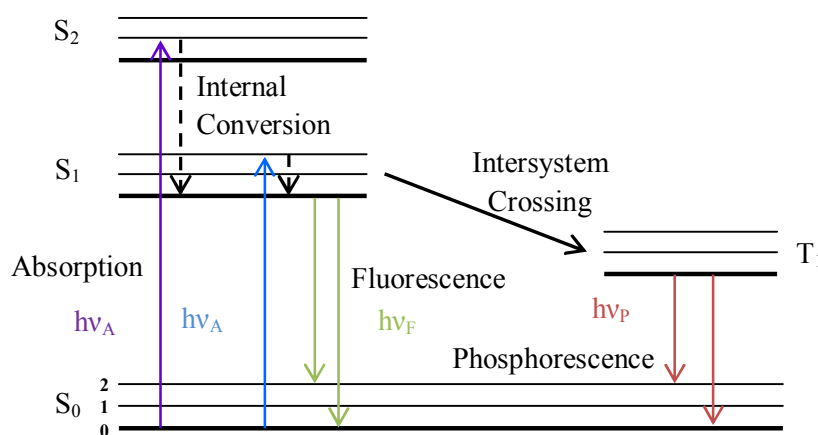


Figure 2.16: A typical Jablonski diagram. Redrawn from [137].

However, many other pathways for de-excitation are possible such as internal conversion (i.e. direct return to the ground state without emission of fluorescence), intersystem crossing (possibly followed by emission of phosphorescence), intramolecular charge transfer and conformational change [136, 138]. The processes occurring between the absorption and emission of light are illustrated in the Jablonski diagram (Figure 2.16).

The second type of luminescence, phosphorescence, is the emission of light from triplet excited states, in which the electron in the orbital has the same spin orientation as the ground-state electron. Transitions to the ground state are forbidden and the emission rates are slow (10^3 to 10^0 s $^{-1}$), so that phosphorescence lifetimes are typically milliseconds to seconds. Even longer lifetimes are possible, as seen from ‘glow in the dark’ items (for example, the fire-fly). Following exposure to light, the phosphorescence substances glow for several minutes while the excited phosphors slowly return to the ground state. Phosphorescence is usually not seen in

fluid solutions at room temperature. This is because there exist many deactivation processes that will compete with emission, such as non-radiative decay and quenching processes [137].

Fluorescence is a powerful tool for investigating the structure and dynamics of matter and living systems at a molecular or supramolecular level [139-147]. The fluorimetric methods offer great advantages like high sensitivity and specificity and they are able to provide dynamics of fast phenomena and structural parameters of the system. They were first used as analytical instruments to determine the concentrations of various species, including neutral and ionic. The fluorescence molecules acting as probes are useful for estimating local parameters such as polarity, fluidity, molecular mobility and electrical potential in diverse systems like polymers, surfactant solutions, solid surfaces, biological membranes, proteins, nucleic acids and even living cells. The fluorescent probes can be intrinsic or introduced on purpose [136].

Fluorescence typically occurs in aromatic molecules. In general, fluorescent probes can be classified into three types. The first is an *intrinsic probe* like tryptophan residues in a protein. Second is an *extrinsic covalently bound probe* where the molecule contains a fluorophore part at a specified location. There are diverse examples of probes covalently attached to a particular system (e.g. surfactants, polymer chains, phospholipids) such as fluorescein, rhodamine and erythrosin derivatives. The third type is an *extrinsic associating probe*, which is used in the investigation due to the difficulty in the synthesis of fluorescence substance. The site where the extrinsic probe resides is very much dependent on its chemical nature and the resulting specific interaction that can be established within the region of the system to be probed. Thus, knowing the hydrophilic, hydrophobic or amphiphilic character of a probe is vital. A few examples of this type of probes

are pyrene (hydrophobic), pyranine (hydrophilic) and 1-pyrenedodecanoic acid (amphiphilic) [136].

In this work, we use extrinsic associating probes for the characterization of several lyotropic liquid crystalline phases. A common fluorophore, i.e. tryptophan (Trp), which gives high quantum yield is selected for the investigation [148]. In addition, its esters may also be used as probes, because their fluorescence is very sensitive to the environment [148, 149]. The emission spectrum of tryptophan is strongly dependent on the solvent polarity. Tryptophan exists in two excited states and the fluorescence from that depends on the nature of the solvent [137]. The two electronic states are termed 1L_a and 1L_b , based on the direction of fluorescence polarization [150, 151]. Fluorescence from the 1L_b state is infrequent. The higher solvent sensitivity of the 1L_a state is expected, since the polar nitrogen atom of the indole system has more interaction with the polar solvent, unlike that of 1L_b as illustrated in Figure 2.17.

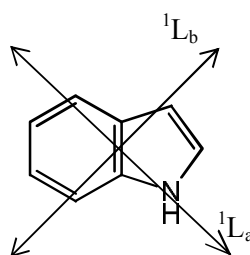


Figure 2.17: Possible electronic states (1L_a and 1L_b) of the indole system of tryptophan [152].

The measurement of fluorescent behaviour, therefore, provides information on the chemical environment of the probes. The chain length of the tryptophan ester determines the degree of probing into the lyotropic phase, thus allowing different polar regions to be investigated.

In order to study the lipid domain as well, a hydrophobic probe, pyrene, is introduced. As a fluorescent probe, the fluorescence spectrum of pyrene monomer is sensitive towards the polarity of the microenvironment [153-155]. The small-sized pyrene leads to only minimum perturbations of the microenvironment and is not attracted to the interfaces due to the absence of the hydrophilic part. Pyrene can also form excimers, or excited dimers, which fluoresce differently from the monomer. The dimer formation only appears upon excitation, thus fluorescence investigations can provide information on the mobility of pyrene in a medium [156]. This can be used to study a variety of phenomena, including membrane ‘fluidity’, phase transitions, membrane fusion and ‘trafficking in living cells’[157].

In order to minimize the perturbation of extrinsic fluorescent probes, it is important to pay attention to the size and shape of the probe with respect to the probed regions.

2.4.1 Steady-State Fluorescence Spectroscopy

Figure 2.18 shows the schematic representation of a commercially available steady-state spectrofluorometer. A high pressure xenon arc lamp is usually used as the light source with continuous emission from about 250–750 nm. A monochromator (excitation monochromator) is used to select the excitation wavelength. Fluorescence is collected at right angle (90°) with respect to the incident beam and detected through a second monochromator (emission monochromator) which is adjustable for both wavelength and slit width, using a photomultiplier. The electronic devices and the computer control the motorized monochromators for automatic scanning of wavelengths.

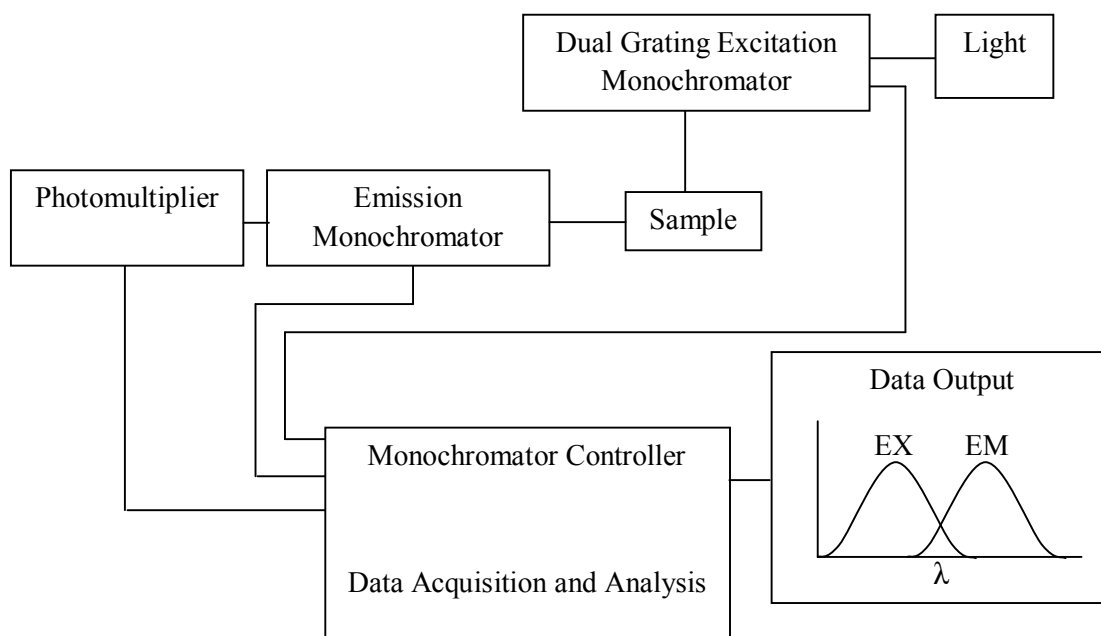


Figure 2.18: Schematic diagram of steady-state fluorescence spectrometer. Redrawn from [137].

2.4.2 Time-Resolved Fluorescence Spectroscopy

Knowledge of the dynamics of excited states is essential for understanding photophysical, photochemical and photobiological processes [136]. Any change in the surrounding environment will result in changes in the excited state behaviour including the average time a molecule resides in its excited state, or fluorescence lifetime. Typically, a fluorescent molecule upon excitation to a higher excited electronic state returns to its ground state in about 10 ns.

The nature of the light and the molecule allows two different approaches to measure the fluorescence lifetime of a fluorophore. These are the *time-resolved* method (direct measurement by following the decay of excited fluorescent molecule in a very short time) and the *phase modulation* method (indirect measurement by measuring the changes in the harmonic characteristics of the light beam). Typically, the fluorescence intensity is measured after the excitation pulse has ended. However, alternative methodologies for decay measurement are available. They include stroboscopic method, a transient recorder, signal averaging or single-photon

counting [138]. Herein, we will describe the lifetime fluorescence spectroscopy using the stroboscopic method in detail since it is this method we have employed throughout the study.

The schematic diagram of the stroboscopic technique is shown in Figure 2.19. The sample is excited by light pulses from the flash lamp. A computer-controlled digital delay unit is used to gate or 'strobe' the photomultiplier by a voltage pulse (whose width defines a time window) at a time accurately delayed with respect to the light pulse. Synchronization with the flash lamp is achieved by a master clock. So, only photons emitted from the sample that arrive at the photocathode of the photomultiplier during the gate time will be detected. The fluorescence intensity as a function of time can be constructed by moving the time window after each pulse from before the pulse light to any suitable end time [136].

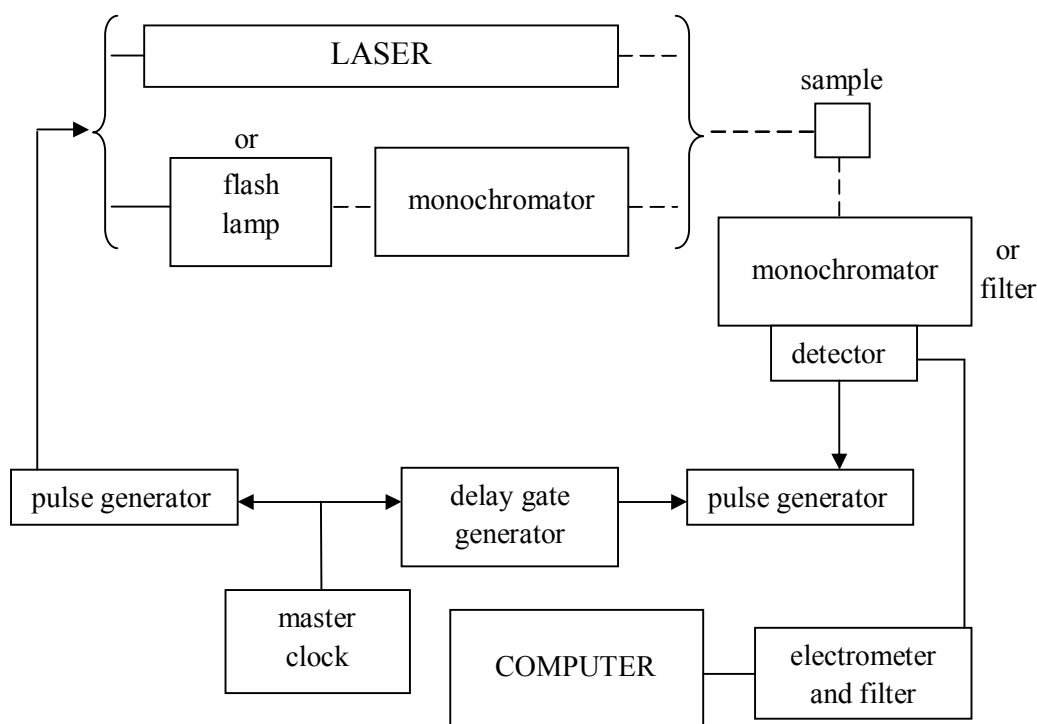


Figure 2.19: Schematic diagram of the time-resolved fluorescence spectrometer (stroboscopic technique). Redrawn from [136].

The stroboscopic method does not require expensive electronics. High-frequency light sources are not necessary because the signal intensity is directly proportional to the light pulse intensity. Conversely, the time resolution is less than single-photon timing technique and a sample with low fluorescence intensity is difficult to measure [136].

Apart from the two dominant techniques used by researchers as discussed above, there are other methods for measuring intensity decays such as the upconversion method and streak camera. An upconversion method involves the bypass of the fluorescence signal through an upconversion crystal and gating the crystal with another picosecond or femtosecond light pulse. The time-resolved decay is obtained by measuring the intensity of the upconverted signal as the delay time is varied. However, its instrumentation is too complex for most biological experiments. For example, a minor change of the emission wavelength requires major readjustment of the angle-tuned crystal detector. Also, decay times of more than 1–2 ns are difficult to measure due to the use of a delay line (~ 1 ns/foot) [137].

Another method in fluorometry is the streak camera, which operates by dispersing the photoelectrons across an imaging screen at high speed using deflection plates within the detector. It can provide simultaneous measurements of both steady-state and time-resolved decays which are valuable in the study of time-dependent spectral relaxation or samples which contain fluorophores emitting at different wavelengths. Due to the low dynamic range of measurable intensity and poor signal-to-noise ratio, the streak camera is not widely used in biochemical fluorescence studies despite its having high time resolution [137].

CHAPTER 3

CHARACTERIZATION OF THE HEAD GROUP AND THE HYDROPHOBIC REGIONS OF A GLYCOLIPID LYOTROPIC HEXAGONAL PHASE USING FLUORESCENT PROBES

The Journal of Physical Chemistry C 2011, 115, 19805–19810

CHARACTERIZATION OF THE HEAD GROUP AND THE HYDROPHOBIC REGIONS OF A GLYCOLIPID LYOTROPIC HEXAGONAL PHASE USING FLUORESCENT PROBES

Lyotropic liquid crystal phases are related to biological entities such as cell membranes, as well as to technological applications, for example emulsifiers and drug-delivery systems. In this chapter, we investigate one of the most stable lyotropic phases of the n-dodecyl β -D-maltoside (β -Mal-OC₁₂), the hexagonal phase, using fluorescent probes. We will show that the results will be useful as a point of reference to employ the present probes combination to characterize other biologically-related lipid phases that are thought to play a crucial role in lipid-membrane interaction.

3.1 Introduction

GLs belong to a large family of molecules known as glycoconjugates [158-160]. They have been extensively studied due to their connection to biological cell membranes. Although GLs are minor components in prokaryotes' and eukaryotes' cell membranes (compared to phospholipids), their widespread occurrence and extensive structural diversity suggest functional importance in cell processes [161-167] such as endo- and exocytosis, apoptosis and molecular-recognition at the cell surface specific to the cell type [160, 168, 169]. Chemically, GLs exhibit surfactant properties due to the dichotomic balance of the carbohydrate head group (with one or more monosaccharide units) and the lipophilic tail. As amphiphilic liquid crystals, [19, 170-172] they are able to self-assemble in both dry (thermotropic) and solvated (lyotropic) states into many different polymorphic forms such as the lamellar, hexagonal, cubic, and gel phases, depending on appropriate conditions.

Phase studies of GLs have mostly focused on lyotropic systems because these are related to biological membranes. The adhesion property of the sugar head groups and their interactions with peptides and surface proteins make them suitable targets for nanoparticle vectors [48]. Their importance in biology and industry has encouraged many synthetic GLs to be developed, including alkyl polyglycosides (APGs), which have been used for numerous surfactants applications [173-175].

In this chapter, we characterize one of the glycoside systems, namely the hexagonal phase of n-dodecyl β -D-maltoside (β -Mal-OC₁₂)/water system (shown in Figure 3.1) using steady-state and time-resolved fluorescence methods. The lipid self-assembly structure and a partial phase diagram of β -Mal-OC₁₂ have been reported previously [176, 177]. In water, β -Mal-OC₁₂ gives a variety of self-assembly structures, including the hydrated solid, lamellar, cubic, and hexagonal phases, as well as the micellar solution as a function of increasing water concentration. β -Mal-OC₁₂ has been used in many applications such as in the purification and stabilization of RNA polymerase, [178] protein solubilization, [179] and the detection of protein-lipid on bacteriorhodopsin [180]. Herein, we study the β -Mal-OC₁₂ hexagonal self-assembly structure, which exists over a wide range of concentration and temperature, [177] at lipid concentration of 65% (w/w).

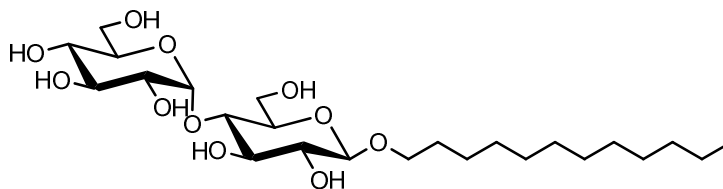


Figure 3.1: The chemical structure of n-dodecyl β -D-maltoside (β -Mal-OC₁₂).

In the present study we use two fluorescent probes namely tryptophan and pyrene, as local reporters in the lipid. These probes are classified as extrinsic associating probes in which the region where the probes reside is very much dependent on their chemical nature and the resulting specific interaction of the system to be probed (see Chapter 2). The tryptophan and its derivatives are used to probe the polar head group region and the pyrene to probe the hydrophobic region of the lipid. In order to access different regions in the hydrophilic domain, variable alkyl chains attached to the tryptophan ester molecule are used, similar to the dynamics study reported by Kim et al. [149]. Figure 3.2 shows the chemical structures of the fluorescent probes used in this study.

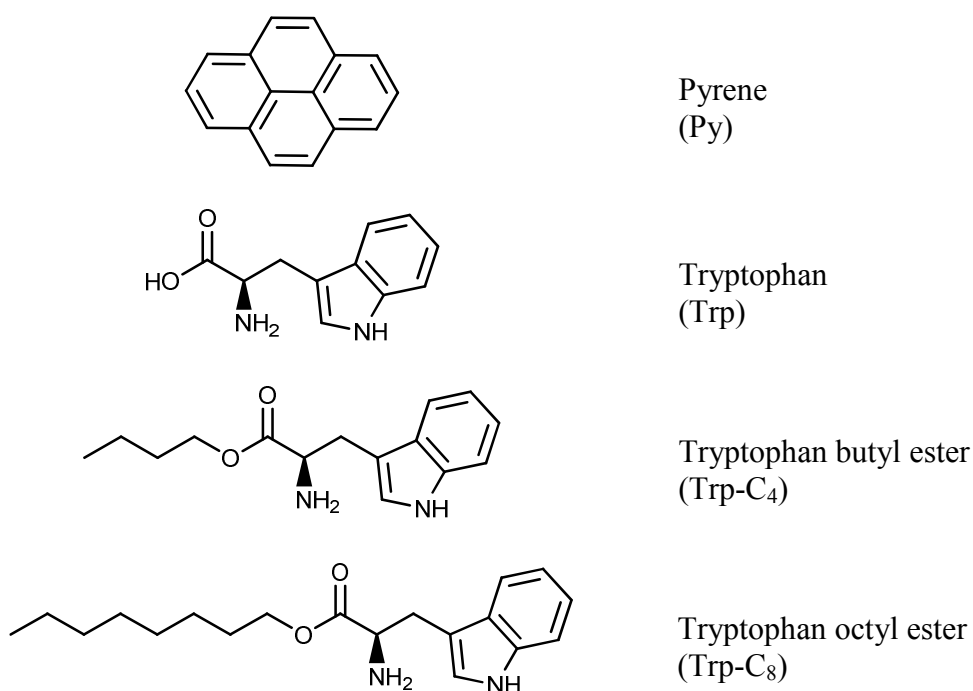


Figure 3.2: The chemical structures of the fluorescent probes.

A schematic diagram showing how the tryptophan molecule approaches the head groups with increasing alkyl chain length is given in Figure 3.3. Pyrene is expected to reside in the hydrophobic region as shown in the diagram. We estimate

the polarity of different regions of the polar domain based on a parallel study in different solvents, and we discuss our results in relation to the flexibility of the lipid self-assembly.

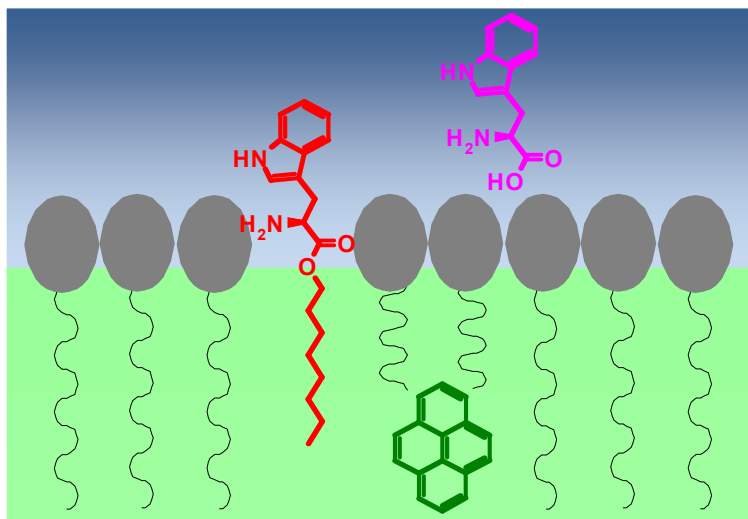


Figure 3.3: A schematic diagram showing one layer of the lipid self-assembly with the expected locations of the probes. Pink: tryptophan (Trp). Red: Trp-C₈. Green: pyrene.

3.2 Research Methodology

3.2.1 Materials

β -Mal-OC₁₂ (98%) and pyrene (99%) were purchased from Sigma-Aldrich. L-tryptophan (99%) was obtained from Merck. Tryptophan butyl ester (Trp-C₄) and its octyl analog (Trp-C₈) used in this work were prepared according to a literature procedure [181]. Anhydrous 1,4-dioxane and methanol were obtained from Sigma-Aldrich Chemical Co. Anhydrous ethanol was received from Acros Organics. Spectroscopic grade cyclohexane was purchased from BDH Chemicals. Deionized water (Millipore) was used. All chemicals and solvents were used without further purification.

3.2.2 Sample Preparation

The concentration of tryptophan/tryptophan ester/pyrene in the aqueous β -Mal-OC₁₂ formulation for both steady state and time-resolved experiments was adjusted to 0.1 mM. The value was based on an estimated density of $\sim 1.3 \text{ g/cm}^3$ for the mixture. The hexagonal phase used for this study was observed at lipid concentration of 65% (w/w) according to its published binary phase diagram [177]. The hexagonal phase was confirmed using optical polarizing microscopy (OPM) by contact penetration. OPM investigations with water and buffer led to the same optical texture. All samples were prepared by mixing the lipids with tryptophan/tryptophan esters/pyrene dissolved in methanol. The methanol was evaporated afterwards and the samples were dried in a high vacuum to remove the solvent traces. 65 mg of the mixture and 35 mg of water were placed in a 4-mm diameter quartz tube. The hydrated sample was immediately flame-sealed and subjected to repeated cycles of centrifugation and heating to ensure that a homogenous mixture was formed. As for reference samples in solution, all were prepared at a concentration of 0.05 mM. For samples which were difficult to dissolve in water (tryptophan esters and pyrene), a stock solution in methanol (5 mM) was prepared. This solution was then diluted with aqueous buffer (25 mM sodium phosphate buffer, pH 7.2) to reach the desired concentration. The final methanol:water (v/v) mixture was 10:90. A ratio above 20:80 was shown to behave like pure water [182-186].

3.2.3 Instrumentation

Fluorescence spectra were recorded on a Shimadzu RF-5301 PC spectrofluorophotometer. Lifetime measurements were performed using a TimeMaster fluorescence lifetime spectrometer obtained from Photon Technology International. Excitation was done at 280 and 340 nm using LEDs. The instrument response function (IRF) was measured from the scattered light and estimated to be approximately 1.5 ns (FWHM). The measured transients were fitted to multiexponential functions convoluted with the system response function. The fit was judged by the value of the reduced chi-squared (χ^2). The experimental time resolution (after deconvolution) was approximately 100 ps, using stroboscopic detection [187]. In all the experiments, samples were measured in a 1-cm path length quartz cell at 23 ± 1 °C.

3.3 Results and Discussion

3.3.1 Probing the Polar Region of the Lipid

In order to understand the spectroscopic behaviour of the probes inside the GLs, it is important to understand how fluorescence from each probe is affected by its local environment. We start this section by discussing the fluorescence results of tryptophan in different solvents. One factor affecting the tryptophan fluorescence is the polarity of its surrounding environment. The fluorescence spectrum of tryptophan is strongly dependent on solvent polarity. Figure 3.4 shows the fluorescence spectra of tryptophan in different solvents of varying polarity. Table 3.1 displays the position of the peak maxima. The sensitivity of the peak position is clearly dependent on the solvent polarity. In a solvent such as 1,4-dioxane (a non-dipolar solvent [188]), fluorescence is peaked at 334 nm, whereas this peak is red-

shifted as the solvent polarity increases. The maximum red shift is observed in aqueous solution.

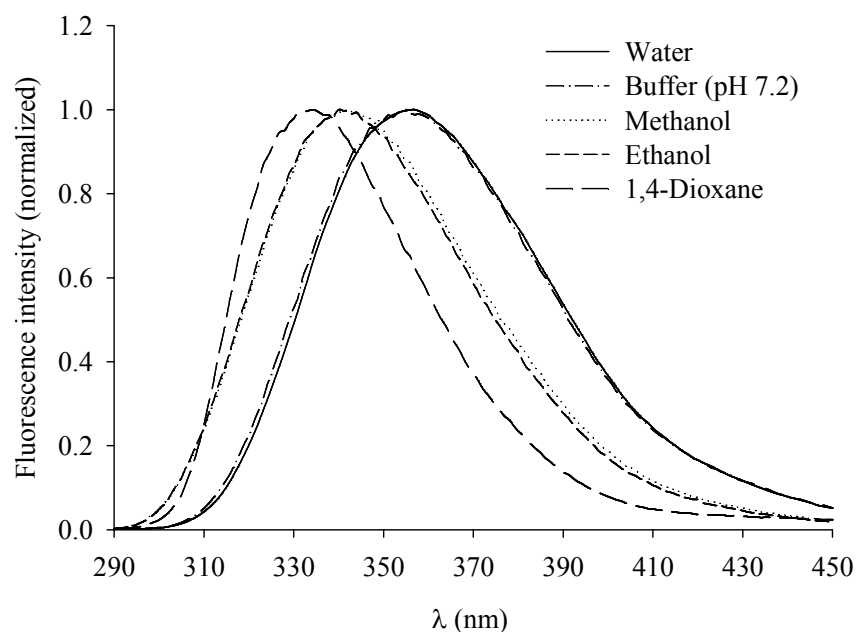


Figure 3.4: Fluorescence spectra of tryptophan in different solvents. $\lambda_{\text{ex}} = 280$ nm.

Table 3.1: Fluorescence spectral peak maxima of tryptophan and its derivatives in different solvents and lipid.

Probe	Solvent / Medium	ϵ^a 25 °C	π^{*a}	E_T^{Na} 25 °C	Peak maximum ^b (nm)
Trp	1,4-Dioxane	2.21	0.49	0.16	334
	Ethanol	24.55	0.54	0.65	340
	Methanol	32.66	0.60	0.76	340
	Buffer	78.30	1.09	1.00	355
	Lipid				345
Trp-C ₄	Buffer				355
	Lipid				345
Trp-C ₈	Buffer				355
	Lipid				337

^a Obtained from reference [189]. ^b $\lambda_{\text{ex}} = 280$ nm.

The detected unstructured fluorescence in all the solvents is due to the 1L_a state, since fluorescence from the 1L_b state is reported to be structured (see Section 2.4) [150, 151]. The 1L_a state is more solvent-sensitive than the 1L_b state and its transition shifts to lower energies in polar solvents [137]. The higher solvent sensitivity for the 1L_a state is expected since the 1L_a transition more directly involves the polar nitrogen atom of the indole ring of the tryptophan moiety [137].

We note here that the fluorescence peak in water and buffer are the same with respect to shape and position, which indicates that there is no salt effect of the buffer on the 1L_a excited state fluorescence of tryptophan. Figure 3.5 shows the fluorescence spectra of tryptophan and its two derivatives (Trp-C₄ and Trp-C₈) dissolved in buffer after excitation at 280 nm. As shown in the graph, the alkyl chain of the tryptophan ester has no effect on the fluorescence peak.

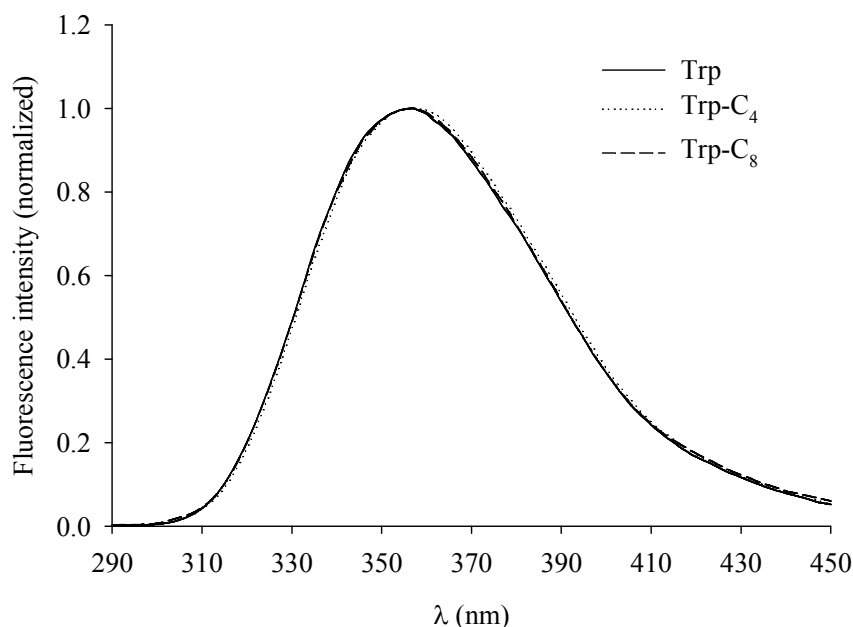


Figure 3.5: Fluorescence spectra of tryptophan and its derivatives in buffer of pH 7.2. $\lambda_{\text{ex}} = 280$ nm.

Figure 3.6 shows the fluorescence spectra of the three probes (Trp, Trp-C₄ and Trp-C₈) embedded in the lipid and measured after excitation at 280 nm. The fluorescence spectrum of Trp in the buffer is included for comparison. As shown in the graph, the spectra in lipid are blue shifted, compared to that in the buffer. This observation is an indication of the different environment experienced by the tryptophan moiety in the polar region of the head groups of the lipid (being less polar than pure water). Table 3.1 summarizes the fluorescence peak maxima in buffer and lipid.

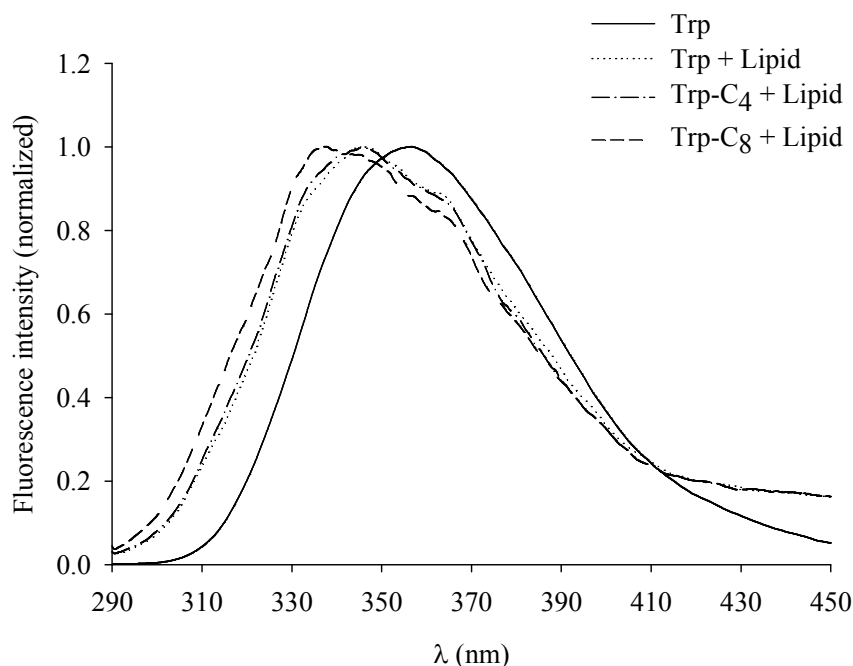


Figure 3.6: Fluorescence spectra of tryptophan and its derivatives in lipid. The spectrum of tryptophan in buffer is included for comparison. The spectra are normalized for easy comparison. $\lambda_{\text{ex}} = 280$ nm.

According to the results of Figure 3.6 and Table 3.1, the tryptophan molecule has a local environment that is less polar than bulk water. As the chain length increases (see the case of Trp-C₈), the tryptophan molecule is pulled closer to the polar head groups and its fluorescence shows the most blue shift. This is due to the nature of the alkyl ester chain being hydrophobic and tending to escape the

hydrophilic region. This tendency results in the chain being buried inside the tail region of the lipid, which in turn brings the tryptophan molecule (attached to the chain) closer to the head groups. The pronounced blue shift observed in the case of Trp-C₈ indicates that water molecules are less polar as they get closer to the head groups. This observation complements earlier results, which show that water molecules tend to be more ordered and less flexible as they get closer to the head groups [149]. This may explain the unique solvation characteristic of water that requires random distribution (disorder) of the water molecules in order to solvate the polar sites of the solute molecule, causing a maximum polarity effect. The less flexible water molecules in the head group region may interrupt the tendency of water molecules to strongly associate with one another through intermolecular hydrogen bonds that allow more than one molecule of water to form a solvent network [189]. The constrained water molecules may cause the reduced polarity effect experienced by the tryptophan moiety.

By comparing the fluorescence peak position of tryptophan in lipid (Figure 3.6) and in different solvents (Figure 3.4), we may estimate the polarity of the local environment around the tryptophan moiety when embedded in lipid. The peak positions in the case of Trp and Trp-C₄ in lipid are close to that in methanol and ethanol (see Table 3.1). This indicates that the polarity of the intermediate region between bulk water and the head groups resembles that of simple alcohols (water in this region is more flexible than water at the head group region). On the other hand, as tryptophan gets closer to the head groups, it experiences a local polarity close to that of 1,4-dioxane (compare the peak position for Trp-C₈ in lipid with that in 1,4-dioxane).

Details about the physical nature of the head group region of the lipid system may be correlated to the physical properties of the 1,4-dioxane molecule as a solvent. A solvent such as 1,4-dioxane, which appears to be non-polar according to its static dielectric constant ($\epsilon = 2.21$), has a high solvent polarity parameter ($\pi^* = 0.49$) and an E_T^N value of 0.16 (see Table 3.1) [189]. 1,4-dioxane has two $\text{CH}_2\text{-O-CH}_2$ groups opposite to each other, which results in a net zero dipole moment. Thus it is considered a non-dipolar solvent [188]. However, 1,4-dioxane exhibits a large quadrupole moment [190, 191] which is reflected in its π^* parameter that mainly takes into consideration the polarizability and the dipolarity of the solvent [188]. The corresponding E_T^N value indicates that 1,4-dioxane exhibits only 16% of the solvent polarity of water, thus classifying 1,4-dioxane as an apolar, non-hydrogen bond donor solvent [189]. Water interaction with the head groups of lipid may resemble the interaction between 1,4-dioxane and water which are miscible in all proportions. Mixtures of 1,4-dioxane and water are proposed as media to study probes in nanoenvironments similar to those encountered in vesicles and at interfaces [182, 183, 192-195].

The above results point to a polarity gradient in the lipid self-assembly system. The reduction in polarity in going from the centre of the hydrophilic region towards the head group region indicates a smooth transition from the polar domain to the hydrophobic domain which is important for the stability of the lipid.

The fluorescence lifetimes of tryptophan and its ester derivatives are measured in buffer and lipid. The data is summarized in Table 3.2. The two measured lifetime components of tryptophan in buffer are due to two different rotamers [137, 196, 197]. The relative contribution from the short lifetime component increases in lipid. The biexponential nature of the tryptophan fluorescence decay in lipid constitutes strong support for the ground state

heterogeneity that is associated with a degree of flexibility of the tryptophan side chain to adapt two different rotamers. The results point to a degree of flexibility of the lipid self-assembly.

Table 3.2: Fluorescence lifetime (ns) measurements of tryptophan and its derivatives in buffer and lipid.

Probe	Buffer			Lipid		
	τ_1^a	τ_2^b	χ^2	τ_1^a	τ_2^b	χ^2
Trp	0.55 (0.10)	3.9 (0.90)	1.05	0.17 (0.49)	3.7 (0.51)	1.03
Trp-C ₄	0.69 (0.15)	3.7 (0.85)	1.00	0.23 (0.46)	3.7 (0.54)	1.02
Trp-C ₈	0.45 (0.16)	3.8 (0.84)	1.01	0.17 (0.56)	3.8 (0.44)	1.00

^a Uncertainty in measurements is ± 0.04 ns. ^b Uncertainty in measurements is ± 0.1 ns. Relative contributions are listed in parentheses. Emission is detected using Schott WG-320 nm filter. $\lambda_{\text{ex}} = 280$ nm.

3.3.2 Probing the Hydrophobic Region of the Lipid

In this section, we investigate the tail region of the lipid by using pyrene as a probe. As a hydrophobic molecule, pyrene is expected to favour the tail region of the lipid assembly. We first show the fluorescence spectra of pyrene measured in buffer and in cyclohexane (Figure 3.7). The sharp and structured band (~ 360 – 450 nm) is due to the monomer fluorescence, whereas the unstructured band centred at ~ 465 nm is fluorescence from the pyrene excimer [137, 198].

Pyrene tends to form excimers even at low concentrations. No excimers are detected in cyclohexane at $[\text{pyrene}] = 0.05$ mM as shown in Figure 3.7. In buffer, the hydrophobic nature of pyrene is expected to cause molecules to cluster close to one another in order to avoid the highly disliked polar nature of the solvent. This is manifested in the high yield of excimer formation at the same solvent:pyrene ratio. The structured fluorescence from the monomer species has two characteristic peaks with maxima at ~ 375 and ~ 385 nm (marked in Figure 3.7 as I_1 and I_3 , respectively).

The ratio of the two peak intensities (I_1/I_3) is environmentally sensitive and has been used to elucidate the local environment of pyrene [156, 199, 200]. An increase in the I_1/I_3 ratio is indicative of increased apparent polarity. This ratio is 0.58 in cyclohexane and 1.08 in buffer, calculated from the spectra in Figure 3.7. The peak at 385 nm completely disappears in buffer, so we take the intensity at this position which puts an upper limit for the I_3 value. This means that the calculated I_1/I_3 ratio of 1.08 may in fact be much higher. The I_1/I_3 ratio along with the dimer fluorescence peak will be used as a benchmark when pyrene is complexed with lipid in order to predict the local environment around the pyrene molecule in lipid.

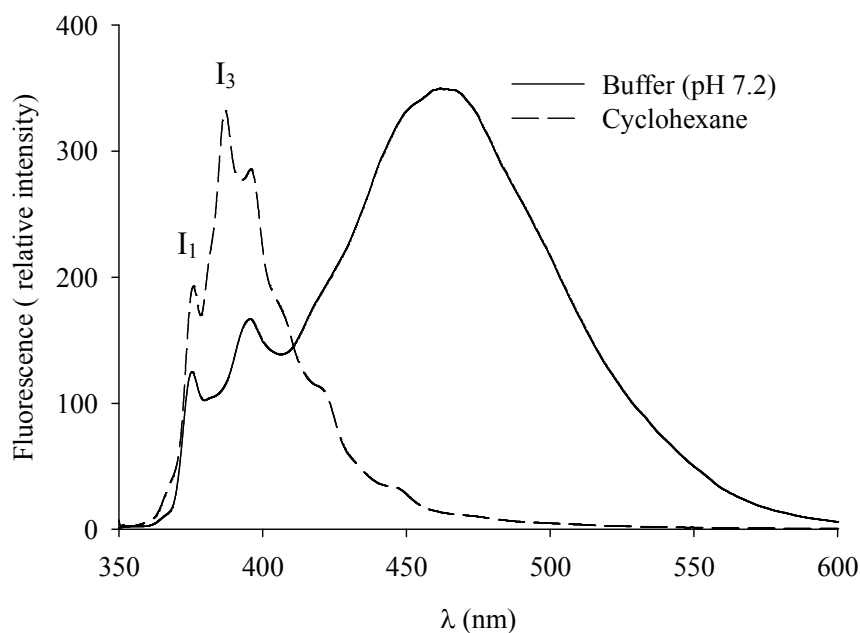


Figure 3.7: Fluorescence spectra of pyrene dissolved in buffer and cyclohexane. $\lambda_{\text{ex}} = 340$ nm.

Figure 3.8 shows the fluorescence of pyrene in lipid and in lipid containing Trp- C_8 . The results show that the excimer fluorescence is completely absent in lipid. This observation indicates that pyrene molecules are distributed among the tails of the lipid assembly and prefer to be isolated from each other (hydrophobic solvation).

As tabulated in Table 3.3, the I_1/I_3 ratio is calculated to be 1.04. The ratio is slightly less than that for pyrene in buffer. We note here that the strong tendency to form excimers in buffer (*vide supra*) is expected to partially shield the pyrene molecule from complete exposure to water and hence lower the I_1/I_3 ratio. Also, using molecular dynamics simulation, it was shown in the lipid assembly (1-palmitoyl-2-oleoyl-phosphatidylcholine) that pyrene prefers a position inside the lipid membrane near the head groups [201]. Although pyrene is a very hydrophobic molecule it is found mainly in the highly ordered upper acyl chain region near the lipid head groups and not in the middle of the membrane, which is the most hydrophobic part. So, the I_1/I_3 ratio in our case indicates a similar situation in which the pyrene molecules may eventually be close to the polar region and yet hidden inside the tail region of the lipid.

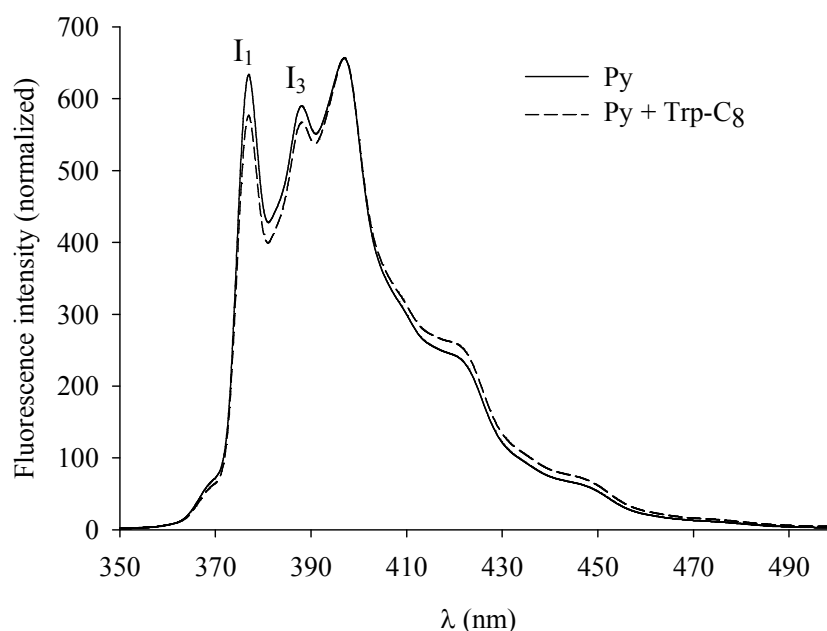


Figure 3.8: Fluorescence spectra of lipid containing pyrene (Py) and Py + Trp-C₈. $\lambda_{\text{ex}} = 340$ nm.

Table 3.3: Fluorescence intensity ratio of the vibronic peaks of pyrene (I_1/I_3) in the hexagonal phase of the β -Mal-OC₁₂ lipid. $\lambda_{\text{ex}} = 340$ nm.

Probe	I_1/I_3
Py	1.04
Py + Trp-C ₈	1.02

The presence of Trp-C₈ causes a slight drop in the I_1/I_3 ratio to 1.02 (see Table 3.3). The results indicate that the C₈-chain is indeed embedded inside the hydrophobic region of the lipid assembly. The presence of the C₈-chains inside the hydrophobic region may be a factor of increasing the hydrophobicity around the pyrene molecules. The incorporation of Trp-C₈ into the lipid layer may reduce the local polarity at the interface, which subsequently reduces the local polarity around the pyrene molecules.

Figure 3.9 and Table 3.4 summarize the fluorescence lifetime measurements of pyrene taken under air-saturated (normal) conditions. We measure a decay component of 28 ns for pyrene in buffer when probing the monomer emission. It was reported that the pyrene lifetime is very sensitive to the presence of oxygen in the sample [202]. A decay component of 382 ns was reported in deoxygenated cyclohexane [202]. In air-saturated cyclohexane, this decay component drops to 20 ns. In lipid, we measure a fast decay component of 0.97 ns and a slow decay component of 51 ns. The presence of two decay components reflects the heterogeneity in the local environment of pyrene inside the hydrophobic region. Comparing the long decay component with that in buffer, the value is almost doubled in lipid. This observation points to the cage effect of the hydrophobic tails in which pyrene is shielded from the solvent.

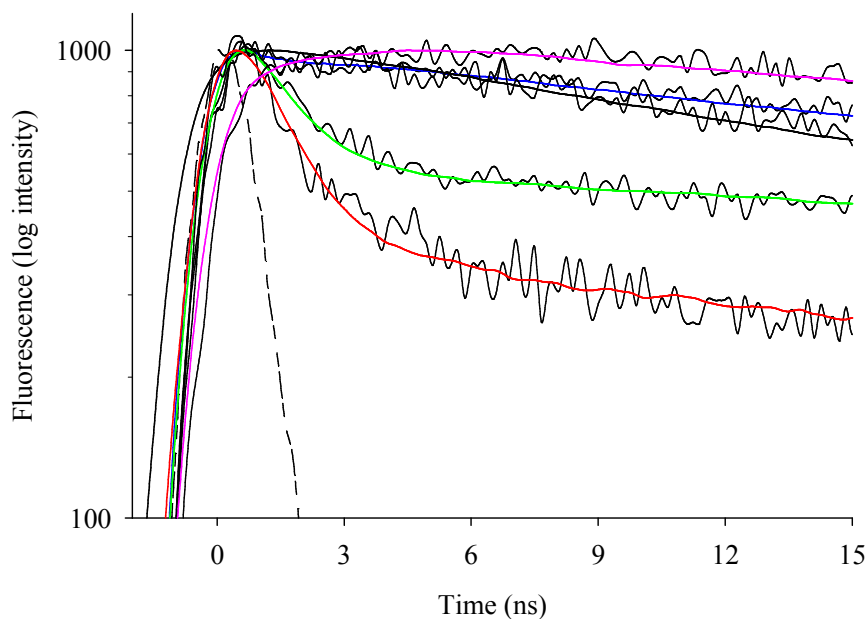


Figure 3.9: Fluorescence decay transients of pyrene probed using Schott WG-380 filter. Black: pyrene in buffer. Blue: pyrene in buffer containing Trp-C₈. Green: pyrene in lipid. Red: pyrene in lipid containing Trp-C₈. Pink: pyrene in buffer probed using Schott WG-455 filter. $\lambda_{\text{ex}} = 340$ nm. IRF is shown by a dashed line.

Table 3.4: Fluorescence lifetime (ns) measurements of pyrene and pyrene with Trp-C₈ in buffer and lipid.

Probe	Buffer		Lipid		
	τ^a	χ^2	τ_1^b	τ_2^a	χ^2
Py	28	1.02	0.97 (0.05)	51 (0.95)	1.07
Py + Trp-C ₈	22	1.12	0.97 (0.16)	27 (0.84)	1.40

^a Uncertainty in measurements is ± 1 ns. ^b Uncertainty in measurements is ± 0.05 ns. Relative contributions are listed in parentheses. Emission is detected using Schott WG-380 nm filter. $\lambda_{\text{ex}} = 340$ nm.

The pyrene lifetime in buffer is shorter when Trp-C₈ is present. The reduction in the lifetime is indicative of interaction between pyrene and Trp-C₈ in solution (Trp-C₈ is expected to act as a surfactant). Two decay components are again measured in lipid. The long decay component is much shorter than the corresponding component measured for pyrene alone (27 vs. 51 ns). The results indicate an interaction between the C₈-chain and pyrene inside the hydrophobic

region, which is another confirmation that the C₈-chain indeed penetrates the tail region of the lipid and is in close proximity to pyrene.

Finally, a rise time of 10 ns is measured when probing the region of the excimer (455 nm and longer) for pyrene in buffer (see Figure 3.9). This lifetime is the time required for excimer formation. We do not detect any rise time for pyrene in lipid which confirms the absence of excimers in the lipid assembly.

3.4 Conclusions

The polar head group region of hexagonal phase of the β -Mal-OC₁₂ lipid was studied by following the change in fluorescence of tryptophan and two of its ester derivatives upon mixing with the lipid, while the hydrophobic region was investigated using pyrene. Comparing the fluorescence peak position of tryptophan in lipid and solution, we estimated the polarity of the region where Trp and Trp-C₄ reside to be close to that of simple alcohols (methanol and ethanol). Increasing the chain length attached to the tryptophan moiety to C₈ pulls the Trp molecule closer to the sugar groups and the local polarity approaches that of 1,4-dioxane. The reduction in polarity points to a smooth transition from the polar domain to the hydrophobic domain, which is important for the stability of the lipid. Two lifetimes were detected for the fluorescence decay of tryptophan and its derivatives in lipid. The results point to a degree of flexibility of the lipid self-assembly that allows the tryptophan side chain to adapt two different rotamers.

Comparing the fluorescence behaviour of pyrene in solution and in lipid indicates the tendency of the pyrene molecules to disperse among the tails of the hydrophobic region as monomers. The ratio of I₁/I₃ implies that pyrene is close to the head groups. Interaction between pyrene and the C₈-chain of Trp-C₈ inside the hydrophobic region is observed as a slight reduction in the I₁/I₃ ratio and in the

pyrene lifetime. The results will be used as a benchmark to investigate other biologically related lipid phases, particularly the bicontinuous cubic phase, that are thought to play a crucial role in lipid membrane interaction.

CHAPTER 4

FLUORESCENCE PROBING OF THE TEMPERATURE-INDUCED PHASE TRANSITION IN A GLYCOLIPID SELF- ASSEMBLY: HEXAGONAL \leftrightarrow MICELLAR AND CUBIC \leftrightarrow LAMELLAR

Langmuir 2012, 28, 4989–4995

**FLUORESCENCE PROBING OF THE TEMPERATURE-INDUCED PHASE
TRANSITION IN A GLYCOLIPID SELF-ASSEMBLY:
HEXAGONAL \leftrightarrow MICELLAR AND CUBIC \leftrightarrow LAMELLAR**

In this chapter, we report on the temperature-induced phase transitions in two compositions of an aqueous self-assembly system of the n-octyl β -D-glucoside (β -Glc-OC₈)/water system, namely hexagonal \leftrightarrow micellar and cubic \leftrightarrow lamellar, using fluorescent probes. The mesophases as a thermodynamic equilibrium structure depend only on the current temperature, regardless of whether it is reached upon heating or cooling.

4.1 Introduction

Lyotropic mesophases of lipids in water have received much attention from the fundamental point of view as well as for application aspects [15, 23-26]. Their self-assembly properties are suitable as model systems for understanding specific membrane function in biosystems. When dispersed in water, lipids can display not only the lamellar phase, but also a variety of non-lamellar curved liquid crystal phases such as the cubic, the hexagonal and the ribbon phases [103, 203-205]. The transition between these possible phases is a result of an abrupt change in the interface curvature. This transition is believed to be governed by competition between the bending elastic-energy of the interface and energies resulting from interfacial separation constraints [206].

Generally, synthetic GLs may be grouped into those which naturally-mimicking membrane lipids usually GLs with branching alkyl chains, and those with a single alkyl chain usually applied as synthetic sugar-based surfactants [29]. The phase behaviour of these amphiphilic liquid crystals is a consequence of intermolecular forces (hydrogen bonding and van der Waals contacts) that depend on composition, temperature and pressure [207-209].

In this chapter, we characterize the GL n-octyl β -D-glucoside (β -Glc-OC₈) using steady-state and time-resolved fluorescence methods. β -Glc-OC₈ consists of a single sugar unit with a straight alkyl chain of eight carbon atoms. The chemical structure is shown in Figure 4.1. We select β -Glc-OC₈ for the present investigation because it has been studied extensively and has demonstrated the ability to form different mesophases as depicted in its temperature-composition phase diagram [23, 33, 96, 112, 210-212]. We investigate here the temperature-induced structural transformations (hexagonal \leftrightarrow micellar and cubic \leftrightarrow lamellar) in this lyotropic system using the same probes as in Chapter 3. Tryptophan (Trp) and two of its ester derivatives (Trp-C₄ and Trp-C₈) are used to probe the polar head group region, and pyrene is used to probe the hydrophobic tail region for the different phases.

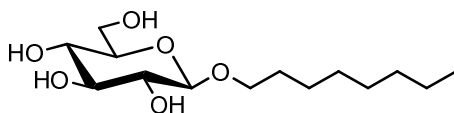


Figure 4.1: The chemical structure of n-octyl β -D-glucoside (β -Glc-OC₈).

4.2 Research Methodology

4.2.1 Materials

β -Glc-OC₈ (98%) and pyrene (99%) were purchased from Sigma-Aldrich. L-tryptophan (99%) was obtained from Merck. Tryptophan butyl ester (Trp-C₄) and its octyl analog (Trp-C₈) were prepared according to a literature procedure [181] as mentioned in the previous chapter. All chemicals and solvents were used without further purification.

4.2.2 Sample Preparation

The concentration of tryptophan/tryptophan esters/pyrene in the aqueous β -Glc-OC₈ formulation for both steady-state and time-resolved experiments was adjusted to 0.1 mM. The hexagonal and cubic phases required for this study were obtained at 23 °C for the 65% (w/w) and 80% (w/w) aqueous formulations of β -Glc-OC₈, respectively, according to the published binary phase diagram [23, 96, 112, 210, 211]. Both phases were confirmed to be formed by illuminating the sample in the flame-sealed tube and examining them through a cross-polarizing filter. The hexagonal phase sample showed a birefringent characteristic under the cross-polarizing filter, a characteristic not observed in the case of the cubic phase sample. All samples were treated with the same procedure as in Chapter 3. The aqueous buffer used was 25 mM sodium phosphate buffer, pH 7.2. Two sets of lipid/water systems were prepared. Each set included the lipid mixed with the different probes, in addition to one sample with no probes, which was used as a standard in the measurements. The first set was a normal hexagonal phase (H_I) with lipid concentration of 65% (w/w) at 23 °C. This hexagonal phase was transformed into a micellar phase (I_I) when heated to 40 °C. The second set was a normal cubic phase (Q_I) with 80% (w/w) concentration at 23 °C, and was transformed into a lamellar

phase (L_a) at 70 °C. Both temperature-induced micellar and lamellar phases showed isotropic and birefringent behaviour respectively, under a cross-polarizing filter.

4.2.3 Instrumentation

Fluorescence spectra were recorded on a Shimadzu RF-5301 PC spectrofluorophotometer and lifetime measurements were performed using a TimeMaster fluorescence lifetime spectrometer. In all the experiments, samples were measured in a 1-cm path length quartz cell and underwent the same procedure as in Chapter 3. The temperature of the samples was controlled within ± 0.1 °C at 23.0 °C, 40.0 °C, or 70.0 °C. All samples were equilibrated overnight in the water bath at the desired temperature to ensure that the required phase was obtained before the measurements were taken.

The effect of temperature on the probes was checked by measuring the steady-state and lifetime fluorescence for the probes in the same buffer without the lipid composition. For tryptophan and its derivatives, a decrease in the fluorescence intensity was observed when the temperature was increased, but no effect was observed on the spectral position or the fluorescence lifetime. The present study is based on the latter two parameters. The changing relative intensity following a change in temperature is not a factor in our study and all the spectra are normalized in this work. In the case of pyrene, the presence of a large percentage of dimer formation in the excited state (excimers) in buffer and the high polarity effect of water on the I_1/I_3 ratio made it difficult to correlate the measurements in buffer to those in lipid. This will be discussed in detail later. In order to minimize the effect of temperature on the pyrene fluorescence, particularly when the oxygen concentration was changed at different temperatures, we sealed all the sample tubes to maintain a constant oxygen concentration.

4.3 Results and Discussion

4.3.1 Probing the Polar Region of the Lipid

We have shown in Chapter 3 that the tryptophan molecule is a useful probe for estimating the polarity of the head group region of lipids. The sensitivity of the tryptophan fluorescence to its local polarity stems from the sensitivity of its excited state (1L_a) to solvent polarity since this transition more directly involves the polar nitrogen atom of the indole ring of the tryptophan moiety. Figure 4.2 shows the fluorescence spectra of tryptophan in solvents of different polarity. A blue shift in the peak maximum by $1,770\text{ cm}^{-1}$ is observed in dioxane (non-dipolar) compared to that in buffer. The spectral positions for tryptophan in both methanol and ethanol lie between those of dioxane and water. As described in the previous chapter, the presence of an alkyl ester chain connected to the tryptophan molecule (Trp-C₄ and Trp-C₈) has no effect on the fluorescence behaviour of the molecule in solution.

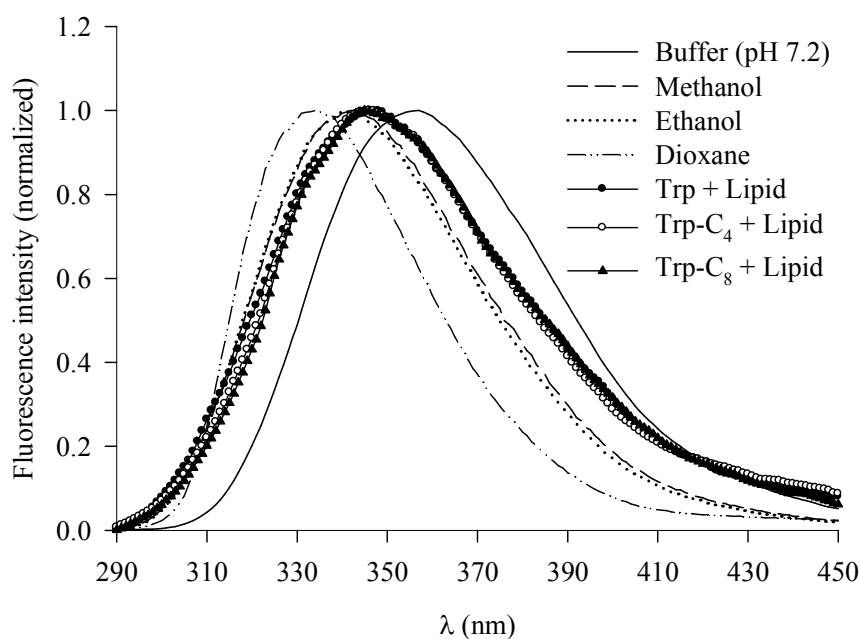


Figure 4.2: Fluorescence spectra of tryptophan and its derivatives in different solvents and in the hexagonal phase of the β -Glc-OC₈ lipid. $\lambda_{\text{ex}} = 280\text{ nm}$.

Figure 4.2 includes the fluorescence spectra of the three probes (Trp, Trp-C₄ and Trp-C₈) embedded in the β -Glc-OC₈ lipid at a composition of 65% (w/w) aqueous formulation and 23 °C. According to the temperature-composition phase diagram, [23, 96, 112, 210, 211] this lipid exists in the normal hexagonal phase. As the graph shows, the fluorescence peak positions of Trp and its derivatives in lipid are blue-shifted compared to those of tryptophan in buffer ($\lambda_{\text{max}} = 355$ nm), and approaching those in methanol and ethanol ($\lambda_{\text{max}} = 340\text{--}342$ nm). This observation is an indication of the different environment experienced by the tryptophan moiety in the polar region of the head groups of the lipid (being less polar compared to pure water). The reduced polarity in the head group region compared to the polarity in free water is due to the tendency of the water molecules in this region to be more ordered and less flexible [149].

We use the two derivatives (Trp-C₄ and Trp-C₈) to probe different parts in the head group region. As the chain length increases, the tryptophan molecule is expected to be pulled closer to the polar head groups. This is due to the nature of the alkyl ester chain being hydrophobic and tending to avoid the hydrophilic region. This tendency results in burying the chain inside the tail region of the lipid, which in turn brings the tryptophan molecule (attached to the chain) closer to the head groups. Similar spectral positions are obtained when Trp, Trp-C₄, and Trp-C₈ are embedded in lipid (Figure 4.2 and Table 4.1), implying that the tryptophan molecule is located in a similar polar environment. This observation indicates that the glucose unit (a monosaccharide) of the head group, unlike the maltose unit (a disaccharide), is too short to show any polarity gradient as the tryptophan molecule gets closer. We confirm this finding by comparing the fluorescence spectra for the hexagonal phase of maltoside (β -Mal-OC₁₂) with that of glucoside (β -Glc-OC₈) lipids when using Trp-C₈ as the probe (see Figure 4.3). It is clear that for the maltoside lipid, the

tryptophan molecule experiences less polarity, approaching that of dioxane (see Table 3.1 in Chapter 3). On the other hand, the spectral position of the three probes in β -Glc-OC₈ is similar to that of Trp and Trp-C₄ in β -Mal-OC₁₂ as shown in Table 4.1. The results indicate that in the case of Trp-C₈ in the maltoside lipid, the tryptophan molecule probes deep in the head group region.

Table 4.1: Fluorescence spectral peak maxima of tryptophan and its derivatives in hexagonal phase of different lipid. $\lambda_{\text{ex}} = 280$ nm.

Probe	Peak maximum (nm)	
	β -Glc-OC ₈	β -Mal-OC ₁₂
Trp	346	345
Trp-C ₄	346	345
Trp-C ₈	345	337

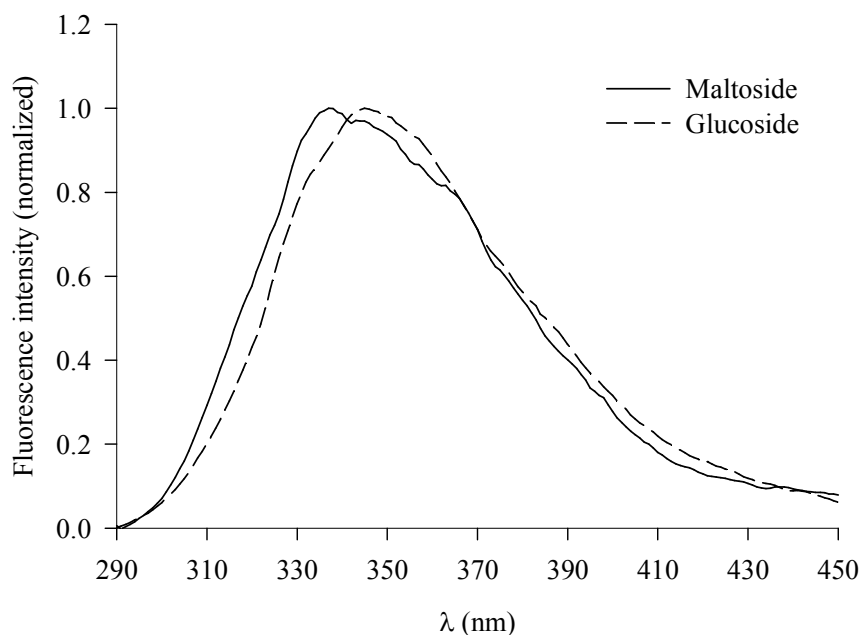


Figure 4.3: Fluorescence spectra of Trp-C₈ embedded in the hexagonal phase of the maltoside lipid (β -Mal-OC₁₂) and the glucoside lipid (β -Glc-OC₈). $\lambda_{\text{ex}} = 280$ nm.

Three other phases are probed by tryptophan and its derivatives in this study. The micellar phase is obtained by heating the β -Glc-OC₈ lipid at a composition of 65% (w/w) aqueous formulation to 40 °C, while the normal bicontinuous cubic phase with *Ia3d* space group is obtained at 23 °C of 80% (w/w) aqueous formulation of β -Glc-OC₈ [96, 112]. Finally, the lamellar phase is produced by heating the cubic phase to 70 °C. As in the hexagonal phase, the three probes behave similarly in each phase i.e. lamellar, cubic, micellar (refer to Table 4.1 for the values). A slight blue-shift in the fluorescence spectra is observed in the cubic phase only. Figure 4.4 shows the spectra for Trp-C₈ in the cubic and lamellar phases. It is clear that the head group region has a local polarity in the cubic phase which is slightly hydrophobic compared to that in the other phases.

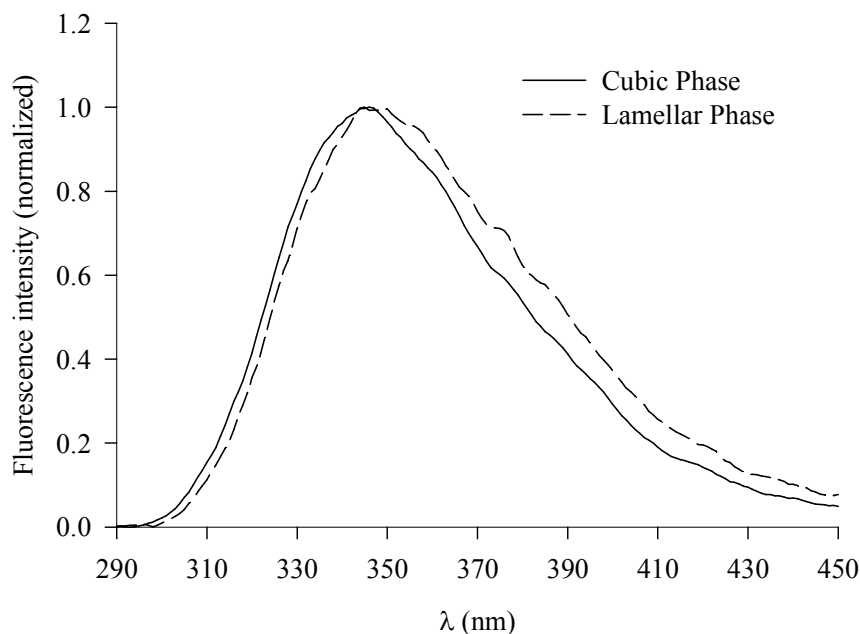


Figure 4.4: Fluorescence spectra of Trp-C₈ embedded in the cubic phase and lamellar phase of the β -Glc-OC₈. $\lambda_{\text{ex}} = 280$ nm.

The fluorescence lifetimes of tryptophan and its ester derivatives are measured in the different phases of the β -Glc-OC₈ lipid. Tryptophan has two lifetime components in buffer which are due to two different rotamers (0.5 and 3.8 ns) [137, 196, 197]. The two components are not affected by changing the lipid phase. The only effect of lipid is observed in the relative contribution from each lifetime component. While the major contribution in solution is from the long lifetime component (85-90%), as tabulated in Table 3.2, Chapter 3, the short lifetime component shows more contribution (50-60%) in all phases of β -Glc-OC₈.

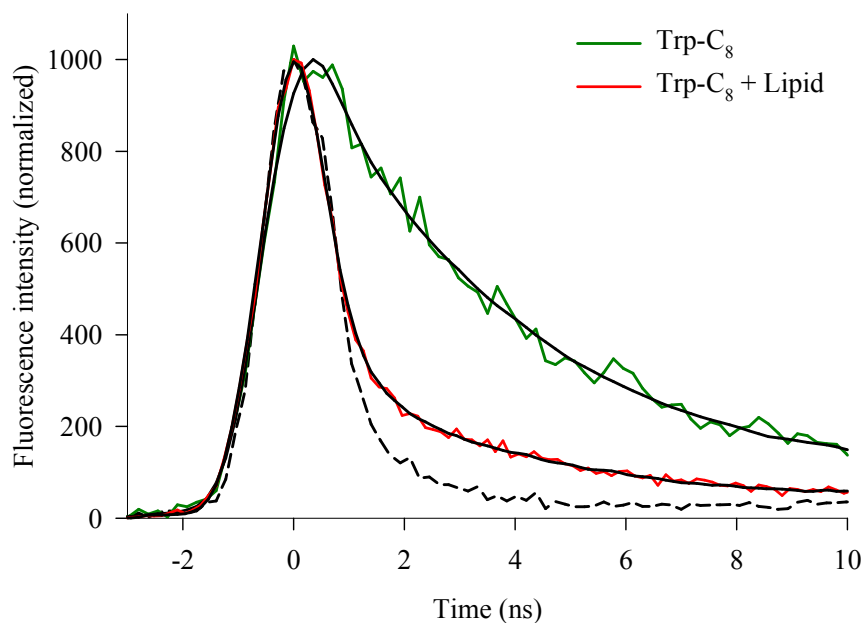


Figure 4.5: Fluorescence decay transients of Trp-C₈ in buffer alone and in buffer containing the hexagonal phase of the β -Glc-OC₈ lipid. $\lambda_{\text{ex}} = 280$ nm. IRF is shown by a dashed line.

Figure 4.5 shows the decay transients for Trp-C₈ in buffer and in the hexagonal phase of the β -Glc-OC₈ lipid as an example. We observed a similar trend for the hexagonal phase of the β -Mal-OC₁₂ lipid. The results imply that the lipid head group region selectively stabilizes the rotamer of the short lifetime component.

The biexponential nature of the tryptophan fluorescence decay in lipid constitutes strong support for the ground state heterogeneity. This heterogeneity suggests that the lipid self-assembly has a degree of flexibility that allows the tryptophan side chain to exist in two different rotamers as mentioned in Chapter 3.

4.3.2 Probing the Hydrophobic Region of the Lipid

As discussed in the previous chapter, pyrene is effective as a local reporter for probing the hydrophobic region of the lipid self-assembly. This is because its fluorescence is sensitive to the local environment [201]. Figure 4.6 shows the spectra of pyrene in cyclohexane, buffer, and in buffer containing the cubic phase of the β -Glc-OC₈ lipid. Yet again, the sharp and structured band (~360–450 nm) is due to the monomer fluorescence, whereas the unstructured band centred at ~465 nm (observed in buffer only) is fluorescence from the pyrene excimer [137, 198]. In buffer, the hydrophobic nature of pyrene is expected to cause molecules to cluster close to one another in order to avoid the highly disliked polar nature of the solvent as shown in the high yield of excimer formation. Excimer fluorescence is completely absent in lipid which indicates that pyrene molecules are distributed among the tails of the lipid assembly and prefer to be isolated from one another (hydrophobic solvation), a behaviour similar to pyrene in cyclohexane.

The ratio of the two peak intensities (I_1/I_3) is environmentally sensitive and has been used to elucidate the local environment of pyrene [156, 199, 200]. An increase in the I_1/I_3 ratio is indicative of increased apparent polarity. In Chapter 3 we reported this ratio to be 0.58 in cyclohexane and ≥ 1.08 in buffer. The strong tendency to form excimers in buffer is expected to partially shield the pyrene molecules from complete exposure to water and thus lower the I_1/I_3 ratio. In the cubic phase in Figure 4.6, the I_1/I_3 ratio is about 0.93. This value points to a

somewhat polar environment around pyrene. It was shown by molecular dynamics simulations that pyrene prefers a position inside the lipid membrane near the head groups [201]. Although pyrene is a very hydrophobic molecule it is found mainly near the lipid head groups and not in the middle of the membrane, which is the most hydrophobic part. So the I_1/I_3 ratio in our case indicates a similar situation in which the pyrene molecules may eventually be close to the polar region and yet hidden inside the tail region of the lipid.

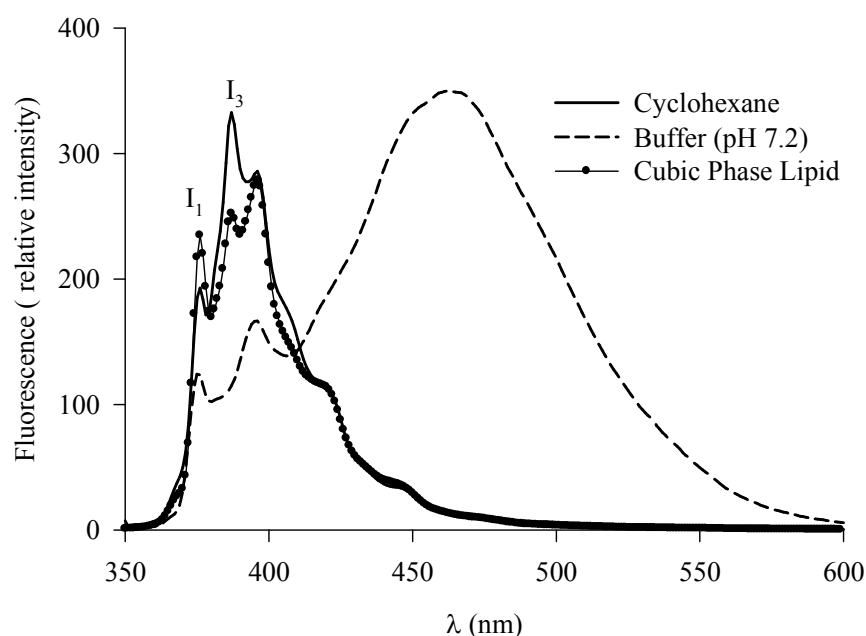


Figure 4.6: Fluorescence spectra of pyrene dissolved in cyclohexane, and in buffer alone, and buffer containing the cubic phase of the β -Glc-OC₈. $\lambda_{\text{ex}} = 340$ nm.

Table 4.2 summarizes the values of I_1/I_3 for the four phases of the β -Glc-OC₈ lipid. The values are the average of three measurements. The presence of tryptophan in the head group region has no effect on the I_1/I_3 values. The slight drop in the I_1/I_3 value in the presence of Trp-C₈ for some phases can be related to a slight increase in hydrophobicity around the pyrene molecule. This is due to the presence of the embedded C₈-chain inside the tail region of the lipid assembly.

Table 4.2: Fluorescence intensity ratio of the vibronic peaks of pyrene (I_1/I_3) in different phases of the β -Glc-OC₈ lipid: hexagonal (H_I); micellar (I_I); cubic (Q_I); and lamellar (L _{α}). $\lambda_{\text{ex}} = 340$ nm.

Lipid Concentration	Probe	I_1/I_3 (phase)		
		23 °C	40° C	70° C
65% (w/w)	Py	0.96 (H _I)	0.93 (I _I)	
	Py + Trp	0.96 (H _I)	0.93 (I _I)	
	Py + Trp-C ₈	0.96 (H _I)	0.92 (I _I)	
80% (w/w)	Py	0.93 (Q _I)		0.87 (L _{α})
	Py + Trp	0.93 (Q _I)		0.87 (L _{α})
	Py + Trp-C ₈	0.91 (Q _I)		0.86 (L _{α})

The hexagonal phase of the β -Glc-OC₈ lipid shows an I_1/I_3 value of 0.96. Compared with our previous measurement of 1.04 for pyrene in the hexagonal phase of β -Mal-OC₁₂, the current lipid shows less polarity around pyrene in the tail region. The reduced polarity in β -Glc-OC₈ may be explained in the light of the difference in the carbon-chain length of the tail part in both lipids. Longer tails (C₁₂ vs. C₈) are expected to have more random and wobbling motion that results in less interaction with the pyrene molecules (less solvation effect). We estimate the length of the pyrene molecule (carbon-to-carbon distance) to be about 7.0 Å. The difference in polarity must then be derived from a more compact interaction between the pyrene molecule and a C₈-tail (approximately 9.0 Å in length) than with a C₁₂-tail (approximately 14.0 Å). This conclusion may explain the results after the addition of Trp-C₈. Upon adding Trp-C₈ to both lipids, we record no effect on the I_1/I_3 value in the β -Glc-OC₈ lipid (see Table 4.2), whereas the I_1/I_3 value has dropped to 1.02 in the β -Mal-OC₁₂ lipid. We attribute this drop to the increased hydrophobicity in the tail region due to the presence of the C₈-chains in the vicinity of the pyrene molecules. The C₈-chains of Trp-C₈ induce more compact hydrophobic interactions with the pyrene molecules in a manner similar to the pyrene: β -Glc-OC₈ system.

The I_1/I_3 values in Table 4.2 show a drop of about 6% when the phase is transformed from cubic to lamellar. The higher polarity in the cubic phase can be correlated to the nature of its interface, which curves towards the bulk water. This unique structure allows interpenetrating channels of water and lipid that provide compatibility with water-soluble, lipid-soluble, and amphiphilic active ingredients. Figure 4.7 shows the geometry of the cubic phase gives pyrene more exposure to the polar water molecules from all directions. In contrast, the lamellar phase self-assembly allows such exposure from one direction only. The geometry of the cubic phase may also explain the more hydrophobic environment around the tryptophan molecule and its derivatives in the vicinity of the head groups compared to that in the other phases (hexagonal, micellar, and lamellar) studied here (*vide supra*).

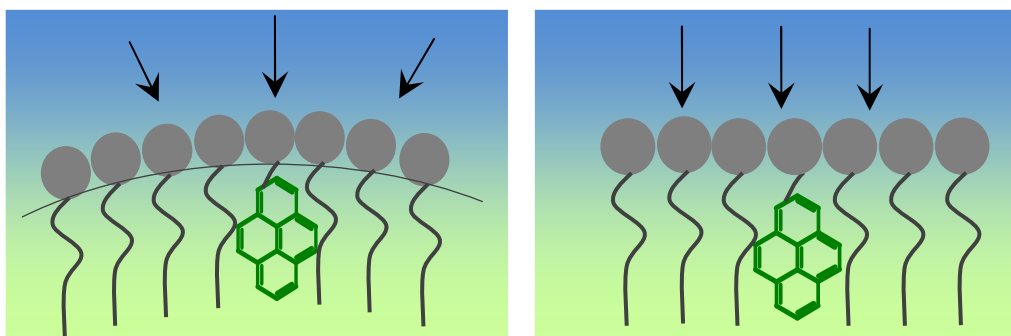


Figure 4.7: A schematic diagram showing the effect of the different geometries of the cubic phase (left) and the lamellar phase (right) on the exposure of pyrene to water. Water direction is represented by arrows.

For both lipid compositions, we find that the temperature-induced phase transition is completely reversible. We arrive at this conclusion by measuring the I_1/I_3 values after cooling the samples to 23 °C, at which the values match those measured for the hexagonal and cubic phases before heating. In a related study, reversible phase transitions have been reported for the monolinolein/water system using SAXS [213]. The authors refer to the internal structure of the mesophases as a

thermodynamic equilibrium structure that depends only on the current temperature, regardless of whether it is reached upon heating or cooling. Fluorescence lifetime measurements are conducted for pyrene in the four lipid phases and the data summarized in Tables 4.3 and 4.4. We have shown recently that pyrene has a single lifetime component of 28 ns in air-saturated buffer (see Table 3.3, Chapter 3).

In all the lipid phases, the fluorescence decay of pyrene is best-fitted to a biexponential function. The two lifetime components in each phase show a short component (0.81–1.08 ns) and a long component (7.8–13.3 ns). The presence of two decay components reflects the heterogeneity in the local environment of pyrene inside the hydrophobic region. This heterogeneity is important for the biological function of the lipid assembly, giving the lipid a degree of flexibility that is necessary in order to accommodate various molecular sizes. We have reported similar results for pyrene in the hexagonal phase of β -Mal-OC₁₂ in Chapter 3. Comparing the long lifetime component for the hexagonal phase of β -Glc-OC₈ and β -Mal-OC₁₂ (11.1 ns (Table 4.3) vs. 51 ns (Table 3.3)), the much longer component in β -Mal-OC₁₂ implies more isolation of the pyrene molecules in the tail region. This is consistent with the above-mentioned discussion that predicted more interactions between the pyrene molecules and the shorter tails in β -Glc-OC₈. To further support this point we compare the long lifetime component in both hexagonal phases after the addition of Trp-C₈. In the case of β -Mal-OC₁₂, the lifetime value drops to 27 ns. The effect of adding Trp-C₈ to the pyrene: β -Glc-OC₈ system is negligible (11.3 ns). Adding Trp-C₈ to β -Mal-OC₁₂ increases the hydrophobic interaction with the pyrene molecules due to the presence of the C₈-chains, similar to the interactions in the pyrene: β -Glc-OC₈ system. The presence of the C₈-chain may also lead to a decrease in the local viscosity of the tail region that

could account for an increased diffusion of oxygen and a consequent reduction in the pyrene lifetime.

Table 4.3: Fluorescence lifetime (ns) measurements of pyrene, pyrene + Trp, and pyrene + Trp-C₈ in 65% (w/w) aqueous formulation of lipid.

Probe	23 °C (H _I)			40 °C (I _I)		
	τ_1^a	τ_2^b	χ^2	τ_1^a	τ_2^b	χ^2
Py	0.89 (0.29)	11.1 (0.71)	1.15	0.81 (0.27)	13.3 (0.73)	1.18
Py + Trp	0.89 (0.28)	11.1 (0.72)	1.16	0.81 (0.25)	12.8 (0.75)	1.08
Py + Trp-C ₈	0.89 (0.28)	11.3 (0.72)	1.04	0.87 (0.27)	13.2 (0.73)	1.41

^a Uncertainty in measurements is ± 0.05 ns. ^b Uncertainty in measurements is ± 0.5 ns. Relative contributions are listed in parentheses. Emission is detected using Schott WG-380 nm filter. $\lambda_{\text{ex}} = 340$ nm.

Table 4.4: Fluorescence lifetime (ns) measurements of pyrene, pyrene + Trp, and pyrene + Trp-C₈ in 80% (w/w) aqueous formulation of lipid.

Probe	23 °C (Q _I)			70 °C (L _a)		
	τ_1^a	τ_2^b	χ^2	τ_1^a	τ_2^b	χ^2
Py	1.08 (0.39)	11.0 (0.61)	1.04	0.79 (0.36)	11.0 (0.64)	1.09
Py + Trp	0.73 (0.32)	11.3 (0.68)	1.35	0.82 (0.33)	11.1 (0.67)	1.55
Py + Trp-C ₈	0.95 (0.40)	7.9 (0.60)	0.88	0.91 (0.39)	7.8 (0.61)	0.89

^a Uncertainty in measurements is ± 0.05 ns. ^b Uncertainty in measurements is ± 0.5 ns. Relative contributions are listed in parentheses. Emission is detected using Schott WG-380 nm filter. $\lambda_{\text{ex}} = 340$ nm.

Table 4.2 shows a small drop in the I_1/I_3 value (about 3%) when the hexagonal phase is transformed into the micellar phase, indicating more caging effect around the pyrene molecules in the latter. This may not be consistent with the geometry of the micellar phase in which the curvature is increased compared to that of the hexagonal phase. This is possibly due to a shift in the pyrene location from the interphase into the bulk, perhaps because of space requirements. This is expected since the micellar phase is curved in two directions and the water interphase may push the pyrene molecules further into the center. The value of the long lifetime

component (τ_2) which is significantly different in the micellar phase from the values in the other phases, reinforces this explanation.

Table 4.4 shows a drop of about 28% in the long lifetime component in the cubic and lamellar phases of β -Glc-OC₈ upon the addition of Trp-C₈. The effect is much more pronounced in the lifetime values than in the steady-state I_1/I_3 values (see Table 4.2). The observation points to the dominant role of the collisional mechanism of interaction (lifetime affected) between pyrene and C₈-chain compared to static interaction (fluorescence spectra affected) [137]. The dynamical mechanism of interaction may be important for these two phases since they participate in the process of membrane fusion [214]. No rise time for pyrene in all the lipid phases is recorded, which confirms the absence of excimers in the lipid assembly.

4.4 Conclusions

We have studied the temperature-induced phase transitions in the GL self-assembly β -Glc-OC₈ using steady-state and time-resolved fluorescence measurements. The two phase transitions, hexagonal \leftrightarrow micellar and cubic \leftrightarrow lamellar, were characterized by probing the polar head group region using tryptophan and two of its derivatives and probing the hydrophobic tail region using pyrene. The fluorescence spectra of Trp, Trp-C₄, and Trp-C₈ embedded in the different phases indicate a local polarity close to that of simple alcohols (methanol and ethanol) for all phases.

The fluorescence characteristics of pyrene indicate that the pyrene molecules tend to disperse among the tails of the hydrophobic region as monomers, yet in close proximity to the polar head group region. By comparing the steady-state fluorescence spectra and lifetimes of pyrene in β -Glc-OC₈ and β -Mal-OC₁₂, we conclude that the shorter alkyl chains in the former (C₈) interact more with the

pyrene molecules. We attribute this observation to the more random and wobbling motion of the longer chains (C_{12}) resulting in less interaction. The decrease in the I_1/I_3 value for the lamellar phase compared to the value in the cubic phase is correlated to the interfacial curvature toward the bulk water in the cubic self-assembly. This geometry also explains the slightly more hydrophobic environment around the tryptophan molecule and its derivatives in the cubic phase compared to that in the other phases (hexagonal, micellar, and lamellar). Upon the addition of Trp- C_8 , the fluorescence lifetime of pyrene is reduced by 28% in the lamellar and cubic phases, whereas the I_1/I_3 value is only slightly reduced. The results reflect the dominant role of the dynamical mechanism of the interaction between the C_8 -chain of Trp- C_8 and pyrene. This mechanism maybe important for these two phases since they participate in the process of membrane fusion. Both lipid compositions show completely reversible temperature-induced phase transitions, reflecting the thermodynamic equilibrium structures of their mesophases.

Probing the polar and the hydrophobic regions of the different lipid phases points to a large degree of heterogeneity and flexibility of the lipid self-assembly. These properties are important for carrying out different biological functions such as the ability to accommodate various molecular sizes.

CHAPTER 5

INVESTIGATION ON THE EFFECT OF SUGAR STEREOCHEMISTRY ON BRANCHED-CHAIN GLYCOLIPIDS SELF- ASSEMBLY BY SMALL-ANGLE X-RAY SCATTERING

submitted to Soft Matter 2013, under review

INVESTIGATION ON THE EFFECT OF SUGAR STEREOCHEMISTRY ON BRANCHED-CHAIN GLYCOLIPIDS SELF-ASSEMBLY BY SMALL- ANGLE X-RAY SCATTERING

Chapter 5 focuses on the characterization of four branched-chain GLs, namely 2-hexyl-decyl- α -D-glucopyranoside (α -Glc-OC₁₀C₆), 2-hexyl-decyl- α -D-glucopyranoside (α -Glc-OC₁₀C₆), 2-hexyl-decyl- α -D-galactopyranoside (α -Gal-OC₁₀C₆) and 2-hexyl-decyl- α -D-galactopyranoside (α -Gal-OC₁₀C₆), with a total alkyl chain length of 16 carbon atoms. These compounds are anomERICALLY (α -Glc-OC₁₀C₆ and β -Glc-OC₁₀C₆) and epimerically (α -Glc/Gal-OC₁₀C₆ and β -Glc/Gal-OC₁₀C₆) related. The phase behaviour of these non-ionic surfactants is investigated by optical polarizing microscopy (OPM), differential scanning calorimetry (DSC) and small-angle X-ray scattering (SAXS). Subsequently, their partial binary phase diagrams are constructed, and their nanostructural studies and anomeric-epimeric relationship is discussed as well.

5.1 Introduction

The cell membrane is normally modelled simply as a lipid bilayer with embedded protein molecules, and assumed to be just a "nano-scale wrapper" separating the cell components from their surroundings [1, 2]. Recently however, the detailed structure of the lipid membrane itself has been recognized as important in determining the organization, dynamics and function of the membrane. New concepts such as lateral segregation [215], domain formation [216], lateral pressure [217], curvature and curvature elasticity [209] have proved important in membrane stability and integrity. In addition, the detailed structure and composition of lipids within the bilayer, including phospholipids and numerous components such as GLs,

have been shown to be equally important in determining biomembrane function [161-167]. A holistic knowledge of these issues however, is still patchy. Understanding the physicochemical properties of the highly complex biomembrane structure is a monumental task, but may be understood piece-wise by uncovering the basic self-assembly properties of the various lipidic components.

The particular lyotropic phase adopted is closely related to the average "shape" of the amphiphilic lipid molecules, which may be cylindrical, wedge-like, or conical in a normal (type 1) or a reversed state (type 2) [218]. Variations in parameters such as concentration and temperature modify this average "shape", and may lead to lyotropic phase transitions (e.g. the lamellar phase to other phases like hexagonal and a whole variety of cubic structures) [79, 219].

The inverse bicontinuous cubic phases are thought to be important for biological functions and have been observed in eukaryotic cells, particularly in the mitochondria and the endoplasmic reticulum [220]. Their structures consist of a curved continuous lipid bilayer, extending in three dimensions and separating two interpenetrating networks of water channels [204]. The spontaneous formation of such a cubic phase is due to a competition between two principal free energy terms namely, the curvature energy of each monolayer and the stretching energy of the lipid chains. To ensure a constant bilayer thickness, these two terms are least frustrated simultaneously in the cubic phase; hence, they are found in between the lamellar and hexagonal phases in the phase diagram [26, 221]. Cubic phases have been observed, usually at relatively low curvatures, based on one of three fundamental triply periodic minimal surfaces (TPMS): the Schoen gyroid (G), the Schwarz diamond (D) and the primitive (P) minimal surfaces. These three complex structures are related by a Bonnet transformation, in which they have the same

volume transformation (isomeric) that leaves the intrinsic geometry intact, such as the Gaussian curvature [222].

Interestingly, these biologically relevant phases have been used in numerous biotechnological applications including delivery system technology [223]. As a result, biocompatible liquid crystalline materials are in high demand. However, natural products such as phosphatidylcholine (PC) from plasma membrane, as well as monogalactosyldiacylglycerol (MGDG) and digalactosyldiacylglycerol (DGDG) from photosynthetic thylakoid membrane, are difficult to extract and purify in large quantities. Therefore, there is a demand for synthetic substitutes, such as GLs, which are cheap, renewable resources, biodegradable, non-ionic and environmentally friendly. The investigation of lyotropic mesophases formed by synthetic GLs is important not only for their technological relevance, but also from a fundamental perspective because of their diverse functions in nature [15, 23-26].

The pre-eminent structural feature observed in many natural GL materials (e.g. MGDG and DGDG) is a double chain. As such we have focused on the design and synthesis of molecules containing two branched-chains which lead to an increased desire for curvature. Many branched-chain designs have been suggested, all having the ability to form non-lamellar inverse lyotropic phases [38, 115-117]. One likely candidate, which successfully mimics its corresponding natural product, is the recently-proposed Guerbet glycoside [13, 37, 114]. This family of glycosides is prepared using a glycosidation procedure described elsewhere [114, 118]. It is a synthesis which involves reacting a protected sugar with Guerbet alcohol, an industrial material first synthesized by Marcel Guerbet [224]. Guerbet alcohol contains two asymmetric chains which differ by two methylene units, and the two chains branch at the β -carbon position, which is also chiral. The Guerbet glycoside series can be viewed as a Guerbet sugar, an addition to the Guerbet materials

including the alcohol, ester and acid, all of which have been used in many industrial applications [225, 226].

Herein, we investigate the biologically relevant inverse phases formed by synthetic Guerbet GLs, and determine their partial phase diagrams via X-ray investigations. In a previous study [119], we have determined that a branched C₁₆-chain, in conjunction with a monosacharride head group such as glucose, can lead to the formation of curved mesophases in excess water. As a continuation of the previous study, four anomerically-pure branched-chain GLs based on C₁₀C₆ Guerbet alcohols, namely 2-hexyl-decyl- α -D-glucopyranoside (α -Glc-OC₁₀C₆), 2-hexyl-decyl- β -D-glucopyranoside (β -Glc-OC₁₀C₆), 2-hexyl-decyl- α -D-galactopyranoside (α -Gal-OC₁₀C₆) and 2-hexyl-decyl- β -D-galactopyranoside (β -Gal-OC₁₀C₆) have been chosen for further detailed X-ray investigation.

They are anomerically and epimerically related compounds. The anomeric pairs are α -Glc-OC₁₀C₆ and β -Glc-OC₁₀C₆, while the epimeric pairs are α -Glc/Gal-OC₁₀C₆ and β -Glc/Gal-OC₁₀C₆. Their chemical structures are depicted in Figure 5.1. The epimers and anomers of GLs were reevaluated [227], and found to affect the thermotropic self-assembly considerably. A new trend on the phase stability was uncovered in relation to the epimeric/anomeric stereochemistry. We investigated the phase behaviour (dry and in aqueous) of these systems in more detail, and determined the relationship to their molecular structure, with a particular focus on obtaining cubic phases suitable for general biotechnological applications such as drug delivery [25, 26, 75] or *in meso* crystallization of membrane proteins [78, 87]. In this chapter, the phases are described using the standard lyotropic nomenclature, both in the dry and hydrated states, as the molecules involved are amphiphilic rather than mesogenic [119].

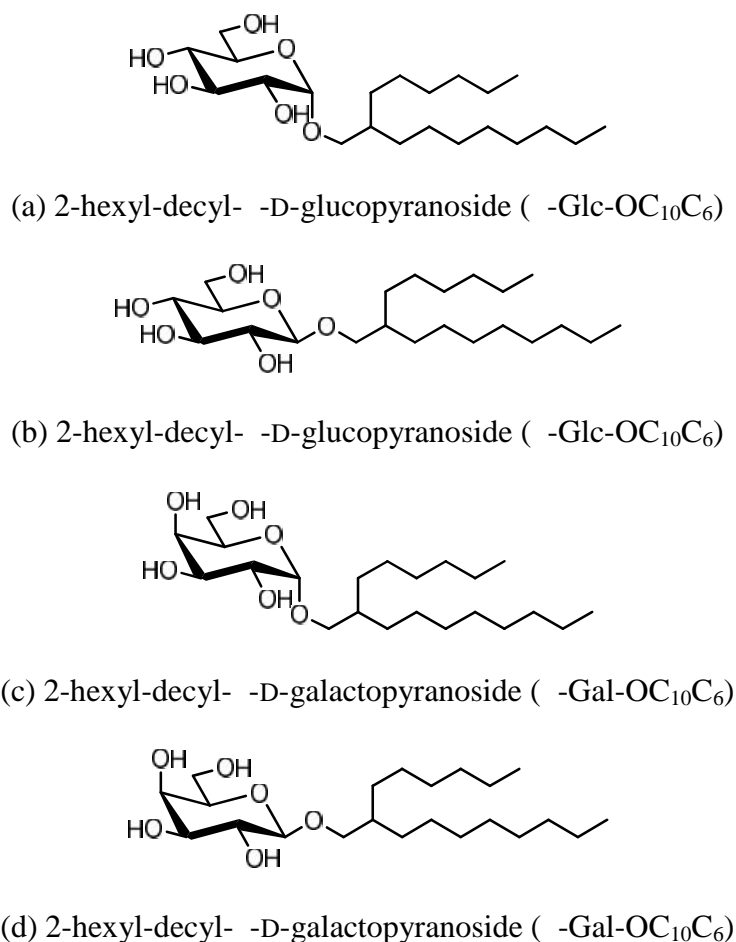


Figure 5.1: The chemical structures of the four branched-chain C₁₆ glycopyranosides.

5.2 Research Methodology

5.2.1 Preparation of Compounds

The synthesis of the four compounds is described elsewhere [114]. The anomeric purity of the materials was confirmed to be at least 98%, using three different techniques, namely nuclear magnetic resonance (NMR), thin layer chromatography (TLC) and optical rotation.

5.2.2 Optical Polarizing Microscopy (OPM)

The thermotropic liquid crystalline behaviour was characterized by using a Mettler Toledo FP82HT hot stage and viewed with an Olympus BX51 microscope fitted with crossed polarizing filters. The microscope was connected to an Olympus camera for image capture, with magnification factors of 10 and 20. The material was heated until it reached its isotropic phase and the mesophase image formed was taken upon slow cooling at the rate of 1 °C/min to obtain the best optical textures. The lyotropic mesophase behaviour was investigated via the water penetration scan technique [127]. A small amount of the sample was placed on a glass slide and covered with a cover slip. The sample was heated to the isotropic phase and cooled to room temperature. A drop of water was then placed on the slide at the edge of the cover slip and the water slowly penetrated the sample by capillary action to form a concentration gradient that ranged from pure water to neat surfactant. Samples were equilibrated at a given temperature for about 30 minutes. The cubic and micellar phases were optically isotropic and black when observed under crossed polarizers, and could be distinguished from each other since the former was more viscous when pressed than the latter. Both lamellar and hexagonal phases were birefringent, although the hexagonal phase tended to produce much larger domains than the lamellar phase, as well as distinctly different optical textures.

5.2.3 Differential Scanning Calorimetry (DSC)

Phase transition temperature and enthalpy of the samples were studied primarily by a Mettler Toledo DSC 822^e equipped with Haake EK90/MT intercooler. Calibration of the instrument was performed with indium for temperature and enthalpy accuracy. STAR^e Thermal Analysis System software was used for analysis. The neat compounds were weighed between 4–8 mg in 40µL-size

aluminum pans. Because GLs are hygroscopic, the weighed samples were dried over phosphorus pentoxide placed under vacuum at 50 °C for 48 hours before being covered, so as to remove any moisture absorbed during the preparation of the pan. The samples were then immediately reweighed before being measured. The measurement was conducted at a rate of 5 °C/min for both heating and cooling cycles over a range of temperature at which the liquid crystal phase existed as determined previously by an optical polarizing microscope.

5.2.4 Binary Phase Behaviour

Amphiphile-water mixtures was prepared by weighing out small amounts of the dry lipid into glass ampoules followed by adding the appropriate volume of water by weight. Samples ranging from 5% (w/w) to 90% (w/w) water content at approximately 2–3% (w/w) water intervals were prepared for phase boundary determination. The glass ampoules were flame-sealed, and the lipid-water mixture was mixed as much as possible by centrifugation and heating followed by rapid cooling. The sealed samples were illuminated and examined through crossed polarizers in a heated water bath. Heating of the water bath was step-wisely increased by 5 °C and then left to equilibrate for 1 hour at each desired temperature.

5.2.5 Small-Angle X-ray Scattering (SAXS)

Sample Preparation

Samples were made up to the required water content by adding a known volume of Millipore water to the pre-weighed dry lipid, and homogenized by centrifugation. The hydrated samples were equilibrated for at least three days before SAXS measurements, whereas the dry samples were kept in a vacuum desiccator until the day of measurements.

Measurements

SAXS experiments were carried out on dry and hydrated samples at the SAXS/WAXS beamline at the Australian Synchrotron. The experiments used a beam of wavelength $\lambda = 1.03320 \text{ \AA}$ (12 keV) with a typical flux of 10^{13} photons per second. 2-D diffraction images were recorded on a Dectris-Pilatus 1 M detector of 10 modules with analysis in the q -range $0.0305\text{--}1.047 \text{ \AA}^{-1}$. Silver behenate ($d = 58.38 \text{ \AA}$) was used as the low-angle X-ray diffraction calibrant for all measurements. Heating scans were recorded between 10 and 62°C with 10 min equilibration time at each temperature. An exposure time of 0.5 s was used to minimize radiation damage to the samples. Image analysis was carried out using AXcess, an IDL-based software package developed by Dr. Andrew Heron at Imperial College London [209].

5.2.6 Calculation of Structural Parameters

The 2-D pattern obtained from SAXS/WAXS was integrated into a 1-D scattering function $I(q)$ where $q = (4\pi/\lambda)\sin\theta$ in which q = the scattering vector modulus (units \AA^{-1}), 2θ = scattering angle, and λ = wavelength of radiation.

The calculation of lattice parameter which we denoted as d for lamellar and a for non-lamellar phases was determined from the positions of the Bragg reflections. The scattering function was expressed in terms of reciprocal spacing, s (units \AA^{-1}), as $s = (2/\lambda)\sin\theta$. For the lamellar phase, $s_{lam} = n/d$ where n = order of reflection = 1,2,3,..., and d = d -spacing (lattice parameter) of the lamellar phase. For the hexagonal phase, $s_{hex} = (2/\sqrt{3}a_h)(h^2 + k^2 + hk)^{1/2}$ where h,k = Miller indices and a_h = lattice parameter of the hexagonal phase. For the cubic phases, $s_{cub} = (1/a_c)(h^2 + k^2 + l^2)^{1/2}$ where h,k,l = Miller indices and a_c = lattice parameter of the cubic phase. For the cubic phases, the shape factor, γ and the

average mean curvature, $\langle H_{hc} \rangle$ were estimated [116, 117], using the following equations:

$$\frac{v_{hc}}{a_s(d_{hc})d_{hc}} = \frac{w_{hc}a_c^3}{2(\zeta a_c^2 + 2\pi\chi_E^u d_{hc}^2)d_{hc}}, \quad \text{Equation 5.1}$$

$$\langle H_{hc} \rangle = \frac{-2\pi\chi_E^u d_{hc}}{\zeta a_c^2 + 2\pi\chi_E^u d_{hc}^2}, \quad \text{Equation 5.2}$$

where a_s = molecular cross-sectional area at the polar–non-polar interface, a_c = cubic lattice parameter, and ζ = a dimensionless constant that represents the surface area per unit cell with a lattice parameter of unity. It has characteristic values for each cubic phase, e.g. $Ia3d$ (Q_{II}^G) = 3.091, and $Pn3m$ (Q_{II}^D) = 1.919 [99, 228]. χ_E^u is the Euler characteristic per unit cell. e.g. -8 for $Ia3d$ (Q_{II}^G) and -2 for $Pn3m$ (Q_{II}^D) [99, 228].

The chain length, d_{hc} was calculated using equation 5.3 which relates w_{hc} as a function of d_{hc} .

$$w_{hc} = 2\zeta \left(\frac{d_{hc}}{a_c} \right) + \frac{4}{3}\pi\chi_E^u \left(\frac{d_{hc}}{a_c} \right)^3. \quad \text{Equation 5.3}$$

The volume fraction of the hydrophobic chain, w_{hc} was determined using equation 5.4.

$$w_{hc} = \frac{n_L v_{hc}}{n_L(v_{hc} + v_{head}) + n_W v_W}, \quad \text{Equation 5.4}$$

where n_L = number of moles of lipid, n_W = number of moles of water, v_{hc} = molar volume of hydrophobic chain, v_{head} = molar volume of head group, and v_w = molar volume of water. The value of v_{hc} was estimated from molecular volumes reported by the literature [117, 229], in which $v(\text{CH}) = 20 \text{ \AA}^3$, $v(\text{CH}_2) = 27 \text{ \AA}^3$, and $v(\text{CH}_3) = 54 \text{ \AA}^3$. The molecular volumes of the head groups, v_{head} , were estimated from the reported density value of glucose (1.54 g/cm^3) [230] and galactose (1.616 g/cm^3) [231] respectively. The density of water was assumed to be 1.00 g/cm^3 .

5.3 Results and Discussion

5.3.1 Thermotropic Phase Behaviour

Optical Polarizing Microscopy

Physically, all four compounds existed as yellowish gel-like syrups at room temperature. Upon heating, various types of liquid crystalline phases were observed. OPM images for neat $\alpha\text{-Glc-OC}_{10}\text{C}_6$ at room temperature displayed a birefringent line at the edge of the sample, characteristic of a fluid lamellar phase (L) as shown in Figure 5.2(a). Upon heating, the sample slowly transformed to an isotropic phase at $47.5 \text{ }^\circ\text{C}$. On cooling the sample, the birefringent texture reappeared at $48 \text{ }^\circ\text{C}$ and no further changes were observed upon cooling the material down to room temperature.

The neat compound of $\alpha\text{-Glc-OC}_{10}\text{C}_6$ gave strong birefringence under an optical polarizing microscope at room temperature, as previously reported [119]. However, upon heating, the recently prepared $\alpha\text{-Glc-OC}_{10}\text{C}_6$ compound became clear at $76 \text{ }^\circ\text{C}$, much higher than the previously reported temperature of $55 \text{ }^\circ\text{C}$ [119] due to the improved anomeric purity of the present sample. Upon cooling to room temperature, a birefringent liquid crystalline state was observed with no other phase transitions recorded. The mesomorphic texture exhibited by $\alpha\text{-Glc-OC}_{10}\text{C}_6$ is shown

in Figure 5.2(b). The highly birefringent fan-shaped texture with a larger homeotropic area is characteristic of a hexagonal or columnar phase [232], as reported previously [119].

No birefringence was observed for α -Gal-OC₁₀C₆ upon heating or cooling (Figure 5.2(c)), and the material appeared as a viscous isotropic sample. However, the viscosity of the sample decreased significantly at 51 °C, suggesting that α -Gal-OC₁₀C₆ adopted a cubic phase up to 51 °C before transforming to an isotropic liquid.

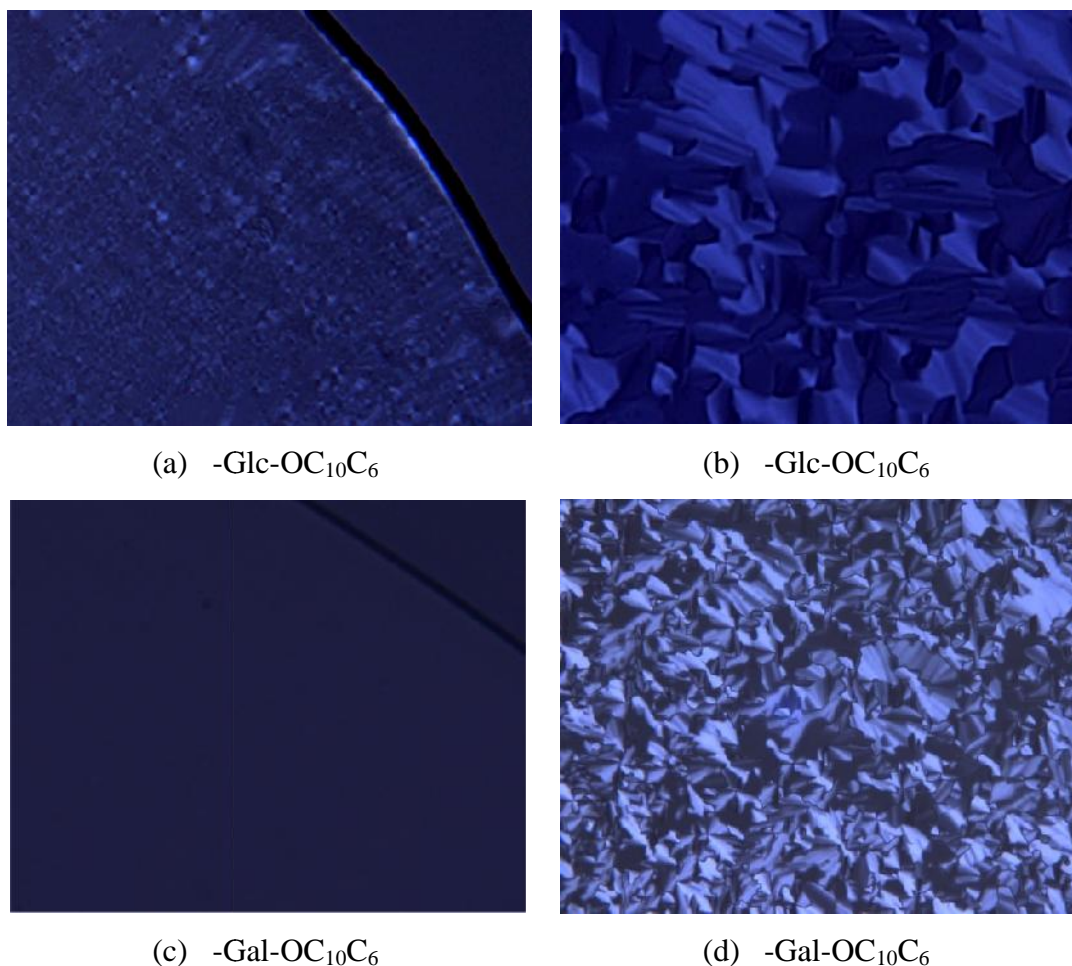


Figure 5.2: The liquid crystalline texture at 30 °C upon cooling for the four compounds at magnification factor of 20.

Neat α -Gal-OC₁₀C₆ exhibited its crystalline nature (Figure 5.3(a)). α -Gal-OC₁₀C₆ started to show changes in crystal shape and anisotropic polarization angle when close to the transition temperature from solid crystalline to hexagonal phase at 43 °C (Figure 5.3(b)). It then transformed to the isotropic phase at 74 °C. On cooling, a birefringent texture characteristic of a hexagonal phase was produced (Figure 5.2(d)) until it reached room temperature. No formation of the crystalline texture was observed due to the sample remaining in the metastable hexagonal phase.

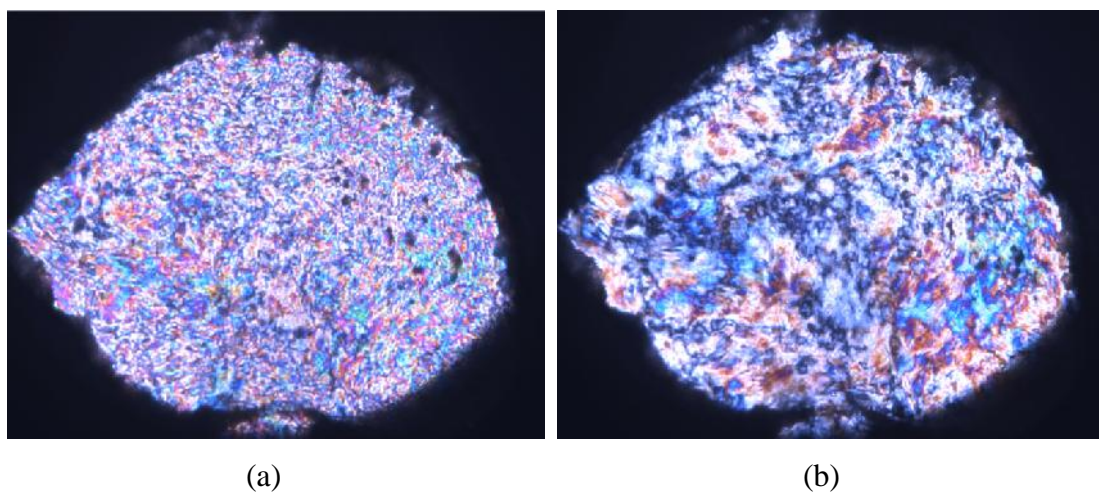


Figure 5.3: The solid crystalline texture of α -Gal-OC₁₀C₆ at magnification factor of 10: (a) at room temperature (b) the same position at 42 °C.

A typical liquid crystal material usually melts from the crystal phase through a liquid crystal phase into the isotropic liquid. However, for three of these GLs the phase transition from the crystalline state to the liquid crystalline state occurred at sub-ambient temperatures. The OPM measurements were conducted at ambient temperature and above, and their thermotropic phase transition temperatures are tabulated in Table 5.1. Both the anomeric and epimeric configuration have significantly affected the thermotropic properties of the dry compounds and this is discussed further in the Section 5.3.3.

Table 5.1: Thermotropic phase transition temperatures measured above 23 °C by OPM.

Compound	Phase and transition temperature (± 0.5 °C)
-Glc-OC ₁₀ C ₆	Cr ? L 47.5 I
-Glc-OC ₁₀ C ₆	Cr ? H _{II} 76 I
-Gal-OC ₁₀ C ₆	Cr ? Q _{II} 51 I
-Gal-OC ₁₀ C ₆	Cr 43 H _{II} 74 I

Differential Scanning Calorimetry

In general, the results obtained from OPM were confirmed by DSC and both methods showed almost the same results within a range of 1–6 °C. Slight differences in temperatures were attributed mostly to the difference in the heat transfer between the sample and supporting substrate (glass slide in OPM vs. aluminum pan in DSC). The DSC scan runs for each of the compounds were started at -55 °C at a scan rate of 5 °C/min. The transition temperatures were obtained from the peak maxima of the second heating cycle to remove the thermal history whereas the enthalpies were obtained by integrating the transition peaks as shown in Figure 5.4. The complete DSC scans for the compounds are given in Figure A1–A4 of the Appendix A.

Upon heating, -Glc-OC₁₀C₆ changed from its liquid crystalline phase to an isotropic phase at 44.4 °C with $\Delta H = 0.42$ kJ/mol. No other phase transitions were detected as previously determined by OPM showing that the solid crystalline to liquid crystal phase transition occurred at a much lower temperature.

From DSC, it was confirmed that -Glc-OC₁₀C₆ changed from liquid crystalline phase to the isotropic liquid at 75.7 °C with $\Delta H = 0.19$ kJ/mol. Similarly, no other phase transitions were observed upon subsequent heating and cooling.

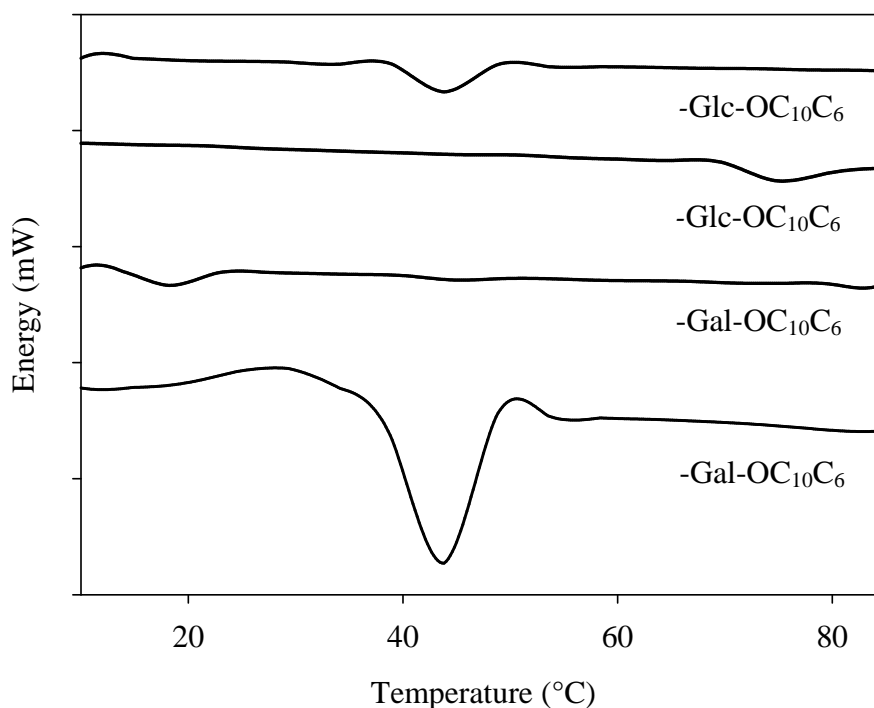


Figure 5.4: DSC scans for the four compounds at heating rate of 5 °C/min.

Unlike the corresponding glucosides, -Gal-OC₁₀C₆ showed a solid-liquid crystalline melting transition at 19.1 °C ($\Delta H = 0.27$ kJ/mol) when measured from sub-ambient temperatures, followed by a transition into isotropic state at 45.2 °C with $\Delta H = 0.06$ kJ/mol.

Similarly, -Gal-OC₁₀C₆ melted at 44.9 °C with $\Delta H = 5.5$ kJ/mol from the crystal phase. The enthalpy value for this transition was significantly larger than that of liquid crystalline to isotropic state transition, indicating that -Gal-OC₁₀C₆ had undergone a transition from a highly ordered crystalline phase to the less ordered liquid crystalline phase. The crystalline nature of this compound was observed under optical polarizing microscope as shown in Figure 5.3. At 80.8 °C, -Gal-OC₁₀C₆ changed from liquid crystalline state to the isotropic liquid state with $\Delta H = 0.12$ kJ/mol.

All the peaks corresponding to the cooling process seemed to have shifted to lower temperatures (see Appendix A), suggesting there was a kinetic process hindering the formation of the more ordered phase. The enthalpy of the phase transition from liquid crystal to isotropic liquid obtained in these measurements was relatively small (less than 6 kJ/mol), indicating that the mesophase was disordered and liquid-like because only a small amount of energy was required for these clearing phase transitions [233]. Table 5.2 displays the phase (determined from OPM), transition temperatures and enthalpies for the transitions obtained from DSC.

Table 5.2: Thermotropic phase transition temperatures and [enthalpies] at heating rate of 5 °C/min.

Compound	Transition temperature, (± 0.1 °C)			[Enthalpy, (kJ/mol)]
-Glc-OC ₁₀ C ₆	Cr	?	L	44.4 [0.42] I
-Glc-OC ₁₀ C ₆	Cr	?	H _{II}	75.7 [0.19] I
-Gal-OC ₁₀ C ₆	Cr	19.1 [0.27]	Q _{II}	45.2 [0.06] I
-Gal-OC ₁₀ C ₆	Cr	44.9 [5.5]	H _{II}	80.8 [0.12] I

The Guerbet alcohols are known to have lower melting points than straight chain alcohols with the same chain length [225, 234]. Comparing the numerous published works on the transition temperatures for neat single chain alkyl glycosides [35, 36, 118], the Guerbet branched-chain GLs, in general, give rise to lower transition temperatures resulting from the chain branching which leads to an increase in conformational disorder in the hydrocarbon chain region [114]. Both monoalkylated glycopyranoside / - anomers behave similarly when the chain length is greater than 12 [36]. In contrast, investigation into the Guerbet branched-chain GL shows that both glucose and galactose anomeric pairs behave differently since the chain length is in the intermediate range, implying that the anomeric effect is significant.

5.3.2 Lyotropic Phase Behaviour

Water Penetration

The sequences of lyotropic phases existing within α -Glc-OC₁₀C₆, α -Glc-OC₁₀C₆, α -Gal-OC₁₀C₆ and α -Gal-OC₁₀C₆ were determined via the water penetration technique by optical polarizing microscopy. Their viscosities and optical textures provided indicative evidence for phase identification. This method offered a qualitative phase diagram with increasing water content but provided no quantitative information on the concentrations at phase boundaries. Therefore, the technique was complemented by SAXS measurements. In Figure 5.5 these phase diagrams are presented with increasing water concentration, from left to right.

The observed phase sequence for α -Glc-OC₁₀C₆ with increasing water content is provided in Figures 5.5(a) and (b). Upon the addition of water at 40 °C, two viscous isotropic phases grew slowly to replace the L phase of the neat compound as a function of concentration gradient which gradually decreased from the edge to the centre of the compound. Cubic phases are generally highly viscous. As the temperature was increased to 60 °C, a less viscous isotropic (putative L₂ phase) region formed within the neat surfactant region, due to clearing of the neat compound (Figure 5.5(b)).

The water penetration scan for α -Glc-OC₁₀C₆, Figure 5.5(c), shows the formation of a viscous isotropic phase at higher water content, replacing the hexagonal phase formed by neat α -Glc-OC₁₀C₆. Both phases were observed in the temperature range of 30 °C to 80 °C.

In the case of α -Gal-OC₁₀C₆ (Figure 5.5(d)), the addition of water resulted in two isotropic phases, presumably two different types of cubic phases since they appeared more viscous than the micellar solution.

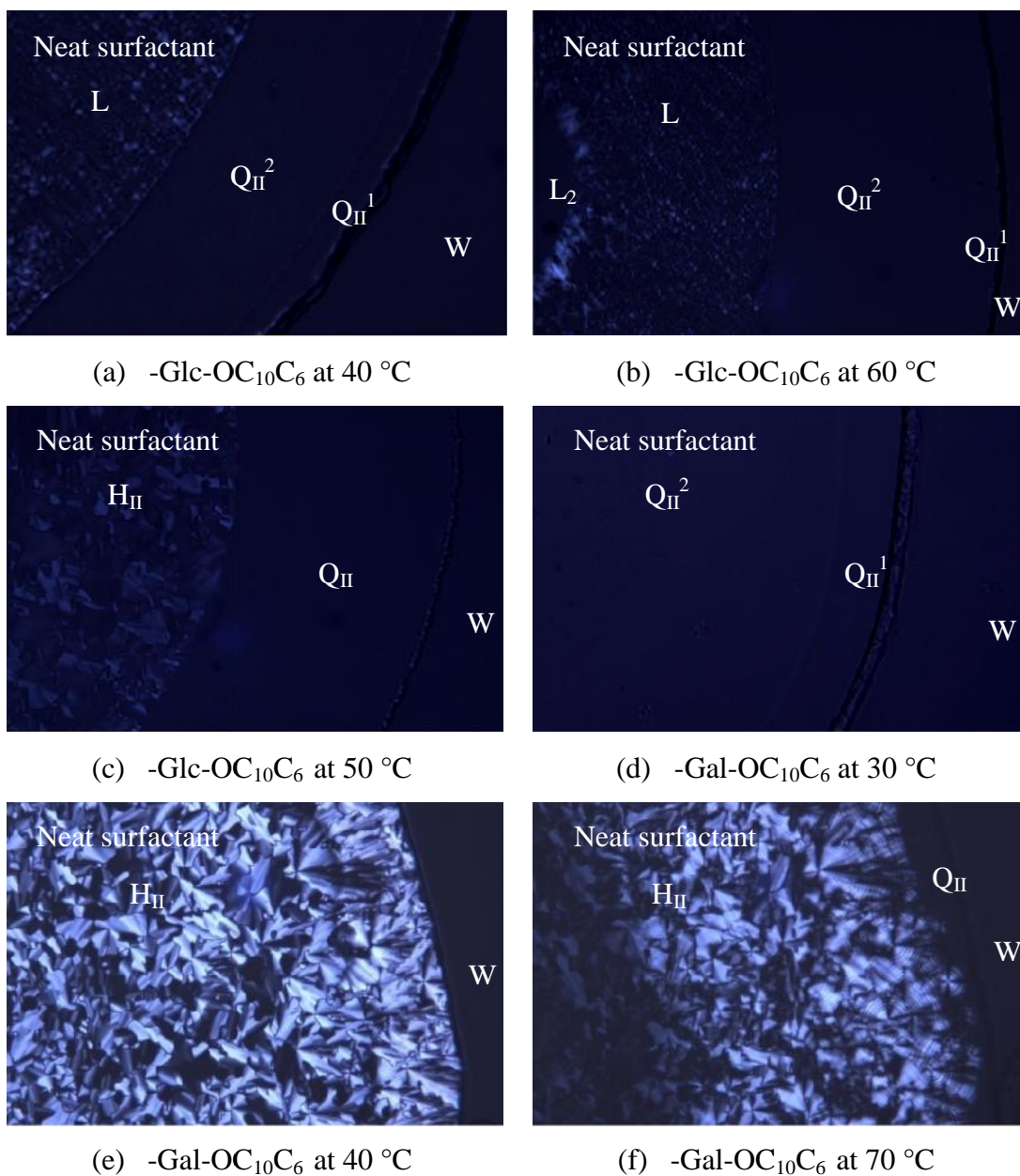


Figure 5.5: Water penetration scans for the four compounds at magnification factor of 20. We label the unidentified cubic phases as, Q_{II} , Q_{II}^1 , and Q_{II}^2 .

Figure 5.5(e) shows that the hexagonal phase observed in dry -Gal-OC₁₀C₆ remained unaffected in the presence of water at 40 °C. This implied that the phase existed as a non-hydrating hexagonal phase. However, at the higher temperature of 70 °C, a viscous isotropic cubic phase started to appear as denoted by the transition bars in the texture pattern of the hexagonal phase (Figure 5.5(f)).

Binary Phase Behaviour

The phase boundaries of the four branched-chain glycopyranoside/water systems were determined by preparing samples with a controlled water content ranging from approximately 5% (w/w) to 90% (w/w) sealed in glass ampoules and examined in the temperature range of 10 °C to 60 °C. The results are represented by dashed lines in Figure 5.6. Seemingly, all compounds were well-mixed and homogenous, except for those of α -Gal-OC₁₀C₆, which appeared as non-hydrating samples over a very wide water content and temperature range. Both α -Glc-OC₁₀C₆ and β -Glc-OC₁₀C₆ were characterized by phases with anisotropic textures in the water content ranging from 3–18 % (w/w) and at temperatures of up to 60 °C. For α -Gal-OC₁₀C₆, the anisotropic behaviour appeared at all water contents and over the whole temperature range. Below 35 °C, α -Glc-OC₁₀C₆/water system at less than 24% (w/w) showed the co-existence of two phases (anisotropic and viscous isotropic). The viscous isotropic phase was observed for α -Glc-OC₁₀C₆ and β -Glc-OC₁₀C₆ at concentrations greater than 24% (w/w). However, for α -Gal-OC₁₀C₆, the viscous phase started to form at very low water concentration (approximately 4.3% (w/w)). The excess water point was estimated at around 35% , 32% , 40% and 37% (w/w) for α -Glc-OC₁₀C₆, β -Glc-OC₁₀C₆, α -Gal-OC₁₀C₆ and β -Gal-OC₁₀C₆ respectively.

SAXS experiments were carried out at the Australian Synchrotron allowing definitive phase assignments to be made, in particular to determine the exact symmetry of the cubic phase formed and provide information on the lattice parameter of individual phases. Samples were prepared at various water contents between 0 and 80% (w/w) and measured from 10 to 62 °C.

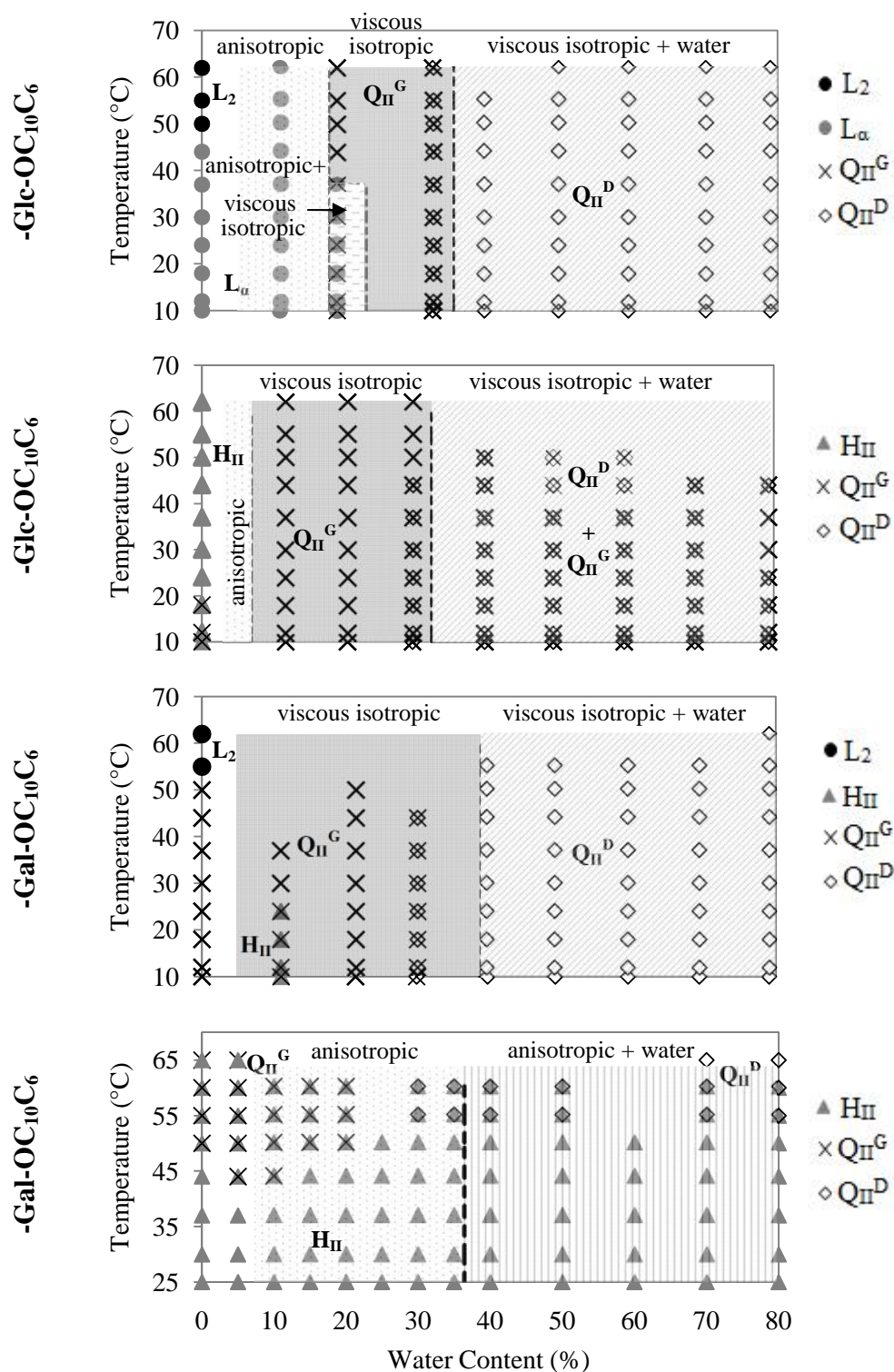


Figure 5.6: Partial binary phase diagrams of the four compounds in the heating direction. SAXS results are represented as L₂ (●); L (◐); Q_{II}^G (×); Q_{II}^D (◇); H_{II} (▲). Polarizing microscopy results are shown as shaded areas. The phases observed include an anisotropic phase, a viscous isotropic phase and a co-existence of both anisotropic and viscous isotropic phases. The excess water points are represented by bold dashed lines.

The SAXS results obtained were in good agreement with those of the contact penetration scans. The phases identified by SAXS together with the phase boundaries, and excess water regions for all compounds are illustrated in Figure 5.6. In general, the self-assembly structures formed by all four GLs/water system were relatively independent of temperature within the measured range (10–62 °C). These sugar surfactants were temperature-insensitive which suggested that there was no significant removal of water molecules from the head group due to the strong hydrogen bond between the OH groups of the sugar unit and water [108]. However, a variety of lyotropic phases were observed with increasing water content. Representative 1-D SAXS patterns of intensity versus s (reciprocal spacing) are illustrated in Figure 5.7 for all types of observed phases at various temperatures and water compositions. The calculated lattice parameters for each phase are tabulated as a function of temperature and water content in Tables B1–B4 of the Appendix B. In addition, the lattice parameters for selected samples are tabulated in Tables 5.3–5.6.

Table 5.3: Phase assignments and lattice parameters for α -Glc-OC₁₀C₆ as a function of water content and temperature. Error in lattice parameter measurements is $< 0.1 \text{ \AA}$.

Water Content (%(w/w))	Lattice parameter (Å)					
	11.0	19.0		32.5		50.2
Temperature (°C)	L	L	Q _{II} ^G	Q _{II} ^G	Q _{II} ^D	Q _{II} ^D
10	26.9	28.4	78.4	92.6	59.7	62.0
24	26.8	28.2	76.9	92.0	58.8	61.6
30	26.7	28.2	76.6	92.5	59.0	61.5
37	26.7	28.2	76.7	91.7	59.0	61.1
55	25.9		76.3	90.1	57.6	59.2

Table 5.4: Phase assignments and lattice parameters for α -Glc-OC₁₀C₆ as a function of water content and temperature. Error in lattice parameter measurements is $< 0.1 \text{ \AA}$.

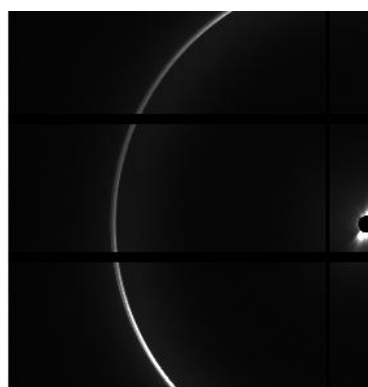
Water Content (% (w/w))	Lattice parameter (\AA)							
	11.9	20.6	29.8		40.1		49.8	
Temperature ($^{\circ}\text{C}$)	$\text{Q}_{\text{II}}^{\text{G}}$	$\text{Q}_{\text{II}}^{\text{G}}$	$\text{Q}_{\text{II}}^{\text{G}}$	$\text{Q}_{\text{II}}^{\text{D}}$	$\text{Q}_{\text{II}}^{\text{G}}$	$\text{Q}_{\text{II}}^{\text{D}}$	$\text{Q}_{\text{II}}^{\text{G}}$	$\text{Q}_{\text{II}}^{\text{D}}$
10	71.3	77.5	87.2	55.4	87.5	55.8	87.7	55.9
24	71.2	75.8	86.7	55.1	87.3	55.5	87.5	55.7
30	71.2	72.7	86.8	55.1	87.4	55.7	87.6	55.6
44	70.4	78.8	86.1	55.0	87.0	55.3	87.3	55.6
50	70.0	77.4	85.6		86.8	55.2	86.2	55.6

Table 5.5: Phase assignments and lattice parameters for α -Gal-OC₁₀C₆ as a function of water content and temperature. Error in lattice parameter measurements is $< 0.1 \text{ \AA}$.

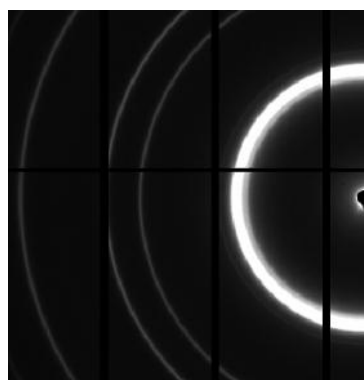
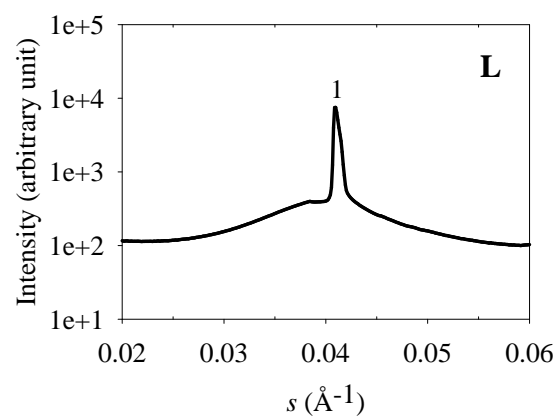
Water Content (% (w/w))	Lattice parameter (\AA)						
	11.2		21.7	30.3		40.3	49.9
Temperature ($^{\circ}\text{C}$)	H_{II}	$\text{Q}_{\text{II}}^{\text{G}}$	$\text{Q}_{\text{II}}^{\text{G}}$	$\text{Q}_{\text{II}}^{\text{G}}$	$\text{Q}_{\text{II}}^{\text{D}}$	$\text{Q}_{\text{II}}^{\text{D}}$	$\text{Q}_{\text{II}}^{\text{D}}$
12	29.0	75.8	82.1	91.3	58.4	60.0	60.3
18	29.0	75.5	81.8	90.4	58.1	59.6	59.7
24	29.0	74.0	81.5	89.9	58.2	59.3	59.3
30		70.5	80.9	89.5	58.6	59.1	59.1
37		69.8	80.0	89.3	57.8	58.4	58.5

Table 5.6: Phase assignments and lattice parameters for α -Gal-OC₁₀C₆ as a function of water content and temperature. Error in lattice parameter measurements is $< 0.1 \text{ \AA}$.

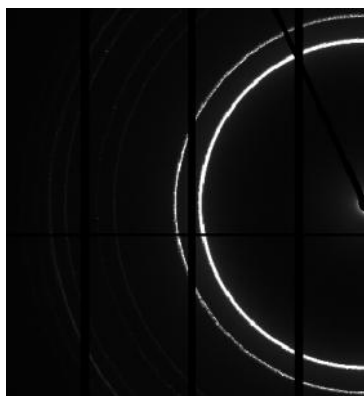
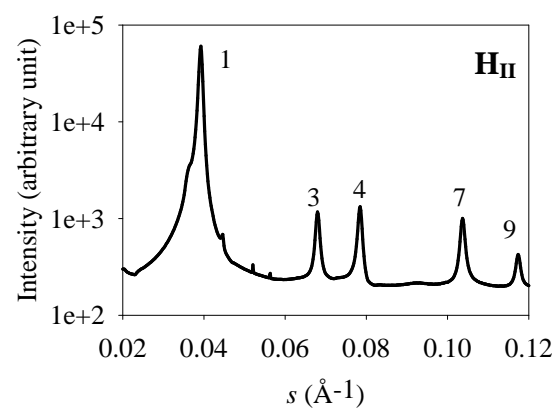
Water Content (% (w/w))	Lattice parameter (\AA)						
	10		20		30	40	50
Temperature ($^{\circ}\text{C}$)	H_{II}	$\text{Q}_{\text{II}}^{\text{G}}$	H_{II}	$\text{Q}_{\text{II}}^{\text{G}}$	H_{II}	H_{II}	H_{II}
25	29.1		29.1		29.1	29.1	29.1
30	29.1		29.1		29.1	29.1	29.1
44	29.2	67.9	29.2		29.2	29.2	29.2
50	29.2	64.9	29.2	82.3	29.2	29.2	29.2



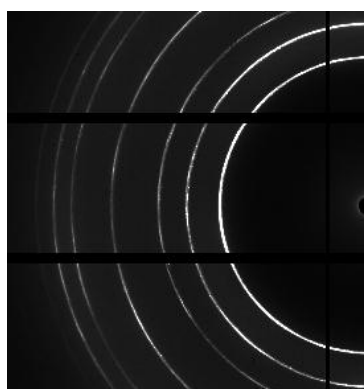
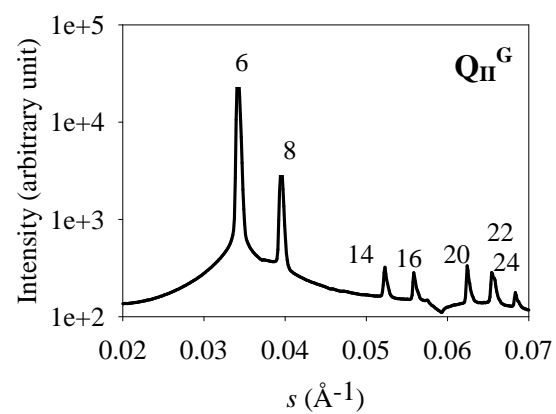
(a)



(b)



(c)



(d)

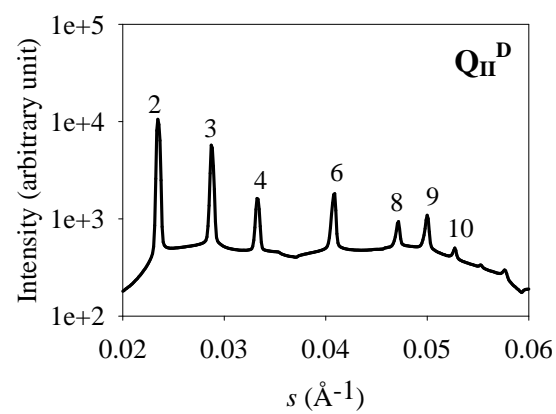


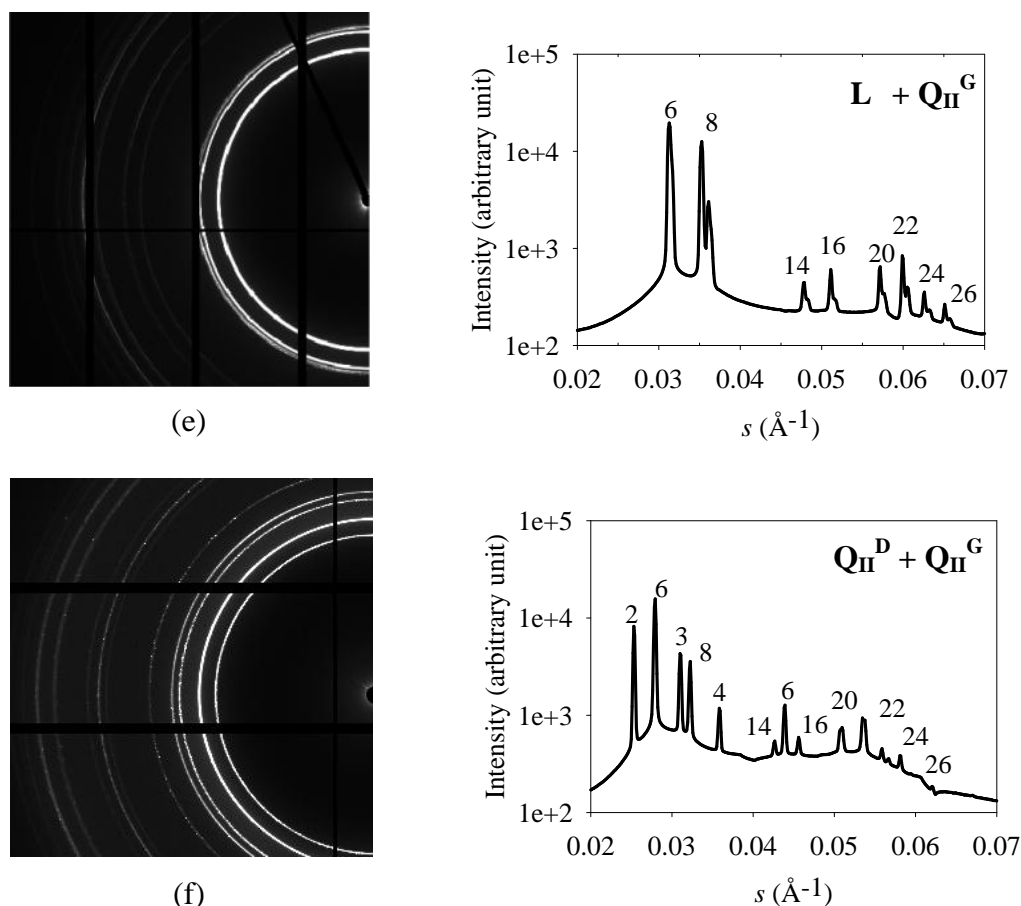
Figure 5.7 (continued)

Figure 5.7: Representative small-angle X-ray scattering (SAXS) patterns for (a) dry α -Glc-OC₁₀C₆ at 30°C. The first order reflection of an L phase is seen. (b) dry α -Gal-OC₁₀C₆ at 44°C. The 1, 3, 4, 7 and 9 reflections of a H_{II} are observed. (c) α -Glc-OC₁₀C₆ with 10% (w/w) at 10°C. The 6, 8, 14, 16, 20, 22 and 24 reflections of a Q_{II}^G phase are seen. (d) α -Gal-OC₁₀C₆ with 60% (w/w) at 10°C. The 2, 3, 4, 6, 8, 9 and 10 reflections of a Q_{II}^D phase are seen. (e) Co-existing L and Q_{II}^G phases of α -Glc-OC₁₀C₆ with 20% (w/w) at 12°C. The first order reflection of an L phase is seen. (f) Co-existing Q_{II}^G and Q_{II}^D phases of α -Glc-OC₁₀C₆ with 60% (w/w) at 30°C. The 2, 3, 4 and 6 reflections of a Q_{II}^D phase are seen, together with the Q_{II}^G peaks.

The phase diagram for α -Glc-OC₁₀C₆ is given in Figure 5.6(a). At low water contents (i.e. below 20% (w/w)), SAXS data confirmed the existence of a lamellar phase. At 20% (w/w) water composition, a co-existence of lamellar and Q_{II}^G phases (crystallographic space group *Ia3d*) was observed in the temperature range of 10 to 37 °C. Above 40 °C, the lamellar phase peak disappeared leaving only those of the Q_{II}^G phase with characteristic peaks of 6, 8, 14, 16, 20, 22 and 24. As the

water content was increased, just before the excess water point (35% (w/w)), we observed a second co-existence of the gyroid Q_{II}^G and the Schwarz diamond Q_{II}^D phase, of crystallographic space group $Pn3m$. In the excess water region, a single Q_{II}^D phase (2, 3, 4, 6, 8, 9 and 10 peaks) was found to be stable.

A partial binary phase diagram for α -Glc-OC₁₀C₆ is provided in Figure 5.6(b). The anhydrous α -Glc-OC₁₀C₆ formed an inverse hexagonal phase, which co-existed with a gyroid phase in the temperature range 10 to 18 °C. This unusual behaviour was most probably due to the presence of trace water in the compound. However, as the temperature was increased, the water molecules were removed, so that only inverse hexagonal phase was observed at ambient temperature. Above 10% (w/w), a single Q_{II}^G phase was observed. At approximately 30% (w/w) this phase co-existed with a Q_{II}^D phase within the temperature range of 10 to 44 °C. Unusually, this co-existence region between Q_{II}^G and Q_{II}^D was stable above the excess water point (30% (w/w)) for all temperatures studied. At an excess water concentration of 80% (w/w), a stable Q_{II}^G phase was detected between 30 and 37 °C. This observation was in good agreement with the previously reported work [119]. Interestingly, the same sample of 80% (w/w) was found to give a perfect Q_{II}^G phase with 6, 8, 14, 16, 20, 22, 24 and 26 peaks after it was equilibrated for 8 months. The formation of the Q_{II}^G phase in excess water was rare since the gyroid (G) surface is the most compact space filling followed by the diamond (D) and the primitive (P), according to the Bonnet relationship of the three minimal surfaces [235]. Consequently, the Q_{II}^G phase normally occurs at a reduced hydration compared to the Q_{II}^D phase, which is more commonly found in excess water systems. The unusual observation of a Q_{II}^D/Q_{II}^G coexistence over a wide temperature and composition range, including under putative excess water

conditions, was backed up by the calculated ratio a_G/a_D which agreed within a few percent with the expected Bonnet relation $a_G/a_D = 1.576$.

According to the horizontal transverse rule, at a constant temperature, the phase sequence upon concentration of any horizontal line in a binary phase diagram should start and end with a homogeneous phase (i.e. one-phase region) and alternate between homogeneous and heterogeneous phases [97]. The phase diagram of α -Glc-OC₁₀C₆/water (Figure 5.6(a)) and α -Gal-OC₁₀C₆/water systems (Figure 5.6(c)) are in agreement with the horizontal transverse rule. In contrast, the phase behaviour of β -Glc-OC₁₀C₆/water and β -Gal-OC₁₀C₆/water are in apparent contradiction to this simple thermodynamic rule. For instance, the wide co-existence Q_{II}^G and Q_{II}^D phases region was sandwiched between the gyroid phase at low and high water concentration up to 80% (w/w) and 30–37 °C. The re-appearance of Q_{II}^G at high water concentration was unexpected and could be due to a kinetically controlled factor related to the asymmetric chain structure of this Guerbet lipid with a C₁₀C₆ hydrocarbon chain. The effect of chain asymmetry on the material properties of bilayer membrane has been investigated by computer simulation using dissipative particle dynamics (DPD) by Illya et. al. in 2005 [236]. Their work showed that chain asymmetry leads to lateral stress re-distribution in membrane, a process thought to be important for the functioning of anaesthetics [237].

The phase diagram for β -Gal-OC₁₀C₆ (Figure 5.6(c)) was slightly different from that of both glucopyranoside compounds. At low water content (less than 20% (w/w)), a Q_{II}^G phase was observed at all temperatures; whereas at a water composition of greater than 40% (w/w), only the Q_{II}^D phase was observed at all temperatures studied. The co-existence of both cubic phases was observed at 30% (w/w) water. For the sample at 10% (w/w), an inverse hexagonal phase was detected via SAXS in the temperature range of 10 to 24 °C. However, the birefringent trace

of a hexagonal texture was not observed via polarizing microscopy. The excess water point was higher than those of α -Glc-OC₁₀C₆ and β -Glc-OC₁₀C₆, occurring above 40% (w/w).

For α -Gal-OC₁₀C₆/water system, the inverse hexagonal phase was formed at all concentrations and temperatures studied (see Figure 5.6(d)). In the presence of water, coexistence between the hexagonal and cubic phases was observed at higher temperatures, where the Q_{II}^G and Q_{II}^D phases were detected at low (less than 20% (w/w)) and high water (above 30% (w/w)) concentrations respectively.

We note that, except for the α -Glc-OC₁₀C₆/water system, many samples gave weak diffraction patterns at higher water compositions (particularly above 40% (w/w)). Some radiation damage was also observed particularly at higher temperatures (above 44 °C) for the α -Glc-OC₁₀C₆/water and α -Gal-OC₁₀C₆/water systems and was manifested as highly spotty diffraction patterns leading to diffuse poorly-defined peaks. Data from samples suspected of radiation damage was not used in developing the partial phase diagrams presented in Figure 5.6.

Figure 5.8 shows representative X-ray scattering patterns for samples both in the dry and hydrated forms. Except for Figure 5.8(c), these scattering patterns are typical of those for the lamellar, inverse hexagonal and inverse cubic bicontinuous phases with characteristic peaks as shown in Table 5.7.

Table 5.7: Characteristics spacing ratios of phases obtained.

Phase	Characteristic peaks
L	1
H _{II}	$\sqrt{1}, \sqrt{3}, \sqrt{4}, \sqrt{7}, \sqrt{9}...$
Q _{II} ^G	$\sqrt{6}, \sqrt{8}, \sqrt{14}, \sqrt{16}, \sqrt{20}, \sqrt{22}, \sqrt{24}....$
Q _{II} ^D	$\sqrt{2}, \sqrt{3}, \sqrt{4}, \sqrt{6}, \sqrt{8}, \sqrt{9}, \sqrt{10}...$

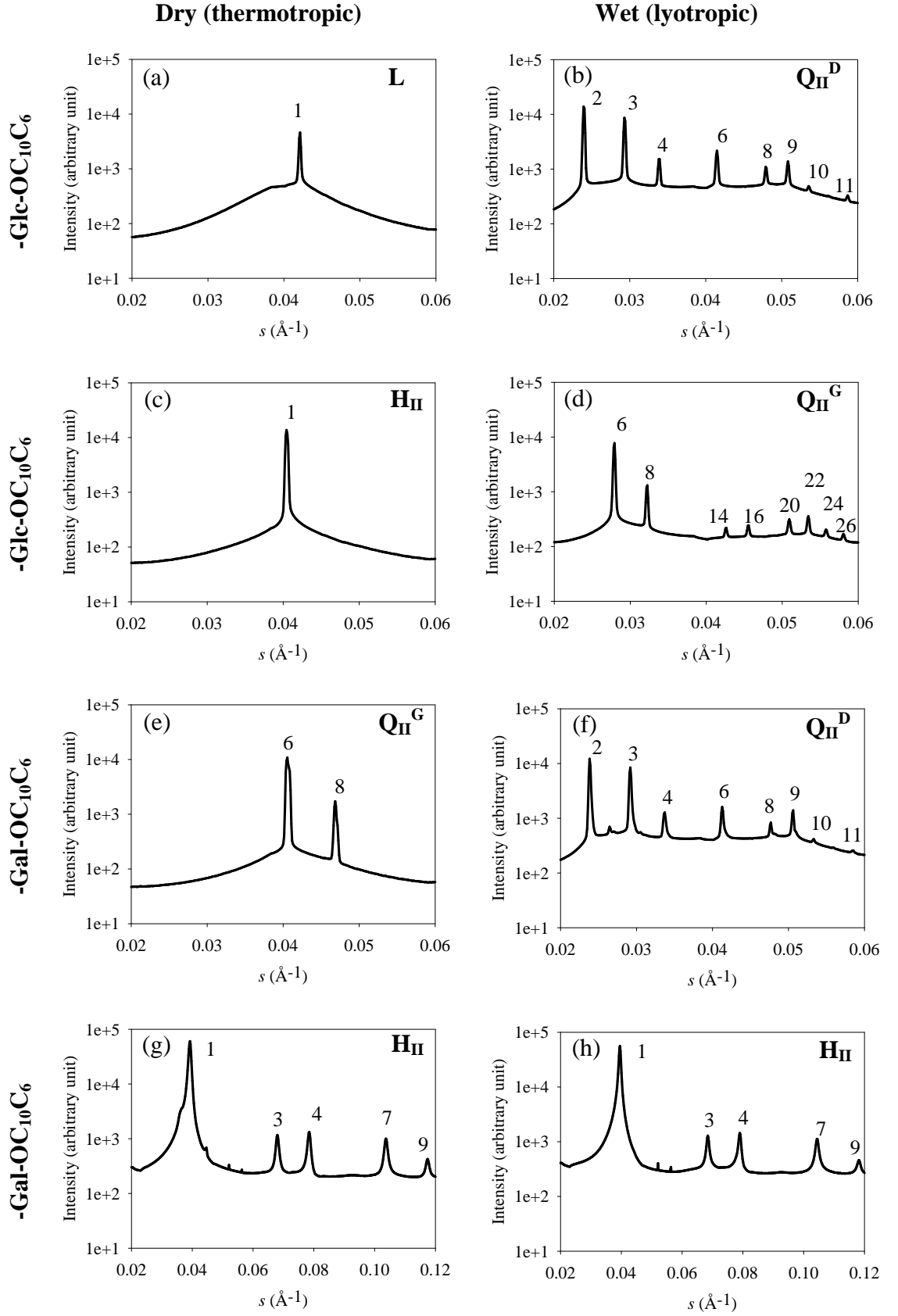


Figure 5.8: SAXS patterns under dry and wet conditions: (a) L at 44 °C, (b) Q_{II}^D at 30 °C with 80% (w/w), (c) H_{II} at 44 °C, (d) Q_{II}^G at 30 °C with 80% (w/w), (e) Q_{II}^G at 44 °C, (f) Q_{II}^D at 24 °C with 80% (w/w), (g) H_{II} at 44 °C, (h) H_{II} at 30 °C with 80% (w/w).

For dry α -Glc-OC₁₀C₆ (see Figure 5.8(c)), the scattering pattern is rather untypical of the hexagonal phase. The characteristic 2-D hexagonal higher-order peaks 3, 4, 7 etc. are not observed. The absence of the higher order peaks in this case is related to the form factor as found similarly for dry H_{II} phase of phospholipids [103]. A dry H_{II} phase can be modelled as a 2-D hexagonal lattice of solid cylinders of uniform electron density (consisting of the dry aggregated head groups), together with fluid hydrocarbon chains of uniform electron density. The form factor of a single such cylinder is a Bessel function, whose first node (zero) lies beyond the 1 peak of the hexagonal lattice, but before the next peak in the pattern. Since the form factor lobes beyond the first node are characteristically of very low amplitude for a solid cylinder, the higher-order peaks are too weak to be observed, and only the 1 peak is seen. In the presence of water (lyotropic H_{II} phase), the water content introduces a core of lower electron density relative to the head groups. As a result, the Bessel function (form factor) is more strongly oscillatory, thereby allowing some of the higher-order peaks to become visible [119].

In the glucose head group, all the peripheral OH groups are equatorial while in galactose, the OH group at the C4 position is axial. As a result, the lattice parameter of the α -Gal-OC₁₀C₆ is relatively larger than that of α -Glc-OC₁₀C₆ (see Table B4 and B2 respectively in Appendix B). In the absence of water, the C4-OH group in the galactose head group may form intralayer hydrogen bonding with neighbouring galactose units. We believe the intralayer hydrogen bonding due to the C4-OH group has resulted in a core of hydroxyl group within the column much in the same manner as a water column for hydrated hexagonal phase sample (discussed above), which will lower the electron density relative to the rest of the head groups. Accordingly, the Bessel function is more strongly oscillatory, thereby allowing higher-order peaks to become visible in the dry α -Gal-OC₁₀C₆ pattern (see Figure

5.8(g)). Thus the dry α -Gal-OC₁₀C₆ sample exhibits similar scattering patterns as the hydrated α -Gal-OC₁₀C₆ (see Figure 5.8(h)). However, the behaviour of α -Gal-OC₁₀C₆ continues to puzzle us, since the lattice parameter (see Table B4 in Appendix B) of the hydrated sample remains the same at different water concentration. This observation is confirmed by the water penetration scan (see Figure 5.5(e)). This implies that α -Gal-OC₁₀C₆ forms a non-hydrating hexagonal phase. In our case, the non-hydrating lipid may be attributed to the formation of the hydroxyl core due to C4-OH of the galactose unit. In a recent modelling work [238], it was shown through bond critical point (BCP) analysis that *n*-octyl- α -D-galactopyranoside formed an extra five-membered ring (compared to *n*-octyl- α -D-glucopyranoside) which possibly contributed to its strong intralayer hydrogen bonding observed in self-assembly structures.

Temperature and Composition Dependence

The lattice parameter temperature dependence for glycopyranosides/water systems at different concentrations are shown in Figure 5.9–5.12. All observed phases, including the L and cubic (Q_{II}^G and Q_{II}^D) phases, display a reduction in lattice parameter with increasing temperature. This may reflect the increased curvature of the interface at higher temperatures due to increased chain splay, and/or the removal of absorbed water leading to a reduction in head group size. The elimination of water molecules is more pronounced when there is more water available (i.e. higher water content); the reduction in lattice parameter is therefore greatest for samples with excess water. The increase in thermal energy and concomitant increase in molecular chain splay and average curvature have been previously reported for these mesophases [94, 218, 239].

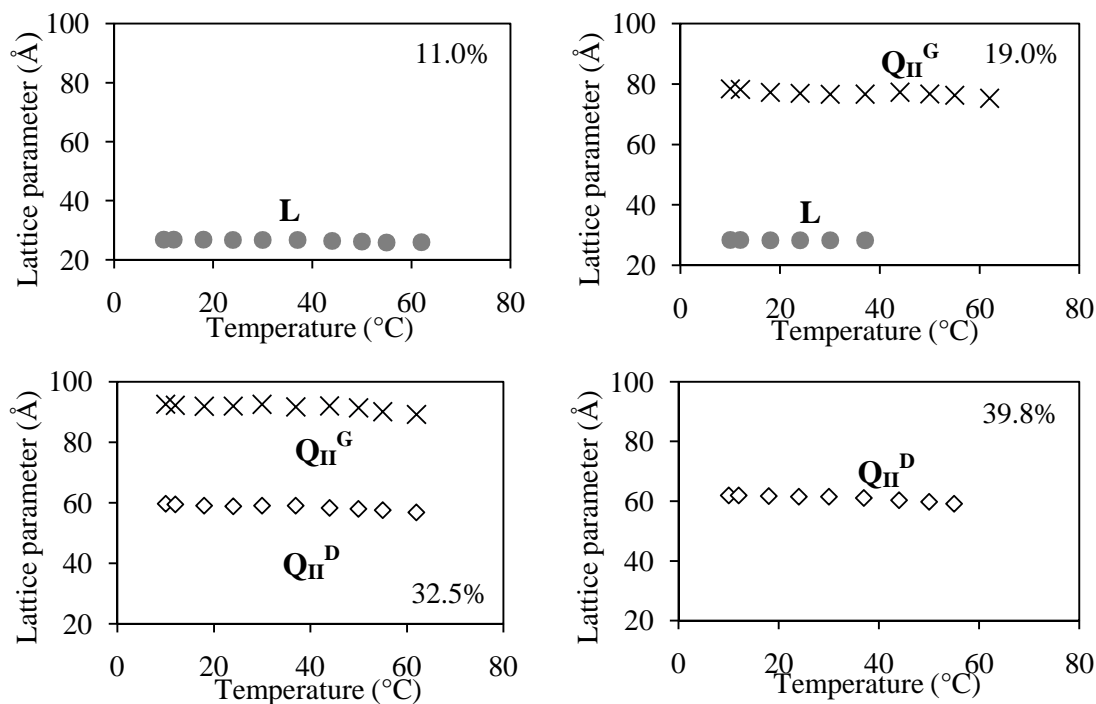


Figure 5.9: Temperature dependence of the lattice parameter of the mesophases for -Glc-OC₁₀C₆/water. Symbols: L (●); Q_{II}^G (×); Q_{II}^D (◇).

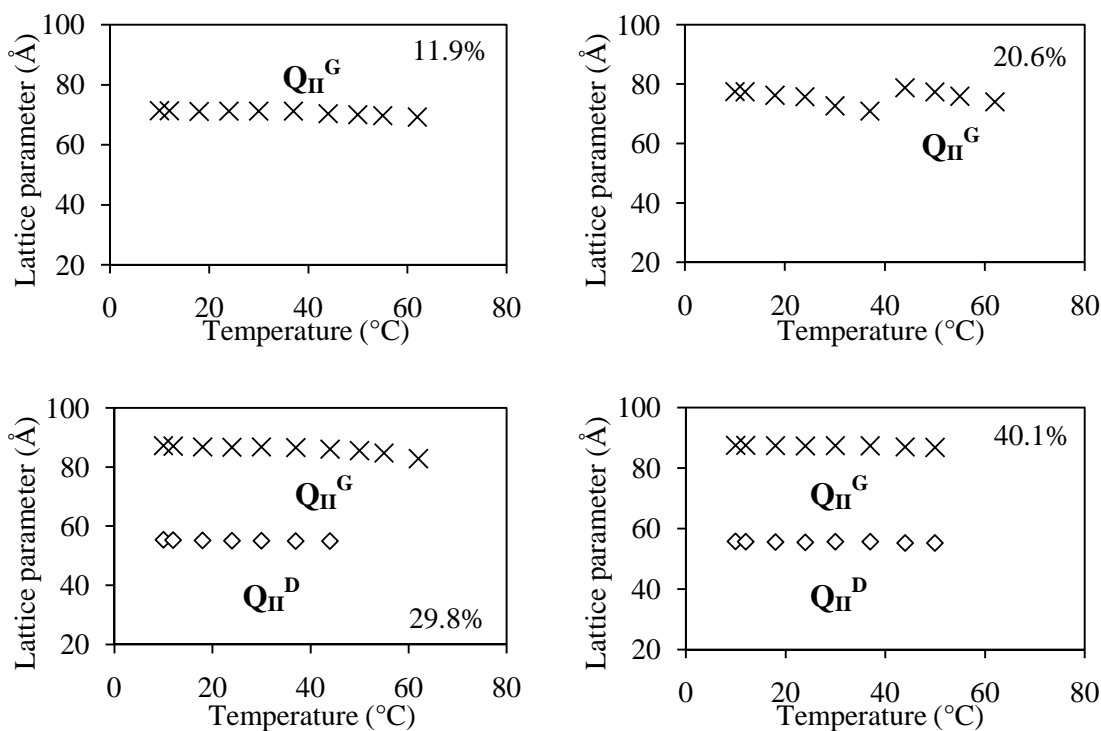


Figure 5.10: Temperature dependence of the lattice parameter of the mesophases for -Glc-OC₁₀C₆/water. Symbols: Q_{II}^G (×); Q_{II}^D (◇).

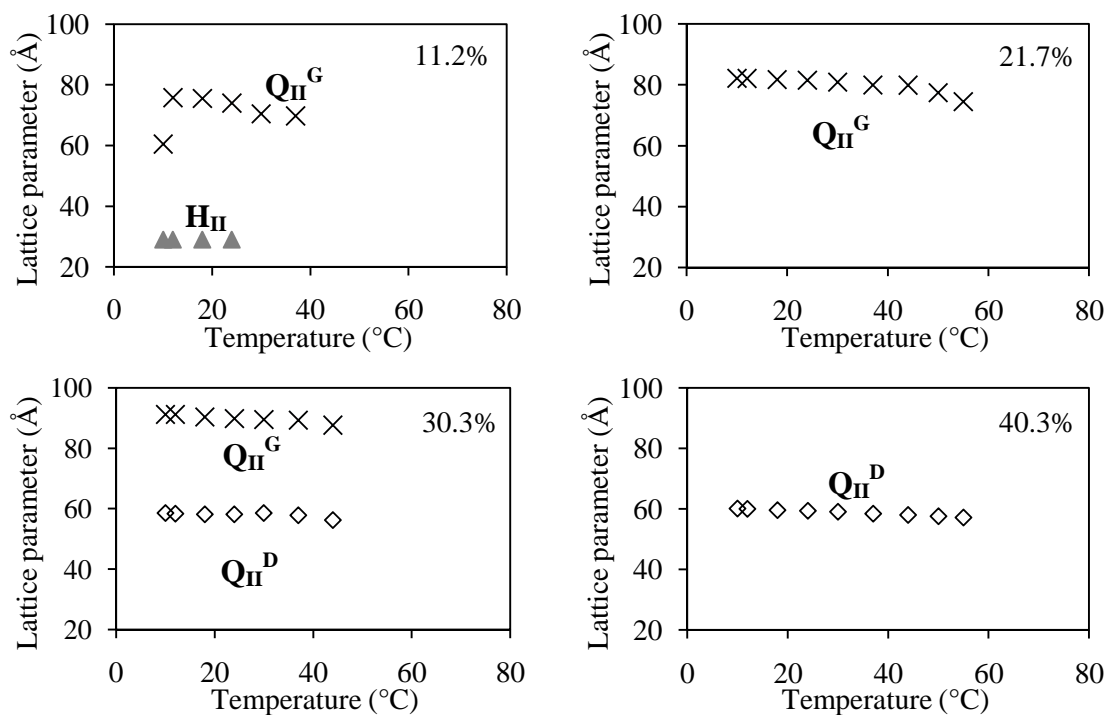


Figure 5.11: Temperature dependence of the lattice parameter of the mesophases for -Gal-OC₁₀C₆/water. Symbols: H_{II} (▲); Q_{II}^G (×); Q_{II}^D (◇).

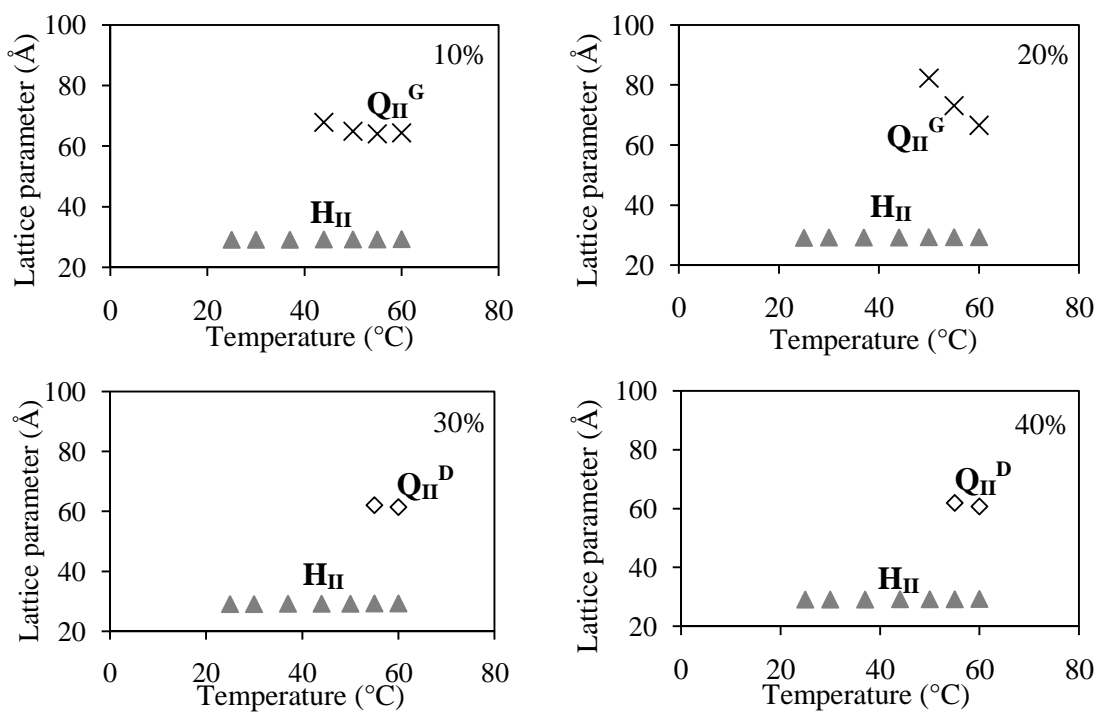


Figure 5.12: Temperature dependence of the lattice parameter of the mesophases for -Gal-OC₁₀C₆/water. Symbols: H_{II} (▲); Q_{II}^G (×); Q_{II}^D (◇).

According to theoretical predictions on triply periodic minimal surfaces (TPMS) [82, 235, 240], the sequence of bicontinuous cubic phases observed with increasing water content should be Q_{II}^G Q_{II}^D Q_{II}^P . The appearance of the Q_{II}^G phase at lower hydration is expected since its underlying minimal surface has the most efficient space packing, followed by Q_{II}^D and finally Q_{II}^P , which has less volume occupied by the lipid bilayer per unit cell volume [235]. However, in the phase diagrams of these glycosides, not all three bicontinuous cubic phases will necessarily appear. Figure 5.13 shows the dependence of the lattice parameter on the water content. In the four lyotropic systems, all phases swell upon hydration implying more water is absorbed by these phases until they reach saturation point or excess water point (indicated by the dashed line in Figure 5.13). At this point, both the Q_{II}^G and Q_{II}^D phases are in equilibrium with excess water and the lattice parameters remain constant.

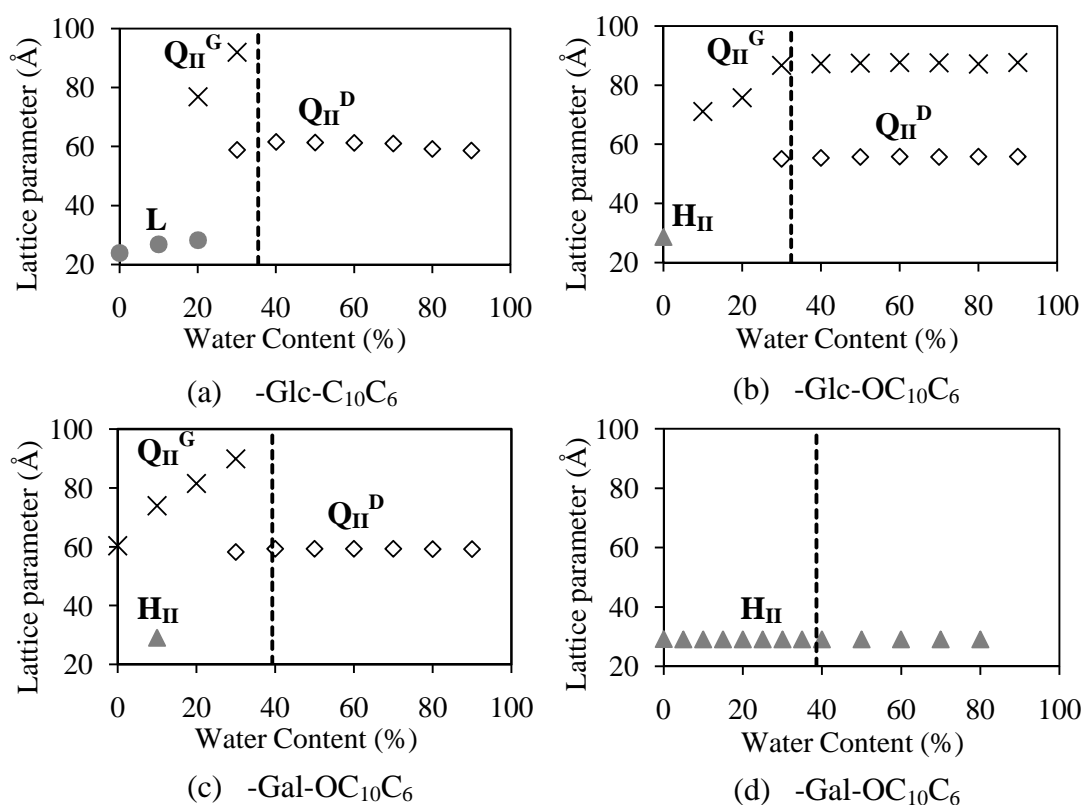


Figure 5.13: Composition dependence of the lattice parameter of the mesophases at 24 °C. Symbols: L (●); Q_{II}^G (×); Q_{II}^D (◇); H_{II} (▲).

The shape factor, $\chi = v_{hc}/(a_s(d_{hc})d_{hc})$, can be used to provide a quantitative description of the molecular shape, useful for rationalizing the self-assembly behaviour of individual lipids. The shape factors of the inverse bicontinuous cubic phases were calculated using equation 5.1. γ was plotted for both the Q_{II}^G and Q_{II}^D phases formed by the α -Gal-OC₁₀C₆/water system in Figure 5.14, as a function of water content (Figure 5.14(a)) and temperature (Figure 5.14(b)). The results indicated that the Q_{II}^G phase gave a higher γ value than the Q_{II}^D phase, consistent with a more pronounced wedge shape for this molecule. In other words, the large shape factor implied the lipid/water interface was more highly curved and the phase could accommodate less water [241]. This finding is in good agreement with the theory in which the average mean curvature of cubic phases decreases from Q_{II}^G to Q_{II}^D to Q_{II}^P . Based on the slopes, clearly the shape factor is strongly dependent on hydration and relatively weakly dependent on temperature as reported by Kulkarni [218] for the monoelaidin/water system. This argument is supported by the calculated averaged mean curvature $\langle H_{hc} \rangle$ values (see Equation 5.2) shown in Figure 5.15.

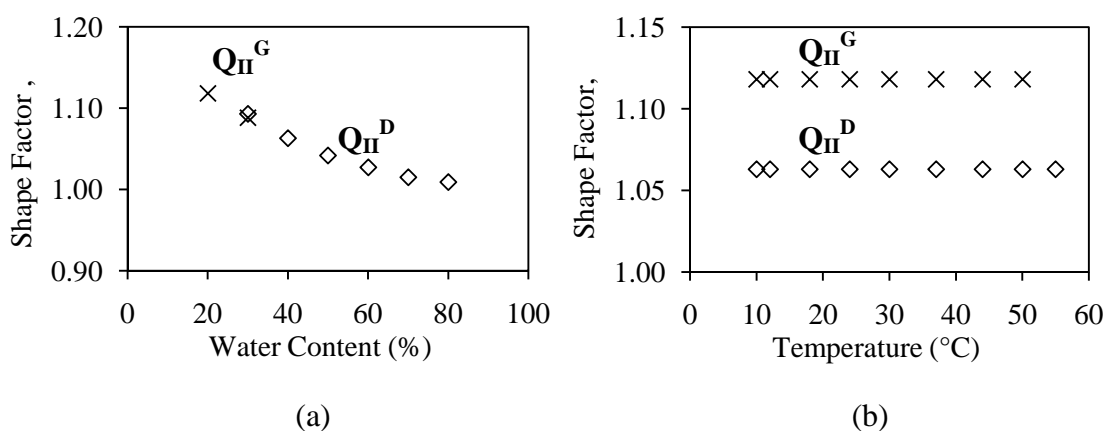


Figure 5.14: Shape factor, γ values for cubic phases and their (a) water content and (b) temperature dependence for α -Gal-OC₁₀C₆/water. Symbols: Q_{II}^G (×); Q_{II}^D (◇).

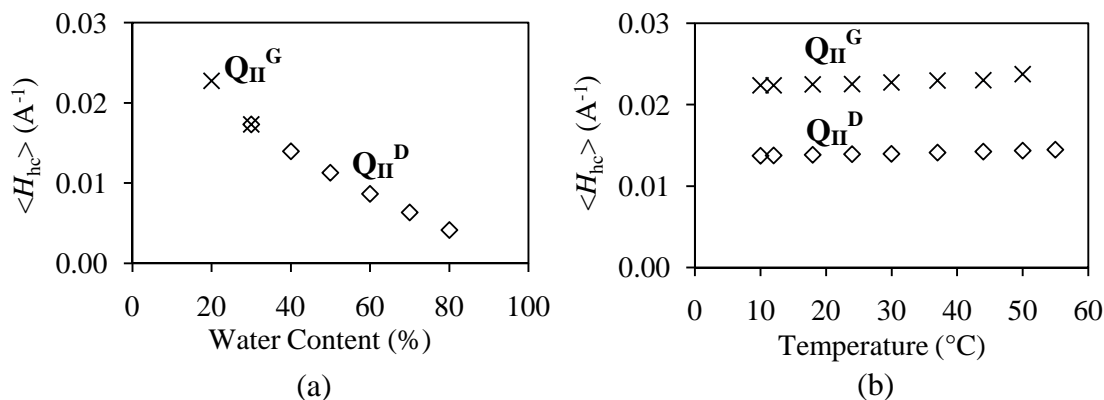


Figure 5.15: $\langle H_{hc} \rangle$ values for cubic phases and their (a) water content and (b) temperature dependence for α -Gal-OC₁₀C₆/water. Symbols: Q_{II}^G (x); Q_{II}^D (◇).

5.3.3 Anomeric-Epimeric Relationships

Considering 10 carbon atoms as the longest chain in these Guerbet glycosides (see Figure 5.1), we may compare these with the structure properties of n-decyl glucopyranosides observed by other authors [36, 210, 242] for both α and β anomers. It is clear that the chain branching effectively increases the hydrophobic tail volume relative to that of the head group, thus increasing the critical packing parameter to greater than one. According to Israelachvili [101, 243], this value favours the formation of inverse structures such as inverse hexagonal and bicontinuous cubic phases since the molecule effectively has a wedge shape such that the hydrophilic head group volume is small compared to that occupied by the hydrophobic chain. Thus, the branched-chain lipids are more likely to adopt non-lamellar phases compared to monoalkylated n-decyl glucopyranosides. Similarly the addition of two aliphatic chains leads to the formation of curved phases as observed in phenylazophenyl glycosides [233].

Table 5.8 gives the structure versus thermotropic phase relationship of the four Guerbet glycosides demonstrating the stereochemical (anomeric vs. epimeric) effect. The α -Glc-OC₁₀C₆ gives an L₁ phase. However, its β -gluco anomer displays an H_{II} phase. This implies that the mean curvature in β -glucoside is higher compared

to α -glucoside and the former is more wedge-like in shape (highly curved). Comparing the molecular structure of both α / β -glucopyranosides, the cross-sectional area of the hydrophobic branched-chain to the sugar head group is larger for the β -anomer than for α -anomer. Again a slight conformational difference in the two anomeric compounds has led to a large difference in the structural property. A similar trend is also observed in α / β -galactopyranosides in which β -Gal-OC₁₀C₆ forms a Q_{II}^G phase whereas α -Gal-OC₁₀C₆ forms a more highly curved H_{II} phase.

Table 5.8: Anomeric-Epimeric relationship of thermotropic liquid crystalline phases determined by OPM (above 23°C).

Anomer pairs		Epimer pairs	
α -Glc-OC ₁₀ C ₆	β -Glc-OC ₁₀ C ₆	α -Glc-OC ₁₀ C ₆	β -Gal-OC ₁₀ C ₆
L 47.5 I	H _{II} 76 (66*) I	L 47.5 I	Q _{II} ^G 51 I
α -Gal-OC ₁₀ C ₆	β -Gal-OC ₁₀ C ₆	α -Glc-OC ₁₀ C ₆	β -Gal-OC ₁₀ C ₆
Q _{II} ^G 51 I	Cr 43 H _{II} 74 I	H _{II} 76 (66*) I	Cr 43 H _{II} 74 I

*previous reported result [119].

In the anhydrous state, α -glucoside adopts an L phase whereas its epimer, α -galactoside gives a Q_{II}^G phase at comparable temperatures. This result shows that the slight conformational difference at the C4 of the OH group between a glucoside (equatorial) and a galactoside (axial) has a profound effect on the phase behaviour. The molecular structure of β -Gal-OC₁₀C₆ has a wedge-like shape and a liquid-like branched-chain. Hence, the cross-sectional areas are larger compared to those in β -Glc-OC₁₀C₆. As a result, molecular splay effect is introduced into the bilayers, favouring the curved Q_{II}^G phase. For α -Glc-OC₁₀C₆, both the sugar head and the two aliphatic chains have an equivalent cross-sectional area value, which results in the formation of the lamellar phase in the neat compound. It seems that both galactosides are more curved than the corresponding C4-epimers. Hence we may

assume that the H_{II} phase of α -Gal-OC₁₀C₆ has more curvature than α -Glc-OC₁₀C₆. Generally, the hydrated samples of the four Guerbet glycosides compounds form curved phases of the inverse bicontinuous cubic type over a wide range of temperatures and compositions.

5.4 Conclusions

In this chapter, we report the partial temperature-composition phase diagrams of four anomeric-epimeric related Guerbet glycosides namely α -Glc-OC₁₀C₆/water, β -Glc-OC₁₀C₆/water, α -Gal-OC₁₀C₆/water and β -Gal-OC₁₀C₆/water systems in the temperature range of 10 to 62 °C. In general, the introduction of chain branching of the hydrocarbon chains leads to the formation of inverse structures such as the inverse hexagonal and bicontinuous cubic phases over a broad range of temperature and water composition. This reflects the characteristic wedge shape of these molecules such that the hydrophilic head group is small compared to the volume occupied by the hydrophobic chain. Besides that, these Guerbet glycosides have lower transition temperatures than single chain glycosides resulting from the chain branching which leads to an increase in conformational disorder in the hydrocarbon chain region. Interestingly, in excess water, α -Glc-OC₁₀C₆ exhibits an inverse bicontinuous cubic phase of space group *Ia3d*, which is very rarely seen in single component amphiphile/water systems. It is presumably the asymmetric chain of this Guerbet lipid with C₁₀C₆ hydrocarbon chain that stabilizes the *Ia3d* phase, although the mechanism of this is not clear at present.

Additionally, β -Gal-OC₁₀C₆ forms a non-hydrating hexagonal phase at all water contents. This result suggests that the axial OH group at C4 position in the galactose head group forms stronger intralayer hydrogen bonding with neighbouring galactose units than with water molecules in the inverse hexagonal phase.

The anomeric-epimeric relationship shows that the α -anomers have a stronger tendency to form inverse phases than the β -anomers. For the C4-epimers, the galactoside is more highly curved than the corresponding glucoside. The formation of liquid crystalline inverse hexagonal and bicontinuous cubic phases by these Guerbet branched-chain glycosides over a wide range of temperatures and water composition, opens up a range of potential applications, including as new drug carriers in drug-delivery systems or for *in meso* crystallization of membrane proteins.

CHAPTER 6

CHARACTERIZATION OF THE INVERSE PHASE OF A BRANCHED-CHAIN GLYCOLIPID SELF-ASSEMBLY USING FLUORESCENT PROBES

CHARACTERIZATION OF THE INVERSE PHASE OF A BRANCHED-CHAIN GLYCOLIPID SELF-ASSEMBLY USING FLUORESCENT PROBES

We continue our investigation using fluorescence spectroscopy to study the inverse bicontinuous cubic phase of the 2-hexyl-decyl- β -D-glucopyranoside (β -Glc-OC₁₀C₆)/water system in order to understand the dynamics of confined water in aqueous nanochannels of the lipidic cubic phase.

6.1 Introduction

Inverse liquid crystalline mesophases, such as the inverse bicontinuous cubic, inverse hexagonal or inverse micellar cubic phase, are being widely studied for their potential to produce new and/or better functionalities in food and pharmaceutical products. So far, among these phases, the inverse bicontinuous cubic phase has shown the finest studied applications in the field of controlled drug-delivery [25, 26, 75] membrane proteins crystallization [78, 87] and material synthesis [244]. In nature, the cubic lipid structures (i.e. cubic membranes) are ubiquitous in biological systems and they are also involved in different biological processes such as membrane fusion and fat digestion [245-248].

The inverse bicontinuous cubic phase is in fact a three-dimensional (3-D) structure composed of a single, continuous bilayer that divides the aqueous component into two interpenetrating but non-contacting channels of diameters between about 20–50 Å, draped over a triply periodic minimal surface (TPMS) [82, 90, 204, 245, 248]. The sponge-like structure of this phase allows the passage of water-soluble as well as lipo-soluble molecules or peptides and proteins [26, 245]. Owing to these properties, cubic phase has proven useful for the nanoencapsulation

of drugs as well as facilitating the crystallization of membrane proteins which do not easily crystallize in bulk solution. The molecular mechanism in membrane protein crystallization for instance, is not yet clear, but interfacial water and transport are thought to play an important role in the nucleation and growth of crystal [249, 250].

In Chapters 3 and 4, we have investigated the lamellar and normal non-lamellar phases (e.g. cubic bicontinuous, hexagonal and micellar) formed by straight chain GLs. Herein, we characterize the inverse bicontinuous cubic phase formed by the Guerbet glycoside, 2-hexyl-decyl- β -D-glucopyranoside (β -Glc-OC₁₀C₆) using the same fluorescent probes and techniques as described before. β -Glc-OC₁₀C₆ consists of a single sugar unit with a branched alkyl chain of total 16 carbon atoms. The β -Glc-OC₁₀C₆ can give an inverse bicontinuous cubic phase with gyroid structure (*Ia3d* symmetry) due to the branched-chain, which leads to an increased desire for curvature. The gyroid structure can be formed by intercellular lipid membranes of the biological systems and this structure has various technological applications such as mesoporous sieves, catalyst and material for making contact lenses [83]. For this study, the cubic phase is observed at 20% (w/w) water content of β -Glc-OC₁₀C₆/water system according to its partial binary phase diagram shown in Figure 5.6(b) of Chapter 5. The chemical structure of β -Glc-OC₁₀C₆ is depicted in Figure 6.1.

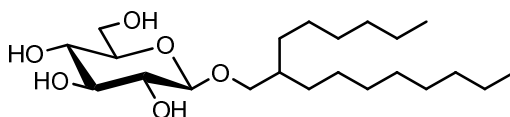


Figure 6.1: The chemical structure of 2-hexyl-decyl- β -D-glucopyranoside (β -Glc-OC₁₀C₆).

6.2 Research Methodology

6.2.1 Materials

The synthesis of β -Glc-OC₁₀C₆ is described elsewhere [114]. Pyrene (99%) was purchased from Sigma-Aldrich. L-tryptophan (99%) was obtained from Merck. Tryptophan butyl ester (Trp-C₄) and its octyl analog (Trp-C₈) were prepared according to the literature procedure [181] mentioned in Chapters 3 and 4. All chemicals and solvents were used without further purification.

6.2.2 Sample Preparation

The concentration of tryptophan/tryptophan ester/pyrene in the β -Glc-OC₁₀C₆/water system for both steady-state and time-resolved experiments was adjusted to 0.1 mM. The value was based on an estimated density of $\sim 1.0 \text{ g mL}^{-1}$ for the mixture. The inverse bicontinuous cubic phase used for this study was observed at 20% (w/w) water content of β -Glc-OC₁₀C₆/water system according to its partial binary phase diagram as reported in Chapter 5 (see Figure 5.6(b)). The inverse bicontinuous cubic phase was confirmed to be formed by illuminating the sample in the flame-sealed tube and examining it through a cross-polarizing filter. These cubic phase samples were optically isotropic under the cross-polarizing filter and highly viscous-two properties characteristic of the cubic lipid phases. All samples were treated with the same procedure used in Chapter 3. The aqueous buffer used was 25 mM sodium phosphate buffer, pH 7.2. The samples included the lipid mixed with the different probes, in addition to one sample with no probes, which was used as a standard in the measurements.

6.2.3 Instrumentation

Fluorescence spectra were recorded on a Shimadzu RF-5301 PC spectrofluorophotometer and lifetime measurements were performed using a TimeMaster fluorescence lifetime spectrometer. In all the experiments, samples were measured in a 1-cm path length quartz cell at 23 ± 1 °C and were treated with the same procedure used previously.

6.3 Results and Discussion

6.3.1 Probing the Polar Region of the Lipid

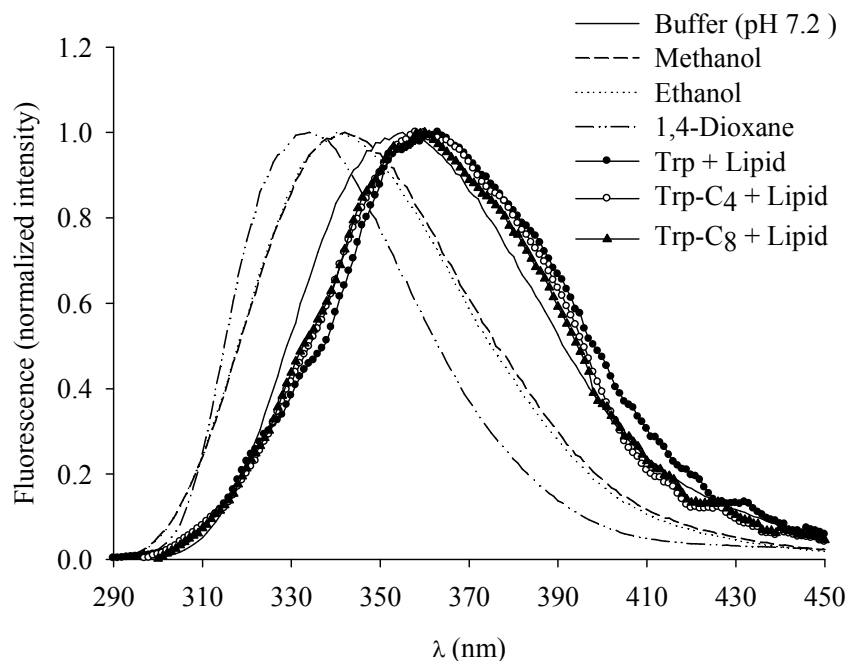


Figure 6.2: Fluorescence spectra of tryptophan and its derivatives in different solvents and in the inverse cubic phase of the β -Glc-OC₁₀C₆ lipid. $\lambda_{\text{ex}} = 280$ nm.

Tryptophan molecule is again used in this work to probe the head group region. Figure 6.2 shows the fluorescence spectra of tryptophan in solvents of different polarity as well as the three probes (Trp, Trp-C₄ and Trp-C₈) embedded in the inverse cubic phase with *Ia3d* space group of the β -Glc-OC₁₀C₆ lipid. From the graph, the fluorescence peak positions of Trp and its derivatives in lipid are red-

shifted ($\lambda_{\text{max}} = 360\text{--}361\text{ nm}$) compared to that of tryptophan in buffer ($\lambda_{\text{max}} = 355\text{ nm}$). This observation is an indication of the different environment experienced by the tryptophan moiety in the polar region of the head groups of the lipid which is slightly more polar compared to water.

The normal and inverse cubic phases show that the tryptophan and its derivatives are clearly experiencing different environments in the head group region (see Figure 6.3 and Table 6.1). In the former, the peak positions of tryptophan moieties are close to those of methanol and ethanol ($\lambda_{\text{max}} = 340\text{--}342\text{ nm}$), whereas in the latter, the fluorescence peak maxima are more polar than buffer ($\lambda_{\text{max}} = 355\text{ nm}$). This probably indicates that tryptophan in the inverse cubic phase is very close to bulk water, a sign for the presence of bulk-water like channels that facilitate the transformation of water-soluble substances to the cell in the inverse cubic phase more than in any other phase.

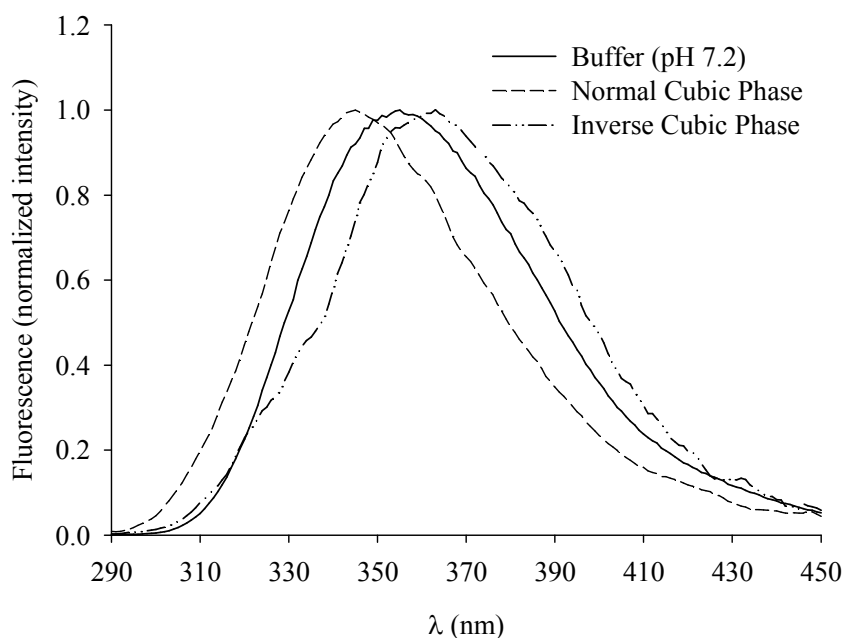


Figure 6.3: Fluorescence spectra of Trp embedded in the normal cubic phase of β -Glc-OC₈ and the inverse cubic phase of β -Glc-OC₁₀C₆. $\lambda_{\text{ex}} = 280\text{ nm}$.

Table 6.1: Fluorescence spectral peak maxima of tryptophan and its derivatives in the normal cubic phase of β -Glc-OC₈ and the inverse cubic phase of β -Glc-OC₁₀C₆. $\lambda_{\text{ex}} = 280$ nm.

Probe	Peak maximum (nm)	
	Normal cubic	Inverse cubic
Trp	346	361
Trp-C ₄	346	360
Trp-C ₈	347	360

The results obtained for tryptophan and its derivatives in the inverse cubic phase of the β -Glc-OC₁₀C₆ lipid are in stark contrast to those obtained for the inverse cubic phase of monoolein reported by Kim et al. [149]. There are a few differences in the lipidic cubic phase used in the present study and in previously reported work that may have led to these differences. First, in monoolein the tryptophan molecule and its derivatives were anchored into the inverse cubic phase of $Pn3m$ instead of $Ia3d$ space group. The water channels in the $Pn3m$ meet in four-way junctions at 109° whereas in the $Ia3d$ they meet in three-way junctions at 120° . Unlike in the $Pn3m$, the two water regions in the $Ia3d$ are no longer identical (enantiomers) and each has a different chirality [85].

Second, the size of water nanochannels in the lipidic cubic phase in monoolein is about 50 Å [149]. In this work, we calculate the aqueous channel diameter to be ~ 23 Å by simply using the following equation described by Kraineva et al. [248]:

$$r_w = 0.248a_c - d_{hc}, \quad \text{Equation 6.1}$$

where the chain length, d_{hc} of the cubic phase can be calculated by using the cubic lattice parameter, a_c which is determined by SAXS of the known sample composition, ϕ_{hc} (refer to Equation 5.3). Moreover, this calculated value was obtained under the experimental conditions described in Chapter 5 (20% (w/w) of the β -Glc-OC₁₀C₆/water system and at 23°C) which form an inverse cubic phase of the space group $Ia3d$ with $a_c=75.8$ Å and $d_{hc}=7.3$ Å. The size of our aqueous nanochannels is half that of the cubic $Pn3m$ space group measured by Kim et al. [149] (23 Å vs. 50 Å).

We estimate the length of the tryptophan molecule to be about 12 Å. The C₄- and C₈-tails are approximately 4.5 and 9.0 Å in length, respectively. Therefore, the molecular length of the Trp-C₄ is about 16.5 Å whereas the Trp-C₈ is about 21 Å. Similar to the observation reported by Kim et al. [149], we anticipate, as the chain length increases, the tryptophan molecule especially Trp-C₈ is likely to be pulled closer to the polar head groups due to the nature of the alkyl ester chain being hydrophobic and tending to avoid the hydrophilic region. However, the fluorescence spectral position contradicts this proposition. Two possible situations may be offered since the length of the Trp-C₈ molecule (21 Å) is comparable to the water channel diameter (23 Å). On the one hand, the Trp-C₈ maybe trapped inside the aqueous nanochannels with restricted movement causing its C₈-chain not to penetrate the tail region of the lipid. Alternatively, the Trp-C₈ molecule may also be dispersed in the continuous phase on the outside of the cubic structure. The results for the behaviour of the tryptophan probes in the head group region of the inverse cubic phase are far from being conclusive and further experiments are needed in order to establish a solid conclusion regarding these findings.

In the next section 6.3.2, we provide some supporting evidences of why the alkyl ester chain of tryptophan does not infuse into the hydrophobic region. Both Trp and Trp-C₄ are presumably experiencing the same condition as Trp-C₈ but with less constraint. As shown in Figure 6.2 and Table 6.1, all the three probes (Trp, Trp-C₄, and Trp-C₈) have similar spectral positions when embedded in lipid which implies that the tryptophan molecule is located in a similar polar environment. This observation confirms that the glucose unit of the head group does not show any polarity gradient as reported in Chapter 4 for other phases.

The fluorescence lifetimes of tryptophan and its ester derivatives are measured in the inverse cubic phase of the β -Glc-OC₁₀C₆ lipid. Tryptophan has two lifetime components in buffer which are due to two different rotamers (0.5 and 3.8 ns) [137, 196, 197]. Figure 6.4 shows the decay transients for Trp-C₈ in buffer and in the β -Glc-OC₁₀C₆ lipid as an example. The two decay components are not much affected by changing the environment from buffer to inverse cubic phase. Lifetime measurements indicate that the lifetimes of tryptophan and its derivatives are close to those in buffer. The biexponential nature of the tryptophan fluorescence decay in lipid establishes a strong support for the ground state heterogeneity. This heterogeneity indicates that the lipid self-assembly has a degree of flexibility that allows the tryptophan side chain to exist in two different rotamers. The only effect of the lipid is observed in the relative contribution from each lifetime component. The major contribution in solution is from the long lifetime component (85–90%), as tabulated in Table 3.2, Chapter 3. This trend is similar to that in the inverse cubic phase of the β -Glc-OC₁₀C₆ where the long lifetime component gives a major contribution of 73–78%.

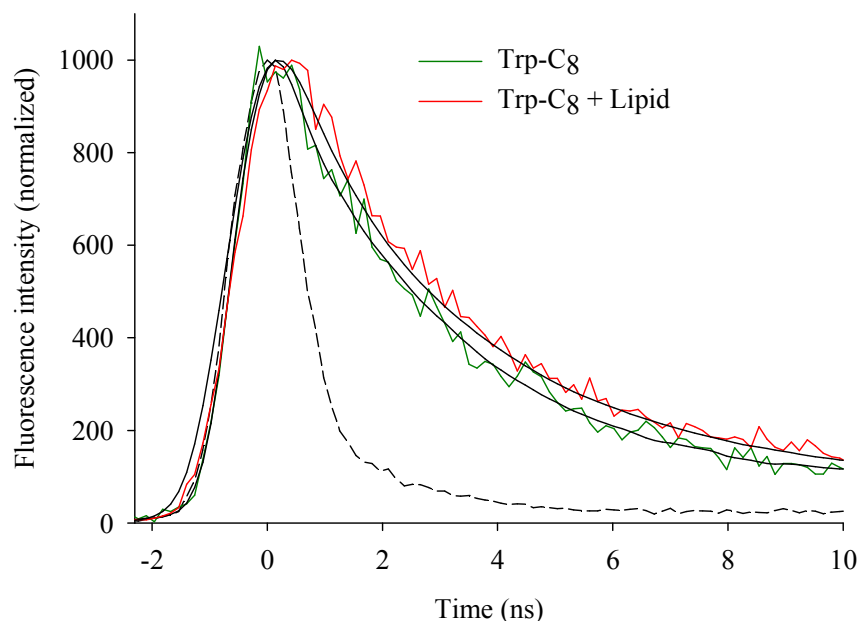


Figure 6.4: Fluorescence decay transients of Trp-C₈ in buffer alone and in buffer containing the inverse cubic phase of β -Glc-OC₁₀C₆. $\lambda_{\text{ex}} = 280$ nm. IRF is shown by a dashed line.

6.3.2 Probing the Hydrophobic Region of the Lipid

Pyrene is used as a probe to explore the tail region of the lipid due to its fluorescence sensitivity towards its local microenvironment [201]. The spectra of pyrene in cyclohexane, buffer, and in buffer containing the inverse cubic phase of the β -Glc-OC₁₀C₆ lipid is depicted in Figure 6.5. In buffer, the hydrophobic nature of pyrene causes aggregation of the pyrene molecules to avoid the highly disliked polar nature of the solvent as shown in the high yield of excimer formation represented by unstructured band centred at ~ 465 nm. The excimer fluorescence is completely absent in the β -Glc-OC₁₀C₆ lipid and only monomer fluorescence is observed, as reflected by the sharp and structured band (~ 360 – 450 nm). This result denotes that pyrene molecules are distributed among the tails of the lipid assembly and prefer to be isolated from one another by hydrophobic solvation, similar to pyrene in cyclohexane [137, 198].

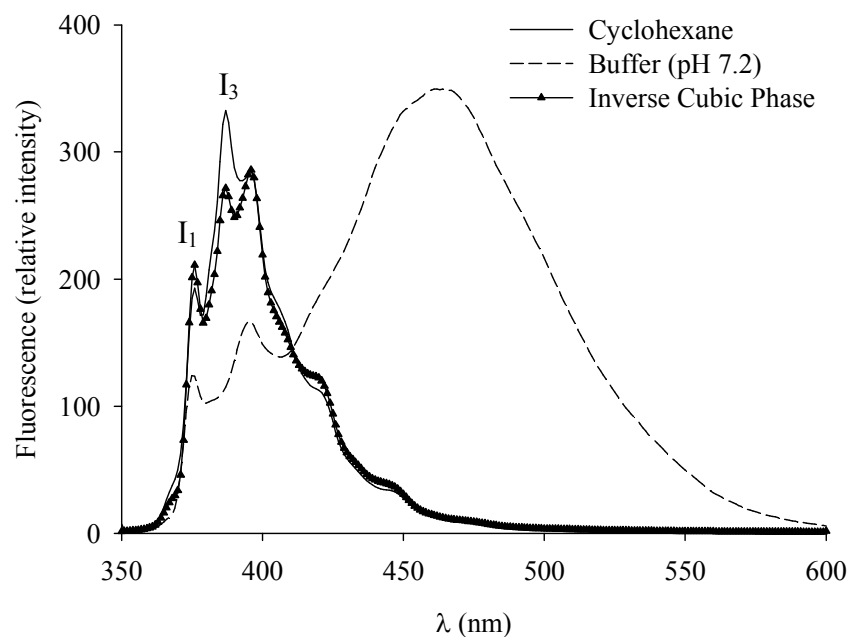


Figure 6.5: Fluorescence spectra of pyrene dissolved in cyclohexane, in buffer alone and buffer containing the inverse cubic phase of the β -Glc-OC₁₀C₆ lipid. $\lambda_{\text{ex}} = 340$ nm.

The intensity ratio of the two vibronic peaks of pyrene (I_1/I_3) with maxima at ~ 375 nm for I_1 and ~ 385 nm for I_3 (marked in Figure 6.5) clarifies the local environment of pyrene in β -Glc-OC₁₀C₆ [156, 199, 200]. An increase in the I_1/I_3 ratio indicates more polarity. The I_1/I_3 ratio in cyclohexane and buffer are reported to be 0.58 and ≥ 1.08 , respectively (see Chapter 3). In the present study, the I_1/I_3 ratio for the inverse cubic phase is calculated to be about 0.78. This ratio indicates that pyrene is in a hydrophobic environment in the tail region of the lipid. This can be attributed to the more compact interaction of the double alkyl chains of β -Glc-OC₁₀C₆ with the pyrene molecules which leads to an increase in the pyrene local hydrophobicity. Although pyrene is hydrophobic in nature, the results presented in Chapters 3 and 4 (see Figure 6.6) indicate that the pyrene molecules reside close to the polar region, yet hidden within the tail region of the lipid.

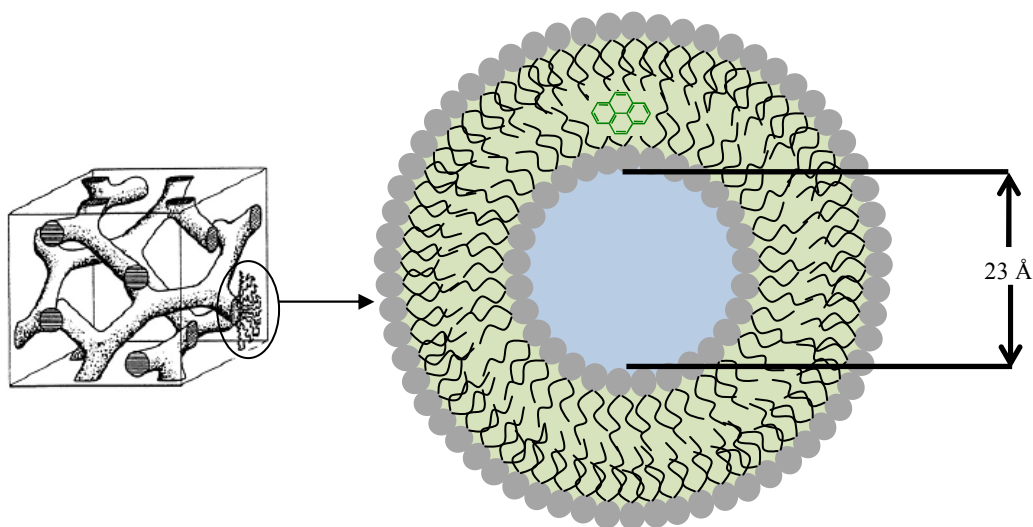


Figure 6.6: A schematic diagram showing the pyrene molecule in the hydrophobic region of the cubic $Ia3d$ phase. The continuous blue area is the aqueous channel of size 23 Å.

Table 6.2 shows the values of I_1/I_3 for the inverse cubic phase of the β -Glc-OC₁₀C₆ lipid. The I_1/I_3 ratios for the normal cubic phase of the β -Glc-OC₈ are also included for comparison. Unlike in the normal cubic phase, the presence of Trp and Trp-C₈ in the head group region of the inverse cubic phase has no effect on the I_1/I_3 values. This finding suggests that the C₈-chain of tryptophan is not embedded inside the hydrophobic region of the lipid system and hence supports the results found for the polar region. On the contrary, the slight decline in the I_1/I_3 value in the presence of Trp-C₈ for the normal cubic phase can be related to a slight increase in hydrophobicity around the pyrene molecules due to penetration of the C₈ chain in the tail region of the lipid assembly. Besides that, comparing the normal cubic phase with the inverse cubic phase, we find a drop of about 16% in the I_1/I_3 values as shown in Table 6.2 where the values are the average of three measurements. The lower polarity in the inverse cubic phase is due to the presence of the double alkyl chains of the β -Glc-OC₁₀C₆ lipid which, as mentioned above, increases the

hydrophobicity around pyrene. In the normal cubic phase of the β -Glc-OC₈ lipid, only straight alkyl chains form the tail region, and have less interaction with the pyrene molecules compared to the double alkyl chains.

Table 6.2: Fluorescence intensity ratio of the vibronic peaks of pyrene (I_1/I_3) in the normal cubic phase of the β -Glc-OC₈ lipid and the inverse cubic phase of the β -Glc-OC₁₀C₆ lipid. $\lambda_{\text{ex}} = 340$ nm.

Probe	I_1/I_3	
	Normal Cubic	Inverse Cubic
Py	0.93	0.78
Py + Trp	0.93	0.78
Py + Trp-C ₈	0.91	0.78

Table 6.3 summarizes the fluorescence lifetime measurements for pyrene in the β -Glc-OC₁₀C₆ lipid. The fluorescence decay of pyrene is best-fitted to a biexponential function. The two lifetime components in this inverse cubic phase show a short component of 0.83–1.11 ns and a long component of 4.5–4.8 ns. The presence of two decay components reflects the heterogeneity in the local environment of pyrene inside the hydrophobic region. There is no change (reduction) in the long lifetime component of pyrene upon the addition of Trp-C₈ which confirms that there is no interaction between pyrene and the C₈-chain of tryptophan as the C₈-chain does not penetrate the tail region of the lipid. A comparison between the long lifetime component of pyrene in the inverse cubic phase (4.8 ns) and that of the normal cubic phase (11.0 ns) as reported in Chapter 4 (see Table 4.4) proves that the former has more interactions between the pyrene molecules and the branched chains of β -Glc-OC₁₀C₆. Again, we do not detect any rise time for pyrene in lipid which confirms the absence of excimers in the lipid assembly.

Table 6.3: Fluorescence lifetime (ns) data of pyrene, pyrene + Trp, and pyrene + Trp-C₈ in the inverse cubic phase of the β -Glc-OC₁₀C₆ lipid.

Probe	Inverse Cubic		
	τ_1^a	τ_2^b	χ^2
Py	1.11 (0.28)	4.8 (0.72)	0.93
Py + Trp	0.83 (0.28)	4.5 (0.72)	1.04
Py + Trp-C ₈	0.93 (0.28)	4.8 (0.72)	0.95

^a Uncertainty in measurements is ± 0.05 ns. ^b Uncertainty in measurements is ± 0.1 ns. Relative contributions are listed in parentheses. Emission is detected using Schott WG-380 nm filter. $\lambda_{\text{ex}} = 340$ nm.

6.4 Conclusions

The fluorescence spectra of Trp, Trp-C₄, and Trp-C₈ embedded in the inverse cubic phase of the β -Glc-OC₁₀C₆ lipid indicate a local polarity slightly larger than that in bulk water. This is probably due to the nature of this inverse cubic phase that forces the tryptophan molecules to be close to water. This configuration may assist the transformation of water-soluble substances to the cell in the inverse cubic phase through water channels that behave as bulk water.

The fluorescence characteristics of pyrene indicate that the pyrene molecules tend to disperse among the tails of the hydrophobic region as monomers. The I_1/I_3 vibronic ratio indicates that the pyrene molecules exist in a hydrophobic environment inside the tail region of the lipid. This can be attributed to the more compact interaction of the double alkyl chains of the β -Glc-OC₁₀C₆ lipid with the pyrene molecules which increases the local hydrophobicity around pyrene. The results indicate that pyrene resides close to the polar region of the head group, yet hidden inside the tail region of the lipid. When adding Trp-C₈ to the lipid assembly, there was no measurable change in the I_1/I_3 ratio of the vibronic peaks of pyrene, nor in its lifetimes which implies that there is no interaction between the pyrene molecules and the C₈-chain of Trp-C₈ inside the tail region. This observation

indicates that the C₈-chain does not penetrate inside the tail region of the lipid. The results presented here are anticipated to help for a better understanding of the processes involving confined water in aqueous nanochannels of the lipidic cubic phase.

CHAPTER 7

CONCLUSIONS

CONCLUSIONS

The single and branched-chain GLs have been observed to exhibit normal and inverse mesophases respectively. These phases are important biologically and technologically, thus our interest to characterize them. In this thesis our investigations were divided into four themes, involving fluorescence approach, to study the microenvironment of the lipidic phases for known monoalkylated GLs (*n*-dodecyl- β -D-maltoside and *n*-octyl- β -D-glucoside). We also studied the liquid crystal phases of four branched-chain lipids derived from Guerbet alcohols using small-angle X-ray scattering to obtain their detailed structural information as well as their partial phase diagram. For one of these branched-chain lipids, which gave extensive inverse bicontinuous cubic phase of *Ia3d* space group, we also conducted similar fluorescence investigation.

The hexagonal phase formed by single chain *n*-dodecyl- β -D-maltoside (β -Mal-OC₁₂)/water system was characterized using tryptophan (including its derivatives) and pyrene as the fluorescent markers, to probe both the hydrophilic and hydrophobic regions of the self-assembly. Probing the different parts of the polar head group region using Trp, Trp-C₄ and Trp-C₈ indicates a polarity gradient. Both Trp and Trp-C₄ reside slightly away from the maltoside sugar units, and the local polarity is similar to that of simple alcohols (methanol and ethanol). For Trp-C₈, the long C₈-chain pulls the Trp moiety closer to the head groups and the local polarity approaches that of 1,4-dioxane. The reduction in polarity indicates a smooth transition from the polar domain to the hydrophobic domain, which is important for the stability of the lipid.

The temperature-induced phase transitions of hexagonal \leftrightarrow micellar and cubic \leftrightarrow lamellar in *n*-octyl- β -D-glucoside (β -Glc-OC₈)/water systems were also studied. Both hexagonal \leftrightarrow micellar and cubic \leftrightarrow lamellar temperature-induced phase transitions completely reversible, reflecting the thermodynamic equilibrium structures of their mesophases. The polarity of the head group region was estimated to be close to that of simple alcohols (methanol and ethanol) for all phases due to the glucose head group. Unlike maltose, it is too short to show any polarity gradient.

Among the important findings in both single chain GLs (β -Mal-OC₁₂ and β -Glc-OC₈) was the hydrophobic region (probed by pyrene) of the lipid self-assembly indicating the tendency of the pyrene molecules to disperse among the hydrophobic tails to avoid dimerization. By comparing the I_1/I_3 ratio in lipid to that in buffer and in cyclohexane, we conclude that pyrene must be close to the head groups. However, the hexagonal phase of β -Glc-OC₈ shows a reduced polarity in I_1/I_3 ratio compared to that of β -Mal-OC₁₂. The results imply that increasing the tail length from C₈ to C₁₂ would lead to less interaction with pyrene, which is attributed to the more random and wobbling motion of the longer alkyl tail. Besides that, in β -Glc-OC₈/water system, we observed a reduction in the I_1/I_3 ratio for the lamellar phase than in the cubic phase. The higher polarity in the cubic phase can be correlated to the nature of its interface, which curves toward the bulk water. This geometry also explains the slight reduction in polarity of the head group region compared to the other phases. Two fluorescence lifetimes were measured for Trp and its derivatives in both β -Mal-OC₁₂ and β -Glc-OC₈ lipids. The results point to a degree of flexibility of the lipid self-assembly that allows the Trp side chain to adapt two different rotamers. Again, two lifetime components were measured for pyrene in lipid which indicate a degree of heterogeneity in the pyrene local environment. Interaction

between the C₈-chain of Trp-C₈ with pyrene is observed as a slight decrease in the I₁/I₃ ratio and the pyrene lifetime.

The partial phase diagram of four branched-chain GLs namely 2-hexyl-decyl- α -D-glucopyranoside (α -Glc-OC₁₀C₆), 2-hexyl-decyl- β -D-glucopyranoside (β -Glc-OC₁₀C₆), 2-hexyl-decyl- α -D-galactopyranoside (α -Gal-OC₁₀C₆) and 2-hexyl-decyl- β -D-galactopyranoside (β -Gal-OC₁₀C₆) with a total alkyl chain length of 16 were investigated extensively by small-angle X-ray scattering (SAXS). The chain branching on the hydrocarbon region supports the formation of inverse hexagonal and bicontinuous cubic phases. The four compounds exhibit different degrees of polymorphism, an effect of anomeric and epimeric stereochemistry. The anomeric-epimeric relationship shows that the β -anomers has a stronger tendency to form inverse phases compared to α -anomers. As for the C4-epimers, the galactoside is more highly curved than in the case of the corresponding glucoside. The formation of inverse non-lamellar phases by these Guerbet branched-chain glycosides over a wide range of temperatures and water composition, has opened up many potential applications such as new drug carriers in delivery systems and for *in meso* crystallization of membrane proteins.

In continuation, the inverse bicontinuous cubic phase formed by one of these Guerbet branched-chain glycosides namely β -Glc-OC₁₀C₆/water was investigated using fluorescent probes to understand the dynamics of confined water in aqueous nanochannels of the lipidic cubic phase. The polarity of the head group in the inverse cubic phase indicate a local polarity slightly larger than that in bulk water, probably due to the nature of this inverse cubic phase that forces the Trp molecules to be close to water. This configuration may assist the transformation of water-soluble substances to the cell in the inverse cubic phase through water channels that behave as bulk water. The fluorescence characteristics of pyrene indicate that the

pyrene molecules tend to disperse among the tails of the hydrophobic region as monomers. The I_1/I_3 ratio indicates that the pyrene molecules exist in a hydrophobic environment inside the tail region of the lipid. This can be attributed to the more compact interaction of the double alkyl chains of the β -Glc-OC₁₀C₆ lipid with the pyrene molecules, thus increasing the local hydrophobicity around pyrene. There was no measurable change in the I_1/I_3 ratio of pyrene, nor in its lifetime which implies the absence of any interaction between the pyrene molecules and the C₈-chain of Trp-C₈ inside the tail region. This observation indicates that the C₈-chain of Trp does not penetrate the tail region of the lipid.

In future studies, we will further investigate the branched-chain GLs which have exhibited the inverse non-lamellar lyotropic liquid crystalline phases. In particular, the inverse bicontinuous cubic phases have shown potential for use in *in meso* crystallization of membrane proteins. The choice of lipids used for the formation of cubic phase remains small in which monoolein is the most common lipid for *in meso* crystallization. Thus the inverse bicontinuous cubic phase formed by these Guerbet branched-chain glycosides makes them potential lipids to be used in membrane protein crystallization.

APPENDIX A: DIFFERENTIAL SCANNING CALORIMETRY SPECTRA

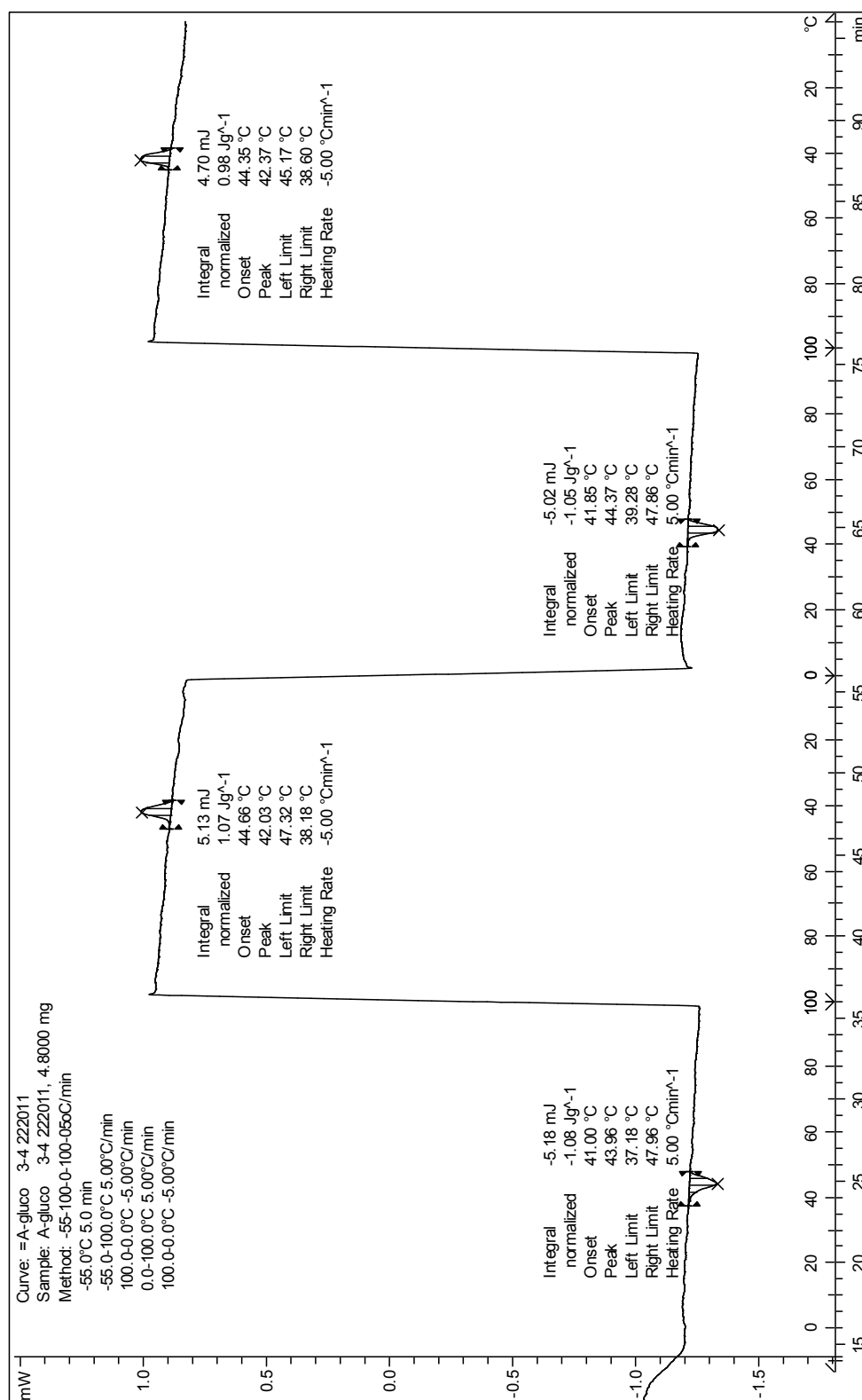


Figure A1: DSC scans for α -Glc-OC₁₀C₆ at heating and cooling rates of 5 °C/min.

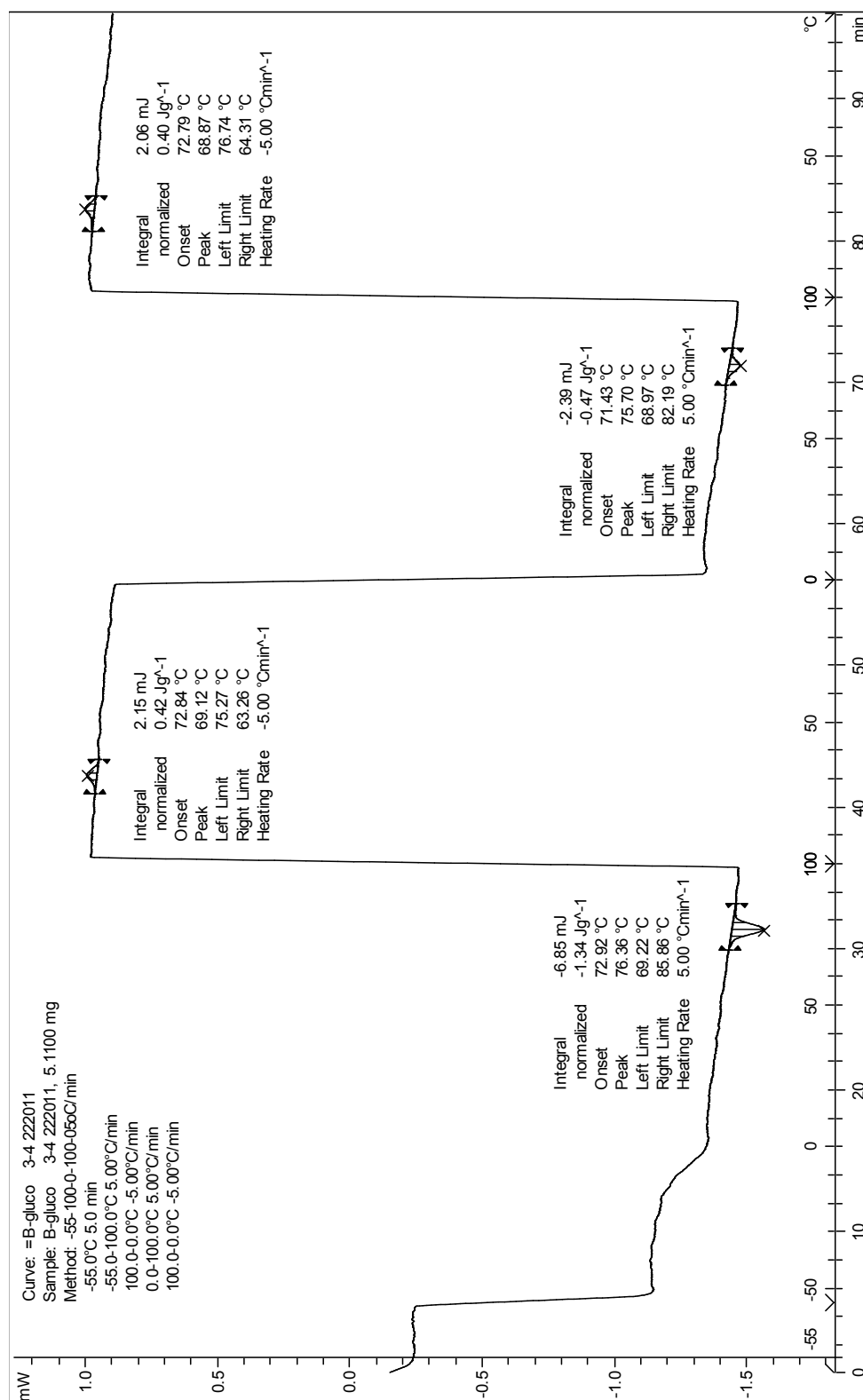


Figure A2: DSC scans for β -Glc-OC₁₀C₆ at heating and cooling rates of 5 °C/min.

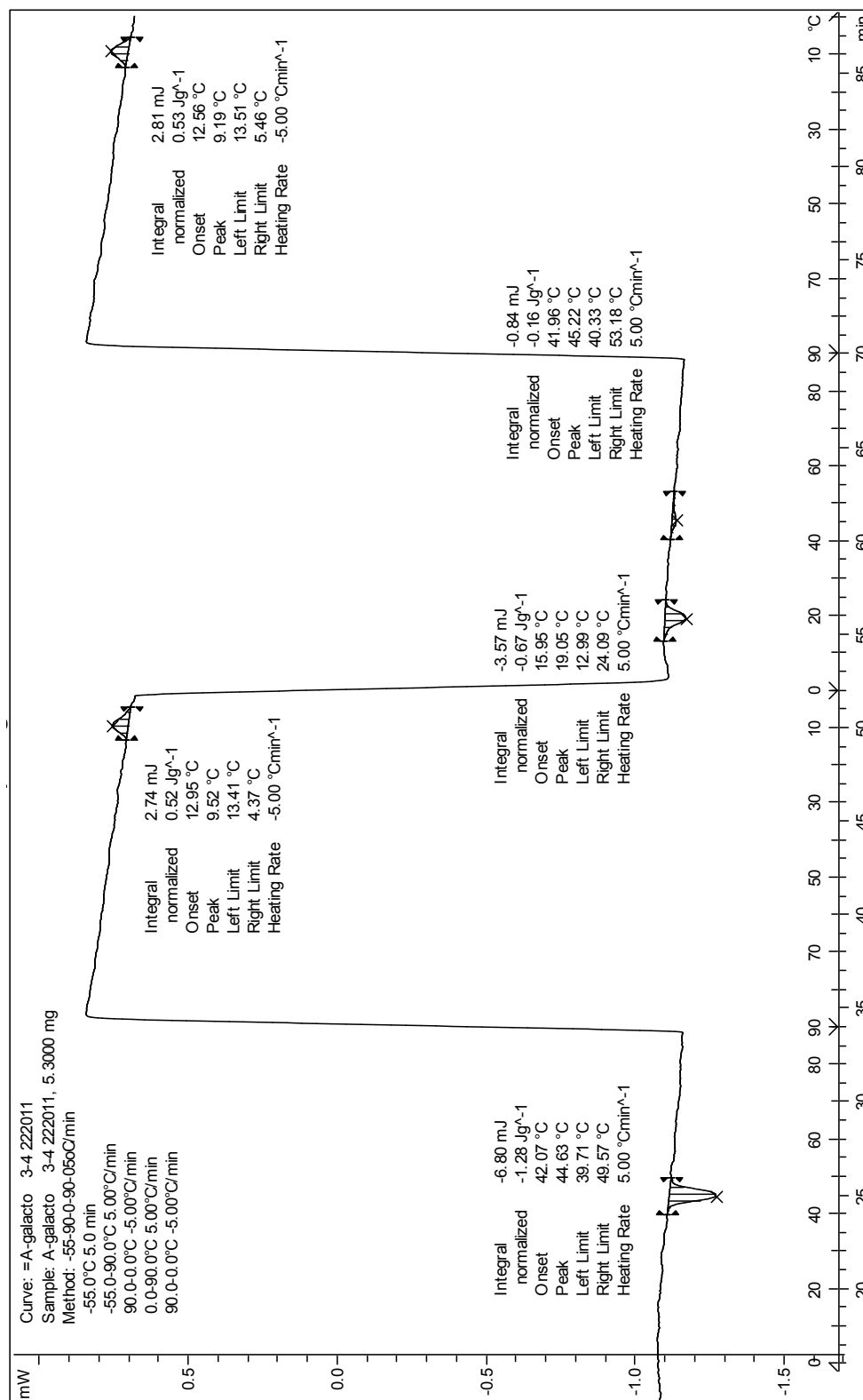


Figure A3: DSC scans for α -Gal-OC₁₀C₆ at heating and cooling rates of 5 °C/min.

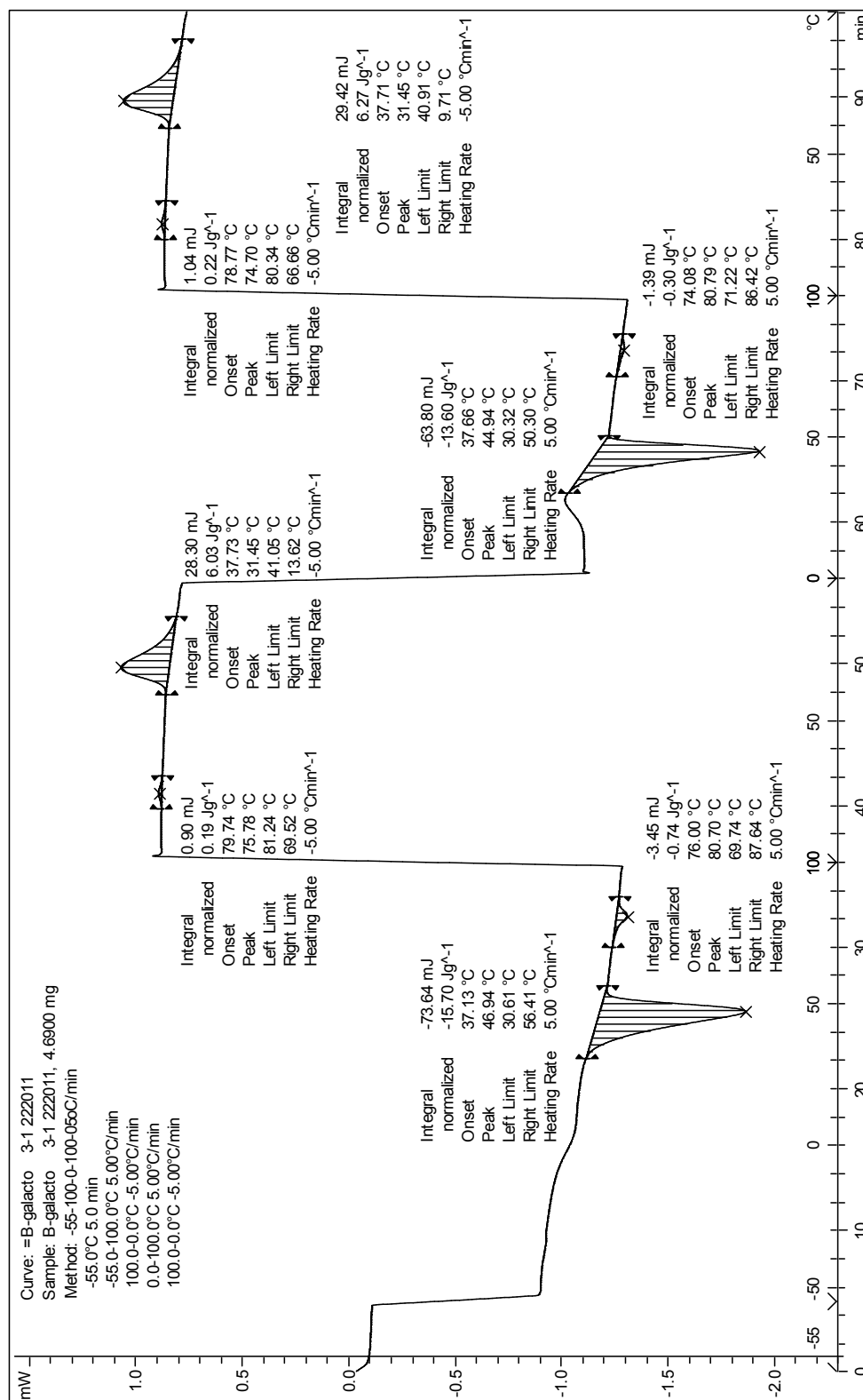


Figure A4: DSC scans for β -Gal-OC₁₀C₆ at heating and cooling rates of 5 °C/min.

APPENDIX B: SMALL-ANGLE X-RAY SCATTERING DATA

Table B1: Lattice parameter of α -Glc-OC₁₀C₆ as a function of water content and temperature.

Water Content (% (w/w))	Temperature (°C)	Lattice parameter (Å)			
		L	Q _{II} ^G	Q _{II} ^D	L ₂
0	10	24.0			
0	12	24.0			
0	18	23.9			
0	24	23.9			
0	30	24.4			
0	37	24.4			
0	44	23.8			
0	50				*
0	55				*
0	62				*
11.0	10	26.9			
11.0	12	26.9			
11.0	18	26.8			
11.0	24	26.8			
11.0	30	26.7			
11.0	37	26.7			
11.0	44	26.4			
11.0	50	26.1			
11.0	55	25.9			
11.0	62	26.0			
19.0	10	28.4	78.4		
19.0	12	28.4	78.2		
19.0	18	28.3	77.2		
19.0	24	28.2	76.9		
19.0	30	28.2	76.6		
19.0	37	28.2	76.7		
19.0	44		77.3		
19.0	50		76.7		
19.0	55		76.3		
19.0	62		75.3		
32.5	10		92.6	59.7	
32.5	12		92.2	59.4	
32.5	18		91.9	59.0	

Table B1 (continued)

Water Content (% (w/w))	Temperature (°C)	Lattice parameter (Å)			
		L	Q _{II} ^G	Q _{II} ^D	L ₂
32.5	24		92.0	58.8	
32.5	30		92.5	59.0	
32.5	37		91.7	59.0	
32.5	44		92.0	58.3	
32.5	50		91.4	58.0	
32.5	55		90.1	57.6	
32.5	62		89.2	56.8	
39.8	10			62.0	
39.8	12			62.0	
39.8	18			61.8	
39.8	24			61.6	
39.8	30			61.5	
39.8	37			61.1	
39.8	44			60.4	
39.8	50			59.8	
39.8	55			59.2	
39.8	62			r.d.	
50.2	10			61.8	
50.2	12			61.8	
50.2	18			61.5	
50.2	24			61.3	
50.2	30			61.3	
50.2	37			60.9	
50.2	44			60.6	
50.2	50			60.2	
50.2	55			59.7	
50.2	62			58.9	
60.0	10			61.7	
60.0	12			61.7	
60.0	18			61.5	
60.0	24			61.3	
60.0	30			61.2	
60.0	37			61.0	
60.0	44			60.6	
60.0	50			60.3	
60.0	55			60.0	
60.0	62			59.4	

Table B1 (continued)

Water Content (% (w/w))	Temperature (°C)	Lattice parameter (Å)			
		L	Q_{II}^G	Q_{II}^D	L ₂
70.9	10			61.4	
70.9	12			61.4	
70.9	18			61.1	
70.9	24			61.0	
70.9	30			61.1	
70.9	37			60.8	
70.9	44			60.6	
70.9	50			60.2	
70.9	55			59.9	
70.9	62			59.5	
80.0	10			60.2	
80.0	12			60.0	
80.0	18			59.6	
80.0	24			59.2	
80.0	30			58.9	
80.0	37			58.3	
80.0	44			60.5	
80.0	50			60.1	
80.0	55			59.5	
80.0	62			58.8	

* denotes L₂ phase is detected. r.d. denotes radiation damaged.

Error in lattice parameter measurements is < 0.1 Å.

Table B2: Lattice parameter of α -Glc-OC₁₀C₆ as a function of water content and temperature.

Water Content (% (w/w))	Temperature (°C)	Lattice parameter (Å)			
		H _{II}	Q _{II} ^G	Q _{II} ^D	L ₂
0	10	28.7	61.1		
0	12	28.7	61.1		
0	18	28.7	61.1		
0	24	28.7			
0	30	28.7			
0	37	29.1			
0	44	28.5			
0	50	28.5			
0	55	28.5			
0	62	28.5			
11.9	10		71.3		
11.9	12		71.3		
11.9	18		71.1		
11.9	24		71.2		
11.9	30		71.2		
11.9	37		71.2		
11.9	44		70.4		
11.9	50		70.0		
11.9	55		69.7		
11.9	62		69.2		
20.6	10		77.5		
20.6	12		77.5		
20.6	18		76.3		
20.6	24		75.8		
20.6	30		72.7		
20.6	37		70.9		
20.6	44		78.8		
20.6	50		77.4		
20.6	55		76.0		
20.6	62		74.1		
29.8	10		87.2	55.4	
29.8	12		87.1	55.3	
29.8	18		86.8	55.3	
29.8	24		86.7	55.1	
29.8	30		86.8	55.1	
29.8	37		86.6	55.0	

Table B2 (continued)

Water Content (% (w/w))	Temperature (°C)	Lattice parameter (Å)			
		H _{II}	Q _{II} ^G	Q _{II} ^D	L ₂
29.8	44		86.1	55.0	
29.8	50		85.6		
29.8	55		84.7		
29.8	62		82.9		
40.1	10		87.5	55.8	
40.1	12		87.5	55.7	
40.1	18		87.4	55.5	
40.1	24		87.3	55.5	
40.1	30		87.4	55.7	
40.1	37		87.3	55.6	
40.1	44		87.0	55.3	
40.1	50		86.8	55.2	
40.1	55		r.d.	r.d.	
40.1	62		r.d.	r.d.	
49.8	10		87.7	55.9	
49.8	12		87.6	55.9	
49.8	18		87.5	55.7	
49.8	24		87.5	55.7	
49.8	30		87.6	55.6	
49.8	37		87.6	55.6	
49.8	44		87.3	55.6	
49.8	50		86.2	55.6	
49.8	55		r.d.	r.d.	
49.8	62		r.d.	r.d.	
59.8	10		87.7	55.9	
59.8	12		87.7	55.9	
59.8	18		87.7	55.8	
59.8	24		87.7	55.8	
59.8	30		87.7	55.8	
59.8	37		87.5	55.7	
59.8	44		87.6	55.8	
59.8	50		86.2	55.7	
59.8	55		r.d.	r.d.	
59.8	62		r.d.	r.d.	
69.8	10		87.5	55.9	
69.8	12		87.6	55.8	
69.8	18		87.6	55.8	

Table B2 (continued)

Water Content (% (w/w))	Temperature (°C)	Lattice parameter (Å)			
		H _{II}	Q _{II} ^G	Q _{II} ^D	L ₂
69.8	24		87.6	55.8	
69.8	30		87.8	55.9	
69.8	37		87.6	55.7	
69.8	44		87.5	55.7	
69.8	50		r.d.	r.d.	
69.8	55		r.d.	r.d.	
69.8	62		r.d.	r.d.	
80.3	10		87.6	55.8	
80.3	12		87.5	55.9	
80.3	18		87.3	55.8	
80.3	24		87.2	55.8	
80.3	30		87.7		
80.3	37		87.5		
80.3	44		87.5	55.7	
80.3	50		r.d.	r.d.	
80.3	55		r.d.	r.d.	
80.3	62		r.d.	r.d.	

r.d. denotes radiation damaged.

Error in lattice parameter measurements is < 0.1 Å.

Table B3: Lattice parameter of -Gal-OC₁₀C₆ as a function of water content and temperature.

Water Content (% (w/w))	Temperature (°C)	Lattice parameter (Å)			
		H _{II}	Q _{II} ^G	Q _{II} ^D	L ₂
0	10		60.5		
0	12		60.5		
0	18		60.4		
0	24		60.4		
0	30		61.6		
0	37		61.0		
0	44		60.3		
0	50		60.2		
0	55				*
0	62				*
11.2	10	28.9	60.5		
11.2	12	29.0	75.8		
11.2	18	29.0	75.5		
11.2	24	29.0	74.0		
11.2	30		70.5		
11.2	37		69.8		
11.2	44		r.d.		
11.2	50		r.d.		
11.2	55		r.d.		
11.2	62		r.d.		
21.7	10		82.2		
21.7	12		82.1		
21.7	18		81.8		
21.7	24		81.5		
21.7	30		80.9		
21.7	37		80.0		
21.7	44		79.9		
21.7	50		77.4		
21.7	55		r.d.		
21.7	62		r.d.		
30.3	10		91.2	58.5	
30.3	12		91.3	58.4	
30.3	18		90.4	58.1	
30.3	24		89.9	58.2	
30.3	30		89.5	58.6	
30.3	37		89.3	57.8	

Table B3 (continued)

Water Content (% (w/w))	Temperature (°C)	Lattice parameter (Å)			
		H _{II}	Q _{II} ^G	Q _{II} ^D	L ₂
30.3	44		87.7	56.2	
30.3	50		r.d.	r.d.	
30.3	55		r.d.	r.d.	
30.3	62		r.d.	r.d.	
40.3	10			60.1	
40.3	12			60.0	
40.3	18			59.6	
40.3	24			59.3	
40.3	30			59.1	
40.3	37			58.4	
40.3	44			58.0	
40.3	50			57.5	
40.3	55			57.1	
40.3	62			r.d.	
49.9	10			60.4	
49.9	12			60.3	
49.9	18			59.7	
49.9	24			59.3	
49.9	30			59.1	
49.9	37			58.5	
49.9	44			57.9	
49.9	50			57.4	
49.9	55			56.9	
49.9	62			r.d.	
60.2	10			60.0	
60.2	12			59.9	
60.2	18			59.6	
60.2	24			59.4	
60.2	30			59.2	
60.2	37			58.5	
60.2	44			58.0	
60.2	50			57.4	
60.2	55			57.0	
60.2	62			r.d.	
70.2	10			60.1	
70.2	12			60.0	
70.2	18			59.6	

Table B3 (continued)

Water Content (% (w/w))	Temperature (°C)	Lattice parameter (Å)			
		H _{II}	Q _{II} ^G	Q _{II} ^D	L ₂
70.2	24			59.3	
70.2	30			59.1	
70.2	37			58.4	
70.2	44			57.9	
70.2	50			57.4	
70.2	55			57.0	
70.2	62			r.d.	
80.1	10			59.9	
80.1	12			59.8	
80.1	18			59.5	
80.1	24			59.2	
80.1	30			59.0	
80.1	37			58.3	
80.1	44			57.9	
80.1	50			57.5	
80.1	55			57.1	
80.1	62			56.8	

* denotes L₂ phase is detected. r.d. denotes radiation damaged.
 Error in lattice parameter measurements is < 0.1 Å.

Table B4: Lattice parameter of β -Gal-OC₁₀C₆ as a function of water content and temperature.

Water Content (% (w/w))	Temperature (°C)	Lattice parameter (Å)			
		H _{II}	Q _{II} ^G	Q _{II} ^D	L ₂
0	25	29.1			
0	30	29.2			
0	37	29.2			
0	44	29.3			
0	50	29.3	66.0		
0	55	29.3	65.6		
0	60	29.3	65.4		
0	65	29.4	65.0		
5	25	29.1			
5	30	29.1			
5	37	29.1			
5	44	29.2	72.6		
5	50	29.2	69.2		
5	55	29.3	67.2		
5	60	29.3	65.9		
5	65	29.3	64.9		
10	25	29.1			
10	30	29.1			
10	37	29.1			
10	44	29.2	67.9		
10	50	29.2	64.9		
10	55	29.3	64.1		
10	60	29.3	64.4		
10	65	r.d.	r.d.		
15	25	29.0			
15	30	29.1			
15	37	29.1			
15	44	29.2			
15	50	29.2	73.5		
15	55	29.2	66.8		
15	60	29.3	65.1		
15	65	r.d.	r.d.		
20	25	29.1			
20	30	29.1			
20	37	29.1			
20	44	29.2			

Table B4 (continued)

Water Content (% (w/w))	Temperature (°C)	Lattice parameter (Å)			
		H _{II}	Q _{II} ^G	Q _{II} ^D	L ₂
20	50	29.2	82.3		
20	55	29.2	73.1		
20	60	29.3	66.6		
20	65	r.d.	r.d.		
25	25	29.0			
25	30	29.1			
25	37	29.1			
25	44	29.2			
25	50	29.2			
25	55	r.d.			
25	60	r.d.			
25	65	r.d.			
30	25	29.1			
30	30	29.1			
30	37	29.1			
30	44	29.2			
30	50	29.2			
30	55	29.3		62.1	
30	60	29.3		61.5	
30	65	r.d.		r.d.	
35	25	29.1			
35	30	29.1			
35	37	29.1			
35	44	29.2			
35	50	29.2			
35	55	29.2		61.9	
35	60	29.3		60.9	
35	65	r.d.		r.d.	
40	25	29.0			
40	30	29.1			
40	37	29.1			
40	44	29.2			
40	50	29.2			
40	55	29.2		61.9	
40	60	29.3		60.7	
40	65	r.d.		r.d.	
50	25	29.0			

Table B4 (continued)

Water Content (% (w/w))	Temperature (°C)	Lattice parameter (Å)			
		H _{II}	Q _{II} ^G	Q _{II} ^D	L ₂
50	30	29.1			
50	37	29.1			
50	44	29.2			
50	50	29.2			
50	55	29.2		62.0	
50	60	29.3		61.5	
50	65	r.d.		r.d.	
60	25	29.0			
60	30	29.1			
60	37	29.1			
60	44	29.1			
60	50	29.2			
60	55	r.d.			
60	60	r.d.			
60	65	r.d.			
70	25	29.1			
70	30	29.1			
70	37	29.1			
70	44	29.2			
70	50	29.2			
70	55	29.3		62.5	
70	60	29.3		61.9	
70	65			61.6	
80	25	29.0			
80	30	29.1			
80	37	29.1			
80	44	29.2			
80	50	29.2			
80	55	29.2		62.6	
80	60	29.3		61.9	
80	65			61.8	

r.d. denotes radiation damaged.

Error in lattice parameter measurements is < 0.1 Å.

REFERENCES

- [1] Lipowsky, R. *Nature* **1991**, 349, 475–481.
- [2] *The Structure of Biological Membrane*; 2nd ed.; Yeagle, P. L., Ed.; CRC Press: Boca Raton, 2005.
- [3] Favor, L. J. *Eukaryotic and Prokaryotic Cell Structures: Understanding Cells With and Without a Nucleus*; Rosen Publishing Group Inc.: New York, 2005.
- [4] Stimola, A. *Cell Biology*; Rosen Publishing Group Inc.: New York, 2011.
- [5] Bloomfield, M. M.; Stephens, L. J. *Chemistry and the Living Organism*; 6th ed.; John Wiley & Sons Inc.: New York, 1996.
- [6] Goodby, J.; Görtz, V.; Cowling, S.; Mackenzie, G.; Martin, P.; Plusquellec, D.; Benvegnu, T.; Boullanger, P.; Lafont, D.; Queneau, Y.; Chambert, S.; Fitremann, J. *Chem. Soc. Rev.* **2007**, 36, 1971–2032.
- [7] Barraud, P.; Stott, S. R. W. In *Glycolipids: New Research*; Sasaki, D., Ed.; Nova Science Publishers Inc.: New York, 2008; pp 79–98.
- [8] Singh, M. K.; Jayaraman, N. *J. Indian Inst. Sci.* **2009**, 89, 113–135.
- [9] Goodby, J. W. *Liq. Cryst.* **1998**, 24, 25–38.
- [10] Dumoulin, F.; Lafont, D.; Boullanger, P.; Mackenzie, G.; Mehl, G. H.; Goodby, J. W. *J. Am. Chem. Soc.* **2002**, 124, 13737–13748.
- [11] Hinwood, B. G. *A Textbook of Science for the Health Professions*; 2nd ed.; Nelson Thornes Ltd.: Cheltenham, 2001.
- [12] Hinz, H.-J.; Kutenreich, H.; Meyer, R.; Renner, M.; Freund, R.; Koynova, R.; Boyanov, A.; Tenchov, B. *Biochemistry* **1991**, 30, 5125–5138.
- [13] Hashim, R.; Sugimura, A.; Minamikawa, H.; Heidelberg, T. *Liq. Cryst.* **2011**, 39, 1–17.
- [14] Seddon, J. M.; Ces, O.; Templer, R. H.; Mannock, D. A.; McElhaney, R. N. *Mol. Cryst. Liq. Cryst.* **2003**, 402, 77–84.
- [15] Hato, M.; Minamikawa, H.; Tamada, K.; Baba, T.; Tanabe, Y. *Adv. Colloid Interface Sci.* **1999**, 80, 233–270.
- [16] Metzler, D. E. *Biochemistry: The Chemical Reactions of Living Cells*; Harcourt/Academic Press: Massachusetts, 2001.
- [17] Cyberlipid. *Glycosides of Fatty Alcohols*. <http://www.cyberlipid.org/glycolip/glyl0062.htm> (accessed 15 August 2012).
- [18] Makita, A.; Taniguchi, N. In *Glycolipids*; Wiegandt, H., Ed.; Elsevier Science Publishers: Amsterdam, 1985; Vol. 10; pp 1–99.
- [19] Vill, V.; Hashim, R. *Curr. Opin. Colloid Interface Sci.* **2002**, 7, 395–409.
- [20] Finean, J. B.; Michell, R. H. In *Membrane Structure*; Finean, J. B., Michell, R. H., Eds.; Elsevier/North-Holland Biomedical Press: Amsterdam, 1981; Vol. 1; pp 1–36.

- [21] Ke, B. *Photosynthesis, Photobiochemistry and Photobiophysics*; Kluwer Academic Publishers: Dordrecht, 2001; Vol. 10.
- [22] Hemming, F. W. In *Glycolipids*; Wiegandt, H., Ed.; Elsevier Science Publishers: Amsterdam, 1985; Vol. 10; pp 261–305.
- [23] Bonicelli, M. G.; Ceccaroni, G. F.; La Mesa, C. *Colloid Polym. Sci.* **1998**, *276*, 109–116.
- [24] Minamikawa, H.; Hato, M. *Chem. Phys. Lipids* **2005**, *134*, 151–160.
- [25] Drummond, C. J.; Fong, C. *Curr. Opin. Colloid Interface Sci.* **2000**, *4*, 449–456.
- [26] Shah, J. C.; Sadhale, Y.; Chilukuri, D. M. *Adv. Drug Delivery Rev.* **2001**, *47*, 229–250.
- [27] Ahmad, N.; Ramsch, R.; Esquena, J.; Solans, C.; Tajuddin, H. A.; Hashim, R. *Langmuir* **2012**, *28*, 2395–2403.
- [28] von Minden, H. M.; Morr, M.; Milkereit, G.; Heinz, E.; Vill, V. *Chem. Phys. Lipids* **2002**, *114*, 55–80.
- [29] Hato, M. *Curr. Opin. Colloid Interface Sci.* **2001**, *6*, 268–276.
- [30] von Rybinski, W. *Curr. Opin. Colloid Interface Sci.* **1996**, *1*, 587–597.
- [31] Fischer, E. *Ber. Dtsch. Chem. Ges.* **1895**, *28*, 1973–1974.
- [32] Schmid, K.; Tesmann, H. In *Detergency of Specialty Surfactants*; Friedli, F. E., Ed.; Marcel Dekker Inc.: New York, 2001; Vol. 98; pp 1–70.
- [33] Teoh, T. C.; Heidelberg, T.; Hashim, R.; Gary, S. *Liq. Cryst.* **2007**, *34*, 267–281.
- [34] Manickam Achari, V. ; Nguan, H. S.; Heidelberg, T.; Bryce, R. A.; Hashim, R. *J. Phys. Chem. B* **2012**, *116*, 11626–11634.
- [35] Sakya, P.; Seddon, J. M. *Liq. Cryst.* **1997**, *23*, 409–424.
- [36] Boyd, B. J.; Drummond, C. J.; Krodziewska, I.; Grieser, F. *Langmuir* **2000**, *16*, 7359–7367.
- [37] Nilsson, F.; Söderman, O.; Johansson, I. *J. Colloid Interface Sci.* **1998**, *203*, 131–139.
- [38] Mannock, D. A.; Lewis, R. N.; McElhaney, R. N.; Akiyama, M.; Yamada, H.; Turner, D. C.; Gruner, S. M. *Biophys. J.* **1992**, *63*, 1355–1368.
- [39] Hato, M.; Minamikawa, H.; Salkar, R. A.; Matsutani, S. *Langmuir* **2002**, *18*, 3425–3429.
- [40] Milkereit, G.; Gerber, S.; Brandenburg, K.; Morr, M.; Vill, V. *Chem. Phys. Lipids* **2005**, *135*, 1–14.
- [41] Milkereit, G.; Brandenburg, K.; Gerber, S.; Koch, M. H. J.; Morr, M.; Andrä, J.; Seydel, U.; Vill, V. *Chem. Phys. Lipids* **2005**, *135*, 15–26.
- [42] Minamikawa, H.; Hato, M. *Langmuir* **1997**, *13*, 2564–2571.
- [43] Minamikawa, H.; Murakami, T.; Hato, M. *Chem. Phys. Lipids* **1994**, *72*, 111–118.
- [44] Fischer, E.; Helferich, B. *Liebigs Ann. Chem.* **1911**, *383*, 68–91.
- [45] Koch, R. *Mitt. K. Gesundh.* **1884**, *2*, 1–88.

- [46] Singh, M. K.; Jayaraman, N.; Rao, D.; Prasad, S. K. *Chem. Phys. Lipids* **2008**, *155*, 90–97.
- [47] Milkereit, G.; Morr, M.; Thiem, J.; Vill, V. *Chem. Phys. Lipids* **2004**, *127*, 47–63.
- [48] Corti, M.; Cant, L.; Brocca, P.; Del Favero, E. *Curr. Opin. Colloid Interface Sci.* **2007**, *12*, 148–154.
- [49] Köberl, M.; Schöppe, A.; Hinz, H. J.; Rapp, G. *Chem. Phys. Lipids* **1998**, *95*, 59–82.
- [50] Goodby, J. W.; Gray, G. W.; Spiess, H. W.; Vill, V. *Handbook of Liquid Crystals*; Wiley-VCH: Weinheim, 1998; Vol. 2.
- [51] Friedel, G. *Ann. Phys* **1922**, *18*, 273–474.
- [52] de Gennes, P. G.; Prost, J. *The Physics of Liquid Crystals*; 2nd ed.; Oxford University Press: Oxford, 1993.
- [53] Chandrasekhar, S. *Liquid Crystals*; 2nd ed.; Cambridge University Press: Cambridge, 1992.
- [54] Muñoz, J.; Alfaro, M. *Gras. Aceit.* **2000**, *51*, 6–25.
- [55] Meier, G.; Sackmann, E.; Grabmaier, J. G. *Applications of Liquid Crystals*; Springer Verlag: Berlin, 1975.
- [56] Collings, P. J.; Hird, M. *Introduction to Liquid Crystals: Chemistry and Physics*; Taylor & Francis Ltd.: London, 1997.
- [57] Collings, P. J. *Liquid Crystals: Nature's Delicate Phase of Matter*; 2nd ed.; Princeton University Press: New Jersey, 2002.
- [58] Barón, M. *Pure Appl. Chem.* **2001**, *73*, 845–895.
- [59] Tschierske, C. *Curr. Opin. Colloid Interface Sci.* **2002**, *7*, 355–370.
- [60] Dierking, I. *Textures of Liquid Crystals*; Wiley-VCH: Weinheim, 2003.
- [61] Kirsch, P.; Bremer, M. *Angew. Chem. Int. Ed.* **2000**, *39*, 4216–4235.
- [62] Hoogboom, J.; Rasing, T.; Rowan, A. E.; Nolte, R. J. M. *J. Mater. Chem.* **2006**, *16*, 1305–1314.
- [63] Jakli, A.; Saupe, A. *One- and Two-Dimensional Fluids: Properties of Smectic, Lamellar and Columnar Liquid Crystals*; Taylor & Francis Group: Boca Raton, 2006.
- [64] Domanski, A. W.; Wolinski, T. R.; Borys, W. *Proc. SPIE: Fiber Optic and Laser Sensors VIII* **1990**, *1169*, 573–581.
- [65] Winterbottom, D. A.; Narayanaswamy, R.; Raimundo Jr., I. M. *Sens. Actuators B* **2003**, *90*, 52–57.
- [66] Singh, S.; Dunmur, D. A. *Liquid Crystals Fundamentals*; World Scientific Pub. Co. Pte. Ltd.: Singapore, 2002.
- [67] Lemaire, V.; da Silva Filho, D. A.; Coropceanu, V.; Lehmann, M.; Geerts, Y.; Piris, J.; Debije, M. G.; van de Craats, A. M.; Senthilkumar, K.; Siebbeles, L. D. A.; Warman, J. M.; Brédas, J.-L.; Cornil, J. *J. Am. Chem. Soc.* **2004**, *126*, 3271–3279.
- [68] Xiao, S.; Myers, M.; Miao, Q.; Sanaur, S.; Pang, K.; Steigerwald, M. L.; Nuckolls, C. *Angew. Chem. Int. Ed.* **2005**, *44*, 7390–7394.

- [69] Schmidt-Mende, L.; Fechtenkötter, A.; Müllen, K.; Moons, E.; Friend, R. H.; MacKenzie, J. D. *Science* **2001**, *293*, 1119–1122.
- [70] Collings, P. J. In *Handbook of Liquid Crystal Research*; Collings, P. J., Patel, J. S., Eds.; Oxford University Press: New York, 1997; pp 99–124.
- [71] Hamley, I. W. *Introduction to Soft Matter: Synthetic and Biological Self-Assembling Materials*; John Wiley & Sons Ltd.: Chichester, 2007.
- [72] Klein, K. *Cosmet. Toiletries* **2002**, *117*, 30–34.
- [73] Boyd, B. J.; Whittaker, D. V.; Khoo, S.-M.; Davey, G. *Int. J. Pharm.* **2006**, *309*, 218–226.
- [74] Guo, C.; Wang, J.; Cao, F.; Lee, R. J.; Zhai, G. *Drug Discov. Today* **2010**, *15*, 1032–1040.
- [75] Engström, S.; Nordén, T. P.; Nyquist, H. *Eur. J. Pharm. Sci.* **1999**, *8*, 243–254.
- [76] Larsson, K.; Dejmek, P. In *Food Emulsions*; 2nd ed.; Larsson, K., Friberg, S. E., Eds.; Marcel Dekker: New York, 1990; pp 97–127.
- [77] Huang, N. M.; Shahidan, R.; Khiew, P. S.; Peter, L.; Kan, C. S. *Colloids Surf. A* **2004**, *247*, 55–60.
- [78] Borshchevskiy, V.; Moiseeva, E.; Kuklin, A.; Büldt, G.; Hato, M.; Gordeliy, V. *J. Cryst. Growth* **2010**, *312*, 3326–3330.
- [79] Burducea, G. *Romanian Rep. Phys.* **2004**, *56*, 66–86.
- [80] Seddon, J. M.; Robins, J.; Gulik-Krzywicki, T.; Delacroix, H. *Phys. Chem. Chem. Phys.* **2000**, *2*, 4485–4493.
- [81] Tresset, G. *PMC Biophys.* **2009**, *2*, 3–28.
- [82] Seddon, J. M.; Templer, R. H. In *Structure and Dynamics of Membranes*; Lipowsky, R., Sackmann, E., Eds.; Elsevier SPC: Amsterdam, 1995; Vol. 1; pp 99–149.
- [83] Garstecki, P.; Holyst, R. *J. Chem. Phys.* **2001**, *115*, 1095–1099.
- [84] Garstecki, P.; Holyst, R. *Langmuir* **2002**, *18*, 2519–2528.
- [85] Squires, A. M.; Templer, R. H.; Seddon, J. M.; Woenkhaus, J.; Winter, R.; Narayanan, T.; Finet, S. *Phys. Rev. E* **2005**, *72*, 011502.
- [86] Squires, A. M.; Templer, R. H.; Seddon, J. M. *Langmuir* **2002**, *18*, 7384–7392.
- [87] Nollert, P.; Royant, A.; Pebay-Peyroula, E.; Landau, E. M. *FEBS Lett.* **1999**, *457*, 205–208.
- [88] Gulik, A.; Delacroix, H.; Kirschner, G.; Luzzati, V. *J. Phys. II France* **1995**, *5*, 445–464.
- [89] Sakya, P.; Seddon, J. M.; Templer, R. H.; Mirkin, R. J.; Tiddy, G. J. T. *Langmuir* **1997**, *13*, 3706–3714.
- [90] Luzzati, V.; Vargas, R.; Mariani, P.; Gulik, A.; Delacroix, H. *J. Mol. Biol.* **1993**, *229*, 540–551.
- [91] Seddon, J. M.; Zeb, N.; Templer, R. H.; McElhaney, R. N.; Mannock, D. A. *Langmuir* **1996**, *12*, 5250–5253.

- [92] Diele, S. *Curr. Opin. Colloid Interface Sci.* **2002**, 7, 333–342.
- [93] Hamley, I. W. *Introduction to Soft Matter: Polymers, Colloids, Amphiphiles and Liquid Crystals*; John Wiley & Sons Ltd.: England, 2000.
- [94] Sagnella, S. M.; Conn, C. E.; Krodziewska, I.; Drummond, C. J. *Soft Matter* **2009**, 5, 4823–4834.
- [95] von Minden, H. M.; Brandenburg, K.; Seydel, U.; Koch, M. H. J.; Garamus, V.; Willumeit, R.; Vill, V. *Chem. Phys. Lipids* **2000**, 106, 157–179.
- [96] Nilsson, F.; Söderman, O.; Johansson, I. *Langmuir* **1996**, 12, 902–908.
- [97] Karukstis, K. K.; Duim, W. C.; Van Hecke, G. R.; Hara, N. *J. Phys. Chem. B* **2012**, 116, 3816–3822.
- [98] Sivasankar, B. *Engineering Chemistry*; Tata McGraw-Hill Pub. Co. Ltd.: New Delhi, 2008.
- [99] Briggs, J.; Caffrey, M. *Biophys. J.* **1994**, 66, 573–587.
- [100] Briggs, J.; Caffrey, M. *Biophys. J.* **1994**, 67, 1594–1602.
- [101] Israelachvili, J. N. *Intermolecular and Surface Forces*; 2nd ed.; Academic Press: London, 1991.
- [102] Nagarajan, R. *Langmuir* **2001**, 18, 31–38.
- [103] Seddon, J. M. *Biochim. Biophys. Acta* **1990**, 1031, 1–69.
- [104] Tolédano, P.; Dmitriev, V. *Reconstructive Phase Transitions: In Crystals and Quasicrystals*; World Scientific Pub. Co. Inc.: Singapore, 1996.
- [105] Singh, S. *Phys. Rep.* **2000**, 324, 107–269.
- [106] Maier, W.; Saupe, A. *Naturforsch. A* **1959**, 14, 882–889.
- [107] Maier, W.; Saupe, A. *Naturforsch. A* **1960**, 15, 287–292.
- [108] Stubenrauch, C. *Curr. Opin. Colloid Interface Sci.* **2001**, 6, 160–170.
- [109] Hato, M.; Minamikawa, H. *Langmuir* **1996**, 12, 1658–1665.
- [110] Sabah, K.; Heidelberg, T.; Hashim, R. *Carbohydr. Res.* **2011**, 346, 891–896.
- [111] Cook, A. G.; Wardell, J. L.; Imrie, C. T. *Chem. Phys. Lipids* **2011**, 164, 118–124.
- [112] Sakya, P.; Seddon, J. M.; Templer, R. H. *J. Phys. II France* **1994**, 4, 1311–1331.
- [113] Gerber, S.; Wulf, M.; Milkereit, G.; Vill, V.; Howe, J.; Roessle, M.; Garidel, P.; Gutsman, T.; Brandenburg, K. *Chem. Phys. Lipids* **2009**, 158, 118–130.
- [114] Hashim, R.; Hashim, H. H. A.; Rodzi, N. Z. M.; Hussen, R. S. D.; Heidelberg, T. *Thin Solid Films* **2006**, 509, 27–35.
- [115] Mannock, D. A.; McElhaney, R. N. *Curr. Opin. Colloid Interface Sci.* **2004**, 8, 426–447.
- [116] Yamashita, J.; Shiono, M.; Hato, M. *J. Phys. Chem. B* **2008**, 112, 12286–12296.
- [117] Hato, M.; Yamashita, J.; Shiono, M. *J. Phys. Chem. B* **2009**, 113, 10196–10209.

- [118] Vill, V.; von Minden, H. M.; Koch, M. H. J.; Seydel, U.; Brandenburg, K. *Chem. Phys. Lipids* **2000**, *104*, 75–91.
- [119] Brooks, N. J.; Hamid, H. A. A.; Hashim, R.; Heidelberg, T.; Seddon, J. M.; Conn, C. E.; Mirzadeh Husseini, S. M.; Zahid, N. I.; Hussien, R. S. D. *Liq. Cryst.* **2011**, *38*, 1725–1734.
- [120] Sackmann, H.; Demus, D. *Mol. Cryst. Liq. Cryst.* **1973**, *21*, 239–273.
- [121] Bouligand, Y. In *Handbook of Liquid Crystals*; Demus, D., Goodby, J. W., Gray, G. W., Spiess, H. W., Vill, V., Eds.; Wiley-VCH: Weinheim, 1998; Vol. 1; pp 406–453.
- [122] Abramowitz, M.; Davidson, M. W. *Optical Birefringence*. <http://www.olympusmicro.com/primer/lightandcolor/birefringence.html> (accessed 24th December 2012).
- [123] Scharf, T. *Polarized Light in Liquid Crystals and Polymers*; John Wiley & Sons Inc.: New Jersey, 2007.
- [124] Murphy, D. B.; Davidson, M. W. *Fundamentals of Light Microscopy and Electronic Imaging*; 2nd ed.; John Wiley & Sons Inc.: New Jersey, 2012.
- [125] Stoiber, R. E.; Morse, S. A. *Crystal Identification with the Polarizing Microscope*; Chapman & Hall: New York, 1994.
- [126] Burgoyne, J.; Holmes, M. C.; Tiddy, G. J. *J. Phys. Chem.* **1995**, *99*, 6054–6063.
- [127] Funari, S. S.; Holmes, M. C.; Tiddy, G. J. *J. Phys. Chem.* **1994**, *98*, 3015–3023.
- [128] Höhne, G. W. H.; Hemminger, W. F.; Flammersheim, H.-J. *Differential Scanning Calorimetry*; 2nd ed.; Springer-Verlag: Berlin, 2003.
- [129] Laye, P. G. In *Principles of Thermal Analysis and Calorimetry*; Haines, P., Ed.; Royal Society of Chemistry: Cambridge, 2002; pp 55–93.
- [130] Kirschbrown, J. *Small-Angle X-ray Scattering: A Concise Review*; 2007.
- [131] Schnablegger, H.; Singh, Y. *The SAXS Guide*; Anton Paar GmbH: Graz, 2011.
- [132] SAXS Analysis in Structural Biology. Paar, A., Ed. Anton Paar GmbH: Graz, 2011.
- [133] Sawyer, L. C.; Grubb, D. T.; Meyers, G. F. *Polymer Microscopy*; Springer: New York, 2008.
- [134] Naik, P. V. *Principles of Physics*; 4th ed.; PHI Learning Pte. Ltd.: New Delhi, 2010.
- [135] Suryanarayana, C.; Norton, M. G. *X-Ray Diffraction: A Practical Approach*; Plenum Press: New York, 1998.
- [136] Valeur, B. *Molecular Fluorescence: Principles and Applications*; Wiley-VCH Verlag GmbH: Weinheim, 2002.
- [137] Lakowicz, J. *Principles of Fluorescence Spectroscopy*; 3rd ed.; Springer Verlag: New York, 2006; Vol. 1.
- [138] Sharma, A.; Schulman, S. G. *Introduction to Fluorescence Spectroscopy*; John Wiley & Sons Inc.: New York, 1999.

- [139] Chattopadhyay, A. *Chem. Phys. Lipids* **2003**, *122*, 3–17.
- [140] Parasassi, T.; Di Stefano, M.; Loiero, M.; Ravagnan, G.; Gratton, E. *Biophys. J.* **1994**, *66*, 763–768.
- [141] Wolber, P.; Hudson, B. *Biochemistry* **1981**, *20*, 2800–2810.
- [142] Koppel, D. E.; Axelrod, D.; Schlessinger, J.; Elson, E. L.; Webb, W. W. *Biophys. J.* **1976**, *16*, 1315–1329.
- [143] Saito, H.; Arais, T.; Shirahama, H.; Koyama, T. *J. Biochem.* **1991**, *109*, 559–565.
- [144] Arora, A.; Raghuraman, H.; Chattopadhyay, A. *Biochem. Biophys. Res. Commun.* **2004**, *318*, 920–926.
- [145] Douhal, A.; Amat-Guerri, F.; Acuña, A. U. *Angew. Chem. Int. Ed. Engl.* **1997**, *36*, 1514–1516.
- [146] García-Ochoa, I.; Díez López, M.-Á.; Viñas, M. H.; Santos, L.; Martínez Atáz, E.; Amat-Guerri, F.; Douhal, A. *Chem. Eur. J.* **1999**, *5*, 897–901.
- [147] Tormo, L.; Organero, J. A.; Cohen, B.; Martin, C.; Santos, L.; Douhal, A. *J. Phys. Chem. B* **2008**, *112*, 13641–13647.
- [148] Xu, J.; Topygin, D.; Graver, K. J.; Albertini, R. A.; Savtchenko, R. S.; Meadow, N. D.; Roseman, S.; Callis, P. R.; Brand, L.; Knutson, J. R. *J. Am. Chem. Soc.* **2006**, *128*, 1214–1221.
- [149] Kim, J.; Lu, W.; Qiu, W.; Wang, L.; Caffrey, M.; Zhong, D. *J. Phys. Chem. B* **2006**, *110*, 21994–22000.
- [150] Pierce, D.; Boxer, S. *Biophys. J.* **1995**, *68*, 1583–1591.
- [151] Callis, P. R.; Burgess, B. K. *J. Phys. Chem. B* **1997**, *101*, 9429–9432.
- [152] *Reviews In Fluorescence 2009*; Geddes, C. D., Ed.; Springer: New York, 2011; Vol. 6.
- [153] Itoh, H.; Ishido, S.; Nomura, M.; Hayakawa, T.; Mitaku, S. *J. Phys. Chem.* **1996**, *100*, 9047–9053.
- [154] Kalyanasundaram, K.; Thomas, J. K. *J. Am. Chem. Soc.* **1977**, *99*, 2039–2044.
- [155] Lianos, P. *J. Phys. Chem.* **1982**, *86*, 1935–1937.
- [156] Saxena, R.; Shrivastava, S.; Chattopadhyay, A. *J. Phys. Chem. B* **2008**, *112*, 12134–12138.
- [157] Somerharju, P. *Chem. Phys. Lipids* **2002**, *116*, 57–74.
- [158] Holmberg, K. *Novel Surfactants: Preparation, Applications, and Biodegradability*; 2nd ed.; Marcel Dekker: New York, 2003.
- [159] Ruiz, C. C. *Sugar-Based Surfactants: Fundamentals and Applications*; CRC Press/Taylor & Francis: Boca Raton, 2008; Vol 143.
- [160] *Glycolipids: New Research*; Sasaki, D., Ed.; Nova Science Publisher: New York, 2008.
- [161] Dembitsky, V.M. *Lipids* **2004**, *39*, 933–953.
- [162] Dembitsky, V.M. *Chem. Biodivers.* **2004**, *1*, 673–781.
- [163] Dembitsky, V. M. *Lipids* **2005**, *40*, 869–900.

- [164] Dembitsky, V. M. *Lipids* **2005**, *40*, 641–660.
- [165] Dembitsky, V. M. *Lipids* **2005**, *40*, 535–557.
- [166] Dembitsky, V. M. *Lipids* **2005**, *40*, 219–248.
- [167] Dembitsky, V. M. *Lipids* **2006**, *41*, 1–27.
- [168] Ernst, B.; Hart, G. W.; Sinaÿ, P. *Carbohydrates in Chemistry and Biology*; Wiley-VCH: Weinheim, 2000; Vol. 1.
- [169] Kates, M. *Glycolipids, Phosphoglycolipids, and Sulfoglycolipids*; Plenum Press: New York, 1990; Vol. 6.
- [170] Jeffrey, G. A. *Acc. Chem. Res.* **1986**, *19*, 168–173.
- [171] Jeffrey, G. A.; Maluszynska, H. *Carbohydr. Res.* **1990**, *207*, 211–219.
- [172] Vill, V.; Böcker, T.; Thiem, J.; Fischer, F. *Liq. Cryst.* **2006**, *33*, 1351–1358.
- [173] von Rybinski, W.; Hill, K. *Angew. Chem. Int. Ed.* **1998**, *37*, 1328–1345.
- [174] Balzer, D.; Lüders, H. *Nonionic Surfactants: Alkyl Polyglucosides*; Marcel Dekker: New York, 2000; Vol. 91.
- [175] Zhang, R.; Zhang, L.; Somasundaran, P. *J. Colloid Interface Sci.* **2004**, *278*, 453–460.
- [176] Warr, G. G.; Drummond, C. J.; Grieser, F.; Ninham, B. W.; Evans, D. F. *J. Phys. Chem.* **1986**, *90*, 4581–4586.
- [177] Auvray, X.; Petipas, C.; Dupuy, C.; Louvet, S.; Anthore, R.; Rico-Lattes, I.; Lattes, A. *Eur. Phys. J. E* **2001**, *4*, 489–504.
- [178] Bujarski, J. J.; Hardy, S. F.; Miller, W. A.; Hall, T. C. *Virology* **1982**, *119*, 465–473.
- [179] Lambert, O.; Levy, D.; Ranck, J. L.; Leblanc, G.; Rigaud, J. L. *Biophys. J.* **1998**, *74*, 918–930.
- [180] Sasaki, T.; Demura, M.; Kato, N.; Mukai, Y. *Biochemistry* **2011**, *50*, 2283–2290.
- [181] Li, J.; Sha, Y. *Molecules* **2008**, *13*, 1111–1119.
- [182] Abou-Zied, O. K. *J. Photochem. Photobiol. A* **2006**, *182*, 192–201.
- [183] Abou-Zied, O. K. *Chem. Phys.* **2007**, *337*, 1–10.
- [184] Andrade, S. M.; Costa, S. M. B. *Phys. Chem. Chem. Phys.* **1999**, *1*, 4213–4218.
- [185] Casassas, E.; Fonrodona, G.; Juan, A. *J. Solution Chem.* **1992**, *21*, 147–162.
- [186] Cheong, W. J.; Carr, P. W. *Anal. Chem.* **1988**, *60*, 820–826.
- [187] James, D. R.; Siemiarczuk, A.; Ware, W. R. *Rev. Sci. Instrum.* **1992**, *63*, 1710–1716.
- [188] Reichardt, C. *Chem. Rev.* **1994**, *94*, 2319–2358.
- [189] Reichardt, C. *Solvents and Solvent Effects in Organic Chemistry*; 3rd ed.; Wiley-VCH: Weinheim, 2003.
- [190] Suppan, P. *J. Photochem. Photobiol. A* **1990**, *50*, 293–330.
- [191] Suppan, P. *J. Lumin.* **1985**, *33*, 29–32.

- [192] Abou-Zied, O. K.; Al-Shihi, O. I. K. *Phys. Chem. Chem. Phys.* **2009**, *11*, 5377–5383.
- [193] Melo, E. C. C.; Costa, S. M.; Maçanita, A. L.; Santos, H. J. *Colloid Interface Sci.* **1991**, *141*, 439–453.
- [194] Belletete, M.; Lachapelle, M.; Durocher, G. J. *Phys. Chem.* **1990**, *94*, 5337–5341.
- [195] Belletête, M.; Lessard, G.; Durocher, G. J. *Lumin.* **1989**, *42*, 337–347.
- [196] Abou-Zied, O. K.; Al-Shihi, O. I. K. *J. Am. Chem. Soc.* **2008**, *130*, 10793–10801.
- [197] Abou-Zied, O. K.; Al-Lawatia, N.; Elstner, M.; Steinbrecher, T. B. *J. Phys. Chem. B* **2013**, *117*, 1062–1074.
- [198] Kinnunen, P. K. J.; Koiv, A.; Mustonen, P. In *Fluorescence Spectroscopy: New Methods and Applications*; Wolfbeis, O. S., Ed.; Springer-Verlag: New York, 1993; pp 159–171.
- [199] Ioffe, V.; Gorbenko, G. P. *Biophys. Chem.* **2005**, *114*, 199–204.
- [200] Haque, M. E.; Ray, S.; Chakrabarti, A. J. *Fluorescence* **2000**, *10*, 1–6.
- [201] Hoff, B.; Strandberg, E.; Ulrich, A. S.; Tieleman, D. P.; Posten, C. *Biophys. J.* **2005**, *88*, 1818–1827.
- [202] Karpovich, D. S.; Blanchard, G. J. *J. Phys. Chem.* **1995**, *99*, 3951–3958.
- [203] *Phospholipids Handbook*; Cevc, G., Ed.; Marcel Dekker Inc.: New York, 1993.
- [204] Chung, H.; Caffrey, M. *Nature* **1994**, *368*, 224–226.
- [205] Shearman, G. C.; Brooks, N. J.; Tiddy, G. J. T.; Sztucki, M.; Templer, R. H.; Law, R. V.; Ces, O.; Seddon, J. M. *Soft Matter* **2011**, *7*, 4386–4390.
- [206] Gruner, S. M. *J. Phys. Chem.* **1989**, *93*, 7562–7570.
- [207] Hughes, R. E.; Hart, S. P.; Smith, D. A.; Movaghar, B.; Bushby, R. J.; Boden, N. J. *Phys. Chem. B* **2002**, *106*, 6638–6645.
- [208] Conn, C. E.; Ces, O.; Mulet, X.; Finet, S.; Winter, R.; Seddon, J. M.; Templer, R. H. *Phys. Rev. Lett.* **2006**, *96*, 108102.
- [209] Seddon, J. M.; Squires, A. M.; Conn, C. E.; Ces, O.; Heron, A. J.; Mulet, X.; Shearman, G. C.; Templer, R. H. *Philos. Trans. R. Soc. A* **2006**, *364*, 2635–2655.
- [210] Hantzschel, D.; Schulte, J.; Enders, S.; Quitzsch, K. *Phys. Chem. Chem. Phys.* **1999**, *1*, 895–904.
- [211] Kocherbitov, V.; Söderman, O.; Wadsö, L. *J. Phys. Chem. B* **2002**, *106*, 2910–2917.
- [212] Teoh, T. C.; Hashim, R.; Bryce, R. A. *J. Phys. Chem. B* **2006**, *110*, 4978–4984.
- [213] de Campo, L.; Yaghmur, A.; Sagalowicz, L.; Leser, M. E.; Watzke, H.; Glatzer, O. *Langmuir* **2004**, *20*, 5254–5261.
- [214] Chernomordik, L. V.; Kozlov, M. M. *Annu. Rev. Biochem.* **2003**, *72*, 175–207.

- [215] Grossmann, G.; Opekarova, M.; Malinsky, J.; Weig-Meckl, I.; Tanner, W. *EMBO J.* **2007**, *26*, 1–8.
- [216] Kim, M.; Carman, C. V.; Springer, T.A. *Science* **2003**, *301*, 1720–1725.
- [217] Cantor, R.S. *Biochemistry* **1997**, *36*, 2339–2344.
- [218] Kulkarni, C.V. *Langmuir* **2011**, *27*, 11790–11800.
- [219] Tschierske, C. *J. Mater. Chem.* **2001**, *11*, 2647–2671.
- [220] Schwarz, U. S.; Gompper, G. *Phys. Rev. Lett.* **2000**, *85*, 1472–1475.
- [221] Anderson, D.M.; Gruner, S. M.; Leibler, S. *Pro. Natl. Acad. Sci. USA* **1988**, *85*, 5364–5368.
- [222] Larsson, K.; Tiberg, F. *Curr. Opin. Colloid Interface Sci.* **2005**, *9*, 365–369.
- [223] Barauskas, J.; Cervin, C.; Tiberg, F.; Johnsson, M. *Phys. Chem. Chem. Phys.* **2008**, *10*, 6483–6485.
- [224] Guerbet, M. *C. R. Acad. Sci. Paris* **1899**, *128*, 1002–1004.
- [225] O'Lenick, A.J. *J. Surfactants Deterg.* **2001**, *4*, 311–315.
- [226] Yasuda, M.; Arai, Y.; Kato, M.; Uehara, K.; Masakazu, O.; Kurosawa, T. JP 09-020628, 1997.
- [227] Hashim, R.; Mirzadeh, S.M.; Heidelberg, T.; Minamikawa, H.; Yoshiaki, T.; Sugimura, A. *Carbohydr. Res.* **2011**, *346*, 2948–2956.
- [228] Anderson, D.; Wennerstroem, H.; Olsson, U. *J. Phys. Chem.* **1989**, *93*, 4243–4253.
- [229] Derek, M. *Chem. Phys. Lipids* **2011**, *164*, 177–183.
- [230] Dinar, E.; Mentel, T. F.; Rudich, Y. *Atmos. Chem. Phys.* **2006**, *6*, 5213–5224.
- [231] Frisch, M. J.; et al. *Gaussian 09 2009*; Gaussian, Inc.: Wallingford CT, 2009.
- [232] Praefcke, K.; Singer, D.; Kohne, B.; Ebert, M.; Liebmann, A.; Wendorff, J. H. *Liq. Cryst.* **1991**, *10*, 147–159.
- [233] Laurent, N.; Lafont, D.; Dumoulin, F.; Boullanger, P.; Mackenzie, G.; Kouwer, P. H. J.; Goodby, J. W. *J. Am. Chem. Soc.* **2003**, *125*, 15499–15506.
- [234] Knothe, G. *Lipid Technol.* **2002**, *14*, 101–104.
- [235] Shearman, G. C.; Ces, O.; Templer, R. H.; Seddon, J. M. *J. Phys.: Condens. Matter* **2006**, *18*, S1105–S1124.
- [236] Illya, G.; Lipowsky, R.; Shillcock, J. C. *J. Chem. Phys.* **2005**, *122*, 244901.
- [237] Cantor, R. S. *Biophys. J.* **1999**, *76*, 2625–2639.
- [238] Mosapour Kotena, Z.; Behjatmanesh-Ardakani, R.; Hashim, R.; Achari, V. M. *J. Mol. Model.* **2012**, *19*, 589–599.
- [239] Sagnella, S. M.; Conn, C. E.; Krodkiewska, I.; Moghaddam, M.; Seddon, J. M.; Drummond, C. J. *Langmuir* **2010**, *26*, 3084–3094.
- [240] Shearman, G. C.; Ces, O.; Templer, R. H. *Soft Matter* **2010**, *6*, 256–262.
- [241] Qiu, H.; Caffrey, M. *Biomaterials* **2000**, *21*, 223–234.

- [242] Shinoda, K.; Carlsson, A.; Lindman, B. *Adv. Colloid Interface Sci.* **1996**, *64*, 253–271.
- [243] Israelachvili, J. N.; Mitchell, D. J.; Ninham, B. W. *J. Chem. Soc. Faraday Trans. 2* **1976**, *72*, 1525–1568.
- [244] Yang, J. P.; Qadri, S. B.; Ratna, B. R. *J. Phys. Chem.* **1996**, *100*, 17255–17259.
- [245] Luzzati, V. *Curr. Opin. Struct. Biol.* **1997**, *7*, 661–668.
- [246] Hyde, S.; Blum, Z.; Landh, T.; Lidin, S.; Ninham, B. W.; Andersson, S.; Larsson, K. *The Language of Shape: The Role of Curvature in Condensed Matter: Physics, Chemistry and Biology*; Elsevier Science B. V.: Amsterdam, 1996.
- [247] Landh, T. *FEBS Lett.* **1995**, *369*, 13–17.
- [248] Kraineva, J.; Smirnovas, V.; Winter, R. *Langmuir* **2007**, *23*, 7118–7126.
- [249] Ai, X.; Caffrey, M. *Biophys. J.* **2000**, *79*, 394–405.
- [250] Clogston, J.; Craciun, G.; Hart, D. J.; Caffrey, M. *J. Control. Release* **2005**, *102*, 441–461.

LIST OF SCIENTIFIC CONTRIBUTIONS

Publications

Academic Journal

1. N. Idayu Zahid, Charlotte E. Conn, Nicholas J. Brooks, Noraini Ahmad, John M. Seddon and Rauzah Hashim. Investigation on the Effect of Sugar Stereochemistry on Biologically Relevant Lyotropic Phases from Branched-chain Synthetic Glycolipids by Small-angle X-ray Scattering. *Soft Matter*, **2013** (under review).
2. N. Idayu Zahid, Osama K. Abou-Zied, Rauzah Hashim, and Thorsten Heidelberg. Fluorescence Probing of the Temperature-Induced Phase Transition in a Glycolipid Self-Assembly: Hexagonal \leftrightarrow Micellar and Cubic \leftrightarrow Lamellar. *Langmuir*, **2012**, 28, 4989–4995.
3. Nicholas J. Brooks, Hairul A. A. Hamid, Rauzah Hashim, Thorsten Heidelberg, John M. Seddon, Charlotte E. Conn, Seyed M. Mirzadeh Hussein, N. Idayu Zahid, and Rusnah Syahila Duali Hussen. Thermotropic and Lyotropic Liquid Crystalline Phases of Guerbet Branched-Chain β -D-glucosides. *Liquid Crystal*, **2011**, 38, 1725–1734.
4. N. Idayu Zahid, Osama K. Abou-Zied, Rauzah Hashim, and Thorsten Heidelberg. Characterization of the Head Group and the Hydrophobic Regions of a Glycolipid Lyotropic Hexagonal Phase Using Fluorescent Probes. *The Journal of Physical Chemistry C*, **2011**, 115, 19805–19810.

Proceeding Paper

1. N. I. M. Zahid, R. Hashim, and T. Heidelberg, Phase Behaviour of Nature-Like Branched-Chain Glycosides, Universiti Malaysia Terengganu 11th International Annual Symposium 2012, 9th–11th July 2012, Ri-Yaz Heritage Marina Resort & Spa, Kuala Terengganu, Malaysia, pp. 1063–1067.

Extended Abstract

1. Noor Idayu Mat Zahid, Rauzah Hashim, Thorsten Heidelberg and Osama K. Abou-Zied, Dynamic Studies of a Glycolipid Bilayer Using Tryptophan Probes, 6th Mathematics and Physical Sciences Graduate Congress 2010, 13th–15th December 2010, Faculty of Science, University of Malaya, Malaysia.

Presentations

Oral

1. Phase Behaviour of Nature-Like Branched-Chain Glycosides, Universiti Malaysia Terengganu 11th International Annual Symposium 2012, 9th–11th July 2012, Ri-Yaz Heritage Marina Resort & Spa, Kuala Terengganu, Malaysia.
2. Fluorescence Spectroscopy of a Glycolipid Self-Assembly Using Pyrene and Tryptophan Ester as Probes, Advanced Concepts and Applications on Functional Materials Workshop, 30th May–1st June 2011, Chemistry Department, University of Malaya, Malaysia.

Poster

1. Fluorescence Steady-State and Time-Resolved Spectroscopy of Glycolipid Self-Assembly Using Pyrene and Tryptophan Ester as Probes, Lipids and Membrane Biophysics: Faraday Discussion 161, 11th–13th September 2012, Burlington House, London, United Kingdom.
2. Probing the Glycolipid Self-Assembly Phases by Fluorescence Steady-State and Time-Resolved Spectroscopy, NanoFormulation 2012, 28th May–1st June 2012, Fira Palace, Barcelona, Spain.
3. Fluorescence Spectroscopy of a Glycolipid Self-Assembly Using Pyrene and Tryptophan Ester as Probes, Fundamental Science of Self-Assembly Seminar 2012, 28th February 2012, Art Gallery, University of Malaya, Malaysia.
4. Fluorescence Spectroscopy of a Glycolipid Self-Assembly Using Pyrene and Tryptophan Ester as Probes, NanoFormulation 2011, 26th June–1st July 2011, SUNTEC, Singapore.

5. Dynamic Studies of a Glycolipid Bilayer Using Tryptophan Probes, 6th Mathematics and Physical Sciences Graduate Congress 2010, 13th–15th December 2010, Faculty of Science, University of Malaya, Malaysia.

Awards

1. Selected to represent Malaysia in the 63rd Lindau Nobel Laureate Meeting with Young Scientists (Chemistry) from 30th June–5th July 2013 in Lindau, Germany.
2. Travel grant awarded by InForm FP 7 for participation in the NanoFormulation 2011 from 26th June–1st July 2011 in Singapore.